

REPORT DOCUMENTATION PAGE			Form Approved OMB NO. 0704-0188		
<p>The public reporting burden for this collection of information is estimated to average 1 hour per response, including the time for reviewing instructions, searching existing data sources, gathering and maintaining the data needed, and completing and reviewing the collection of information. Send comments regarding this burden estimate or any other aspect of this collection of information, including suggestions for reducing this burden, to Washington Headquarters Services, Directorate for Information Operations and Reports, 1215 Jefferson Davis Highway, Suite 1204, Arlington VA, 22202-4302. Respondents should be aware that notwithstanding any other provision of law, no person shall be subject to any penalty for failing to comply with a collection of information if it does not display a currently valid OMB control number.</p> <p>PLEASE DO NOT RETURN YOUR FORM TO THE ABOVE ADDRESS.</p>					
1. REPORT DATE (DD-MM-YYYY) 12-01-2011		2. REPORT TYPE Final Report		3. DATES COVERED (From - To) 1-Jun-2004 - 31-Jul-2010	
4. TITLE AND SUBTITLE Nano Engineered Energetic Materials (NEEM)			5a. CONTRACT NUMBER W911NF-04-1-0178		
			5b. GRANT NUMBER		
			5c. PROGRAM ELEMENT NUMBER 611103		
6. AUTHORS David Allara, Dana Dlott, Tim Eden, Greg Girolami, Rajiv Kalia, Kenneth Kuo, Aiichiro Nakano, Ralph Nuzzo, Priya Vashishta, Vigor Yang, and Richard Yetter			5d. PROJECT NUMBER		
			5e. TASK NUMBER		
			5f. WORK UNIT NUMBER		
7. PERFORMING ORGANIZATION NAMES AND ADDRESSES Pennsylvania State University Office of Sponsored Programs The Pennsylvania State University University Park, PA 16802 -7000			8. PERFORMING ORGANIZATION REPORT NUMBER		
9. SPONSORING/MONITORING AGENCY NAME(S) AND ADDRESS(ES) U.S. Army Research Office P.O. Box 12211 Research Triangle Park, NC 27709-2211			10. SPONSOR/MONITOR'S ACRONYM(S) ARO		
			11. SPONSOR/MONITOR'S REPORT NUMBER(S) 46655-EG-MUR.2		
12. DISTRIBUTION AVAILABILITY STATEMENT Approved for Public Release; Distribution Unlimited					
13. SUPPLEMENTARY NOTES The views, opinions and/or findings contained in this report are those of the author(s) and should not be construed as an official Department of the Army position, policy or decision, unless so designated by other documentation.					
14. ABSTRACT The ARO Nano Engineered Energetic Materials (NEEM) MURI program has been exploring new methodologies for developing energetic material formulations with control of all constituents over a wide range of length scales from 1 nm to 1 mm and larger and employing the latest techniques in molecular self-assembly and supramolecular chemistry for synthesizing and assembling NEEMs. The synthetic efforts have been guided by theoretical calculations and dynamic performance testing methodologies that also operate on all length scales. This final report					
15. SUBJECT TERMS Energetic materials, nanotechnology, nano aluminum, self-assembly, supercritical fluid processing, atomistic and molecular dynamics modeling, ultra-fast molecular spectroscopy, combustion					
16. SECURITY CLASSIFICATION OF:		17. LIMITATION OF ABSTRACT		15. NUMBER OF PAGES	19a. NAME OF RESPONSIBLE PERSON
a. REPORT UU	b. ABSTRACT UU	c. THIS PAGE UU	UU		Richard Yetter
					19b. TELEPHONE NUMBER 814-863-6375

## Report Title

### Nano Engineered Energetic Materials (NEEM)

#### ABSTRACT

The ARO Nano Engineered Energetic Materials (NEEM) MURI program has been exploring new methodologies for developing energetic material formulations with control of all constituents over a wide range of length scales from 1 nm to 1 mm and larger and employing the latest techniques in molecular self-assembly and supramolecular chemistry for synthesizing and assembling NEEMs. The synthetic efforts have been guided by theoretical calculations and dynamic performance testing methodologies that also operate on all length scales. This final report provides a summary of the accomplishments. In particular, new methods to generate metal nanoclusters were developed that are stabilized against environmental degradation while preserving their high energy content. Rapid expansion supercritical solution processes were developed and applied to synthesize nanosized particulate oxidizers and energetic oxidizer shell/fuel core composites. Surface science and experimental chemistry methods were applied to study the structures and energy releasing reaction pathways of NEEMs. Unique diagnostic capabilities were developed and applied to study the fundamental mechanisms that underlie NEEM dynamic performance. Combustion mechanisms of various NEEMs, including nanothermites and nanoparticulate fuel/liquid oxidizer systems, were experimentally analyzed. The reactive and thermal characteristics of NEEMs were studied using large (billion atoms) multiscale simulations that couple quantum-mechanical calculations to molecular dynamics calculations. In particular, the stability, structure and energetics of metallic nanoparticles with a special focus on the relationships between particle size, shape and excess surface free energy were studied. A unified theory of ignition and combustion of aluminum particles for a wide range of sizes, from nano to meso scales was established.

#### List of papers submitted or published that acknowledge ARO support during this reporting period. List the papers, including journal references, in the following categories:

##### (a) Papers published in peer-reviewed journals (N/A for none)

1. "A metascalable computing framework for large spatiotemporal-scale atomistic simulations," K. Nomura, H. Dursun, R. Seymour, W. Wang, R. K. Kalia, A. Nakano, P. Vashishta, F. Shimojo, and L. H. Yang, in Proceedings of the 2009 International Parallel and Distributed Processing Symposium (IEEE, Rome, Italy, 2009)
2. "Density functional study of 1,3,5-trinitro-1,3,5-triazine molecular crystal with van der Waals interactions," F. Shimojo, Z. Wu, A. Nakano, R. K. Kalia, and P. Vashishta, *Journal of Chemical Physics* 132, 094106: 1-8 (2010)
3. P. Puri, V. Yang, Effect of Voids and Pressure on Melting of Nano-Particulate and Bulk Aluminum, *Journal of Nanoparticle Research*, Vol. 11 (5), 2009, pp.1117-1127
4. P. Puri, V. Yang, Thermo-mechanical Behavior of Nano Aluminum Particles with Oxide Layers During Melting, *Journal of Nanoparticle Research*, 2010, Available Online (DOI: 10.1007/s11051-010-9889-2)
5. Y. Huang, G.A. Risha, V. Yang, R.A. Yetter, Effect of Particle Size on Combustion of Aluminum Particle Dust in Air, *Combustion and Flame*, Vol.156, 2009, pp.5-13
6. Essel, J. T., Cortopassi, A. C., and Kuo, K. K., "Synthesis and Characterization of Coated Energetic Materials Using a RESS System," Accepted for publication in the *International Journal of Energetic Materials and Chemical Propulsion*, 2010
7. Wawiernia, T. M., Cortopassi, A. C., Essel, J. T., Ferrara, P. J., and Kuo, K. K., "Nano-RDX Synthesis by RESS Process and Sensitivity Characterization," Accepted for publication in the *International Journal of Energetic Materials and Chemical Propulsion*, 2010
8. Peng, Y. J., Wang, Y. H., Zhang, S. P., Dlott, D. D., and Yang, Y. Q., Simulation of the absorption spectroscopy of nanometallic aluminum particles with core-shell structure, *J. Nanoparticle Res.* 12, 777-787 (2010).
9. Conner, R. W. and Dlott, D. D., Ultrafast condensed-phase emission from aluminized explosives: Nano-aluminum in Teflon, *J. Phys. Chem.* 114, pp. 6731-6741.
10. Fujiwara, H., Brown, K. E., and Dlott, D., Laser-driven flyer plates for reactive materials research, *AIP Conf. Proc.* 1195, 1317-1320 (2010).
11. Fujiwara, H., Brown, K. E., and Dlott, D. D., High-energy flat-top beams for laser launching using a Gaussian mirror, *Appl. Opt.* 49, 3723-3731 (2010).
12. Bellott, B. J.; Noh, W.; Nuzzo, R. G.; Girolami, G. S. Nanoenergetic materials: boron nanoparticles from the pyrolysis of decaborane and their functionalisation. *Chem. Commun.*, 2009, 22, 3214-3215.
13. Sabourin, JL; Yetter, RA; Asay, BW, et al., Effect of Nano-Aluminum and Fumed Silica Particles on Deflagration and Detonation of Nitromethane, *PROPELLANTS EXPLOSIVES PYROTECHNICS* 34, 5, 385-393, 2009.
14. Sabourin, JL; Yetter, RA; Parimi, S, Exploring the Effects of High Surface Area Metal Oxide Particles on Liquid Nitromethane Combustion, *JOURNAL OF PROPULSION AND POWER* 26, 5, 1006-1015, 2010.
15. Sabourin, JL; Dabbs, DM; Yetter, RA; Dryer, FL; Aksay, IA, Functionalized Graphene Sheet Colloids for Enhanced Fuel/Propellant Combustion, *ACS NANO* 3, 13, 3945-3954, 2009.
16. Weismiller, MR; Lee, JG; Yetter, RA Effects of Fuel and Oxidizer Particle Dimensions on the Propagation of Aluminum Containing Thermites, *PROCEEDINGS OF THE COMBUSTION INSTITUTE* Volume: 33, DECEMBER 2010.
17. Weismiller, MR; Lee, JG; Yetter, RA, Multiwavelength Pyrometry of Aluminum Containing Nano-Thermite Reactions *PROCEEDINGS OF THE COMBUSTION INSTITUTE* Volume: 33, DECEMBER 2010.
18. Malchi, JY; Foley, TJ; Yetter, RA, Electrostatically Self-Assembled Nanocomposite Reactive Microspheres *ACS APPLIED MATERIALS & INTERFACES* Volume: 1 Issue: 11 Pages: 2420-2423, 2009.

Number of Papers published in peer-reviewed journals: 18.00

---

**(b) Papers published in non-peer-reviewed journals or in conference proceedings (N/A for none)**

Number of Papers published in non peer-reviewed journals: 0.00

---

**(c) Presentations**

1. USC group, "Multibillion-atom simulations of nano-mechano-chemistry on petaflops computers," First International Symposium on Global Center of Excellence for Mechanical Systems Innovation, Tokyo, Japan, February 2, 2009
2. USC group, "Large spatiotemporal-scale material simulations on petaflops computers," Winter School on "Multiscale Simulation Methods in Molecular Sciences," Jülich, Germany, March 2, 2009
3. USC group, "Metascalable atomistic simulations of nano-mechano-chemistry on petaflops computers," European Materials Research Society 2009 Spring Meeting, Strasbourg, France, June 10, 2009
4. PSU group (Kuo), Essel, J. T., Cortopassi, A. C., and Kuo, K. K., "Synthesis and Characterization of Coated Energetic Materials Using a RESS System," presented at the 8th International Symposium on Special Topics of Chemical Propulsion, Cape Town, South Africa, 2009
5. PSU group (Kuo), Wawiernia, T. M., Cortopassi, A. C., Essel, J. T., Ferrara, P. J., and Kuo, K. K., "Nano-RDX Synthesis by RESS Process and Sensitivity Characterization," presented at the 8th International Symposium on Special Topics of Chemical Propulsion, Cape Town, South Africa, 2009
6. PSU group (Allara), Kinetic vs Thermodynamic Driving Forces in Formation of Nanostructured Assemblies at Interfaces, Dept. of Applied Physics, U. California Davis, 01/19/09
7. UIUC group (Dlott), (invited) Gordon Conference on Vibrational Dynamics at Surfaces, Proctor Academy, Andover, NH, Aug. 2009, "Dynamics at interfaces probed by time-resolved sum-frequency spectroscopy".
8. UIUC group (Dlott), (invited) 21st Century Needs and Challenges of Compression Science Workshop, Santa Fe, NM, Sept. 2009, "Shock compression of molecules with high time and space resolution"
9. UIUC group (Dlott), (invited) Federation of Analytical Chemistry and Spectroscopy Societies (FACSS) annual meeting, Louisville, KY, Oct. 2009. "Vibrational energy in molecules studied with 2D vibrational sum-frequency generation"
10. UIUC group (Dlott), (invited) Army Research Office Review of Nano-engineered energetic materials, Aberdeen, MD, Mar. 2010, "Ultrafast dynamics of NEEMs".
11. UIUC group (Dlott), (invited) American Chemical Society Annual Meeting, San Francisco, CA Mar. 2010, "Vibrational Energy in Molecules with High Time and Space Resolution"
12. UIUC group (Dlott), NATO Munitions Safety Information Analysis Center (MSIAC) Workshop on Insensitive Energetic Materials, Nato Headquarters, Brussels, Belgium, May 2010, "Molecular mechanisms of insensitive explosives".
13. UIUC group (Dlott), (invited) Army Research Office Symposium on Insensitive Energetic Materials, Aberdeen, MD, June 2010, "Fundamental Processes and Properties of Insensitive Energetic Materials".
14. UIUC group (Dlott), (invited) Gordon Research Conference on Noble Metal Nanoparticles, Mt. Holyoke MA, June 2010, "Ultrashort pulses and surface enhanced Raman scattering".
15. PSU group (Yetter), M.R. Weismiller, J.G. Lee, and R.A. Yetter, Temporally Analyzed Multi-wavelength Pyrometry of an Al/CuO Nanothermite, 2009 Fall Technical Meeting Organized by the Eastern States Section of the Combustion Institute and Hosted by the University of Maryland College Park, October 18-21, 2009.

Number of Presentations: 15.00

---

**Non Peer-Reviewed Conference Proceeding publications (other than abstracts):**

1. Conner, R. W. and Dlott, D. D., Ultrafast emission spectroscopy measurements of ignition of nano-aluminum in Teflon, Proceedings of the 2010 Technical Meeting of the Central States Section of The Combustion Institute submitted Feb 2010, 2010).
2. Essel, J. T., Cortopassi, A. C., and Kuo, K. K., "Rapid Expansion of Supercritical Solution for Synthesizing of Energetic Materials," presented at National Capital Region Energetics Symposium, La Plata, MD, April 27-28, 2009.

Number of Non Peer-Reviewed Conference Proceeding publications (other than abstracts):

2

---

**Peer-Reviewed Conference Proceeding publications (other than abstracts):**

---

**(d) Manuscripts**

1. P. Puri, V. Yang, Pyrophoricity of Aluminum at Nano Scales, Combustion and Flame, In review
2. D.S.Sundaram, P.Puri, V.Yang, Thermo-Mechanical Behavior of Nickel-Coated Nano-Aluminum Particles, 49th AIAA Aerospace Sciences Meeting, Orlando, Florida, Submitted
3. D.S. Sundaram, Y. Huang, P. Puri, G.A. Risha, R.A. Yetter, V. Yang, Flame Propagation of Nano-Aluminum-Water Mixture, Combustion and Flame, In Preparation
4. D.S. Sundaram, P. Puri, V. Yang, Thermo-Mechanical Behavior of Nickel-Coated Nano-Aluminum Particles, Journal of Physical Chemistry, In Preparation
5. P. Puri, D.S. Sundaram, V. Yang, Ignition and Combustion of Aluminum Particles at Micro and Nano Scales, Progress in Energy and Combustion Science, In Preparation
6. P. Puri, D.S. Sundaram, V. Yang, A Multi-Scale Theory on Ignition and Combustion of Aluminum Particles, Combustion and Flame, In Preparation
7. Charles W. Spicer, Brian J. Bellott, Richard L. Jew, Ralph G. Nuzzo, and Gregory S. Girolami "Aluminum and Boron Nanoparticles for High-Energy Applications"
8. Brian J. Bellott, Sergio I. Sanchez, Ralph G. Nuzzo, and Gregory S. Girolami "Highly Energetic Aluminum Nanoparticles 'passivated' with Transition Metal Nanoparticles"

**Number of Manuscripts:** 8.00

---

**Patents Submitted**

---

**Patents Awarded**

---

**Awards**

- Aiichiro Nakano, Fellow, American Physical Society, Division of Computational Physics (2009): For the development and implementation of scalable parallel and distributed algorithms for large-scale atomistic simulations to predict, visualize, and analyze reaction processes for novel nano-mechano-chemical phenomena encompassing diverse spatiotemporal scales.
  - Kenneth Kuo, In July 2010, Prof. Kenneth Kuo and Drew Cortopassi received the best paper award in the solid-rocket category from AIAA at the Joint Propulsion Conference, Nashville, Tennessee.
  - David Allara, Elected Fellow of The Royal Society of Chemistry, UK
  - UIUC (Dlott), Merck Fellowship in Analytical and Physical Chemistry (to Jeffrey A. Carter)
  - Gregory S. Girolami, Notre Dame University, South Ben, IN, 28 Aug 2009. "Microelectronics and Nanotechnology: The Chemistry of Chemical Vapor Deposition"
  - Richard A. Yetter, 2009 Best Poster Paper Award, Eighth International Symposium on Special Topics in Chemical Propulsion
- 

**Graduate Students**

<u>NAME</u>	<u>PERCENT SUPPORTED</u>
Jonathan Essel	0.30
Rusty Conner	0.50
Yuanxi Fu	0.25
Kathryn Brown	0.00
Jeffrey Carter	0.00
Brian Bellott	1.00
Dilip Srinivas Sundaram	1.00
Richard Clark	0.25
Steven Dean	
Mike Weismiller	
Andrew Cortopassi	0.00
Timothy Wawiernia	0.00
<b>FTE Equivalent:</b>	<b>3.30</b>
<b>Total Number:</b>	<b>12</b>

#### Names of Post Doctorates

<u>NAME</u>	<u>PERCENT SUPPORTED</u>
Orlando Cabarcos	1.00
Hiroki Fujiwara	1.00
Ken-ichi Nomura	0.75
Weiqiang Wang	0.80
<b>FTE Equivalent:</b>	<b>3.55</b>
<b>Total Number:</b>	<b>4</b>

#### Names of Faculty Supported

<u>NAME</u>	<u>PERCENT SUPPORTED</u>	National Academy Member
Rajiv K. Kalia	0.10	No
Aiichiro Nakano	0.10	No
Priya Vashishta	0.10	No
Vigor Yang	0.08	No
Dana D. Diott	0.08	No
Ralph G. Nuzzo	0.08	No
Gregory S. Girolami	0.08	No
David Allara	0.13	No
Kenneth K. Kuo		No
Richard A. Yetter	0.17	No
<b>FTE Equivalent:</b>	<b>0.92</b>	
<b>Total Number:</b>	<b>10</b>	

#### Names of Under Graduate students supported

<u>NAME</u>	<u>PERCENT SUPPORTED</u>
Aaron White	0.16
Sidharth Abrol	0.15
<b>FTE Equivalent:</b>	<b>0.31</b>
<b>Total Number:</b>	<b>2</b>

**Student Metrics**

This section only applies to graduating undergraduates supported by this agreement in this reporting period

The number of undergraduates funded by this agreement who graduated during this period: .....	1.00
The number of undergraduates funded by this agreement who graduated during this period with a degree in science, mathematics, engineering, or technology fields:.....	1.00
The number of undergraduates funded by your agreement who graduated during this period and will continue to pursue a graduate or Ph.D. degree in science, mathematics, engineering, or technology fields:.....	1.00
Number of graduating undergraduates who achieved a 3.5 GPA to 4.0 (4.0 max scale):.....	1.00
Number of graduating undergraduates funded by a DoD funded Center of Excellence grant for Education, Research and Engineering:.....	0.00
The number of undergraduates funded by your agreement who graduated during this period and intend to work for the Department of Defense .....	0.00
The number of undergraduates funded by your agreement who graduated during this period and will receive scholarships or fellowships for further studies in science, mathematics, engineering or technology fields: .....	0.00

**Names of Personnel receiving masters degrees**

<u>NAME</u>	
Aaron Lozano	
Jonathan Essel	
Mike Weismiller	
<b>Total Number:</b>	<b>3</b>

**Names of personnel receiving PHDs**

<u>NAME</u>	
Richard Clark	
Rusty Conner (anticipated 2010)	
Brian Bellot	
Mike Weismiller (anticipated 2011)	
<b>Total Number:</b>	<b>4</b>

**Names of other research staff**

<u>NAME</u>	<u>PERCENT SUPPORTED</u>	
Jongguen Lee	0.12	No
Eric Boyer	0.13	No
Ragini Acharya	0.06	No
Bao Zhang	0.06	No
Mary Newby	0.01	No
Mehan Sweeney	0.04	No
Tim Eden	0.08	No
John Potter	0.08	No
Patricia Wong	0.03	No
<b>FTE Equivalent:</b>	<b>0.61</b>	
<b>Total Number:</b>	<b>9</b>	

**Sub Contractors (DD882)**

**Inventions (DD882)**

**REPORT DOCUMENTATION PAGE (SF298)  
(Continuation Sheet)**

**Table of Contents**

List of Figures	2
List of Tables	8
I. Introduction	9
I.1 Objectives and Approach	9
I.2 Organization	10
II. Scientific Progress and Accomplishments	12
II.1 Synthesis and Assembly	12
II.1.1 Synthesis and functionalization of boron nanoparticles	12
II.1.2 Synthesis and functionalization of aluminum nanoparticles	14
II.1.3 Chemistry and Structure of Al-SAM Surfaces	19
II.1.4 Ultra-High Pressure Supercritical Fluid Processing of Energetic Materials	25
II.1.4.1 Different Supercritical Fluid Precipitation Processes	30
II.1.4.2 Motivation/Objectives	33
II.1.4.3 Experimental Procedure (Method of Approach)	36
II.1.4.4 Discussion and Results	51
II.1.4.5 Conclusions	69
II.2 Theoretical Modeling and Simulation	71
II.2.1 Scalable Parallel Algorithms for Multimillion-Atom Simulations of Chemical Reactions	71
II.2.2 Quantum Mechanical Calculation of an RDX Molecule on Aluminum Surface	72
II.2.3 Molecular Dynamics Simulation of Shock Compression of Self Assembled Monolayers	75
II.2.4 Fast Reaction Mechanisms of an Aluminum Nanoparticle with Crystalline and Amorphous Alumina Shells	76
II.2.5 Burning of Aluminum Nanoparticle by Slow Heating	79
II.2.6 Enhanced Reactivity of Nanothermite	84
II.2.7 Multi-Scale Modeling of Nano-Aluminum Particle Ignition and Combustion	88
II.2.7.1 Molecular Dynamic Simulations	89
II.2.7.2 Macroscale Theoretical Model	96
II.3 Experimental Characterization and Diagnostics	98
II.3.1 Ultrafast Diagnostics of Nano Energetic Materials	98
II.3.2 Combustion Dynamics of Nano Energetic Materials	107
II.3.2.1 Gaseous Oxidizers	107
II.3.2.2 Liquid Oxidizers	109
II.3.2.3 Solid Oxidizers	112
II.3.2.4 Electrostatic Self-Assembly of a Nanoscale Thermite System into ordered Microspheres	120
II.3.2.5 Energetic Properties of Ni/Al Composites Formed Through HVPC	121
III. Summary of Research	127
IV. Technology Transfer and Interactions	130
V. References	132

## List of Figures

<b>Figure 1</b>	NEEM MURI program structure.....	11
<b>Figure 2</b>	TEM images of the boron nanoparticles. The large net-like structure is the carbon grid used to support the sample.....	13
<b>Figure 3</b>	DSC results for boron nanoparticles as-prepared (brown), surface-fluorinated (red), and surface-brominated (green). .....	13
<b>Figure 4</b>	Above: TEM images of boron nanoparticles after oxidation. Red line shows the approximate thickness of the resulting boron oxide overlayer. Below: EELS line profile showing composition of oxidised boron nanoparticles from centre of particle outward. Note that the scales for the boron and oxygen contents are different. ....	14
<b>Figure 5</b>	(Left) $C_s$ -STEM micrograph of a Cu nanocrystal deposited on an Al nanoparticle, magnified from the boxed region in the inset (also on the left). Spots (numbered 1 and 2) at which EDX spectra were collected are marked with circles. (Top right) EDX spectra of the corresponding spot 1 (the Al particle) and 2 (the Cu nanoparticles). (Bottom right) XRD profile (in black) along with the Bragg peaks for bulk Al (in red) and bulk Cu (in green).....	16
<b>Figure 6</b>	(Left) $C_s$ -STEM micrograph of an Ag nanoparticle deposited on an Al nanoparticle, magnified from the boxed region in the inset (also on the left). Spots (numbered 1 and 2) at which EDX spectra were collected are marked with circles. (Top right) EDX spectra of spot 1 (the Al particle) and 2 (the Ag nanocrystal). (Bottom right) The XRD profile (in black) along with the Bragg peaks for bulk Al (in red) and bulk Ag (in green). ....	16
<b>Figure 7</b>	(Left) $C_s$ -STEM micrograph of a Au nanoparticle deposited on an Al nanoparticle, magnified from the boxed region in the inset (also on the left). Spots (numbered 1 and 2) at which EDX spectra were collected are marked with circles. (Top right) EDX spectra of spot 1 (the Al particle) and 2 (the Au nanocrystal). (Bottom right) The XRD profile (in black) along with the Bragg peaks for bulk Al (in red) and bulk Au (in green). ....	17
<b>Figure 8</b>	(Left) $C_s$ -STEM micrograph of a Ni nanoparticle deposited on an Al nanoparticle, magnified from the boxed region in the inset (also on the left). Spots (numbered 1 and 2) at which EDX spectra were collected are marked with circles. (Top right) EDX spectra of spot 1 (the Al particle) and 2 (the Ni nanocrystal). (Bottom right) The XRD profile (in black) along with the Bragg peaks for bulk Al (in red) and bulk Ni (in green). ....	17
<b>Figure 9</b>	(Left) $C_s$ -STEM micrograph of a Pd nanoparticle deposited on an Al nanoparticle, magnified from the boxed region in the inset (also on the left). Spots (numbered 1 and 2) at which EDX spectra were collected are marked with circles. (Top right) EDX spectra of spot 1 (the Al particle) and 2 (the Pd nanocrystal). (Bottom right) The XRD profile (in black) along with the Bragg peaks for bulk Al (in red) and bulk Pd (in green). ....	18
<b>Figure 10</b>	(Left) $C_s$ -STEM micrograph of a Pt nanoparticle deposited on an Al nanoparticle, magnified from the boxed region in the inset (also on the left). Spots (numbered 1 and 2) at which EDX spectra were collected are marked with circles. (Top right) EDX spectra of spot 1 (the Al particle) and 2 (the Pt nanocrystal). (Bottom right) The XRD profile (in black) along with the Bragg peaks for bulk Al (in red) and bulk Pt (in green). ....	18
<b>Figure 11</b>	Aluminum metal vapor deposited on p-nitrobenzenethiol SAM on a Au(111) surface. The $NO_2$ modes disappear after the addition of $\sim 1.8$ equivalent monolayers (1.8 deposited Al atoms per SAM molecule) of Al. [Ref Spectra, f- L. Andrews, M. Zhou, W. D. Bare <i>JPC</i> , 102 5019 (1998)]. .....	21
<b>Figure 12</b>	Depiction of different SAM molecules studied and their likely coordination with a deposited Al atom. A) <i>p</i> -nitrobenzoic acid B) 3,4 dinitrobenzoic acid C) (4'-nitrophenyl)ethynyl-4-benzenethiolate and D) 12-nitrododcanoic acid. ....	22
<b>Figure 13</b>	DFT calculated structure of two aluminum atoms complexed to a simulated SAM layer consisting of 8 molecules. ....	23

<b>Figure 14</b>	XPS of N 1s binding energy region of nitrodimer. A) The N1s peak shifts as increasing amounts of Al metal vapor are deposited on the SAM. B) Similar to A except the SAM is initially doped with an equivalent monolayer of K metal. ....	24
<b>Figure 15</b>	Initially deposited Al metal begins to complex the oxygen atoms present in the nitro functional groups. As the oxygen reacts with aluminum, a protective layer is formed which prevents further Al from reaching the bulk of the SAM monolayer. ....	25
<b>Figure 16</b>	Projected drop height $H_{50}$ vs. inverse crystal size of energetic materials (from Armstrong [72]). ....	26
<b>Figure 17</b>	Potential propellant or explosive benefits from oxidizer (red) coating on metal (black) nano-sized particles (shaded portion could have oxidizer particles and binders).....	28
<b>Figure 18</b>	Density-pressure diagram of $CO_2$ (point A is supercritical fluid state and point B is a gas-phase state). ....	30
<b>Figure 19</b>	Solubility of RDX in Carbon Dioxide. [101]. ....	30
<b>Figure 20</b>	Description of the RESS process.....	31
<b>Figure 21</b>	FE-SEM image of Class I Type II RDX. ....	34
<b>Figure 22</b>	Molecular structure of BTAT molecule [109]. ....	35
<b>Figure 23</b>	FE-SEM images of BTAT before supercritical fluid processing. ....	35
<b>Figure 24</b>	FE-SEM images of uncoated ALEX <sup>®</sup> aluminum particles.....	35
<b>Figure 25</b>	Flow Diagram of Ultra-High-Pressure RESS System. ....	36
<b>Figure 26</b>	Test cell portion of RESS system. ....	37
<b>Figure 27</b>	Cross-sectional view of the saturation vessel. ....	38
<b>Figure 28</b>	Cross-sectional view of the nozzle assembly for the RESS system. ....	39
<b>Figure 29</b>	Pressure-enthalpy phase diagram of $CO_2$ illustrating the isenthalpic expansion path from pre-expansion temperature and pressure conditions. ....	40
<b>Figure 30</b>	Remotely controlled portion of RESS system.....	41
<b>Figure 31</b>	RDX coated glass beads located in saturation vessel. ....	41
<b>Figure 32</b>	Schematic representation of the RESS-AS process.....	42
<b>Figure 33</b>	Flow diagram of RESS-AS process. ....	43
<b>Figure 34</b>	RESS-AS expansion vessel. ....	44
<b>Figure 35</b>	Zeta Potential of RDX in water. ....	45
<b>Figure 36</b>	Adopted dispersing agents a) 1-Vinyl-2-pyrrolidinone (NVP) and b) Sodium Dodecyl Sulfate (SDS). ....	45
<b>Figure 37</b>	ALEX <sup>®</sup> Particle Coating Concept with the RESS-N process.....	46
<b>Figure 38</b>	Flow diagram for coating nano-sized aluminum particles by the RESS-N process with particle entrainment vessel. ....	47
<b>Figure 39</b>	Particle entrainment vessel for introducing aluminum particles into a supercritical solution. ....	48
<b>Figure 40</b>	Cross-sectional view of particle entrainment vessel.....	48
<b>Figure 41</b>	Captured particles in dry ice in the collection container. ....	49
<b>Figure 42</b>	RESS-N flow diagram for particle injection. ....	50
<b>Figure 43</b>	Linear actuated nano-sized aluminum particle injector.....	51
<b>Figure 44</b>	FE-SEM images of RESS synthesized RDX particles. ....	53
<b>Figure 45</b>	Particle size distributions for 100 $\mu$ m nozzle with a) $T_0=328$ K b) $T_0=348$ K. ....	54
<b>Figure 46</b>	Particle size distributions for 150 $\mu$ m nozzle with a) $T_0=328$ K b) $T_0=348$ K. ....	54
<b>Figure 47</b>	Median RDX particle sizes for 100- $\mu$ m nozzle a) $T_0=328$ K b) $T_0=348$ K.....	55
<b>Figure 48</b>	Median RDX particle sizes for 150- $\mu$ m nozzle a) 328 K b) 348 K.....	55
<b>Figure 49</b>	XRD data for RESS synthesized RDX.....	56
<b>Figure 50</b>	FE-SEM Image of RESS Synthesized BTAT Particles ( $P_0=68.9$ MPa, $T_0=323$ K).....	59
<b>Figure 51</b>	Images taken during RESS-AS tests a) without a dispersing agent and b) with a dispersing agent. ....	60
<b>Figure 52</b>	Close-up view of the discharging jet during a RESS-AS test. ....	60

<b>Figure 53</b>	RESS-AS for producing nano-sized RDX in H <sub>2</sub> O (T <sub>0</sub> =353 K, P <sub>0</sub> =34.5 MPa) at a) 5,000x magnification and b) 60,000x magnification.....	61
<b>Figure 54</b>	Comparison of RDX particles produced at T <sub>0</sub> =353 K, P <sub>0</sub> =34.5 MPa between the a) RESS process and b) RESS-AS process in H <sub>2</sub> O under the same magnification.....	61
<b>Figure 55</b>	RESS-AS results of produced nano-sized RDX particles using SDS surfactant at a)2,000x magnification and b) 10,000x magnification.....	62
<b>Figure 56</b>	Size distribution of nano-sized RDX particles synthesized by RESS-AS process, showing extremely small particle size with a narrow distribution.....	62
<b>Figure 57</b>	FE-SEM image of RESS-AS synthesized BTAT particles with neat water, showing significant agglomeration. ....	63
<b>Figure 58</b>	RESS-AS synthesized BTAT particles in the SDS and water solution resulted in the shape of rectangular rods. ....	64
<b>Figure 59</b>	Representation of supercritical fluid expansion dispersion of ALEX <sup>®</sup> particles.....	65
<b>Figure 60</b>	FE-SEM image of RDX coated ALEX particles from the particle entrainment vessel. ....	67
<b>Figure 61</b>	EDS spectrum of a section of test sample recovered from Test 008. ....	67
<b>Figure 62</b>	Comparison of SEM images of the recovered ALEX <sup>®</sup> coated with RDX with a)before strong electron beam exposure and b) after strong electron beam exposure. These images show deformation of the particles under electron beam radiation (more round particles are seen after a portion of the RDX was decomposed). ....	68
<b>Figure 63</b>	Comparison of SEM images of the recovered ALEX <sup>®</sup> coated with RDX with a)before strong electron beam exposure and b) after strong electron beam exposure. These images show significant mass loss from the particles under electron beam radiation (exposed ALEX <sup>®</sup> particles are clearly seen after RDX decomposition in image b). ....	69
<b>Figure 64</b>	Benchmark tests of reactive and nonreactive MD simulations on 1,920 Itanium2 processors of the Altix 3000 (open symbols), 2,000 Opteron processors (solid symbols), and 212,992 BlueGene/L processors. The execution time per MD step is shown as a function of the number of atoms for: EDC-DFT (circles); F-ReaxFF (squares); and MRMD (triangles). Lines show <i>O(N)</i> scaling. ....	72
<b>Figure 65</b>	Total execution (circles) and communication (squares) times per MD time step as a function of the number of processors <i>P</i> of BlueGene/L (open symbols) and BlueGene/P (solid symbols) for three MD simulation algorithms: (a) MRMD for 2,044,416 <i>P</i> atom silica systems; (b) F-ReaxFF MD for 16,128 <i>P</i> atom RDX systems; and (c) EDC-DFT MD for 180 <i>P</i> atom alumina systems. ....	72
<b>Figure 66</b>	Snapshots of DFT-based quantum mechanical MD simulation of an RDX molecule on Al (111) surface. At 193.48 fs, N1-O2 bond is broken and O2 starts bonding with an aluminum atom. Some other oxygen atoms are also bonding with aluminum atoms. Subsequently, more N-O bonds (N2-O4 and N3-O6) and an N-N are broken (483.7 fs), producing an NO fragment (denoted as N3-O5). Moreover, a ring of RDX, which consists of 3 carbon and 3 nitrogen atoms, is opened by a C-N bond breakage. At 967.4 fs, several oxygen atoms are completely dissociated from the RDX molecule and they oxidize the Al surface. The rest of the molecule is, however, still attached to the surface. ....	73
<b>Figure 67</b>	Temperatures of O and N atoms (upper panel), and C, H, and Al atoms (lower panel), in comparison with that of the RDX molecule and the total system. ....	74
<b>Figure 68</b>	Time variation of the Mulliken overlap populations of N-O bonds. N1-O2 bond is weakened and completely broken after 200 fs. The overlap populations of N1-O1, N2-O4 and N3-O6 bonds are decreased from the initial value of 0.8. ....	75
<b>Figure 69</b>	Code-up views of a shock compressed alkanethiol SAM at time 3 and 30 ps for <i>n</i> = 14 at temperature 300 K, where white, cyan and yellow spheres represent hydrogen, carbon and sulfur atoms, respectively.....	75
<b>Figure 70</b>	SFG intensities of a shock-compressed alkanethiol SAM as a function of time for <i>n</i> = 14 at temperature 300 K. ....	76

<b>Figure 71</b>	(a) Initial setup of the system consisting of a single aluminum nanoparticle embedded in oxygen. Most of the oxygen atoms surrounding the nanoparticle are not shown for clarity. To show the inside of the nanoparticle, a quarter of the nanoparticle has been removed. (b) Increase of kinetic energy per aluminum atom in the process of explosion for the C3, C6 and C9 systems.....	77
<b>Figure 72</b>	Snapshots of the nanoparticle at different times with initial core temperature of (a) 3000K, (b) 6000K, and (c) 9000K. The core aluminum is shown as white; shell aluminum, yellow; shell oxygen, red; and environmental oxygen, blue.....	78
<b>Figure 73</b>	(a) and (c) are snapshots of shell morphology with crystalline and amorphous shells, respectively, at 100 ps with colors representing the number density in the shell as shown by the color bar (in unit of # of atom/nm <sup>3</sup> ). (b) and (d) are snapshots of the shell morphology combined with core aluminum atoms (yellow) for the two systems. ....	79
<b>Figure 74</b>	Flowchart of runaway reaction leading to burning.....	80
<b>Figure 75</b>	(a) Temperature of particle during nanosecond simulation. (b) Rate of temperature change in system. Shift from confined burn into spallating burn (identified by red arrow).....	81
<b>Figure 76</b>	Radial temperature of particle during initiation phase. Initial heating seen at core-shell (inner) boundary.....	82
<b>Figure 77</b>	Fragment analysis of ANP during initiation phase.....	82
<b>Figure 78</b>	Time variation of the inner radius of shell boundary, showing increasing penetration of oxygen into core area throughout phase.....	82
<b>Figure 79</b>	Snapshots of central slice of particle during burn, hiding core Al atoms to allow viewing of oxygen penetration at 0 and 100 ps. ....	83
<b>Figure 80</b>	Graph of aluminum atoms present outside the outer shell boundary (i.e., ejected or spalled atoms). Shows transition from confined burn to spallation burn. ....	83
<b>Figure 81</b>	Fragment analysis of ANP during spallation burn phase, showing dramatic increase in oxygen-rich fragments.....	84
<b>Figure 82</b>	Snapshots of particle at 200 and 800 ps. Core aluminum atoms have been removed to show oxidation throughout core. ....	84
<b>Figure 83</b>	Snapshots of the atomic configuration. The green, red and grey spheres show the positions of Fe, O and Al atoms, respectively. Yellow meshes at time 0 ps show the non-overlapping cores used by the DC-DFT method. Two interfacial regions are defined as slabs with a thickness of 4 Å parallel to the <i>xy</i> plane (length scale in angstrom is marked in the <i>z</i> direction). The Al- and Fe-side regions are defined between the two interfacial regions as shown in the figure. ....	85
<b>Figure 84</b>	Enhanced diffusion at the metal-oxide interface. Mean square displacements of O atoms along the <i>z</i> direction are plotted as a function of time. The solid and dashed curves are for O atoms in the interfacial and Fe-side regions, respectively.....	86
<b>Figure 85</b>	Concerted metal-oxygen flip mechanism. (Top panel) Time evolution of the total and partial SBOP, $O_i(t)$ and $O_i^a(t)$ , associated with the oxygen atom labeled as ‘O’ in the bottom panel. The black, red and blue curves show $O_i(t)$ , $O_i^{Fe}(t)$ and $O_i^{Al}(t)$ , respectively. (Middle panel) Time evolution of the <i>z</i> coordinates of the O and Al atoms labeled as ‘O’ and ‘Al’ in the bottom panel, respectively. (Bottom panel) Atomic configurations near the O and Al atoms of interest (labeled as ‘O’ and ‘Al’) at 2.3 and 2.8 ps. The green, red and blue spheres are Fe, O and Al atoms, respectively. ....	86
<b>Figure 86</b>	(a) Negative correlation associated with concerted Al and O motions at the interface. Correlation functions between displacements of O and Al atoms along the <i>z</i> direction (defined in Eq. (1)) are shown as a function of time. The solid and dashed curves are obtained in the interfacial and Al-side regions. (b) Two-stage reactions of thermite. Time evolution of the positions $z_c(t)$ of the reaction fronts. The gray shade highlights the rapid first-stage reaction due to concerted Al-O motions, which is followed by slow reaction based on uncorrelated diffusion. ....	87

<b>Figure 87</b>	Size dependence on the melting point of pure Al (in vacuum). .....	90
<b>Figure 88</b>	Effect of void size on the melting point of (a) bulk aluminum; (b) 5.5 nm Al particle.....	90
<b>Figure 90</b>	Effect of core size and shell thickness on the melting points of the core and shell of nAl particles. ....	91
<b>Figure 89</b>	Diffusion of Al cations into the oxide shell.....	91
<b>Figure 91</b>	A unified theory on Al particle ignition and combustion.....	92
<b>Figure 92</b>	Melting points of Ni-coated Al cores. ....	93
<b>Figure 93</b>	(a) Infiltration temperature; (b) adiabatic reaction temperature rise. ....	94
<b>Figure 94</b>	Cross-sections of 14 nm particle (1 nm shell) at different temperatures (red is Al and green is Ni).....	95
<b>Figure 95</b>	Flame speed of Al-air mixture at 1 atm.....	96
<b>Figure 96</b>	Flame speed and temperature distributions of bi-modal (100 nm, 6.5 $\mu$ m) Al-air mixtures at 1 atm. ....	96
<b>Figure 97</b>	Variation of linear burning rate of nAl-water mixtures with pressure (38 nm, $\Phi=1$ ), equivalence ratio (3.65 MPa, 38 nm), and particle size (3.65 MPa, $\Phi=1$ ). ....	97
<b>Figure 98</b>	Diagnostics available in the laboratories of the UIUC team.....	98
<b>Figure 99</b>	Concept for flash-heating sample (left) and photos of a flash-heating array. ....	98
<b>Figure 100</b>	Nanosecond microscopy of the laser-induced explosion of nano(Al) + Teflon. Each frame represents an area 640 $\mu$ m wide. ....	99
<b>Figure 101</b>	Concept for ultrafast infrared probing of flash-heated nanoenergetics.....	99
<b>Figure 102</b>	Block diagram of femtosecond laser apparatus for flash-heating infrared. ....	100
<b>Figure 103</b>	(a) IR spectrum in CF stretch region of Teflon <sup>AF</sup> with and without nano(Al). (b) IR spectrum of Teflon. (c) IR spectrum of nanoenergetic before and after flash-heating.....	100
<b>Figure 104</b>	Time-dependent spectra of Teflon <sup>AF</sup> + nano(Al) after flash heating. ....	100
<b>Figure 105</b>	Sum-frequency spectra of alkane monolayer on Au heated at indicated temperatures. The narrower dips are CH-stretch transitions. The SAM decomposes at about 120°C.....	101
<b>Figure 106</b>	(a) Schematic of ultrafast flash-heating apparatus. (b) Some self-assembled monolayers we studied. (c) Model for heat transfer from metal fuel to monolayer. ....	101
<b>Figure 107</b>	Diagram of femtosecond laser apparatus used for flash-heating studies of monolayers on metal. ....	102
<b>Figure 108</b>	Sum-frequency spectrum of alkane self-assembled monolayer after flash heating to 800°C. CH-stretch transitions are the dips with labels in the spectra.....	102
<b>Figure 109</b>	Change in vibrational spectral intensity of the methyl groups at the ends of the self-assembled monolayers after flash-heating of the metal. The first real-time measurement of heat flow along a molecular chain.....	102
<b>Figure 110</b>	Pulse sequence to suppress the nonresonant (NR) background in sum-frequency spectroscopy. ....	103
<b>Figure 111</b>	Sum-frequency spectra of self-assembled monolayer with flash-heating using the non-resonant suppression method.....	103
<b>Figure 112</b>	Apparatus schematic for time-resolved emission measurements from flash-heated nanoenergetic materials.....	104
<b>Figure 113</b>	Photos of nanoenergetic materials after a single flash-heating pulse at the indicated fluence. Al/PB is nano(Al) in unreactive poly-(butadiene) and Al is nano(Al) alone. ....	104
<b>Figure 114</b>	Time-integrated emission after flash-heating of Al/Teflon, unreactive Al/PB and Al powder alone. ....	104
<b>Figure 115</b>	Ultrafast emission of Al/Teflon after flash-heating compared to unreactive Al/PB. The longer-duration emission in Al/Teflon gives time constants for ignition.....	105
<b>Figure 116</b>	Schematic diagram for laser-launched flyer plates and target array.....	106
<b>Figure 117</b>	Schematic of ultrafast fiber interferometer to measure the flight of laser-launched flyer plates. ....	106

<b>Figure 118</b>	(a) Target array for laser-launched flyer plates. (b) (c) recovered flyer plate and witness plate after launch. (d) Interferogram detailing launch, flight and impact at a velocity of 1.2 km/s. (f) Time dependence of emission due to impact with witness plate. ....	106
<b>Figure 119</b>	Emission from Ar compressed between 1.8 km/s flyer plate and witness plate. ....	107
<b>Figure 120</b>	Schematic representation of the experimental setup for nano aluminum propagation studies. ....	108
<b>Figure 121</b>	Three consecutive waves in baseline run with velocity ( $v_{ox}$ ) of 20 cm/s and oxygen concentration ( $\%O_2$ ) of 20%. ....	108
<b>Figure 122</b>	Photographs of fingering instability for nAl combustion reacting in air that show the integrated flame histories of beds of 38 nm nAl and a Peclet number ( $Pe$ ) of 3. ....	109
<b>Figure 123</b>	Flame front velocity ( $v_f$ ) vs. diameter of particle ( $d_p$ ). Flame front velocity ( $v_f$ ) vs. oxygen percentage ( $\%O_2$ ) in oxidizer ....	109
<b>Figure 124</b>	Burning rates of the Al- liquid water system as a function of pressure. ....	110
<b>Figure 125</b>	Chemical efficiency of the Al-liquid water reaction. ....	111
<b>Figure 126</b>	Captured images of the normal deflagration process of a nAl-H <sub>2</sub> O-H <sub>2</sub> O <sub>2</sub> mixture. ....	111
<b>Figure 127</b>	Effect of H <sub>2</sub> O <sub>2</sub> concentration on the mass burning rate per unit area of nAl/H <sub>2</sub> O mixtures. .	112
<b>Figure 128</b>	Linear and mass burning rates of mixtures of 38-nm aluminum particles and nitromethane as a function of aluminum loading. ....	112
<b>Figure 129</b>	Schematic of tube (left) and slot (right) experiments. The largest tube used was acrylic. The smaller tubes are borosilicate glass thick walled capillary tubes. On the right are examples of two metal slot sizes showing the entire channel and the reservoir at the ends of the channels. ....	113
<b>Figure 130</b>	Part a) is the measured propagation rate as a function of mass fraction of nAl (%). In part b), calculated adiabatic temperature and total gas products are shown. ....	114
<b>Figure 131</b>	Propagation velocity as a function of inverse diameter. Propagation velocity as a function of the inverse of hydraulic diameter. ....	114
<b>Figure 132</b>	Typical position versus time graphs for reaction waves in the burn tube with various weight percentages of Al <sub>2</sub> O <sub>3</sub> . ....	116
<b>Figure 133</b>	Comparison of average experimental peak pressure values in the burn tube to the calculations for the peak pressure with added Al <sub>2</sub> O <sub>3</sub> percentage for constant volume explosion. ....	116
<b>Figure 134</b>	Linear burning rate versus chamber pressure for nanoscale Al/CuO. ....	117
<b>Figure 135</b>	Intensity and temperature versus time results for Al/CuO ( $\Phi=1.1$ ) nano-thermite burn tube experiment. ....	117
<b>Figure 136</b>	High speed camera images for Al/CuO ( $\Phi=1.1$ ) nano-thermite burn tube experiment, illustrating the thickness of the temperature rise. ....	118
<b>Figure 137</b>	Equilibrium species concentration and gas generation for CuO decomposition assuming constant pressure (1 atm) and temperature conditions. ....	119
<b>Figure 138</b>	Linear burning rates of Al/CuO thermites ( $\phi=1.1$ ). ....	119
<b>Figure 139</b>	Pressure traces from dynamic pressure transducers positioned along the length of the burn tube during combustion of (a) nm-Al/nm-CuO, (b) $\mu$ m-Al/ $\mu$ m-CuO, (c) nm-Al/ $\mu$ m-CuO, and (d) $\mu$ m-Al/nm-CuO. ....	120
<b>Figure 140</b>	Schematic of salt formation and electrostatic self-assembly of particles. ....	121
<b>Figure 141</b>	SEMs of nAl and nCuO self-assembled nanothermite microspheres (SANTMs). The particles shown are a few micron in diameter. ....	121
<b>Figure 142</b>	Schematic of the HVPC system [193]. ....	122
<b>Figure 143</b>	Al/Ni propagation rates versus density. ....	123
<b>Figure 144</b>	Images of an Al/Ni HVPC-matching pellet ignition and combustion (70% TMD). ....	124
<b>Figure 145</b>	Images of a HVPC material ignition and propagation. ....	124
<b>Figure 146</b>	(left) DSC analysis of stoichiometric Ni/Al powder and (right) DSC analysis of HVPC-matching powder. ....	125

<b>Figure 147</b> (left) DSC of HVPC-matching powder and HVPC material and (right) DSC data from all tested materials. ....	125
<b>Figure 148</b> Schematic of LIBS experiment.....	126
<b>Figure 149</b> Illustration of laser induced plasma generation. ....	126
<b>Figure 150</b> LIBS spectra taken from cold-sprayed Al-Ni post reaction.....	127

## List of Tables

Table 1. Brief History of NEEM MURI Program.....	11
Table 2. Test matrix for studying effects pre-expansion conditions in the RESS process on RDX .....	52
Table 3. High performance liquid chromatography results for the chemical purity of RESS synthesized RDX .....	57
Table 4. RDX Sensitivity Testing Results Conducted Under Collaboration between PSU and NSWC-IHD .....	58
Table 5. Test Conditions for the RESS-N process with the particle entrainment vessel.....	66

## I. Introduction

Novel energetic materials science and nanotechnology are recognized as critical enablers in support of a changing armed-force structure that will require new and advanced explosives and propellants.

External to the energetic materials community, there has been tremendous progress in the molecular sciences toward the total command of chemistry at all length scales (supramolecular chemistry). This progress has been inspired primarily by advances in structural determination of biological systems, for instance the chromosome, where meter-long individual DNA molecules are intricately wound around protein spools to fit into micron-long cells, and the abalone shell, which consists of millions of intricate biological layers that provide scaffolds for the assembly of hard inorganic layers. Similar advancements in assembly of molecular and nanoscale elements have been made in the pharmaceutical and microelectronics fields as well. These developments make it clear that in the foreseeable future it will be possible to synthesize any desired macroscopic structure with precise location of every atom.

This document is the final report of the ARO MURI program on **Nano Engineered Energetic Materials (NEEM)**, which has been exploring new methodologies for development of energetic material formulations with control of all constituents on all length scales from 1 nm to 1 mm and larger. In particular, new methods employing the latest techniques in molecular self-assembly and supramolecular control for synthesizing and assembling nano-structured energetic materials were studied. The synthetic efforts of the program were guided by state-of-the-art theoretical calculations and advanced dynamic performance testing methodologies that also operate on all length scales.

Out the outset of this program, two critical observations relevant to the future development of nanostructured energetic materials were made: *(1) self-assembly and supramolecular chemistry of the fuel and oxidizer elements of energetic materials has lagged far behind other chemistries, and (2) there is no fundamental understanding of exactly what supramolecular structures provide desirable performance, mechanical, and hazard characteristics. With advancements on these two fronts, it is conceivable that macroscale formulations of energetic materials could be designed to preserve the intrinsic nanoscale structure of individual components, thus achieving the true potential of nanoscale energetic materials.*

### I.1 Objectives and Approach

The two overall objectives of the NEEM MURI program were:

- The development of new methodologies for synthesis and assembly of nano-engineered energetic materials (NEEMs), which will also provide concurrent improvement in performance and managed energy release while providing reduced sensitivity and ease of processing and handling.
- The fundamental understanding of the relationship between the structures of NEEMs and their reactive and mechanical behavior, particularly with regard to sensitivity, ignition, burning characteristics, mechanical properties, and optimum loading density, thus enabling design optimization of NEEMs.

To accomplish these objectives, the program made use of a combination of novel nanotechnology fabrication techniques, state-of-the-art theoretical modeling techniques that can interrogate events occurring from the atomistic/molecular scale through the mesoscale to the macroscale, and experimental diagnostic techniques that can capture the reactive dynamics at femtosecond timescales to those that evaluate overall combustion performance. As will be evident from the details of the report below, the program has made significant progress towards these objectives advancing the knowledge and understanding of nano-engineered energetic materials.

## I.2 Organization and Brief History

Scientists and engineers from three universities were included in the program: the Pennsylvania State University (PSU), the University of Illinois at Urbana-Champaign (UIUC), and the University of Southern California (USC). The team consisted of chemists with expertise at the juncture of organic and inorganic chemistry who were among the original developers of molecular self-assembly (**Allara, Nuzzo, Girolami**), mechanical engineers with expertise in the formulation of real, practical propellants (**Kuo, Yetter**), theoreticians who use teraflop supercomputers to understand the chemical reactions of fuels and oxidizers from the level of individual atoms (**Vashishta**) to the macroscale (**Nakano, Kalia, Yang**), a physical chemist who pioneered the use of ultrafast laser spectroscopy to study initiation of energetic materials (**Dlott**), and mechanical engineers with expertise in the experimental and theoretical characterization of real-world performance parameters of energetic materials (**Kuo, Yetter, Yang**).

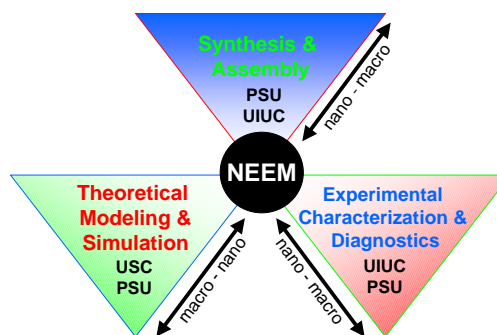


**Figure 1** NEEM MURI program structure.

The overall research program was divided into three major inter-related areas: (1) synthesis, self-assembly and supramolecular chemistry of NEEMs, (2) theoretical modeling of the physiochemical processes and mechanical behavior of NEEMs, and (3) experimental characterization of the reaction dynamics of NEEMs (**Fig. 1**).

A brief history of the NEEM MURI program is provided in Table 1.

**Table 1 Brief History of NEEM MURI Program**

Meeting	Location	Date
MURI Kickoff Meeting	Nittany Lion Inn, The Pennsylvania State University, University Park, PA	14 September 2004
ARO Annual Review of Nanoenergetic Materials Initiatives MURI / DURINT	Holiday Inn Aberdeen, Aberdeen, MD	16-17 November 2005
ARO 2 <sup>nd</sup> Annual Review of Nano Engineered Energetic Materials (NEEM) MURI	Aberdeen Proving Ground, Top of the Bay Officers' Club, Aberdeen, MD	7 November 2006
ARO 3 <sup>rd</sup> Annual Review of Nano Engineered Energetic Materials (NEEM) MURI	Battelle Science and Technology (BEST) Center, Aberdeen, MD	11 December 2007
ARO Final Review of Nano Engineered Energetic Materials (NEEM) MURI	Heat Center, Aberdeen, Maryland	15 March 2010

The present report provides a brief description of scientific progress and accomplishments during the entire program with an emphasis on the last 1½ years. Details of the research may be found in the many publications that resulted from the effort. In addition, some of the recent interactions and technology transfer among the team members and with the DoD and DOE scientists are described. Finally, publications, presentations, and demographics of the program are reported.

## II. Scientific Progress and Accomplishments

### II.1 Synthesis and Assembly

The objectives of this effort have been to develop new methodologies for synthesis and assembly of nano-structured energetic materials, to develop new methods to generate metal nanoclusters that are stabilized against environmental degradation while preserving their high energy content, and to develop strategies for manipulating the larger mesoscopic organization of high-energy nanoscale materials by directed design using soft lithographic techniques. These efforts have been led by **Nuzzo** and **Girolami** at **UIUC**. **Kuo** at **PSU** has applied rapid expansion solution processes to synthesize nanosized oxidizers and organic oxidizer shell/fuel core composites. An additional goal led by **Allara** at **PSU** was to use surface science and chemistry experimental methods to study the structures and energy releasing reaction pathways of nano-structured energetic materials (NEEMs) at the atomic/molecular scale, particularly Al metal atoms with nitro-containing oxidizers. A summary of important and recent results is provided below.

#### II.1.1 Synthesis and functionalization of boron nanoparticles

Elemental boron is a highly attractive fuel for propellants and explosives [1, 2]. Of all the chemical elements, boron has the highest volumetric heat of combustion ( $140 \text{ kJ/cm}^3$ ) and the third highest gravimetric heat of combustion ( $59 \text{ kJ/g}$ ), after  $\text{H}_2$  and Be. These values are over 3 times higher per unit volume, and 1.4 times higher per unit mass, than those of hydrocarbon fuels [3, 4].

In order to increase the rate of energy release during the combustion of boron and make it a more attractive fuel for propellants and explosives, it is advantageous to prepare it in a nanoparticulate form. Boron nanoparticles have been obtained previously from diborane by thermolysis at temperatures between  $700 \text{ }^\circ\text{C}$  and  $2250 \text{ }^\circ\text{C}$ , although often the size distribution produced is broad or the particles are extensively aggregated [5-7]. Boron nanoparticles have also been obtained by reduction of boron trihalides with  $\text{H}_2$  [5] or sodium naphthalenide [8]. Boron nanowires [9, 10] and thin films [11-20] have been grown by a variety of methods.

To incorporate nanoparticles into larger assemblies and to stabilize them for long term storage under ambient conditions, it is desirable to functionalize their surfaces. In addition, derivatization of boron nanoparticles with fluorine-containing groups could lead to significant increases in energy release, owing to both the kinetics and thermodynamics of  $\text{BF}_3$  formation [1]. Although there has been one previous report of the surface-modification of boron nanoparticles [8], the yield is low and there is only indirect evidence that the functional groups were actually resident on the particle surfaces. Here we describe the preparation of boron nanoparticles by a new method, and reaction chemistry that clearly results in derivitization of the particle surfaces.

Decaborane,  $\text{B}_{10}\text{H}_{14}$ , is an air stable crystalline solid that was at one time produced industrially on a scale of  $>1000$  tons/yr. It is known to decompose on surfaces at temperatures as low as  $200 \text{ }^\circ\text{C}$  to give boron films [11,15,18,19]. By adjusting the experimental procedure, we find that decaborane can also serve as a convenient starting material for the laboratory-scale preparation of boron nanoparticles. Passage of decaborane vapor in an Ar carrier at 1 atm through a hot zone at  $700\text{-}900 \text{ }^\circ\text{C}$  affords a grey-brown, non-pyrophoric powder. The powder consists of  $>97 \%$  boron and is free of hydrogen as judged by combustion analysis. The particles are easily suspended in organic solvents such as toluene and pentane, and the resulting suspensions settle slowly over the course of a few hours.

Transmission electron microscopy images show that the majority of the particles have diameters in the range 10 to 150 nm, and that they are textureless and quasispherical (**Fig. 2**). Two broad peaks at  $d$ -spacings of  $2.5 \text{ \AA}$  ( $2\theta = 35.0^\circ$ ) and  $4.0 \text{ \AA}$  ( $2\theta = 22.5^\circ$ ) are present in the Cu  $K\alpha$  XRD pattern. A Scherrer analysis of the XRD peak widths suggests that the crystalline domains are about  $25 \text{ \AA}$  in size. The small crystalline domain size is expected, because the nanoparticles are synthesized at temperatures far below

the 2075 °C melting point of boron [21]. The *d*-spacings and intensities are consistent with the  $\alpha$ -rhombohedral phase of boron [22,23,24]. However, the possibility that amorphous boron may also be present cannot be ruled out. The XPS spectrum of the as-prepared particles show a signal at 189 eV (B 1s); the value is higher than the reported value owing to charging effects [25-28]. Most notably, no evidence of any boron oxide phase is observed, which suggests that the as-synthesized boron particles are relatively inert towards oxidation at room temperature. (S)TEM-EELS analysis of the as-synthesized boron particles gives a signal at 210 eV that is also characteristic of pure boron.

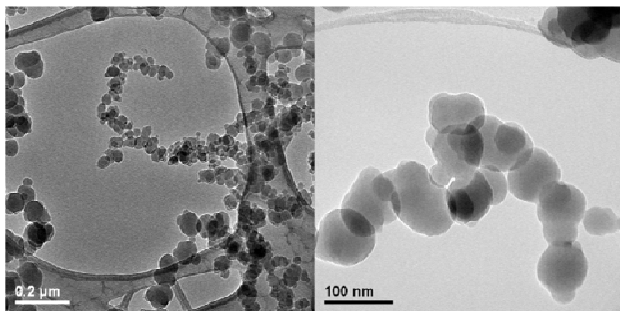


**Figure 2** TEM images of the boron nanoparticles. The large net-like structure is the carbon grid used to support the sample.

DSC experiments conducted on the boron nanoparticles under pure oxygen show that an exothermic reaction occurs with an onset temperature of 530 °C (**Fig. 3**). The amount of heat released, 17.2 kJ/g, indicates that, under these mild conditions, the oxidation of the nanoparticles is incomplete, and only the surfaces of the particles are oxidized. (S)TEM-EELS studies of boron nanoparticles heated in air for 4 hours at 600 °C show that a thin oxide shell (~7 nm thick) is present, with the core being pure boron (**Fig. 4**).

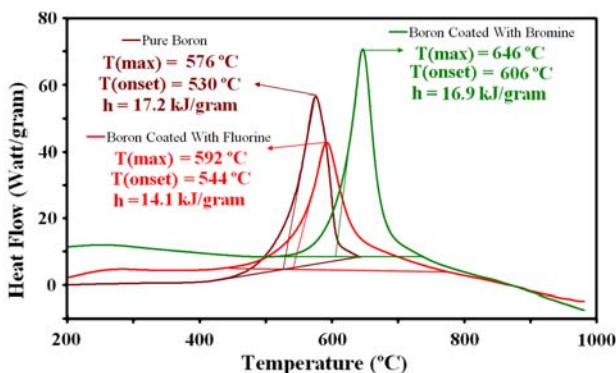


**Figure 3** DSC results for boron nanoparticles as-prepared (brown), surface-fluorinated (red), and surface-brominated (green).

Treatment of the boron nanoparticles with bromine in benzene for 12 h affords black nanoparticles with a bromine content of 4.1%. Similarly, treatment with a benzene solution of XeF<sub>2</sub> for 72 h affords grey particles whose surfaces are fluoride terminated. The XPS spectrum of the fluorinated particles shows signals at 189 eV (B 1s) and 691.0 eV (F 1s) due to bulk boron and to surface fluoride, respectively. As judged from an XPS depth profile study and a TOF-SIMS sputtering experiment, the fluorine atoms are confined to the surfaces of the particles, whereas the interiors remain pure boron.

DSC experiments show that the surface-halogenated particles are slightly passivated toward combustion under pure oxygen relative to the untreated material. The onset temperature for oxidation is

544 and 606 °C, respectively, for the fluorinated and brominated nanoparticles. The amount of heat released is 14.1 and 16.9 kJ/g for the F- and Br-terminated boron particles, respectively.

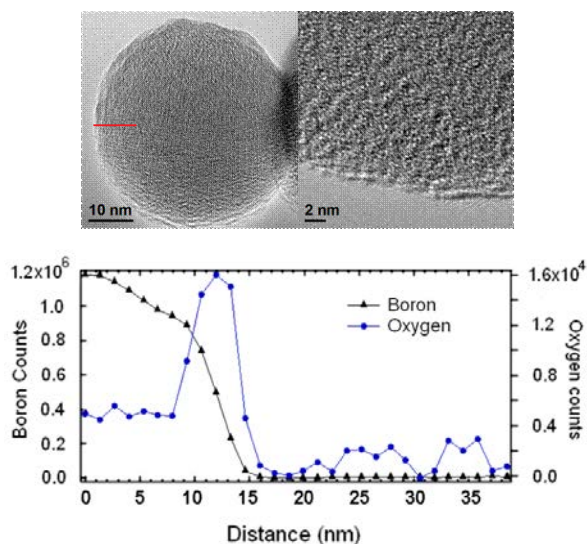


**Figure 4** Above: TEM images of boron nanoparticles after oxidation. Red line shows the approximate thickness of the resulting boron oxide overlayer. Below: EELS line profile showing composition of oxidised boron nanoparticles from centre of particle outward. Note that the scales for the boron and oxygen contents are different.

The present results show that highly pure boron nanoparticles can be synthesized by the gas phase pyrolysis of decaborane. The surface of the particles can be further functionalized by halogenation. Thermal analysis studies of the particles show that an exothermic combustion reaction takes place at temperatures above 500 °C, and that surface halogenation somewhat passivates the particles against further oxidation. Studies are underway to further exploit this new ability to prepare surface-functionalized boron nanoparticles.

### II.1.2 *Synthesis and functionalization of aluminum nanoparticles*

High energy nanomaterials such as nanothermites [29-32] and Al nanoparticles [33-36] have been a topic of increasing research for applications as propellants and explosives [37-42]. It is well known that a strong correlation often exists between the energy density of a nanomaterial and its sensitivity; a related issue is that nanoparticles are strongly driven to agglomerate and densify, owing to their relatively high surface free energies [43]. Considerable effort has been directed towards the development of chemistries to decouple these phenomena and thus make the materials safer and easier to handle [43]. One approach toward achieving this goal is to passivate the nanomaterials by functionalizing their surfaces [44,45]. The Al clusters of interest in this work present an additional challenge related to their sensitivity to oxidative decomposition [46]. An important goal of this research is to identify and develop new methods that will generate Al nanoclusters that are effectively stabilized against environmental degradation. These chemistries must also preserve the value of the cluster as a high-energy additive material.

It has been shown that treating Al nanoparticles with long chain carboxylic acids [47,48] or perfluoroalkyl carboxylic acids [49] increases the active aluminum content compared to unpassivated Al nanoparticles, owing to the surface oxidation of the unpassivated particles. The major drawback with utilizing organic capping groups is the lowering of weight percent active Al compared to the content of organic material.

In 2005, Higa and co-workers reported the use of transition metals to inhibit the formation of an oxide layer over the surface of aluminum nanoparticles [50]. They claimed that treatment of aluminum particles with solutions of certain transition metal complexes resulted in the deposition of a uniform coat

of the zerovalent transition metal [50]. These reactions, which take advantage of the strongly reducing nature of metallic aluminum, may be termed redox transmetalation reactions [51-55]. The metal complexes are reduced to the zerovalent state, the resulting transition metal atoms deposit on the surface, and at the same time the aluminum is oxidized to  $\text{Al}^{3+}$ , which dissolves in the solvent. The authors proposed that a thin layer of amorphous transition metal coated the entire surface of the Al nanoparticle, although this assertion has not been proven.

This study is intended to provide definitive information about the three-dimensional composite architectures that these reactions actually generate. Advanced analytical electron microscopy techniques [56] were used to image and differentiate the metallic components in atomistic detail. Instead of coating the entire surface of the aluminum nanoparticle with a thin shell of transition metal, the aluminum nanoparticles were found to be decorated with smaller crystalline transition metal nanoparticles that form an incomplete shell.

Aluminum particles were synthesized by thermolysis of dimethylethylamine-alane in toluene/triethylamine, in the presence of a titanium(IV) isopropoxide catalyst. Powder X-ray diffraction experiments showed that the as-prepared (untreated) aluminum particles are crystalline, and give distinct Bragg peaks at  $2\theta = 38.5, 44.7, 65.1,$  and  $78.2^\circ$  that respectively correspond to the d-spacings associated with the (111), (002), (022) and (113) planes in face-centered-cubic (fcc) aluminum [57]. Additionally, X-ray photoelectron spectroscopy (XPS) analysis shows the characteristic binding energy for Al 2p electrons at 73 eV [26].

The freshly prepared Al particles were then treated at room temperature under argon with 0.08 equiv of a transition metal complex in 1,2-dimethoxyethane, in order to deposit the transition metals on the surfaces of the Al particles. The surface derivatizing agents studied were the coinage metal complexes  $\text{Cu}(\text{acac})_2$ ,  $\text{Ag}(\text{acac})$ , and  $\text{AuCl}(\text{SMe}_2)$ , and the nickel subgroup complexes  $\text{Ni}(\text{acac})_2$ ,  $\text{Pd}(\text{acac})_2$ , and  $\text{Pt}(\text{acac})_2$ , where  $\text{acac} = 2, 4$ -pentanedionate. After a reaction time of 17 h, the treated Al particles were collected, washed, and dried under vacuum. The resulting particles, recovered in 70-90% yields, are highly reactive and spontaneously combust in air. They vary in sizes ranging from 10 to 250 nm with an average size of  $68 (\pm 52 \text{ nm})$  (SI 1), this mean was unchanged after treatment.

Using the Al/Ni system as a case study, we determined how the final composition of the nickel-treated Al particles depends on the reaction temperature, reaction time, and transition metal complex loading. Somewhat surprisingly, these reaction parameters have very little influence on the final compositions. Specifically, the nickel content is identical for Al particles treated for 17 h with 0.08 equiv of  $\text{Ni}(\text{acac})_2$  at 25 °C, at 40 °C, and at 80 °C (refluxing dme). Similarly, for treatment with 0.08 equiv of  $\text{Ni}(\text{acac})_2$  at room temperature, the composition is identical for reaction times of 1, 2.5, 3.5, 18, and 72 h.

The transition metals are confined to the surfaces of the particles and the particle interiors are still pure Al, as shown by XPS experiments conducted with argon sputtering. Spherical aberration-corrected scanning transmission electron microscopy ( $\text{C}_s$ -STEM) images were acquired for both as-prepared Al particles and particles that had been treated with the transition and the results should be interpreted accordingly. **Figures 5-10** show Al particles treated with copper, silver, gold, nickel, palladium, and platinum complexes in that order.

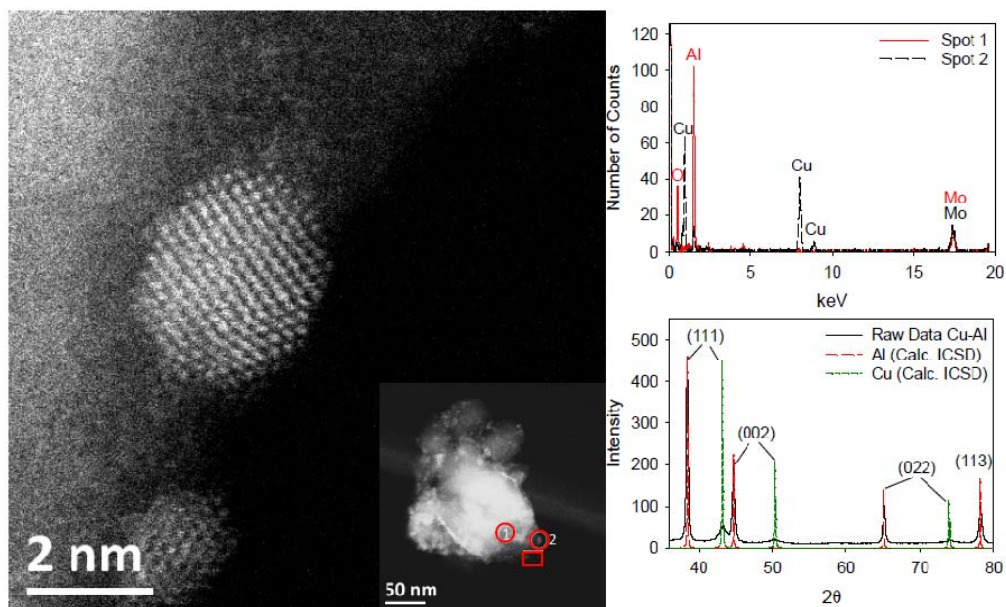


**Figure 5** (Left)  $C_s$ -STEM micrograph of a Cu nanocrystal deposited on an Al nanoparticle, magnified from the boxed region in the inset (also on the left). Spots (numbered 1 and 2) at which EDX spectra were collected are marked with circles. (Top right) EDX spectra of the corresponding spot 1 (the Al particle) and 2 (the Cu nanoparticles). (Bottom right) XRD profile (in black) along with the Bragg peaks for bulk Al (in red) and bulk Cu (in green).

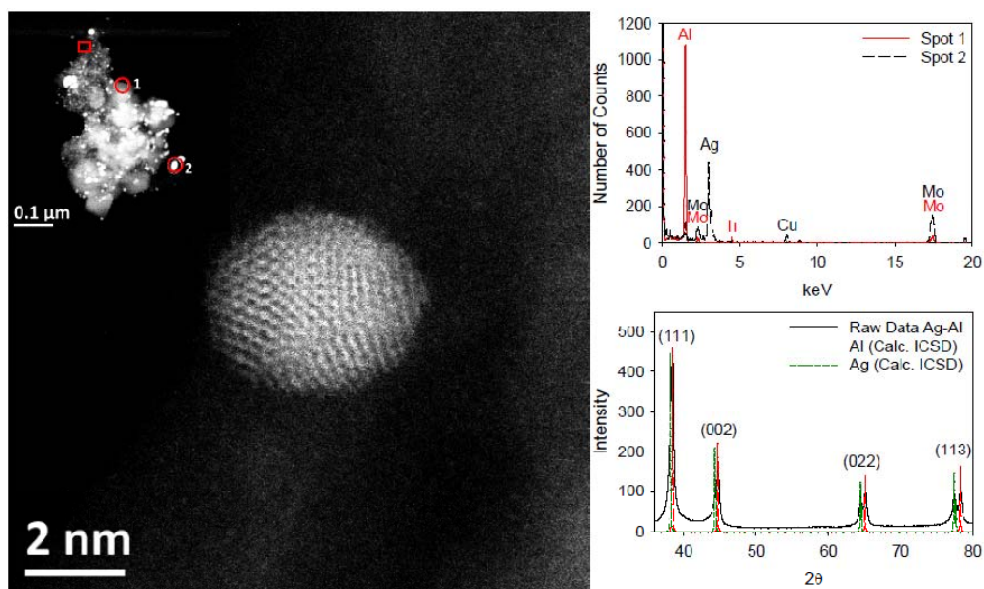


**Figure 6** (Left)  $C_s$ -STEM micrograph of an Ag nanoparticle deposited on an Al nanoparticle, magnified from the boxed region in the inset (also on the left). Spots (numbered 1 and 2) at which EDX spectra were collected are marked with circles. (Top right) EDX spectra of spot 1 (the Al particle) and 2 (the Ag nanocrystal). (Bottom right) The XRD profile (in black) along with the Bragg peaks for bulk Al (in red) and bulk Ag (in green).

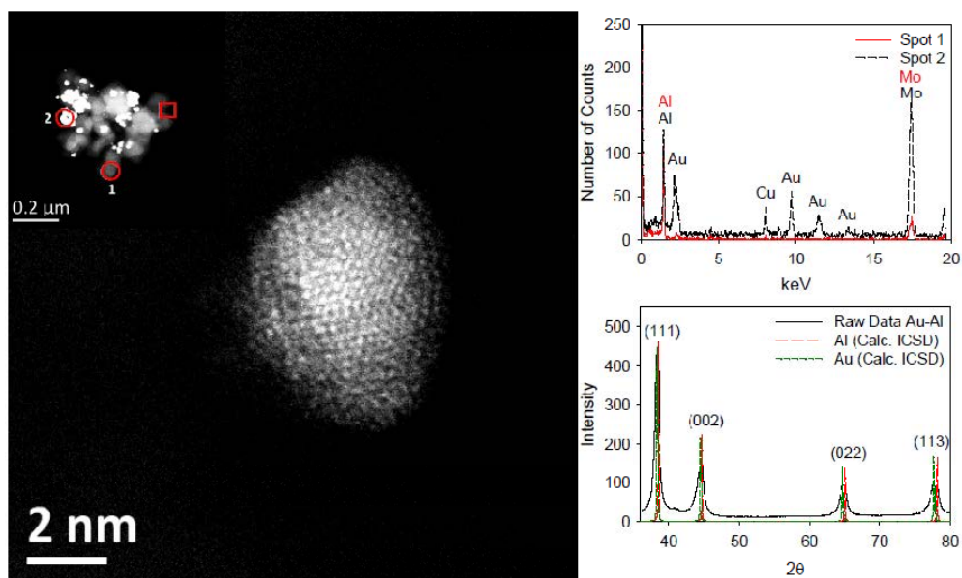


**Figure 7** (Left)  $C_s$ -STEM micrograph of a Au nanoparticle deposited on an Al nanoparticle, magnified from the boxed region in the inset (also on the left). Spots (numbered 1 and 2) at which EDX spectra were collected are marked with circles. (Top right) EDX spectra of spot 1 (the Al particle) and 2 (the Au nanocrystal). (Bottom right) The XRD profile (in black) along with the Bragg peaks for bulk Al (in red) and bulk Au (in green).

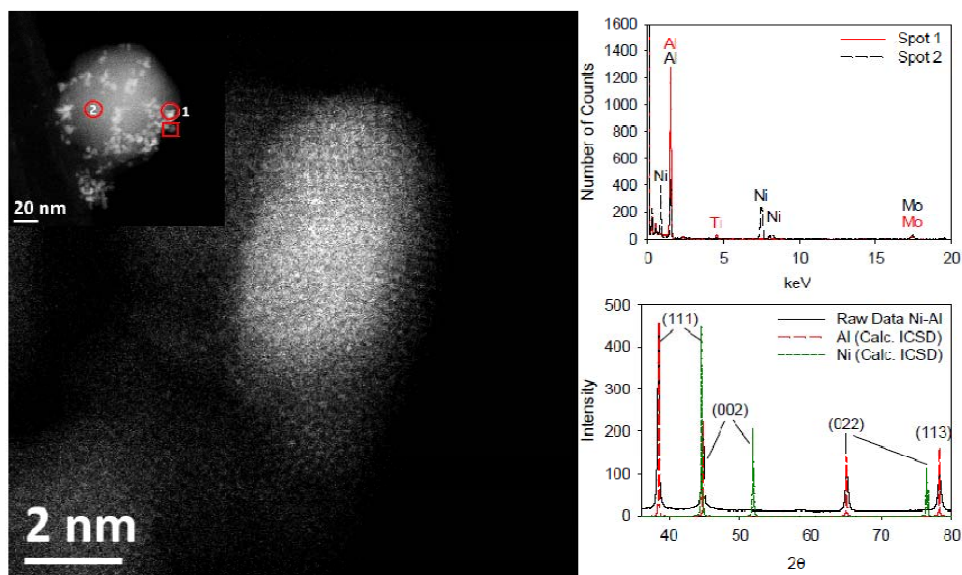


**Figure 8** (Left)  $C_s$ -STEM micrograph of a Ni nanoparticle deposited on an Al nanoparticle, magnified from the boxed region in the inset (also on the left). Spots (numbered 1 and 2) at which EDX spectra were collected are marked with circles. (Top right) EDX spectra of spot 1 (the Al particle) and 2 (the Ni nanocrystal). (Bottom right) The XRD profile (in black) along with the Bragg peaks for bulk Al (in red) and bulk Ni (in green).

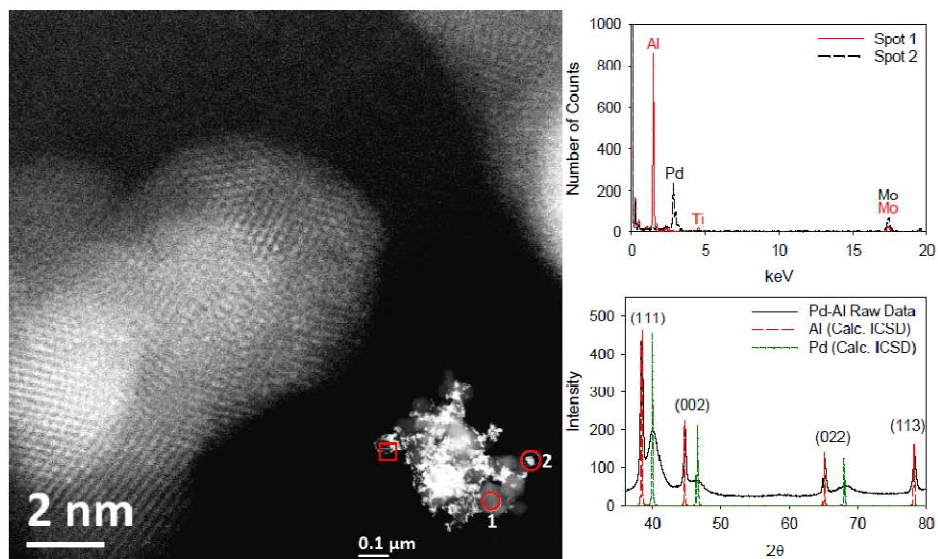


**Figure 9** (Left) C<sub>s</sub>-STEM micrograph of a Pd nanoparticle deposited on an Al nanoparticle, magnified from the boxed region in the inset (also on the left). Spots (numbered 1 and 2) at which EDX spectra were collected are marked with circles. (Top right) EDX spectra of spot 1 (the Al particle) and 2 (the Pd nanocrystal). (Bottom right) The XRD profile (in black) along with the Bragg peaks for bulk Al (in red) and bulk Pd (in green).

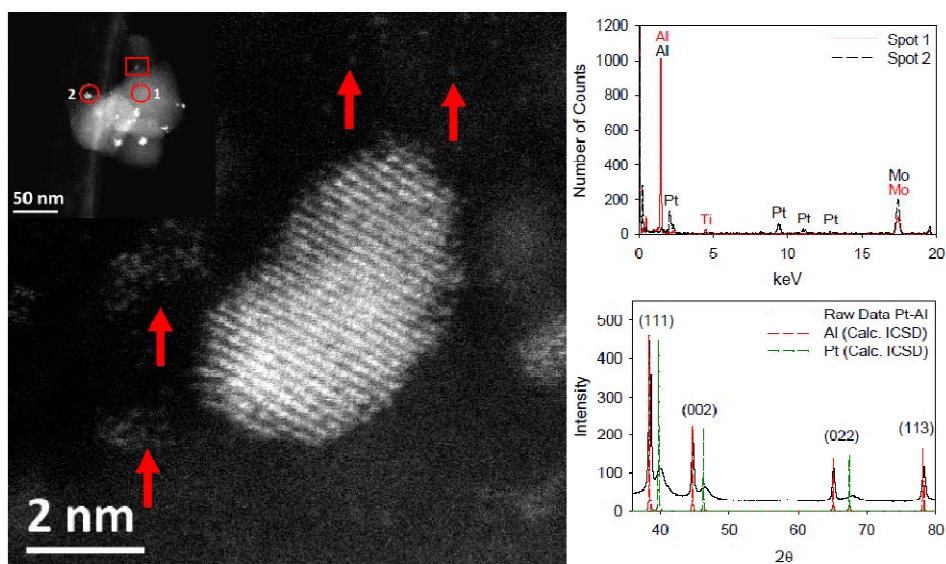


**Figure 10** (Left) C<sub>s</sub>-STEM micrograph of a Pt nanoparticle deposited on an Al nanoparticle, magnified from the boxed region in the inset (also on the left). Spots (numbered 1 and 2) at which EDX spectra were collected are marked with circles. (Top right) EDX spectra of spot 1 (the Al particle) and 2 (the Pt nanocrystal). (Bottom right) The XRD profile (in black) along with the Bragg peaks for bulk Al (in red) and bulk Pt (in green).

The electron micrographs, EDX spectra, and XRD profiles show that, in every case, treatment of the Al particles with the transition metal complexes does not afford a uniform coating, but instead results in the formation of small zerovalent transition metal nanocrystal dispersions on the Al particle surfaces. These transition metal nanocrystals vary in size from atomic dispersions to sizes exceeding 50 nm in diameter, depending on which transition metal was used. The nanocrystals, whose average size was

typically about 5 nm, often exhibit crystalline features as demonstrated by clearly observable atomic planes and faceted shapes.

The lattice constants of the nanocrystals determined by XRD, along with the EDX results, suggested strongly that the transition metal nanocrystals were unmixed with the aluminum. For example, the binary phase diagram for Al-Cu indicated that for an fcc alloy of  $\text{Al}_x\text{-Cu}_{1-x}$ , where  $x$  is less than 30 % of the total composite [58], the lattice constant should measure  $4.047 \text{ \AA}$  [59] which was not observed in the XRD results in **Fig. 5**. In the Al-Ag system two phases exist at low Ag concentrations [60], an Al-rich phase and  $\text{Ag}_{0.67}\text{Al}_{0.33}$  phase [58]. The latter phase however, adopts hexagonal close packing (hcp) structure [61] which would generate distinctly different peaks from the fcc Bragg peaks revealed in the XRD data. Low concentrations of Au in the Au-Al binary phase diagram afford an  $\text{AuAl}_2$  alloy with a fcc crystal structure [62]. The lattice constant for this structure measures  $5.9988 \text{ \AA}$  [63] which far exceeds what we observed experimentally and rules out its presence in our Al/Ag specimen. The  $\text{Ni}_{0.08}\text{Al}_{0.92}$  structure in the Ni-Al phase diagram [64] is also fcc and is measured as having a lattice parameter ( $4.025 \text{ \AA}$ ) [65] that is significantly different from the lattice parameter refined for the Al ( $4.0483 \pm 0.0022 \text{ \AA}$ ) in the Al/Ni specimen. Examination of the Pd-Al phase diagram found  $\text{PdAl}_4$  [66] as the closest stoichiometric match to the system examined here ( $\sim\text{Pd}_{0.08}\text{Al}_{0.92}$ ), however has  $\text{P6}_3\text{22}$  space group indicative of a hcp structure [63] crystal system which clearly is not observed in the XRD data for the Al/Pd sample in **Fig. 9**. Lastly, the Al-Pt phase diagram designates an Al-rich phase and a  $\text{Pt}_5\text{Al}_{21}$  alloy phase at Pt concentrations below 20% [67]. The lattice value of this Pt-Al structure measures at  $1.923 \text{ \AA}$  and, based on the XRD data, is not suitable as an alternative structure to describe the Al/Pt system [68].

Taken together, critical examination of the corresponding phase diagrams indicate that the Al/M systems examined here are not alloys of any form. In the same token,  $\text{C}_s$ -STEM results make it apparent that the decorating metal is not in the form of a uniform film. The results are more demonstrative of an arrangement of transition metal nanoparticles deposited on top of larger, pre-existing Al nanoparticles. Although lattice constants for some of the nanocrystals deviated somewhat from those seen for bulk samples of the pure metals, especially for the Pt and Cu nanocrystals, the contractions in the lattice constants of the right magnitude expected for nanoparticles of these sizes.

The formation of decorated particles rather than core-shell structures is likely a consequence of the deposition mechanism, which involves a redox transmetalation reaction between zerovalent aluminum and the transition metal salt [69-71]. Inevitably the surfaces of the aluminum nanoparticles are passivated with a nonuniform coat of oxide. We propose that the site for growth of the transition metal nanoparticles is in the defect zones where the aluminum nanoparticle is not fully oxidized. The random growth of the transition metal nanocrystals could be explained by the randomness of the oxide coat on the aluminum nanocrystal.

In conclusion, the UIUC results of **Nuzzo** and **Girolami** show that Higa's protocol – treating the Al particles with a solution of a transition metal salt – does not result in the formation of a uniform coat, but instead generates nanocrystals of the zerovalent transition metal randomly distributed over the surface of the existing aluminum particles.

### II.1.3 Chemistry and Structure of Al-SAM Surfaces

**Allara** and his group have applied surface science and experimental chemistry methods to study the structures and energy releasing reaction pathways of nano-structured energetic materials (NEEMs). The results were intended to provide a rational basis for engineering of NEEMs and to provide input and experimental tests of the parallel theory efforts. The main experimental approach was based on the preparation of new types of self-assembled monolayers (SAMs) containing  $\text{NO}_2$  groups that serve as models for the surfaces of explosive material particles, e.g., TNT, HMX, and direct characterization of the chemistry that evolves when Al atoms are deposited from the vapor under high vacuum conditions onto the SAMs. The SAMs provide a quantitative, systematic way to precisely control surface coverage, composition and stoichiometry of model oxidizer compounds. The SAMs were exposed to precise doses

of reactive metal vapor to model the metal nanoparticle and oxidizer particle reaction interface inherent in any energetic system. Multiple complementary techniques including infrared spectroscopy (IR), X-ray photoelectron spectroscopy (XPS), conducting-probe atomic force spectroscopy (CP-AFM), and spectroscopic ellipsometry (SE) were used to study the progress and characteristics of the reactions systems. In general, extensive work was carried out to modify the instruments for *in-situ* tracking of the metal/SAM reactions. The XPS, IR and AFM instruments were further modified to allow studies of the temperature dependence of the Al metal-SAM reaction. Significant effort was devoted to density functional theory (DFT) calculations designed to gain insight into the behavior of some of the systems. The initial effort in the DFT theory was greatly helped by collaborative interactions with and the kind assistance of **Drs. Rajiv Kalia** and **Priya Vashishta** of the MURI team.

SAMs were prepared from carboxylic acid and thiol precursors on oxide and coinage metal substrates, including p-nitrobenzoic acid, 3,4 di-nitro benzoic acid, and 12-nitrododecanoic acid, all on the native oxides of Al and Ag; and p-nitrobenzenethiol and (4'-nitrophenyl)ethynyl-4-benzenethiol on Au{111}. After preparation and characterization the SAMs were loaded into a vacuum chamber interfaced with a selected diagnostic tool and then exposed to Al metal vapor under ultra-high vacuum conditions with characterization carried out to identify changes in properties indicative of an Al-nitro reaction.

The results of a typical aluminum deposition experiment is given for a p-nitrobenzenethiol SAM in which the reaction progress was followed via grazing incidence IR reflection spectroscopy (IRS) with the result displayed in **Fig. 11**. The initial IR scan, labeled "Bare SAM", shows the symmetric and asymmetric stretch frequencies of the nitro group at  $\sim 1350$  and  $1520\text{ cm}^{-1}$  respectively along with the nitro group bend mode at  $\sim 850\text{ cm}^{-1}$ . As aluminum metal is vapor deposited, all associated nitro group stretch and bend modes begin to decrease in intensity until they completely disappear at  $\sim 1.8$  Al atoms/SAM molecule. While the nitro groups are damped in intensity, various ring modes of the phenyl group persist as indicated by the continued presence of peaks at  $\sim 1480$  and  $\sim 1590\text{ cm}^{-1}$ . This suggests that as the nitro group is complexed by the incoming Al metal vapor, the remainder of the molecule remains unaffected. Another important observation is the distinct lack of an actual Al-O stretch mode which should occur at  $\sim 1280\text{ cm}^{-1}$ . As more Al metal is deposited on the SAM, a large broad peak begins to develop at  $\sim 850\text{ cm}^{-1}$ , which is attributed to an Al-O stretch mode. We surprisingly do not see any evidence of the formation of any aluminum nitride, aluminum oxynitride or aluminum carbide compounds which would be expected if the aluminum-nitro compound were proceeding to the full thermodynamic reaction limit. These results were corroborated by tandem XPS measurements on similar systems. Depositions carried out at an elevated temperature of  $\sim 333\text{ K}$  had no effect on reactivity of the system.

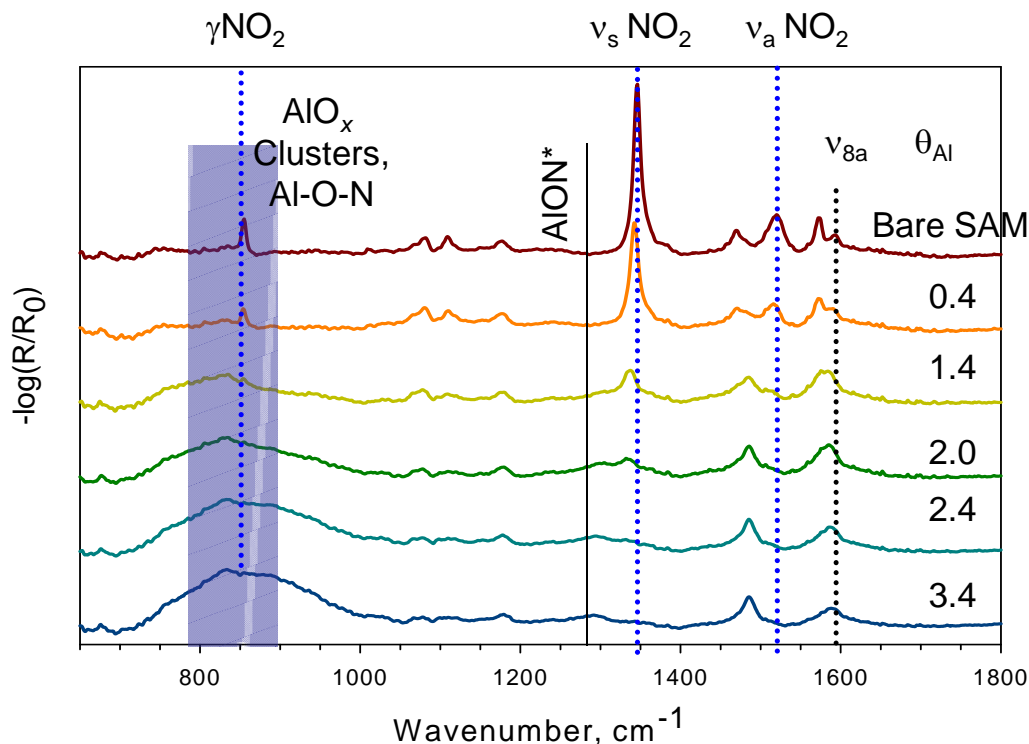


**Figure 11** Aluminum metal vapor deposited on *p*-nitrobenzethiol SAM on a Au(111) surface. The NO<sub>2</sub> modes disappear after the addition of ~ 1.8 equivalent monolayers (1.8 deposited Al atoms per SAM molecule) of Al. [Ref Spectra, f- L. Andrews, M. Zhou, W. D. Bare *JPC*, 102 5019 (1998)].

Summarized in **Fig. 12** are the results of several years of calculations on various different nitro containing SAM systems. Proceeding from left to right, the amount of Al metal atoms/SAM molecule required to fully complex the nitro functional group varies. Interestingly, in the case of 12-nitrododecanoic acid (12-NDDA), **Fig. 12D**, the nitro group was found to align parallel to the surface, forcing the top of the aliphatic chain to bend. This is in marked contrast to *p*-nitrobenzoic acid, **Fig. 12A**, where the rigid structure of the benzene ring forces the NO<sub>2</sub> group to align more perpendicularly to the surface. For 12-NDDA, the asymmetric NO<sub>2</sub> stretching frequency is completely diminished after the addition of only ~1 Al atom per surface molecule. The differing orientations end up yielding a disparity in the chemical reactivity of the nitro group. The more perpendicular orientation of the NO<sub>2</sub> in *p*-NBA leaves both oxygen atoms available to complex vapor deposited Al atoms and, as was discussed previously, it was found that it takes ~1.8 Al atoms per surface molecule to completely complex the NO<sub>2</sub> group. In this case, each Al atom is able to bridge an average of two different neighboring SAM molecules. Once an oxygen atom is complexed to an aluminum atom, it leaves the 2<sup>nd</sup> oxygen atom on the same nitro group dangling and more reactive. Hence, any further incoming Al atoms will prefer to stick near where an Al atom has already reacted to coordinate with the dangling higher reactivity uncomplexed oxygen. In other words, once one oxygen atom on a nitro group is complexed by an aluminum atom, it increases the probability of a second aluminum atom complexing at the same site to react with the remaining dangling oxygen atom. However, in the case of 12-NDDA, it appears that the surface parallel orientation of the oxidizing functional group, leaves only one exposed oxygen atom available to coordinate with the incoming Al atoms, and the second oxygen is presumably sterically hindered from participating. This leads to a 1:1 deposited Al atom per nitro functional group ratio.

To further examine the effect of reactivity of the nitro functional group with aluminum metal vapor, a third SAM molecule, (4'-Nitrophenyl)ethynyl-4-benzenethiolate (or nitrodimer for short), was

studied. By increasing the overall aromaticity of the SAM molecule, the reactivity of the nitro functional group should increase due to conjugation of the pi electron system. In this instance, only  $\sim 1.3$  Al atoms per SAM molecule are required to fully complex the nitro group. This falls in-between the ratio observed in the two earlier systems and is consistent with the expected increase in nitro group reactivity. By making the nitro group more labile, it can more effectively compete with the greater reactivity of the dangling oxygen atoms.

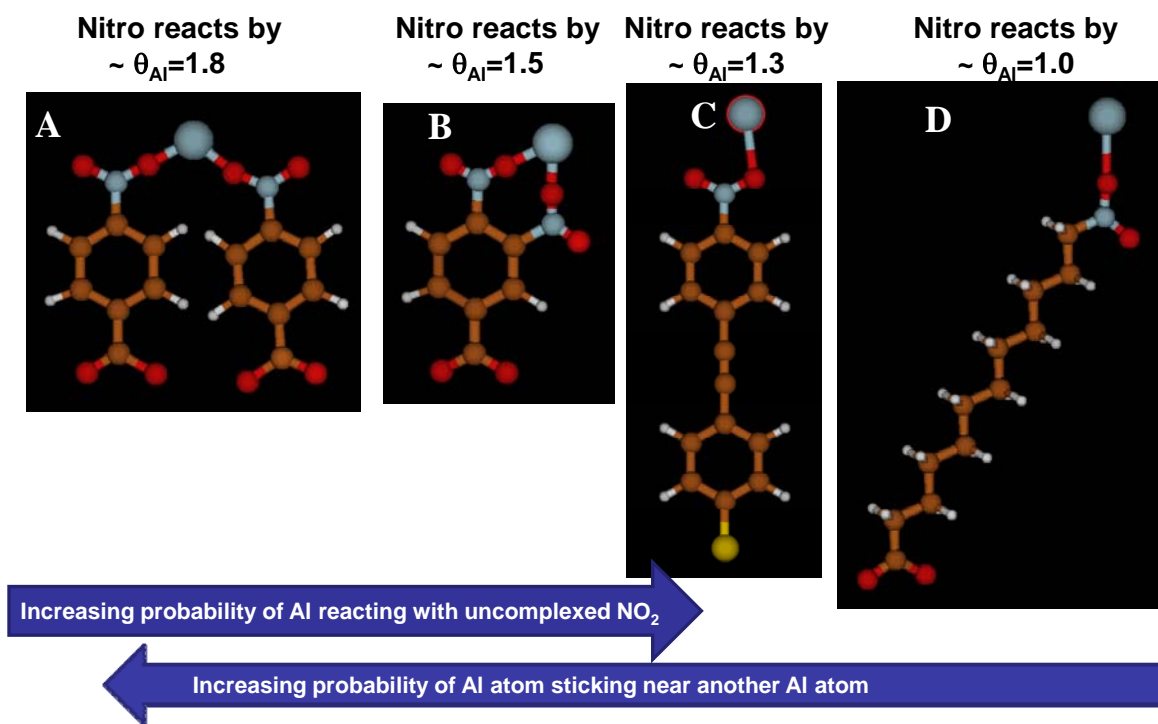


**Figure 12** Depiction of different SAM molecules studied and their likely coordination with a deposited Al atom. A) *p*-nitrobenzoic acid B) 3,4 dinitrobenzoic acid C) (4'-nitrophenyl)ethynyl-4-benzenethiolate and D) 12-nitrododecanoic acid.

Interestingly, for the 3,4 dinitrobenzoic acid SAM molecule, displayed in **Fig. 12B**, the number of Al atoms per molecule required to fully complex the two nitro groups is unexpectedly lower than that observed in the corresponding single nitro molecule, *p*-nitrobenzoic acid. Since there are now two nitro groups per molecule, an aluminum atom does not necessarily need to bridge neighboring molecules to coordinate effectively. There are still two dangling oxygen bonds present, but in the case of the dinitro group, one of the dangling oxygens is sterically hindered in comparison to the earlier case of the single nitro group, where the two dangling oxygen bonds formed are both still easily accessible. The net effect is to lower the relative reactivity of the dangling oxygen atoms allowing uncomplexed dinitro molecules to compete more effectively for the deposited Al atom. There is thus a complex competition between dangling oxygen sites and fresh  $NO_2$  sites for unreacted Al atoms. In **Fig. 12** moving to the right, the Al atom prefers fresh  $NO_2$  sites, either due to a relative increase in nitro functional group reactivity or steric hindrance. Moving to the left, the Al atom tends to prefer sticking near where an earlier Al atom already reacted.

To gain further insight into the enhanced reactivity of a site where an aluminum atom was already present, a series of DFT calculations were done at the B3LYP//6-31g(d,p) level of theory. The starting SAM structure was provided by fellow MURI co-members R.V. **Kalia** and co-workers. It consists of a

set of eight nitrobenzethiol molecules classically equilibrated in the form of a SAM monolayer at 300 K using the ReaxFF potential. A DFT geometry optimization was then performed on the starting structure with two added Al atoms placed in the center. All atoms were constrained with the exception of the Al atoms and the nitro functional groups. As seen in **Fig. 13**, preliminary results show that both Al atoms preferred to cluster next to each other instead of independently complexing separate nitro molecules. In the case of the Al atom labeled **a**, three distinct nitro groups on three separate molecules were bridged. The second Al atom clustered near the first Al atom and only complexed with a single nitro group. The DFT results are consistent with the experimental results obtained via IR, XPS and SE.

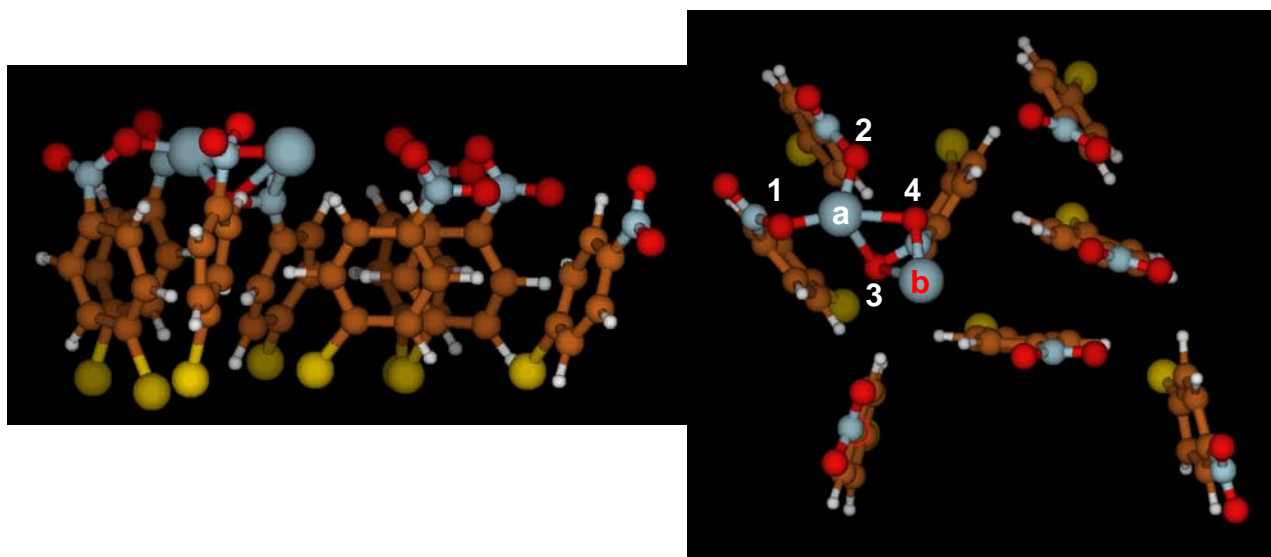


**Figure 13** DFT calculated structure of two aluminum atoms complexed to a simulated SAM layer consisting of 8 molecules.

In an attempt to drive the Al reaction with the nitro functional groups closer to the full thermodynamic limit, a series of experiments involving the deposition of potassium metal on top of nitro containing SAMs was performed. It is well known that potassium will readily give up its  $4s^1$  electron to a nitro functional group to form  $K^+$  and the  $NO_2^-$  radical anion. It should be emphasized that the potassium does not covalently react with the nitro group but instead forms an ion pair, leaving the nitro group radicalized and intact. Thus, by first priming the SAM with a partial layer of potassium metal and then depositing the Al metal vapor on top, the reaction barrier to full reaction between Al and the  $NO_2$  functional should be affected.

A set of X-ray photoelectron spectra detailing the N 1S binding energy region of a nitrodimer SAM is displayed below in **Fig. 14**. The series on the left hand side of the figure show the effect of increasing amounts of deposited Al on the peak position of the N 1s band. Initially for the bare SAM monolayer, the N 1s peak is at 405.5 eV which is typical value for oxidized nitrogen. As Al metal is deposited, a new feature begins to appear near 399 eV at the expense of the oxidized peak at 405.5 eV. This indicates that there are two chemically distinct types of nitrogen present in the monolayer, an oxidized species and a reduced nitrogen species as indicated by the peaks at 405.5 and 399 eV respectively. Note in particular that two distinct nitrogen atoms are present at 1.0 equivalent monolayers of Al indicating that some unreacted nitro functional groups remain. Past 1.3 Al atoms/ nitrodimer molecule, only the reduced nitrogen species at  $\sim 399$  eV is observed. The complete reduction of the nitrogen by 1.3 equivalent monolayers is consistent with results obtained via IRS and spectroscopic ellipsometry.

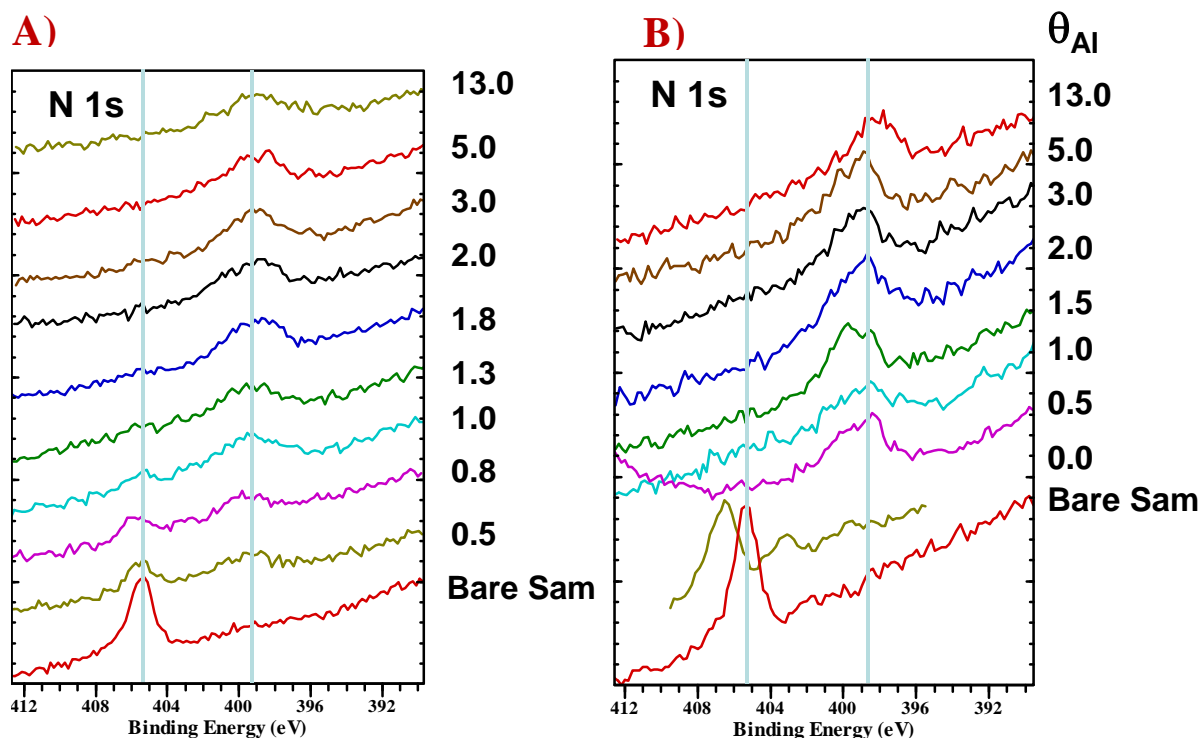


**Figure 14** XPS of N 1s binding energy region of nitrodimer. A) The N1s peak shifts as increasing amounts of Al metal vapor are deposited on the SAM. B) Similar to A except the SAM is initially doped with an equivalent monolayer of K metal.

On the right hand side of **Fig. 14**, the monolayer is first primed by depositing 1 K atom/nitrodimer molecule in the plot labeled  $\theta_{\text{Al}}=0.0$ . The presence of potassium shifts the original nitrogen peak position up to 406.5 eV. The nitrogen peak also splits into two components, with a new feature appearing at 403 eV which is most likely due to the formation of the radical anion. The original peak position is shifted to higher binding energy most probably because of the presence of a dipole layer formed by the  $\text{K}^+\text{-NO}_2^-$  ion pair. However, as soon as Al is deposited on the SAM, the nitrogen 1s band reduces and shifts to lower binding energy at 399 eV. In the presence of potassium, it now takes less Al to fully reduce the nitrogen group. However, with or without the presence of potassium, the nitrogen peak shifts similarly indicating that the potassium has little effect on pushing the reaction toward the full thermodynamic limit. This is corroborated by examination of the XPS spectra of the other elements present in the system such as oxygen, aluminum and carbon as well as complementary spectroscopic ellipsometry and IR results (neither shown).

Overall, the Al-nitro group chemistry was surprisingly relatively stable with the reaction never proceeding towards the full thermodynamic of the complete oxidation of Al. Instead, the Al appears to complex with the oxygen atoms present in the nitro groups, forming a protective layer at which point Al metal begins to amass on top of the monolayer as depicted in **Fig. 15**. This was corroborated with numerous experiments on various model oxidizing model SAM systems and with different experimental techniques including infrared spectroscopy, x-ray photoelectron spectroscopy, spectroscopic ellipsometry and atomic force microscopy. Attempts at forcing the system over any thermodynamic barriers by heating the sample to higher temperature (discussed in previous reports) and by potassium doping to form a radical anion did not ultimately affect the reactivity of the system.

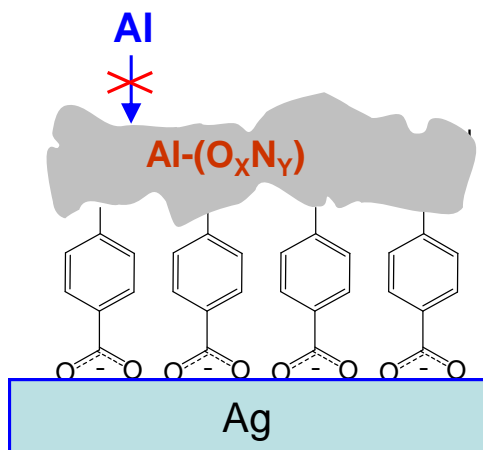


**Figure 15** Initially deposited Al metal begins to complex the oxygen atoms present in the nitro functional groups. As the oxygen reacts with aluminum, a protective layer is formed which prevents further Al from reaching the bulk of the SAM monolayer.

A large number of metal atom/ NO<sub>2</sub>-SAM experiments were run, some of which are included in the sections above and others can be obtained directly from **Allara**. In addition, extensive DFT quantum chemical theory calculations were run on the Al/nitrobenzene SAM system. Overall, the results conclusively show that an exposed NO<sub>2</sub> group at a surface when exposed to nascent Al atoms from a vapor source only reacts partially to form Al-O-N types of metallo-organic complexes, as opposed to the expected highly exothermic reaction to form Al nitrides, oxides and carbides. Thus, when an Al atom impinges on a NO<sub>2</sub> oxidizer molecule at ambient temperatures only a small fraction of the potential energy is released. Clearly there is a large energy barrier to be overcome before the thermochemical maximum exotherm can be realized. The data suggests that this barrier may require in excess of ~400 K or so at the sample before energetic reaction.

#### II.1.4 Ultra-High Pressure Supercritical Fluid Processing of Energetic Materials

Energetic oxidizers are commonly used as additives in explosive formulations. In particular, they are used in large quantities in a number of applications ranging from solid-rocket propellants to explosive compositions for demolition and mining. Generally, performance is an important parameter. Performance is usually related to the molecular properties of the energetic material. In particular, atomic constituents in the molecule and the crystal density are important for performance. However, there are other characteristics of an energetic material that are important. For example, if an energetic material is too sensitive to handle then its application becomes greatly limited. In most heterogeneous propellants, the sensitivity is determined by the energetic crystalline oxidizer, which makes up a large percentage of the propellant. Hence, a reduction in sensitivity of the oxidizer ingredients should result in the formation of a less sensitive propellant.

In order to develop insensitive munitions (IM) it is prudent to decrease the sensitivity of the individual energetic oxidizer ingredients to impact, shock, electrostatic discharge (ESD), and friction. Reducing the risk of initiation of the energetic ingredients is also important for raw energetic material handling and transport as well as during the mixing and production stages of explosives and propellants. The size and shape of crystalline particles, particle size distribution, impurities, and any defects in individual crystals all affect the sensitivity of energetic materials. It has been shown for cyclo-1,3,5-trimethylene-2,4,6-trinitramine (RDX) and other energetic materials that as the average particle size is decreased, sensitivity to impact decreases as well. Armstrong et al. [72] suggested that a reduction in

crystal size can significantly reduce the impact sensitivity of energetic materials. They related the drop height to the average particle size of an RDX test sample on a log-log plot (**Fig. 16**). One can clearly see that higher drop heights are associated with smaller crystals. Although extrapolations can be made from currently available values of  $H_{50}$  (the height for 50% chance of initiation) for micron-scale RDX, although the values of  $H_{50}$  for nano-sized RDX are unknown and any extrapolation of the micron-sized data could be inaccurate [73]. It was proposed that this decrease in impact sensitivity comes from a reduction of imperfections or dislocations in a crystal. Also, it has been shown that particles with a spherical shape are less sensitive to initiation as well [74,75].

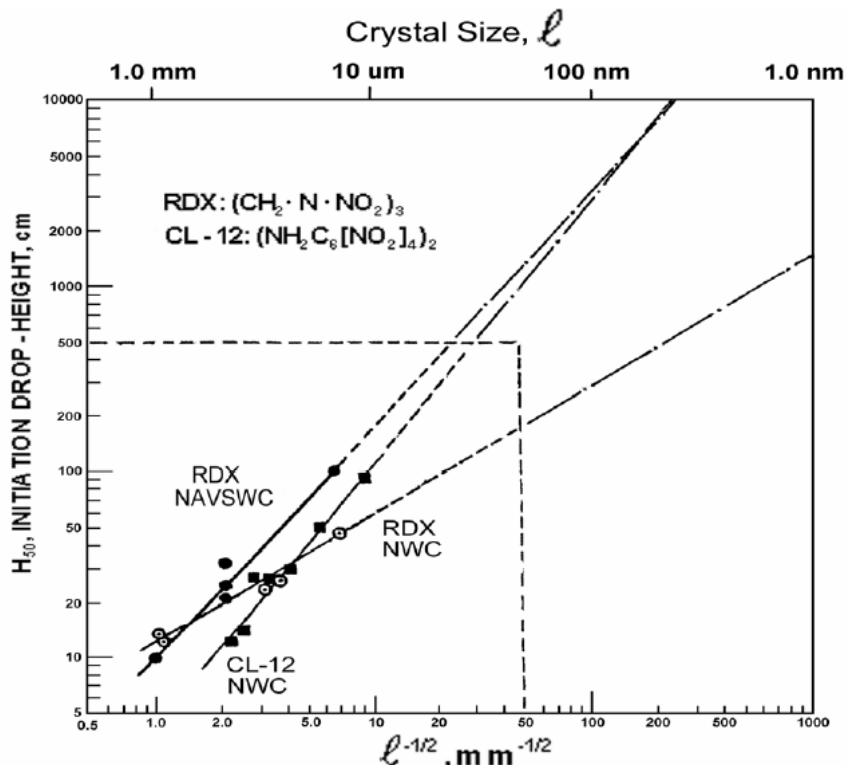


**Figure 16** Projected drop height  $H_{50}$  vs. inverse crystal size of energetic materials (from Armstrong [72]).

Not only are spherical particles a more optimal shape for sensitivity reasons, they are also more ideal for processing applications in comparison to needle-like particles [76]. Spherical particles possess higher solids loadings than higher aspect ratio particles, allowing the density of a propellant or explosive to increase. Therefore, it would be optimal to produce small spherical particles for an energetic oxidizer to be incorporated into a propellant or explosive.

While processing energetic oxidizers can reduce sensitivity, it has also been shown that nano-sized oxidizer particles could react differently than larger oxidizer particles. Recent research has shown that nano-sized oxidizer particles show different reaction onset temperatures as well as faster burning rates. These traits could be advantageous for propellants. Pivkina et al. [77] has shown that nano-sized particles of RDX react exothermically at lower temperatures from DTA measurements than micron-sized particles of RDX. Pressed strands of nano-sized RDX burned faster at pressures above 10 MPa as well. It was proposed that this was because the enhanced surface of the nano-sized particles allowed for a more developed particle-gas interface. Also, if nano-sized oxidizer particles are mixed intimately with nano-sized fuel particles then faster reaction rates could also occur.

It is apparent that further processing of energetic oxidizer particles can greatly benefit propellants and explosives. Processing can help with the sensitivity, manufacturing, and even the performance of a propellant or explosive. From the above research, it is apparent that a process that creates nano-sized particles with a spherical morphology can be of great use to the energetic material community.

Aluminum is used extensively in solid-rocket motors and thermobaric explosives. Aluminum has traditionally been used as a propellant additive in solid propellants due to its high energy density and large amount of heat release from the formation of  $\text{Al}_2\text{O}_3$ . It is extensively used in solid-rocket propellants because of the high energy it produces during combustion with oxidizers [78]. Adding aluminum to solid-propellant grains can increase the specific impulse ( $I_{sp}$ ) of a rocket [79]. Aluminum has also been shown to have the ability to reduce combustion instabilities in rocket motors when used as a fuel additive [80].

Recent advances in technology have allowed aluminum to be produced in nano-sized particles. Nano-sized aluminum has many different traits than micron-sized aluminum. These traits include significantly reduced ignition temperatures and different heats of formation and vaporization. Nano-sized aluminum particles have been shown to increase solid-rocket motor performance if they are used as an additive in solid-propellants. Nano-sized aluminum shows increased burning rates over standard aluminum when added to a propellant. It has been shown that the burning rate can increase by two to five times with shortened ignition delays [81,82]. One special characteristic of nano-sized aluminum particles is that it has an ignition temperature ranging from 800-1,020 K [83], depending on the average diameter of the aluminum particle. These ignition temperatures are lower than micron-sized aluminum usually ranging from 1,900-2,100 K.

While the performance increases seen with nano-sized aluminum are promising, there are certain drawbacks. A thin layer of alumina ( $\text{Al}_2\text{O}_3$ ) usually forms on the exterior surface of the aluminum particle; the existence of this oxide layer can significantly degrade the propulsive performance and increase the ignition temperature drastically. This shell tends to be approximately 3 nm thick or greater at room temperature, so it becomes a significant percentage of a nano-sized aluminum particle's mass. The oxide layer raises the ignition temperature of the particles [84] and decreases the performance of a solid-rocket motor by lowering the active aluminum content of the particles. Because of these drawbacks, surface protection in the form of coatings is often used to help protect nano-sized aluminum particles from this oxide layer.

Because of the large number of potential benefits to coating nano-sized aluminum particles, multiple coating methods have been developed. One of the coating methods developed by Brousseau et al. [85] involves a polymer coating. This is primarily for slowing down the growth of the oxide shell. Nano-sized aluminum and boron particles were coated using a direct Ziegler-Natta polymerization on the particles with polyethylene and polypropylene. The polymer coating was proven to be successful in batch quantities in slowing down the aging or the growth of the alumina layer on the particles. Brousseau and Dubois [86] used a polymerization process to coat nano-sized aluminum with thermoplastics. The aluminum particles used were ALEX<sup>®</sup> particles and had approximately a 2 nm thick oxide layer. The polymer coating was used to prevent the nano-sized particles from developing a larger oxide layer and to create particles that were highly compatible with the polymer binders that are often used in propellants. The coating is unique in that it takes advantage of the hydroxyl site that is common on aluminum particle surfaces. The biggest challenge with coating the nano-sized aluminum particles was achieving adequate dispersion of the particles. In further work by Dubois et al. [87], similar nano-sized aluminum particles with polymer coatings were tested. Significant aging experiments and materials characterization was performed on the particles. The aging experiments were performed to see how long the nano-sized aluminum particles could retain their active aluminum content. Uncoated particles would lose all their active aluminum within ten hours of an accelerated aging environment while coated particles would only lose 30% of their aluminum content after 150 hours of aging. The quality of the coatings was

investigated through thermogravimetric analysis (TGA), x-ray photoelectron spectroscopy (XPS), and scanning electron microscopy (SEM).

An alternative coating process involves using supercritical fluids (SCF), mainly carbon dioxide ( $\text{CO}_2$ ). Researchers such as Glebov [88] used a supercritical solution of poly(vinylidene fluoride) and  $\text{CO}_2$  to coat nano-sized aluminum particles in a reaction vessel by causing the poly(vinylidene fluoride) to precipitate onto the aluminum particles. He immersed aluminum and magnesium nanoparticles in a supercritical solution inside a  $300 \text{ cm}^3$  reactor vessel. The vessel was then depressurized to condense the solute onto the particles. The supercritical solution consisted of poly(vinylidene fluoride) and poly(4-vinylbiphenyl) (PVB). Using a SCF to coat energetic materials has several key advantages. One advantage is that the supercritical temperature and pressure of carbon dioxide is relatively low ( $T_c=31.1^\circ\text{C}$ ,  $P_c=7.39 \text{ MPa}$ ). This keeps the operating conditions away from most energetic materials' decomposition temperatures. Supercritical  $\text{CO}_2$  is also relatively non-toxic, inexpensive, and is more environmentally friendly than many other organic solvents.

While all previously mentioned coatings provided surface protection, coatings can also serve other useful purposes. Coatings on nano-sized aluminum particles could provide easier ignition of the core material if they are coated with another energetic material such as RDX. The easier ignition would occur from bringing an easy-to-ignite energetic material in close contact with the nano-sized aluminum. This is a possibility since the ignition temperature for nano-sized aluminum particles has been shown to be as low as  $799\pm 10 \text{ K}$  [82] while the auto ignition temperature of RDX is  $498 \text{ K}$ . Another benefit of oxidizer coatings on a fuel particle is that the intimate contact between a fuel additive and a main propellant ingredient from a coating could greatly enhance the combustion performance of the two materials [89] by putting the oxidizer material and the fuel in closer proximity as shown in **Fig. 17**. Ordinarily, oxidizer particles are much larger than nano-sized fuel particles. Therefore, mixing is not great and relatively large distances can separate the fuel and oxidizer particles. Coatings would put two particles in closer contact than conventional mixing would and could increase the rate of reaction substantially [90]. Burn rates of propellants could be increased with these coatings.

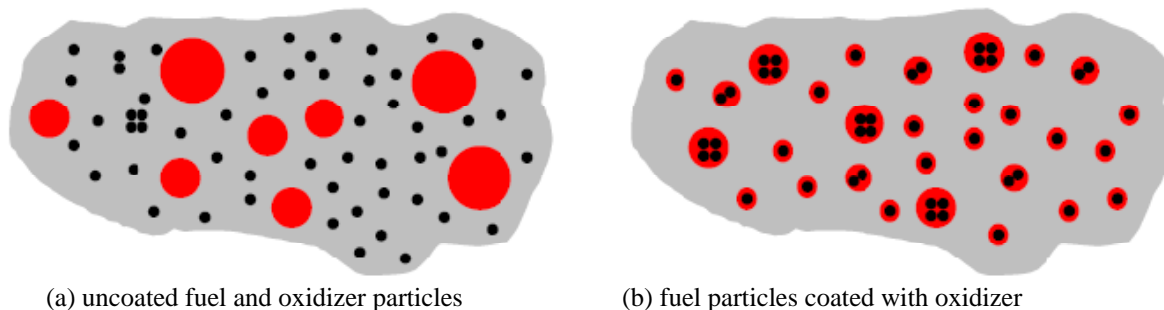


**Figure 17** Potential propellant or explosive benefits from oxidizer (red) coating on metal (black) nano-sized particles (shaded portion could have oxidizer particles and binders).

Traditionally energetic materials are processed through liquid solvent precipitation or by mechanical means such as milling or grinding. Both processes have drawbacks which prevent them from processing energetic materials in an ideal way. Current mechanical particle size reduction techniques, such as grinding, milling, and prilling, reduces particle size by shear force. However, the process creates crystals with surface defects [91]. Also, physical grinding does not produce particles much smaller than around a micrometer [92]. There is also the obvious safety concern due to the resultant frictional heating of the grinding process which may lead to explosion. Recently, improved grinding techniques have been used to create some particles with sub-micron dimensions [93]. However, controlling the shape and size

distribution of the particles is very difficult. Due to these limitations, an alternative method to synthesize energetic materials at the nanoscale is needed.

The other common method of processing energetic materials involves precipitation techniques. Usually energetic materials are precipitated with a liquid solvent. Liquid solvent precipitation has a few drawbacks in regards to synthesizing energetic materials. One disadvantage is that it is hard to achieve a high-degree of supersaturation with liquid solvent precipitation. This is because solubility is controlled by the solution temperature and it is hard to rapidly drop the temperature of a liquid solvent in a way that creates a high-degree of supersaturation. Because of this, liquid solvent precipitation often leads to particles that have a wide size distribution from non-uniform supersaturations. Additionally, particles smaller than the micron-size scale cannot be formed by liquid solvent precipitation. Another disadvantage involves the low diffusivity of the liquid solvent, which ensures that solvent inclusions can be found in the final particles. This is a disadvantage as this can increase sensitivity and reduce performance. Therefore, for precipitation to be a more attractive means of processing energetic materials, a method that can achieve a high-degree of supersaturation with a solvent that has a high diffusivity is desired.

An alternative method of processing energetic materials is through supercritical fluid precipitation. It is known that certain solids can become soluble in fluids if the solvent reaches a supercritical state. Supercritical fluid precipitation involves creating a supercritical solution of solute and supercritical fluid. Supercritical fluids have a few unique advantages as a solvent; they experience a large change in density by their critical point and they have gas-like transport properties. The large change in density of supercritical fluids allow for a large degree of supersaturation if they are used as a solvent and mechanically expanded. Due to the compressible nature of supercritical fluids, a pressure drop can reduce the density of a supercritical fluid dramatically (**Fig. 18**). This is important as the solubility of a solute in a supercritical fluid is highly dependent on the density of the solvent. Also, the gas-like transport properties allow for high diffusivities and fast mechanical perturbations leading to uniformly sized particles that do not possess solvent inclusions. Both of these attractive features are ideal for energetic oxidizers because the size and shape of the particles strongly affects their sensitivity. The supercritical fluid of choice is often carbon dioxide beyond its moderate critical point of  $T_c = 304$  K and  $P_c = 7.4$  MPa. Supercritical fluid precipitation has been used to precipitate solid particles of significantly smaller size and different morphology than in conventional liquid solvent precipitation [94]. For all of these reasons supercritical fluid (SCF) processing is being examined in this study to precipitate nano-sized oxidizer particles and to also coat nano-sized aluminum particles with an oxidizer.

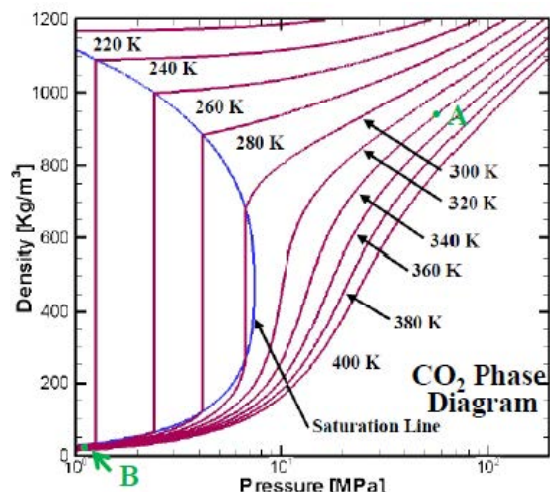


**Figure 18** Density-pressure diagram of CO<sub>2</sub> (point A is supercritical fluid state and point B is a gas-phase state).

To better understand the degree of supersaturation in the supercritical fluid precipitation process, the solubility of the solute in supercritical CO<sub>2</sub> needs to be known. While the solubility of many different solutes have been recorded in supercritical CO<sub>2</sub> in the past, the information on the solubility of many energetic materials including RDX is somewhat limited to narrow pressure and temperature ranges. Solubility measurements of RDX in dense CO<sub>2</sub> have been performed at pressures below 48.3 MPa by Morris [95]. Trends show higher pressures lead to a higher solubility. This is from the compressed solvent interacting more with the solute. It has been reported by Morris that solubility greatly increases from 3,000 to 5,800 psi and then begins to plateau as can be seen in **Fig. 19** [95]. However without further investigation at higher pressures the solubility of RDX in carbon dioxide is not fully known.

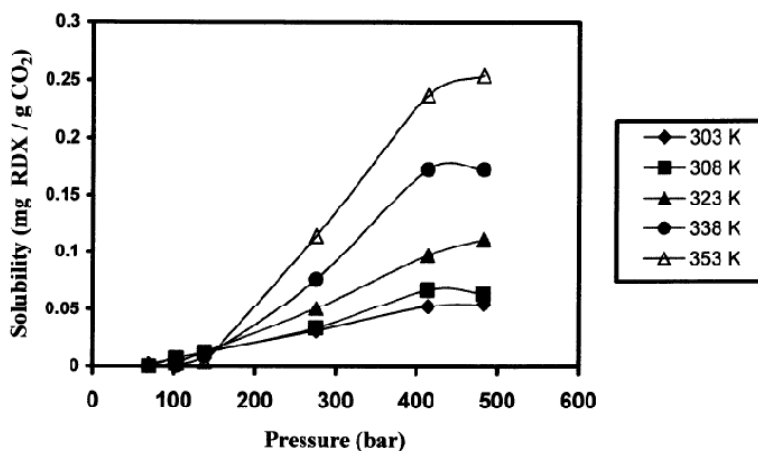


**Figure 19** Solubility of RDX in Carbon Dioxide. [101].

#### II.1.4.1 Different Supercritical Fluid Precipitation Processes Used

##### *RESS Process*

The first application of using supercritical fluids to precipitate particles was performed in 1986 by Smith, Matson, and Peterson [96]. They dissolved a material in a supercritical fluid, then expanded it out of a small orifice. This process was later titled the rapid expansion of a supercritical solution (RESS). The first experiments were done with carbon dioxide as a solvent and metal oxides and polymers as the

solutes. In 1989, Coffey and Krukonis developed the process for the pharmaceutical industry. Using a scanning electron microscope one could see that particles were reduced in size when utilizing RESS [96].

The RESS process is of interest in the synthesis of energetic materials. This is due to the fact that these smaller sized materials generally have fewer surface defects and can also be controlled to have high purity; therefore, they are less sensitive to accidental ignition by impact. A diagram illustrating the steps in the RESS process is shown in **Fig. 20**. The RESS process is a precipitation process that begins by dissolving the solute, in this case a low vapor pressure energetic material, in a supercritical fluid. The solute can be any type of material as long as it is soluble in the solvent. The solute is placed in the saturation vessel and becomes dissolved in the supercritical solvent. The solution is then expanded through a micro-orifice or capillary nozzle. This rapid expansion of the now supersaturated solution initiates homogeneous nucleation. Particle growth then continues with the processes of coagulation and condensation. This expansion process creates micro or nano-sized particles, which can then be collected.

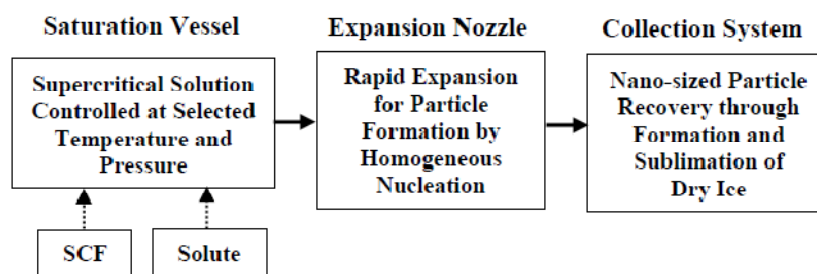


**Figure 20** Description of the RESS process.

The RESS process has been shown to produce particles on the nano-scale [97,98]. This is because as the degree of supersaturation increases, the critical nucleus size decreases meaning that many small particles are precipitated rather than a small amount of larger particles [99]. Therefore, as the critical nucleus size decreases more critical nuclei are formed, which results in ultra-fine particles.

Research by Teipel et al. [100] used the RESS process with carbon dioxide to synthesize energetic materials. They successfully created micron-size particles of trinitrotoluene (TNT) and 3-nitro-1,2,4-triazole-5-one (NTO) at pre-expansion pressures up to 22 MPa. Synthesized TNT particles were around 10 to 14  $\mu\text{m}$  with primarily needle-like shaped particles. NTO particle size distribution by laser diffraction showed a mean particle size of 540 nm. Acetone was used as a modifier (co-solvent) due to NTO's low solubility in the supercritical fluid. Stepanov [101] used the RESS process to synthesize nano-sized RDX particles at pre-expansion pressures up to 29 MPa. The system used supercritical carbon dioxide ( $\text{CO}_2$ ) as a solvent. The results were favorable with an average particle size being reported between 110 to 220 nm. In his study, the pre-expansion pressure ranged from 15.0 to 29.5 MPa and the pre-expansion temperature ranged from 343 to 368 K. It was shown that higher pre-expansion pressures tended to reduce the average particle size and size distribution. From his research study, it has been shown that the RESS process is able to produce nano-sized energetic materials under certain expansion conditions; however, the optimum conditions for nano-sized RDX particle production were not determined since it was beyond the scope of his research. Therefore a RESS system capable of reaching a wider range of pre-expansion conditions would be needed to find these optimum conditions.

#### *RESS-AS Process*

While the RESS process has been successful at producing fine and uniform particles, collected particles have been larger than what calculations predicted from particle nucleation and growth from classical nucleation theory. It seems that the extra growth from the RESS process comes from particle coagulation in the free jet after the nozzle exit since the discharging jet is often under-expanded [102]. This results in particles that are bridged together, larger than expected, and show significant

agglomeration from the coagulation process. Also, limited control over the final particle shape is allowed with the RESS process. This is because only pre-expansion conditions can be modified, rather than post-expansion conditions, as the expansion environment can affect the free energy of a precipitating solute, thereby changing the size and shape of the synthesized particles. To account for these issues, it has been proposed by researchers that the RESS process could be optimized by expanding the supercritical solution into a stabilizing solution often made of water and a dispersing agent [103]. The dispersing agents would then adsorb onto the precipitating solute and prevent agglomeration by coagulation. The process is called the rapid expansion of a supercritical solution into an aqueous solution (RESS-AS). It has been used by researchers to produce submicron particles from materials that could only be produced at micron size from the RESS process [104-106]. The process has yet to be used in the energetic material community. Not only has the RESS-AS process shown to reduce the size of particles even further than the RESS process, it has only shown that it can prevent agglomeration and change the shape of particles. From the positive results experienced in other industries, the process could be highly useful for processing energetic materials into an ideal size and shape.

#### *RESS-N Process*

Besides making small particles of a homogeneous material, supercritical fluid precipitation can have other potentially useful applications. One potential application of a rapidly expanding supercritical solution would be for coating purposes. For example, with limited modifications, further tailoring of energetic ingredients can be performed by coating nano-sized particles with a precipitating solute. The desired particles to coat would be suspended in a supercritical solution. The solution would then be expanded to induce a high-degree of supersaturation. The suspended particles would then be coated by heterogeneous nucleation. Coating materials with the RESS process would be more energetically favorable than homogeneous nucleation. This is because the presence of the suspended particles during the rapid expansion actually lowers the free energy for precipitation. When precipitation occurs, the insoluble particles act as nucleating agents for the precipitating particles. Todorova et al. [107] revealed that adding foreign nucleation sites can lower the kinetic barrier to the nucleation process. This means that heterogeneous nucleation can occur with a lower degree of supersaturation. The precipitation method by heterogeneous nucleation in the RESS process could be used to coat energetic materials that are not soluble in supercritical CO<sub>2</sub>, in particular metallic energetic materials such as nano-sized aluminum particles. This coating could change the combustion behavior of propellants with nano-sized aluminum particles.

Using supercritical CO<sub>2</sub> to coat energetic materials has several key advantages. One advantage is that the supercritical temperature and pressure of carbon dioxide is relatively low ( $T_c=31.1^\circ\text{C}$ ,  $P_c=7.39$  MPa). This low critical temperature is significantly below the decomposition temperatures of most energetic materials. Another advantage is that a high degree of supersaturation can be reached by a small change in pressure within the vessel. The large degree of supersaturation promotes conditions favorable for heterogeneous nucleation which would be used to coat the particles. Supercritical CO<sub>2</sub> is also relatively non-toxic, inexpensive, and is more environmentally friendly than many other organic solvents.

Using a modified RESS process to coat nano-sized particles has several benefits. The modified RESS process can be a continuous process rather than a batch process. This would increase the yields of the produced material. Also, the rapid expansion through an orifice produces a higher degree of supersaturation than what would occur in a reaction vessel. Mishima et al. [108] used the RESS process to coat an insoluble protein with a PEG polymer. The process was called the Rapid Expansion of a Supercritical Solution with a Nonsolute (RESS-N). The PEG polymer was dissolved in supercritical CO<sub>2</sub> and the proteins lysozyme and lipase were entrained in the flow of the supercritical solution. The resulting suspension was then expanded through a nozzle to encapsulate the proteins with PEG. Kim and coworkers (Kim et al., 1996) used the RESS process to coat naproxen with poly(L-lactic acid). The process involved dissolving both substances in supercritical CO<sub>2</sub> and allowing co-precipitation to occur in

which naproxen precipitates first and poly(L-lactic acid) precipitates subsequently on the naproxen to encapsulate it.

From past research success it is probable that the RESS-N process could be used to coat nano-sized aluminum particles with an energetic material such as RDX. The proposed process would entail entraining nano-sized aluminum particles into a supercritical solution of RDX and CO<sub>2</sub> before the supercritical solution is expanded through a micro-orifice. The rapid expansion of the supercritical solution can cause high degrees of supersaturation making the RDX solute nucleate on any surface it can find. This foreign surface can be the nano-sized aluminum particles such as ALEX<sup>®</sup>.

#### II.1.4.2 Motivation/Objectives

The overall motivation of the effort by **Kuo** and his group was to use supercritical fluid precipitation to synthesize energetic materials for multiple applications. Supercritical fluid precipitation was used to make homogeneous oxidizer materials and to coat an energetic particle with another energetic material. A goal was to synthesize oxidizer particles on the nanoscale with a uniform size. Different shapes were attempted to be synthesized as well. Finally, the sensitivity and material characteristics of the particles were investigated. Both the RESS and RESS-AS processes were used for these applications.

In regards to supercritical fluid coating, the objective of the study was to explore the possibility for coating nano-sized aluminum particles by RDX with a modified RESS system. The first item investigated was whether nano-sized aluminum particles can be entrained by the supercritical solution prior to flowing through a nozzle with a rapidly expanding supercritical solution of CO<sub>2</sub> containing dissolved RDX. The nano-sized aluminum particles (ALEX<sup>®</sup>) were used to demonstrate the feasibility of the RESS-N process. Optimization parameters were created to form uniform coatings by varying the operating conditions including the pre-expansion temperature and pressure and the feeding rate of aluminum particles.

The main tasks of this research were:

- 1) To evaluate the particle size and morphology of synthesized energetic materials using the RESS system under different temperature, pressure, and nozzle geometry conditions
- 2) To create stable colloidal suspensions of energetic materials through the RESS-AS process and determine if the size and shape are different than the RESS process
- 3) To characterize potential benefits and attributes of the RESS synthesized particles such as chemical purity, crystal structure, and sensitivity
- 4) To successfully coat nano-sized metallic particles with an energetic material such as RDX and characterize the coating properties

RDX is a commonly used military explosive. The properties of RDX are well understood so it was determined that this would be a good energetic material to investigate. Also, military grade RDX has properties that could be improved by supercritical fluid precipitation such as its impact sensitivity.

The RDX used for this study was Class I, Type II. These RDX crystals are on the micrometer size scale. A SEM image of an original military grade RDX particle can be seen in **Fig. 21**. From the image one can see that the particles have imperfect surfaces with rugged edges. A significant amount of surface defects are readily observed with cracks, voids, and inclusions. These defects should increase the sensitivity of the material.

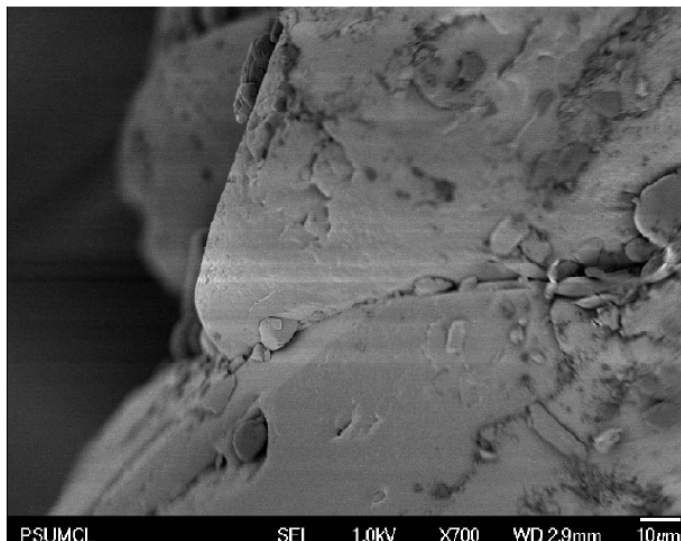


**Figure 21** FE-SEM image of Class I Type II RDX.

The other energetic material investigated for processing through the RESS and RESS-AS process is Bis(2,2,2-trinitroethyl)-3,6-diaminotetrazine (BTAT ( $C_6H_6N_{12}O_{12}$ )) which is a new and novel energetic material synthesized recently by Klapötke [109]. BTAT is a novel ingredient, since it has higher nitrogen and oxygen content than a conventional energetic material such as RDX. This leads to a positive oxygen balance, which is favorable considering that most energetic materials are oxygen deficient. The molecular structure of BTAT is shown in **Fig. 22**. BTAT crystallizes in the orthorhombic  $Pna2_1$  space group with dimensions of  $a=2.328$  nm,  $b=0.592$  nm, and  $c=1.113$  nm. Therefore, BTAT crystallizes with a much higher aspect ratio than RDX does. Each unit cell contains four BTAT molecules that are held together by hydrogen bonding between the two hydrogen atoms on each molecule and dipolar interactions between the nitrous groups at the end of the molecule. The crystal density of BTAT is fairly high at 1.889 g/cc. This is good for performance as detonation velocity depends on density. A FE-SEM image of BTAT particles can be seen in **Fig. 23**. From the image it is clear that the particles tend to be plate-like and stack easily. This is not uncommon with some crystals, but the particle structure in its natural form can be improved tremendously if the particle shape was more spherical. The sensitivity of the material to initiation by shock and impact could be reduced if the size and shape of the particles are altered. Also, larger packing densities can be achieved if the particles are more spherical in shape. The decomposition temperature and sensitivity of BTAT are comparable to RDX. BTAT decomposes at a temperature of 457 K. BTAT has a  $H_{50}$  impact sensitivity of 0.113 m for a 2.5 kg drop weight and an ABL friction sensitivity of 160 psig. Therefore, BTAT could benefit from reduced impact sensitivity like RDX can. For processing reasons, BTAT could also benefit from a change in morphology as well.

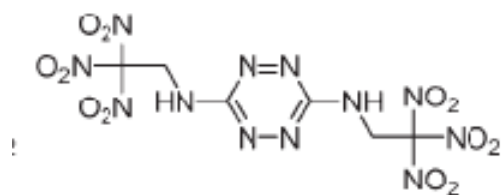


**Figure 22** Molecular structure of BTAT molecule [109].

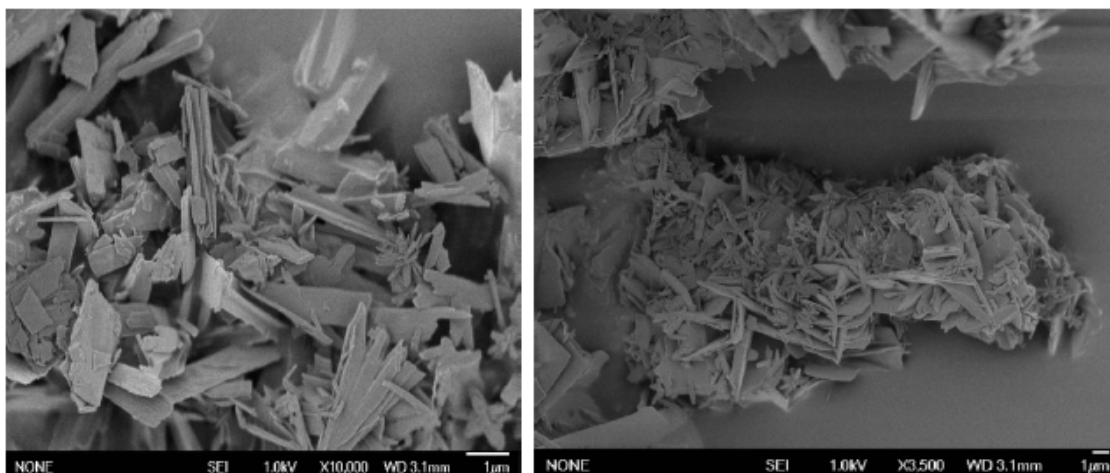


**Figure 23** FE-SEM images of BTAT before supercritical fluid processing.

The nano-sized aluminum particles that were used with the RESS-N process in this study were made by exploding an aluminum wire in an argon environment. The method is called the electroexplosion of metal wire (EEW). The produced particles are called ALEX<sup>®</sup> which stands for aluminum exploded. FE-SEM images taken of these nano-sized aluminum particles can be seen in **Fig. 24**. The particles are nearly spherical and have an average size of approximately 100 nm in diameter and have a wide size distribution.

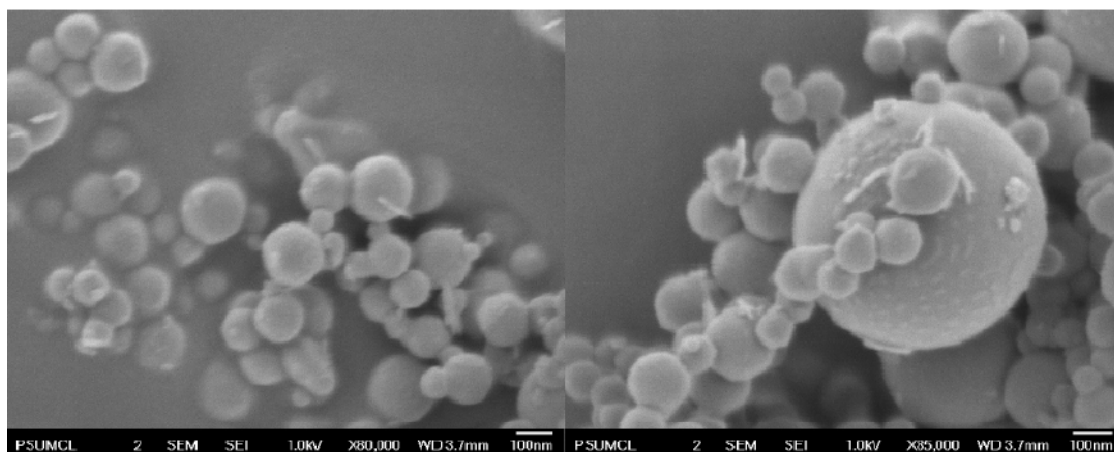


**Figure 24** FE-SEM images of uncoated ALEX<sup>®</sup> aluminum particles.

### II.1.4.3 Experimental Procedure (Method of Approach)

#### RESS Process

In order to investigate the effects of rapidly expanding ultra-high pressure supercritical solutions of energetic solute and supercritical fluid, a custom-built RESS system was designed, fabricated, and tested at the Pennsylvania State University's High Pressure Combustion Lab. A flow diagram of the experimental system can be seen in **Figs. 25** and **26**. This system consists of several main components: 1) a 207-MPa high-pressure compressor, 2) a windowed high-pressure saturation vessel ( $p \leq 207$ -MPa) with temperature control, 3) a heated expansion nozzle section containing an interchangeable nozzle elements with throat diameters varying from 100 – 300  $\mu\text{m}$ , 4) a jet expansion tube for facilitating dry ice formation, 5) nano-sized particle collection vessel, 6) a scrubber for filtering energetic particles from exhaust gases, 7) a flow meter for measuring the amount of solvent used and 8) a remotely operated control system with LabVIEW<sup>®</sup> control software and a data acquisition unit.

Carbon dioxide is the solute of choice for RESS due to its relatively low critical temperature and pressure. Other solvents considered were nitrous oxide, water, neon, and different types of Freon. However, it was determined that carbon dioxide is the best solvent for RESS due to its safe handling characteristics and its low critical pressure and temperature. For this study, the solute was RDX and BTAT.

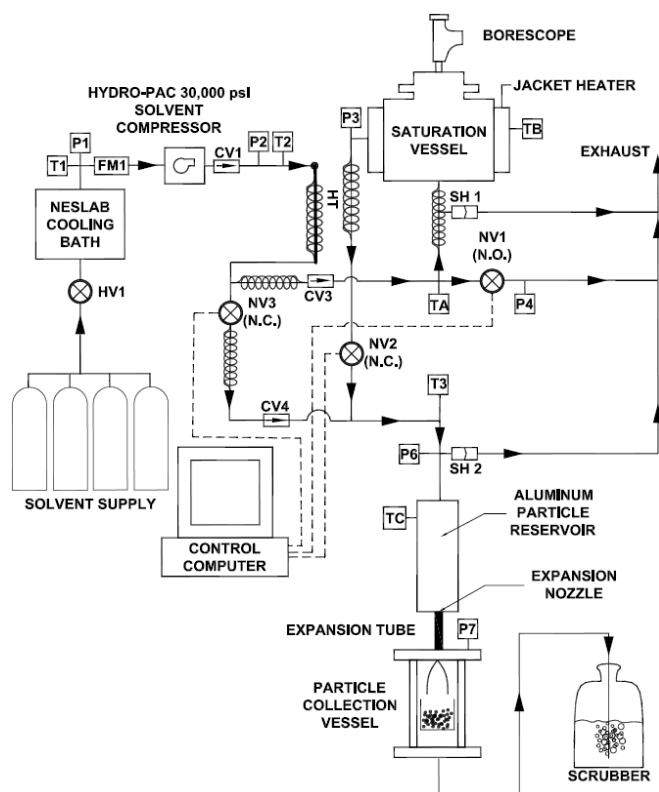


**Figure 25** Flow Diagram of Ultra-High-Pressure RESS System.

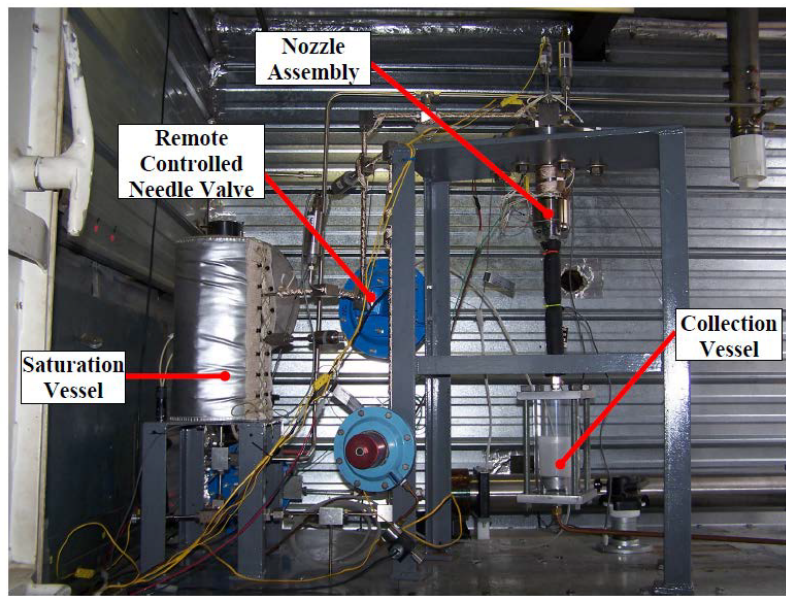


**Figure 26** Test cell portion of RESS system.

In order to achieve a high pre-expansion pressure of 207 MPa (~30,000 psi), a means of compressing the CO<sub>2</sub> and co-solvent is required. To achieve this, a Hydro-Pac “Li'l Critter” high-pressure compressor has been utilized for compressing CO<sub>2</sub>. It is critical to make sure that the CO<sub>2</sub> entering the Hydro-Pac compressor is liquid to prevent flashing of the CO<sub>2</sub> from liquid to gas to ensure that the fluid is pressurized efficiently. In order to ensure this, a NESLAB cooling bath, which can cool the CO<sub>2</sub> to -20°C (-4°F), has been utilized. To make sure that CO<sub>2</sub> is in the liquid phase while in the compressor, a pressure transducer and a K-type thermocouple probe have been used to measure the temperature and pressure of the CO<sub>2</sub> to monitor its phase. The Hydropac compressor can pressurize the working fluid to pressures up to 207 MPa for the experimental conditions considered. The compressor can pressurize fluid much more effectively than syringe pumps which are typically used in most RESS systems. This allows the PSU RESS system to operate at significantly higher pre-expansion pressures than other RESS systems

The saturation vessel is a HiP cloverleaf pressure vessel, rated to 207 MPa (~30,000 psi). A HiP jacket heater has been used to heat the vessel and the enclosed CO<sub>2</sub>. The vessel is controlled by an Omega temperature controller. A safety head has been in place to prevent any over pressurization of the system. A cross-sectional view of the saturation vessel can be seen in **Fig. 27**. The vessel is sealed through a piston seal with a PTFE coated o-ring. Fluid enters the vessel through a port in the bottom and exits out of the side. A basket of solute coated glass beads is placed in the vessel for the supercritical fluid to extract. The saturation vessel lid also has a sapphire window to allow for visualization of the dissolution process. The vessel also has a port that allows for a boroscope to illuminate the inside of the vessel for imaging purposes.

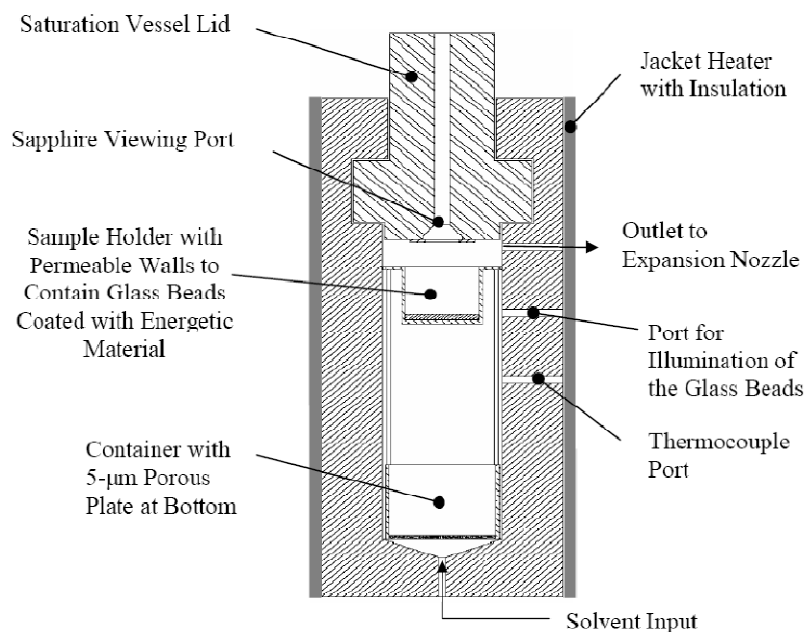


**Figure 27** Cross-sectional view of the saturation vessel.

In order to rapidly expand the supercritical solution, a nozzle assembly was needed. A cross-sectional schematic of the nozzle assembly used in the RESS process can be seen in **Fig. 28**. The nozzle assembly consists of 3/8" connection that allows for the supercritical solution to enter. A K-type thermocouple is used to measure the temperature of the supercritical solution before it rapidly expands. This is to ensure that the solution has the same temperature as the saturation vessel so that premature precipitation will not occur prior to the rapid expansion. The assembly also has four slots for cartridge heaters to be placed inside. The heaters ensure that the nozzle temperature does not drop as the rapid expansion would otherwise cool the nozzle down. The nozzle assembly also has a micro-frit to prevent large foreign particles or prematurely precipitated particles from clogging the nozzle. Finally, a sapphire micro-orifice insert (A. M. Gatti; Trenton, New Jersey) is screwed into the assembly to serve as the nozzle. This readily purchased product allows for multiple nozzle sizes to be easily used. The nozzle assembly also has a fitting that allows for an expansion tube to be directly coupled to the assembly. The nozzle assembly helps to facilitate in the formation of dry ice for gravimetric collection of the synthesized particles.

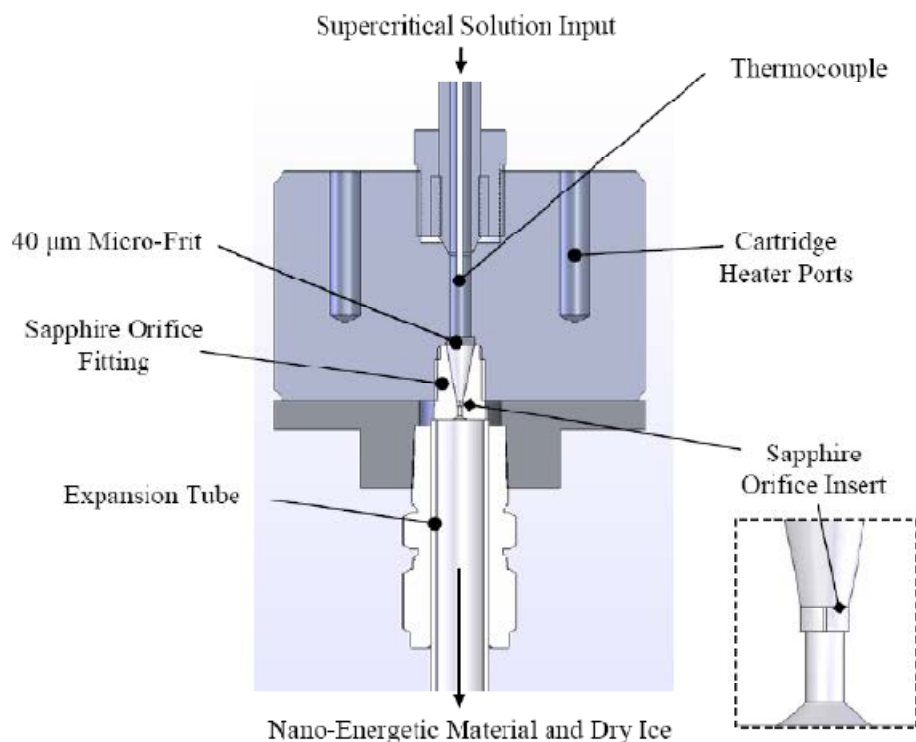


**Figure 28** Cross-sectional view of the nozzle assembly for the RESS system.

One of the major challenges encountered in the RESS process was the collection of generated nano-sized RDX particles. These ultra-fine particles can easily be entrained by the flowing  $\text{CO}_2$  discharging from the system. Also, nano-sized particles tend to coat the walls of the expansion tube and the collection vessel. The handling of ultra-fine RDX particles must avoid generation of sparks due to any static charges. Friction can also cause the final products of the RESS system to reach ignition conditions. Special care must be taken when handling all recovered materials. After various iterations, the method adopted in collecting ultra-fine particles was the formation of dry ice (solid  $\text{CO}_2$ ) in the expansion tube downstream of the nozzle exit and in the particle collection vessel. From **Fig. 29**, one can see that the expansion in the RESS process is favourable for forming dry ice, as the expansion through the orifice can be approximated as an isenthalpic throttling (constant enthalpy) process. However, if the supercritical  $\text{CO}_2$  was just expanded into an ambient environment no dry ice was formed in actual experiments. This problem was resolved by adding an expansion tube after the sapphire nozzle. When an expansion tube is placed directly downstream of the nozzle, the  $\text{CO}_2$  jet is confined. This confinement forces the  $\text{CO}_2$  flow to reach high concentrations and makes the newly formed dry ice interact with each other. Due to coagulation of  $\text{CO}_2$  particles, larger chunks of dry ice can form. Due to the heterogeneous nucleation of dry ice with RDX particles serving as nuclei, RDX particles are encapsulated in dry ice. This process prevents RDX particles from coagulating early in the particle growth process. These large chunks are affected by gravity with less chance for entrainment by the exhaust gas. The end result of the rapid expansion and growth processes leads to larger dry ice particles, which contain numerous nano-sized RDX particles. Thus, the formation of dry ice is beneficial for the collection of nano-sized RDX particles.

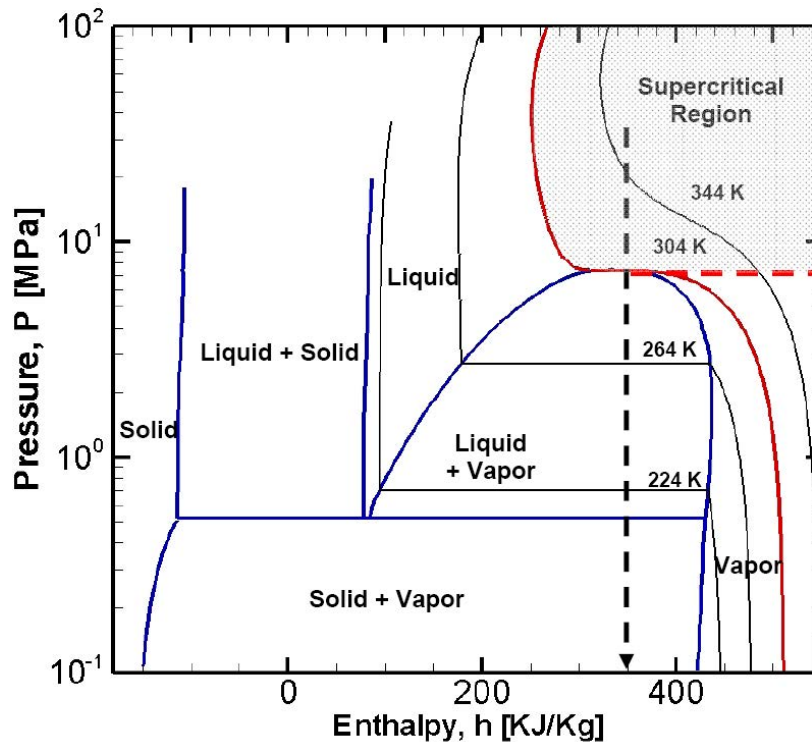


**Figure 29** Pressure-enthalpy phase diagram of CO<sub>2</sub> illustrating the isenthalpic expansion path from pre-expansion temperature and pressure conditions.

The user operated section of the RESS system can be seen in **Fig. 30**. This section of the RESS system is protected from the ultra-high pressure section by a solid wall. The solvent manifold, chiller, control panel, and control computer are all located in this section. The control panel consists of an emergency stop that cuts power to the system and relieves pressure if anything unexpected occurs. The control panel is also where the temperature controllers are located for the saturation vessel, line, and nozzle heaters along with the power to the entire system. The control panel also allows one to control the needle valves in the system. The computer program for the system allows one to control the system pressure and the needle valves. It also allows the user to observe the temperature and pressure of the supercritical solution at various points in the system.

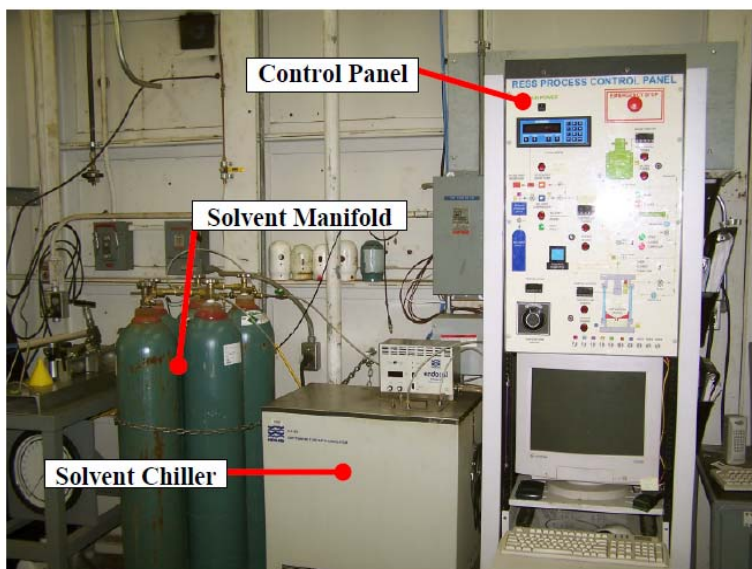


**Figure 30** Remotely controlled portion of RESS system.

For tests using RDX, military grade RDX was obtained from a supplier containing a non-negligible percentage of HMX (~5% by mass). Through a single recrystallization process the percentage of HMX was significantly reduced, increasing the percentage of RDX to nearly 100%. In this process the as-received RDX was dissolved in high-purity acetone at elevated temperature. The temperature of the solution was then reduced. As HMX is more soluble in acetone, it remained in suspension and a majority of the RDX condensed out of the solution.

Once the energetic material was purified and suitable for testing, an acetone and energetic material solution was created. The solution was then applied over warm glass beads. As the solution was applied over the beads, the acetone quickly vaporized, leaving a thin film of energetic material on the glass beads. This process was done to enhance the surface area over which the solute and solvent could interact in the RESS system. This step is necessary to aid in the dissolution of the energetic material into the supercritical solution. An image of RDX coated glass beads can be seen in **Fig. 31**.

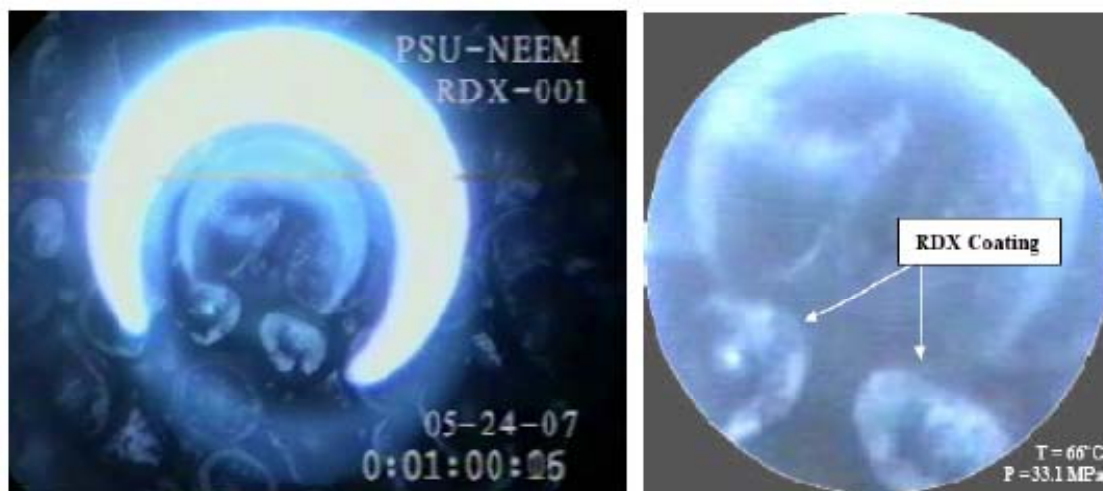


**Figure 31** RDX coated glass beads located in saturation vessel.

A transparent particle collection vessel was designed to connect to the downstream end of the expansion tube. The collection vessel consisted of a removable particle container, a clear acrylic outer wall for viewing the motion of the dry ice exiting the expansion tube, and a supporting stand for the particle container in order to allow any remaining CO<sub>2</sub> gas to escape from the particle collection vessel. The particle container was grounded to make sure that it had the same charge as the rest of the system. The exhaust gas was then guided through a water bath in the scrubber for removing any RDX particles entrained in the exhaust gas. After the RESS process, the particle collection container was removed prior to the sublimation of accumulated dry ice. In this manner, high percentages of nano-sized RDX are still contained in the dry ice. The dry ice is allowed to sublimate leaving the RDX particles behind in the collection container. Samples were then properly stored for analysis.

#### *RESS-AS Process*

A representational schematic of the RESS-AS process is given in **Fig. 32**. The process is similar to the RESS process, except that supercritical solution is not expanded into an ambient gas. Rather, the supercritical solution is expanded into a water and dispersing agent solution. The benefit of the RESS-AS process is that the dispersing agents in the solution can adsorb onto the newly formed particles and therefore form dispersed colloidal suspensions. The adsorption of the dispersing agents should also discourage further growth of the newly formed particles as the adsorbed molecules would discourage solute molecules from condensing onto the newly formed particles. Thus, smaller and less agglomerated particles were obtained from this process. The dispersing agent can be washed away by the appropriate solvents.

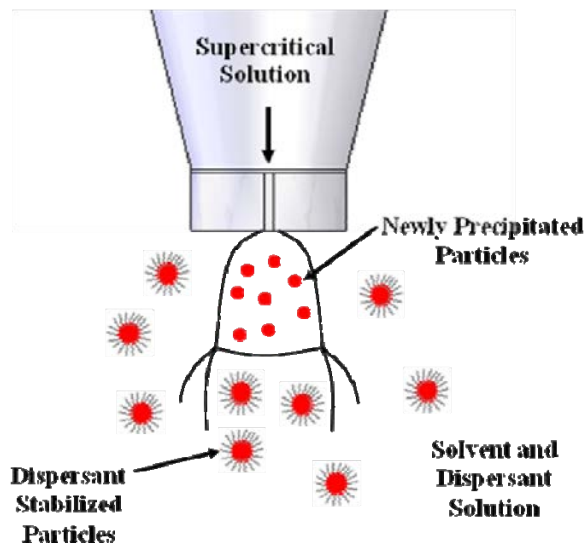


**Figure 32** Schematic representation of the RESS-AS process.

The system flow diagram for the RESS-AS process is shown in **Fig. 33**. The main difference between the RESS system and the RESS-AS system is the expansion vessel. With the RESS process the expansion vessel was filled with ambient air as the supercritical solution is expanded into it. In contrast, the supercritical solution is expanded into a water and dispersant solution for the RESS-AS process. For the RESS-AS system, the nozzle was placed about two inches under the water and dispersant solution. The water and dispersing agent solution volume was approximately 500 mL for all tests. A test began by having the supercritical CO<sub>2</sub> expand into the aqueous solution. Once steady state flow conditions were achieved, the supercritical solution was then flown through the orifice. The RESS-AS expansion vessel can be seen in **Fig. 34**. The nozzle assembly has a silicon heater to heat the tubing before it reaches the

nozzle assembly and two cartridge heaters to heat the nozzle assembly. The cartridge heaters are sealed and protected from any solution contacting them. The expansion vessel contains three K-type thermocouples. One thermocouple monitors the solution temperature, another monitors the temperature of the nozzle assembly, and the final thermocouple monitors the temperature of the tubing in the vessel to protect important equipment items in the chamber. The pH level of the solution was monitored before and after to record the ionic activity of the solution. Different amounts of dispersant and different types of dispersant were used. Care had to be used to prevent the solution from leaving the expansion vessel from too much foam being created by the dispersant. To mitigate this problem, a N<sub>2</sub> purge was used to suppress the foam during a test. The nozzle assembly was also heated to keep the solution temperature fairly constant and to prevent the nozzle from freezing. All tests were conducted with a pre-expansion pressure of 34.5 MPa and an orifice nozzle diameter of 100 μm. Tests were conducted for approximately 6 minutes. The resulting suspension was then collected in a container and analysis was performed on the colloidal suspensions.

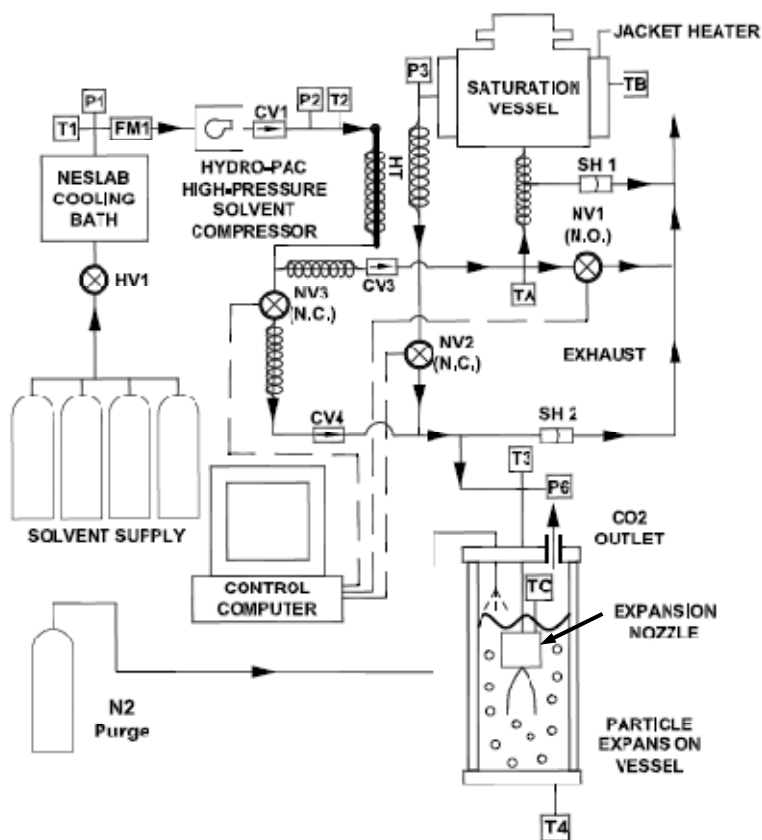


**Figure 33** Flow diagram of RESS-AS process.

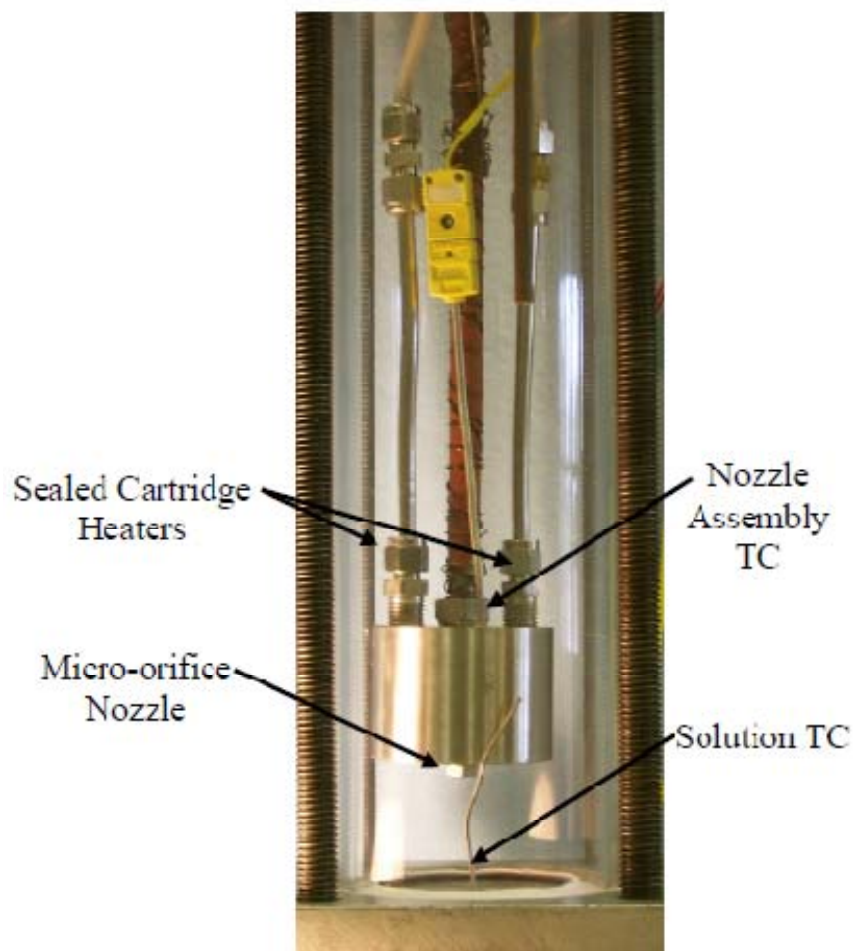


**Figure 34** RESS-AS expansion vessel.

Due to the nature of their small size, nano-sized particles behave differently than larger particles. Nano-sized particles are more controlled by Van der Waals forces than gravitational forces. Due to these forces, nano-sized particles will tend to be attracted to each other or any surface they can find that has a net charge. In order to stabilize these particles and prevent them from agglomerating, methods are needed and they differ depending on whether the particles are organic or inorganic in nature. However, before any methods can be applied, the surface charge of the particle in water needs to be understood.

The charge of the synthesized energetic particles in water was not known. Therefore, this information was needed before any dispersants could be selected. To measure the charge of RDX in ACS grade water, the zeta potential of RDX had to be determined. In order to determine this value, RESS synthesized RDX was placed into water and analyzed with a ZetaPALS zeta potential measuring instrument (Brookhaven Instrument Company; Holtsville, New York). The zeta potential is the electrostatic potential at a particle's slipping plane or the distance from the particle where the viscosity of the fluid remains constant. The slipping plane is located at the outer boundary of the electric double layer (composed of the Stern layer and Gouy-Chapman layer). It was determined that RDX has a large negative zeta potential of  $-80 \pm 6\text{mV}$ , meaning that the particles are somewhat stable in water, but their stability could be improved. Therefore, the selected dispersants can adsorb onto the negatively charged particles.

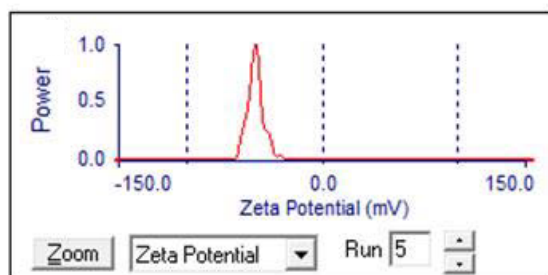


**Figure 35** Zeta Potential of RDX in water.

Different types of dispersing agents were used to observe their effect on the final particle morphology, agglomeration, and size. Making sure that fine particles are adequately dispersed and stable in an aqueous suspension requires balancing the forces from attractive Van der Waals forces and repulsive electrostatic forces. Colloidal stability is achieved when the repulsive forces are stronger than the attractive forces [110]. Colloids tend to coagulate from net charges in the electrical double layer around each particle in the medium that it is in. Often, electrolytes or surfactants are used to provide the repulsive electrostatic dispersive force. This is achieved by changing the charge of the electric double layer or by steric methods. It is of interest to use surfactants that are charged (ionic) and uncharged (nonionic) in an aqueous suspension to see their effect on the final collected particles. For this study, an anionic surfactant sodium dodecyl sulfate (SDS;  $C_{12}H_{25}SO_4Na$ ) was used as it would adsorb onto a negatively charged particle. Along with SDS, the polymer 1-Vinyl-2-pyrrolidinone (NVP;  $C_6H_9N_1O_1$ ) was used as it is known that this polymer can coat negatively charged particles rather easily [111]. The molecular structures of both these dispersants (surfactants) can be seen in **Fig. 36**.

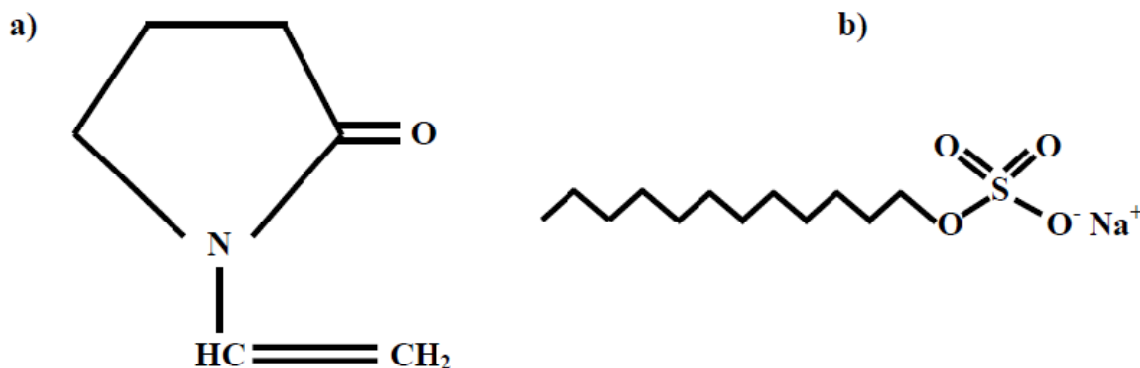


**Figure 36** Adopted dispersing agents a) 1-Vinyl-2-pyrrolidinone (NVP) and b) Sodium Dodecyl Sulfate (SDS).

#### RESS-N Process

For this project, the RESS-N process was used to coat nano-sized aluminum particles (ALEX<sup>®</sup>) with RDX. In order to coat ALEX<sup>®</sup> particles in a manner that would take advantage of the rapid expansion of a supercritical solution, ALEX<sup>®</sup> particles needed to be present in the supercritical solution when it is expanded. This is because the rapid expansion of the supercritical solution can cause a high-degree of supersaturation and the seeded particles should act as a nucleation catalysis. Therefore, the metastable RDX wants to nucleate onto anything in its immediate vicinity. The objects that it can coat

were ALEX<sup>®</sup> particles. A schematic of this concept can be seen in **Fig. 37**. The RESS-N process is similar to the RESS process, except that supercritical CO<sub>2</sub> nonsoluble particles are seeded into the supercritical solution. Therefore, the challenge of making a working RESS-N system lies in properly seeding the desired particles (like ALEX<sup>®</sup>) to be coated into the supercritical solution.

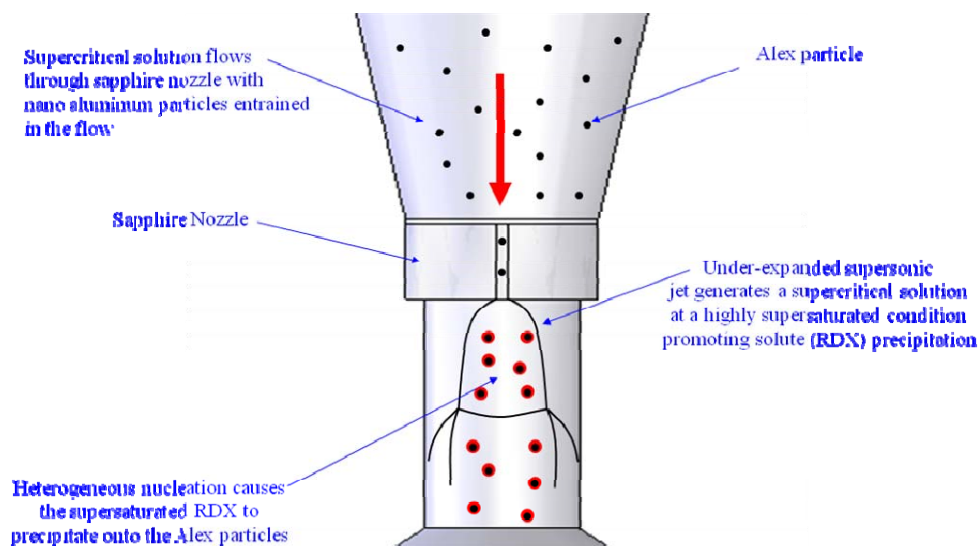


**Figure 37** ALEX<sup>®</sup> Particle Coating Concept with the RESS-N process.

Two slightly different experimental setups were used to achieve this goal. The first experimental setup consisted of placing a particle entrainment vessel upstream of the nozzle assembly used for the RESS process. The flow diagram of this RESS-N setup can be seen in **Fig. 38**. The overall system operates in a similar manner as the RESS system does for homogeneous nucleation. RDX and supercritical CO<sub>2</sub> form a supercritical solution. The supercritical solution is then allowed to flow through the system by air-operated remote controlled needle valves. The temperature and pressure of the solution are monitored at specific points in the flow path by thermocouples and pressure transducers. A bypass line then pressurizes the whole system including the particle entrainment vessel. Once the system is at a steady state condition in regards to fluid flow, the supercritical solution flows through the particle entrainment vessel and suspends ALEX<sup>®</sup> particles in the supercritical solution. The entrained aluminum particles then flow through a sapphire micro-orifice nozzle so that the supercritical solution becomes supersaturated from the rapid expansion. The RDX in the solution will then tend to nucleate onto the aluminum particles, which provide active nucleation sites. The system also has an expansion tube that facilitates the formation of dry ice. Dry ice will precipitate onto the newly coated particles giving them enough body weight for gravimetric collection in a steel collection container. Changing the degree of supersaturation by varying the pre-expansion temperature and pressure as well as the concentration of aluminum particles in the supercritical solution can change the coating thickness on the nano-sized aluminum particles. Due to clogging of the sapphire orifice, only orifices larger than 300  $\mu\text{m}$  were used. This limited the maximum pre-expansion pressure of the system to 34.5 MPa for the RESS-N process.

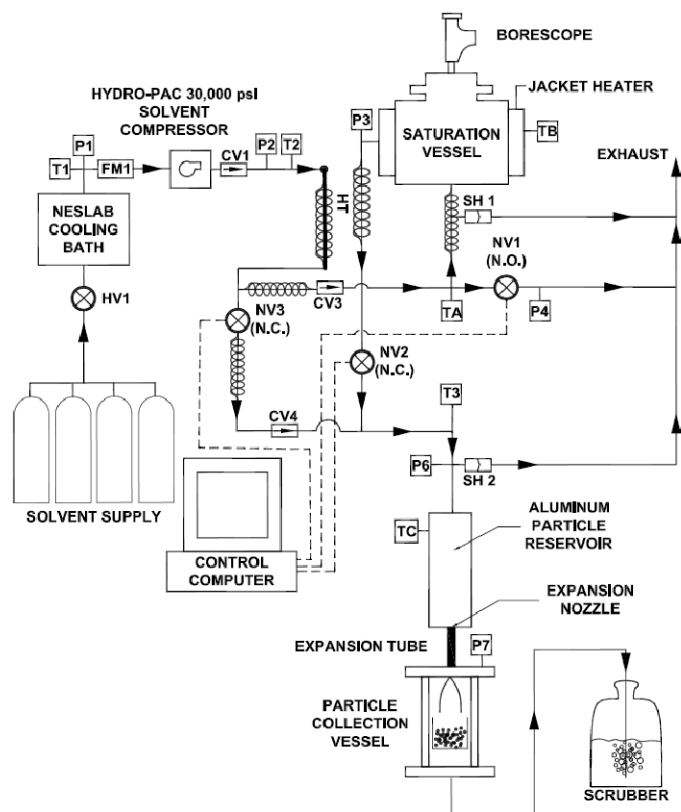


**Figure 38** Flow diagram for coating nano-sized aluminum particles by the RESS-N process with particle entrainment vessel.

A view of the particle entrainment vessel can be seen in **Fig. 39**. Nano-sized ALEX<sup>®</sup> aluminum particles are placed in a special holder inside the vessel. The vessel is initially prefilled with CO<sub>2</sub> so that the vessel is pressurized before the supercritical solution containing RDX enters the chamber. This prevents the supercritical solution from prematurely expanding, causing RDX precipitation inside the vessel. The supercritical solution then flows over the aluminum particles in the holder, which entrains them in the flow. The entrained particles and solution then flow through a micro-orifice nozzle; the rapid expansion process promotes the coating of the ALEX<sup>®</sup> particles. A cross sectional view of the entrainment vessel is shown in **Fig. 40**.



**Figure 39** Particle entrainment vessel for introducing aluminum particles into a supercritical solution.

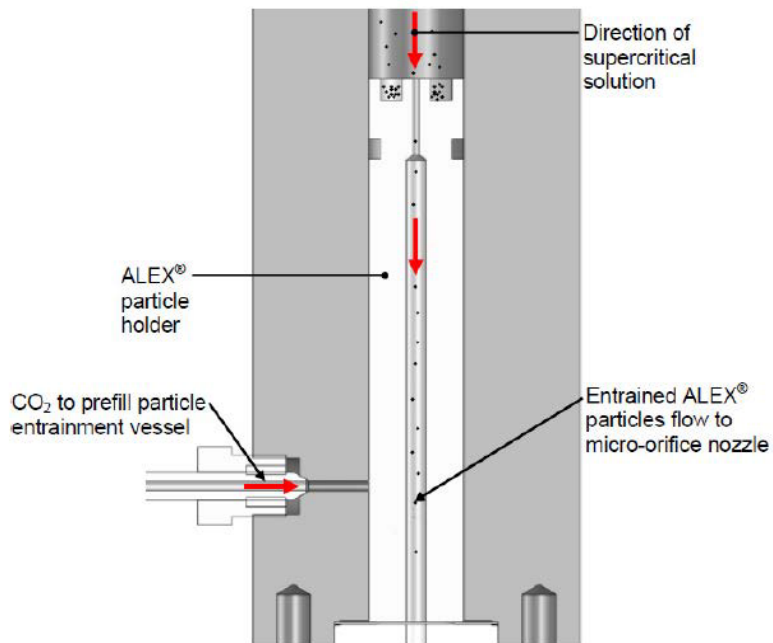


**Figure 40** Cross-sectional view of particle entrainment vessel.

Special precautions had to be taken with the collection of aluminum particles. Due to the high electrostatic discharge (ESD) sensitivity of nano-sized aluminum particles, safety measures were put into place. The particle collection container was grounded to ensure that any static charges that the particles picked up would be conducted away. A photograph of the particles collected in the container is shown in **Fig. 41**. Also, the entire test structure was grounded and any operators working on the collection of particles were electrically connected to the test stand by their wrist bands.

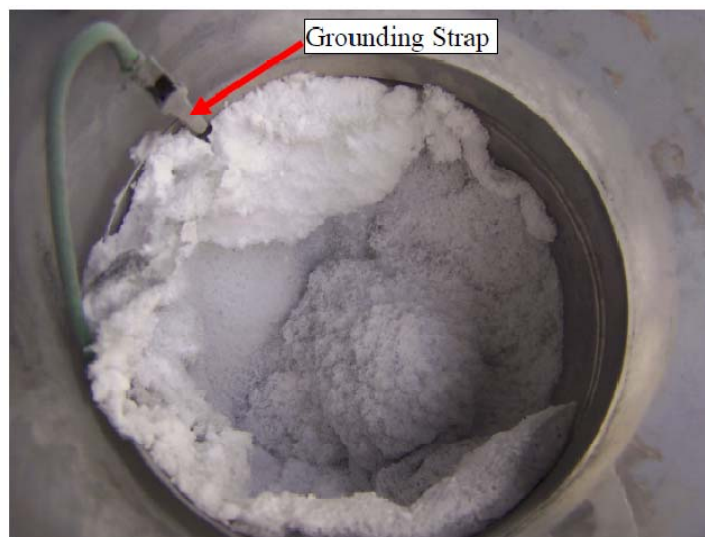


**Figure 41** Captured particles in dry ice in the collection container.

While the particle entrainment vessel was beneficial in suspending particles into the supercritical solution, the feeding rate of the aluminum particles could not be controlled. This was because the entrainment rate was dependent on the fluid mechanics inside the system which were dictated by the choked flow at the nozzle throat. Also, it was determined that too many ALEX<sup>®</sup> particles left the system during the initial pressurization process. It was determined that it would be beneficial to introduce a component to the RESS-N system that would allow for ALEX<sup>®</sup> particles to be suspended in the supercritical solution independent of the system fluid mechanics. To allow for more experimental manipulation, an aluminum particle feeder was designed and introduced into the system. A flow diagram of this experimental system is shown in **Fig. 42**. The particle feeder consists of a linear actuator (Ultra Motion; Cutchogue, New York) which is controlled by serial commands from a computer. The linear actuator is directly attached to a piston which pushes a reservoir of ALEX<sup>®</sup> particles into the supercritical solution. The piston is sealed by an o-ring and backup ring. The linear actuator is capable of multiple speeds and distances, so different injection rates and amounts can be utilized to allow for different particle concentrations in the supercritical solution. The actuator was directly integrated into a LABVIEW<sup>®</sup> program to control the device remotely and to couple the device directly to a program that also controls the needle valves in the system and directly monitors the temperature and pressure of the system. The actuator was then mechanically connected to a HipCo<sup>®</sup> three way needle valve to introduce particles into the solution.

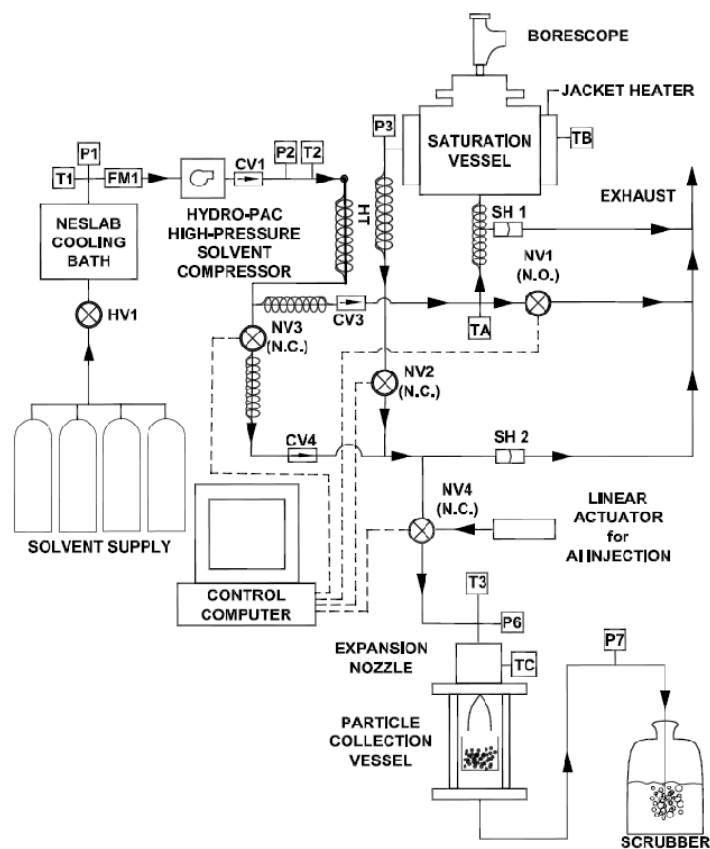


**Figure 42** RESS-N flow diagram for particle injection.

An image of the actuator integrated into the RESS-N system can be seen in **Fig. 43** along with a cross-sectional illustration of the injection system. The particle injector was connected to a three-way HipCo<sup>®</sup> valve. The connection is a product from HipCo<sup>®</sup> and allowed for a remote controlled needle valve to isolate the flowing fluid from the ALEX<sup>®</sup> reservoir before an injection. The three ports of the connection consist of an inlet for the supercritical fluid to travel through, one for ALEX<sup>®</sup> particles to be injected, and one for the suspension to exit the connection and travel to the nozzle assembly. The piston assembly that was attached to the three way connection was removed before a test and preloaded with ALEX<sup>®</sup> powder before being reattached to the three way connection. Before particles are injected, a bypass line fills the system with supercritical CO<sub>2</sub>. Once the supercritical solution was flowing through the tubing, the needle valve was remotely opened and the linear actuator was activated to allow the piston to move the ALEX<sup>®</sup> powder into the supercritical solution to seed the solution with particles. The particle injector then introduces ALEX<sup>®</sup> particles into the supercritical solution at a controlled rate. After this, the suspension flows through the nozzle assembly so that the supersaturated solution precipitates the energetic material onto the ALEX<sup>®</sup> substrate. Particles are collected in the same manner that they are for the RESS system.

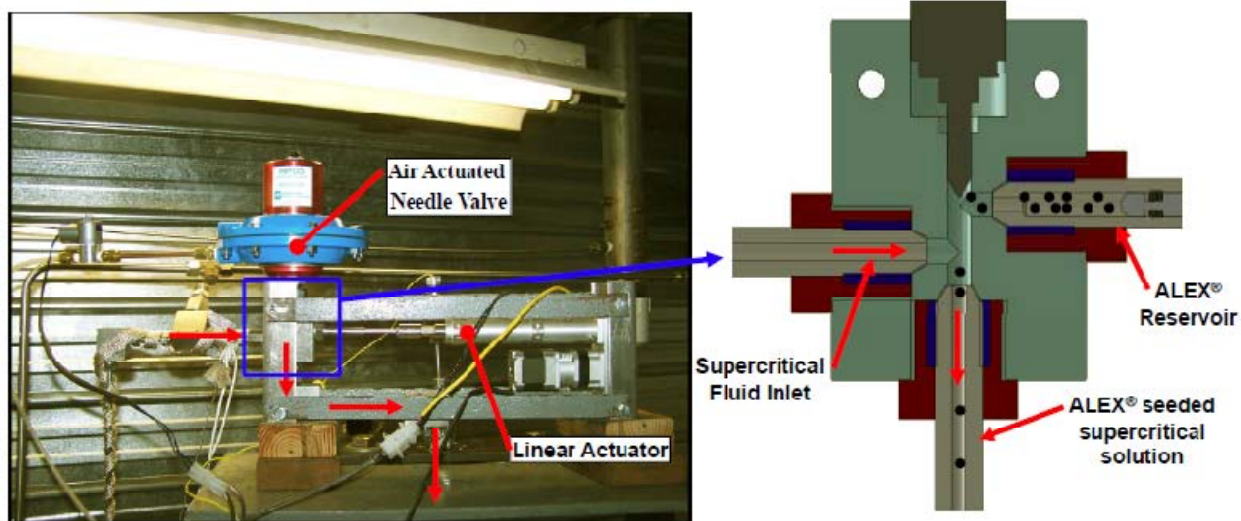


**Figure 43** Linear actuated nano-sized aluminum particle injector.

#### II.1.4.4 Discussion and Results

##### *RESS Results*

Two energetic materials were tested with the RESS system; RDX and BTAT. RESS synthesized particles were analyzed for their size and morphology through electron microscope analysis. Their chemical purity and crystal structure were also analyzed. Once these critical properties were determined, the particles were tested to see if they possessed any difference in sensitivity in comparison to larger military grade particles.

For RESS synthesized RDX, the effect of nozzle size, pre-expansion pressure, and pre-expansion temperature were to be investigated. A test matrix of the tests considered can be seen in

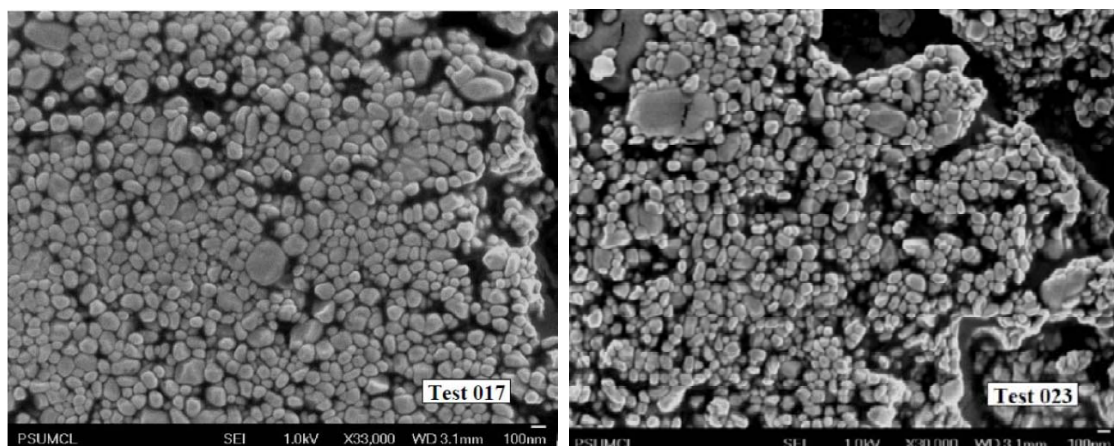
Table 2. A total of 24 different test conditions were studied to see what effect experimental conditions have on the final synthesized particles. Of particular interest is the effect of the supercritical fluid pre-expansion pressure on the final particle size and size distribution. As mentioned before, previous work showed that the final collected particles were smaller for increasing pre-expansion pressures. However, the highest pre-expansion pressures investigated in that study was 29 MPa. For this study significantly higher pre-expansion pressures will be investigated to see if there is a benefit to operating the RESS process in a higher pressure regime. This is because higher pressures increase the density of the solvent, promoting more interaction between solute and solvent [96]. This could increase solubility and supersaturation when the solution is expanded.

Table 2. Test matrix for studying effects pre-expansion conditions in the RESS process on RDX

Test	P <sub>0</sub> (MPa)	T <sub>0</sub> (K)	Nozzle Diameter (μm)	Test	P <sub>0</sub> (MPa)	T <sub>0</sub> (K)	Nozzle Diameter (μm)
001	34.5	328	100	013	34.5	328	150
002	51.7	328	100	014	51.7	328	150
003	68.9	328	100	015	68.9	328	150
004	86.2	328	100	016	86.2	328	150
005	103.4	328	100	017	103.4	328	150
006	120.7	328	100	018	120.7	328	150
007*	34.5	348	100	019	34.5	348	150
008	51.7	348	100	020	51.7	348	150
009	68.9	348	100	021	68.9	348	150
010	86.2	348	100	022	86.2	348	150
011	103.4	348	100	023	103.4	348	150
012	120.7	348	100	024	120.7	348	150

\* Test did not yield suitable particle shapes due to some outside contamination

For electron microscope analysis of the synthesized particles, a JEOL 6700F field emission scanning electron microscope (FE-SEM) was used in order to obtain images of all the samples collected. Samples were prepared by obtaining the produced dry ice with nanoparticles embedded in it. The dry ice was allowed to sublime leaving the particles behind. The particles were then placed on an aluminum stub with conductive carbon tape. The samples were then iridium coated to increase their conductivity for imaging purposes. The prepared samples are then placed in the FE-SEM and images were taken. FE-SEM images of the RESS synthesized particles can be seen in **Fig. 44**. For RDX RESS testing, the microscope images from the FE-SEM reveal that the synthesized particles are drastically different than the original military grade particles. The RESS synthesized particles tend to be very similar in size with a few particles that are noticeably bigger than the others. This indicates that they have a narrow size distribution. The particles are also noticeably smaller than conventional RDX particles with sizes around 100 nm. The particles also appear to be fairly smooth in shape as well. All of these qualities imply that the RESS synthesized RDX particles should be noticeably less sensitive to accidental initiation by impact than military grade RDX. The consistency of the synthesized particles is also an optimal feature as it suggests that the produced product has little variation and is very uniform.



**Figure 44** FE-SEM images of RESS synthesized RDX particles.

While microscope images allow qualitative analysis of the produced samples, quantifying the average size and the particle size distributions of the synthesized particles is more informative and useful. From numerous FE-SEM images of each test the particle size distributions and median particle sizes were quantified for each test. The particle size distributions for various tests can be seen in **Fig. 45** and **Fig. 46**. In general, the size distributions are very narrow, which is a result of the uniform conditions achieved with supercritical fluid precipitation. A large amount of the solute is expected to precipitate out of solution by homogeneous nucleation, creating particles of the critical size. One can see that smaller size distributions can be observed for tests conducted with higher pre-expansion pressures. This does not necessarily mean that a higher pre-expansion pressure will always produce smaller particles. In fact, there is probably an optimum pre-expansion pressure. For both experiments conducted with a 100 and 150  $\mu\text{m}$  nozzle, there were no noticeable benefits from increasing the pre-expansion pressure above 86 MPa. At a pre-expansion pressure of 86 MPa, particle size distribution curves are at their narrowest and are farthest to the left (indicating a smaller size). Increasing the pre-expansion pressure increases the density of  $\text{CO}_2$  which has been shown to have a favorable increase in dissolution for supercritical fluids. Larger solubility's in the beginning of the expansion results in higher supersaturations. However, if the supercritical fluid is too dense, retrograde behavior can occur from repulsive forces between the solvent and solute. Also, increasing the pre-expansion pressure results in a more under expanded free jet after the solution exits the nozzle. The under expanded jet will be at a higher pressure and will have more severe shock waves. These can contribute to the particles growing by coagulation from slip velocities between the particles and the  $\text{CO}_2$ . It is these competing factors that imply that there would be an optimum pre-expansion pressure. Previous research did not find this optimal pre-expansion pressure and it is beneficial to know that higher pre-expansion pressures than the upper limit in previous research (29 MPa) will yield a narrower size distribution.

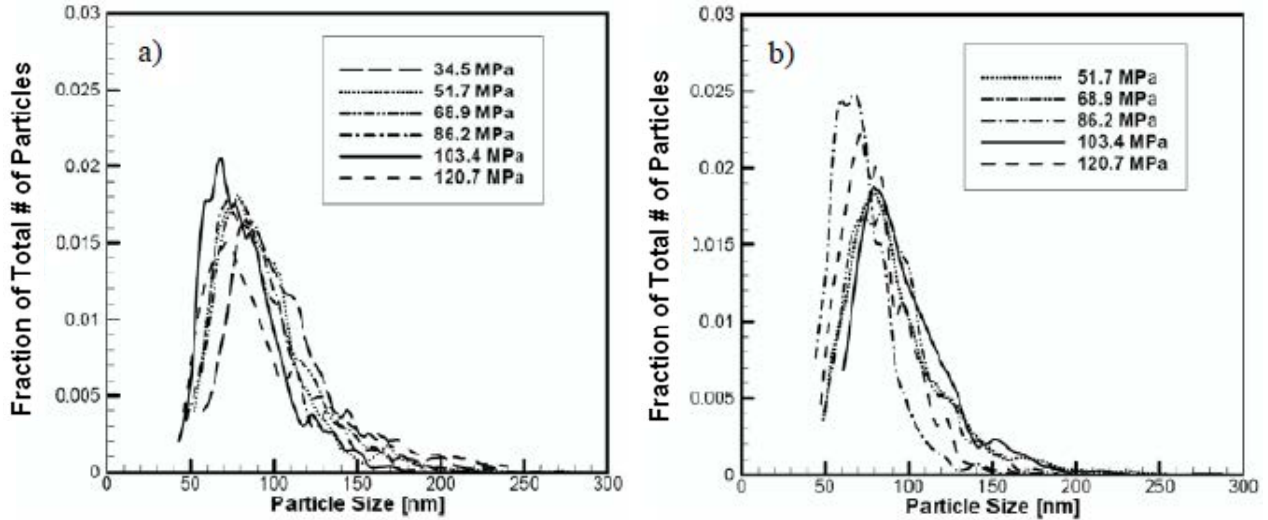


**Figure 45** Particle size distributions for 100  $\mu\text{m}$  nozzle with a)  $T_0=328\text{ K}$  b)  $T_0=348\text{ K}$ .

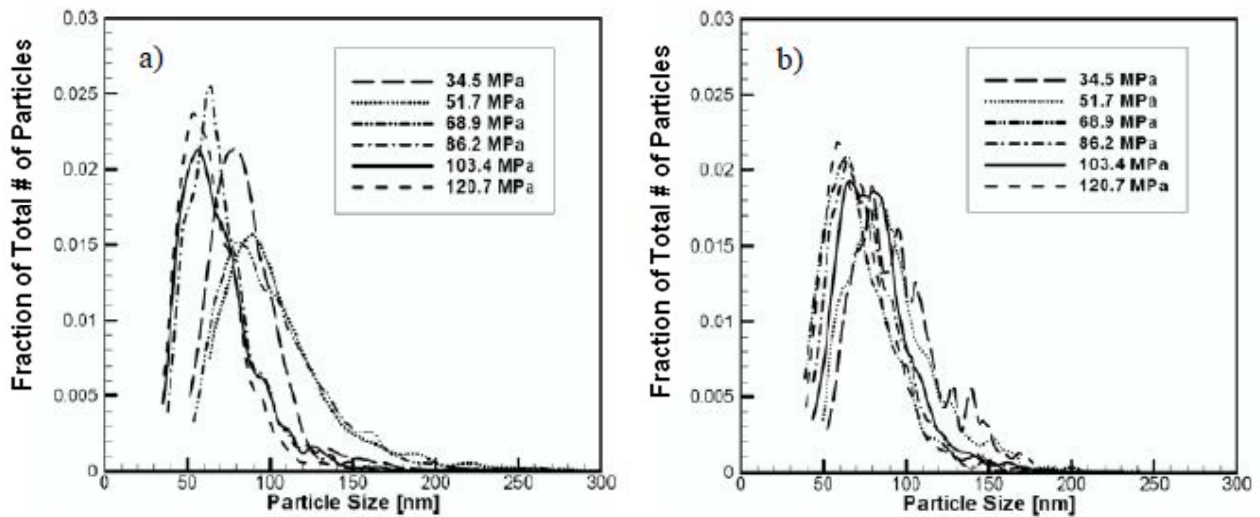


**Figure 46** Particle size distributions for 150  $\mu\text{m}$  nozzle with a)  $T_0=328\text{ K}$  b)  $T_0=348\text{ K}$ .

Along with particle size distributions, median RDX particle sizes were also observed to decrease with increasing pre-expansion pressures. Results from the experiments can be seen in **Fig. 47** and **Fig. 48**. Median particle sizes are shown with their deviations represented by the error bars. The deviations were taken as the full width at half maximum from the particle size distributions. For the tests with the 150  $\mu\text{m}$  nozzle, increasing the pre-expansion pressure did lower the median particle size. For tests conducted with the 100  $\mu\text{m}$  nozzle, trends were less apparent. The differences in pre-expansion pressures and temperatures did have a greater effect on the amount of dry ice that was produced during the expansion process. More dry ice could have prevented the particles from interacting with each other further by coagulation. It was previously shown that higher pre-expansion pressures could produce more dry ice. Also, dissolution was probably increased at higher pressures inside the saturation vessel. This would increase the initial supersaturation and would produce smaller particles by homogeneous nucleation. However, as explained before higher pre-expansion pressures can increase coagulation indicating that there might be an optimum pre-expansion pressure. Operating at higher pre-expansion

pressures is beneficial with the RESS process (up to  $P_0=86$  MPa), but it might also be beneficial to vary other parameters (e.g. the environment that the supercritical solution expands into) to see if this has a greater effect on particle size and morphology, as this could reduce growth by coagulation. This was investigated with the RESS-AS system.

From published data of Stepanov et al. [101] their collected RDX particles are in the range of 110 to 220 nm for the average size with maximum operating temperature and pressure up to 353 K and 29.5 MPa, respectively. They indicated that the smaller diameter expansion nozzle would yield smaller RDX particles. However, this trend was not seen at the elevated pressures employed in the present study. Reasons for this could be not enough experiments were conducted or differences in experimental setup. The collected RDX particles in the present work, ranged from  $65 \pm 15$  nm to  $85 \pm 25$  nm for the median size and the larger diameter (150- $\mu\text{m}$ ) nozzle produced relatively smaller particles than those from the 100- $\mu\text{m}$  nozzle. The particle size range was determined from the particle size distribution plots using the full-width at half-maximum method. This method is straight forward, taking the points at the widest part of the particle size distribution at a height that is half of the highest point for each individual test. The size ranges between the upper and lower bounds shows a degree of uniformity.

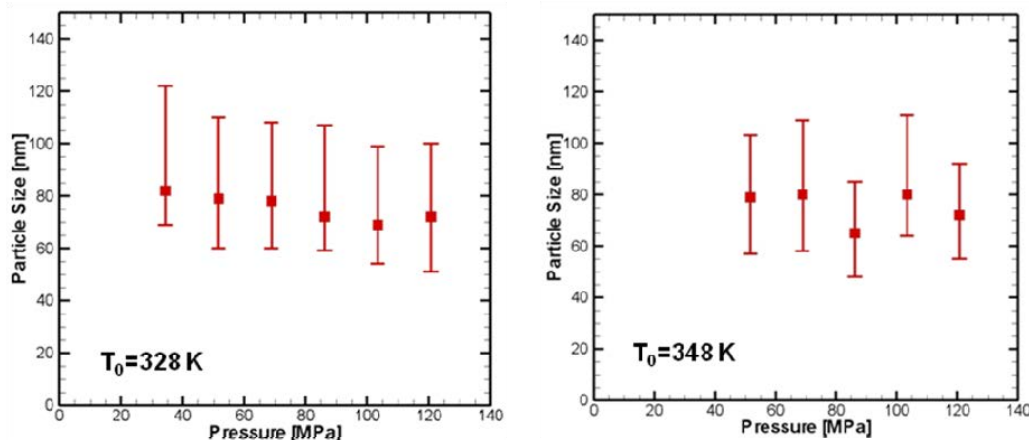


Figure 47 Median RDX particle sizes for 100- $\mu\text{m}$  nozzle a)  $T_0=328$  K b)  $T_0=348$  K.

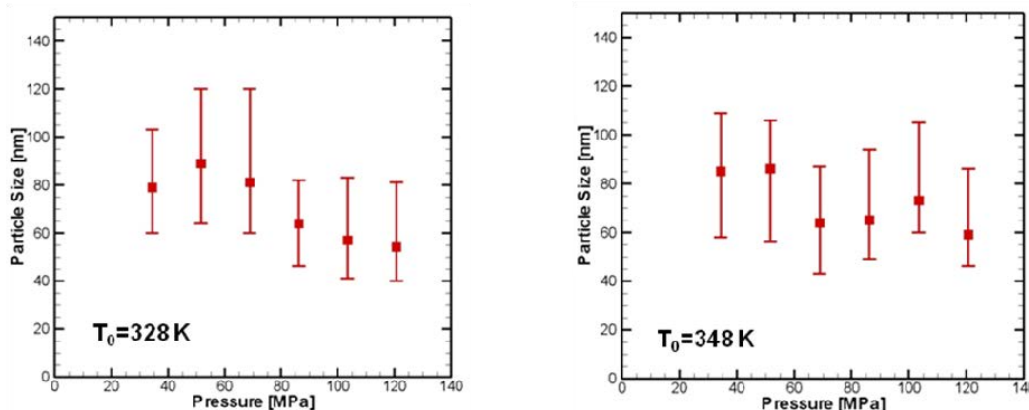
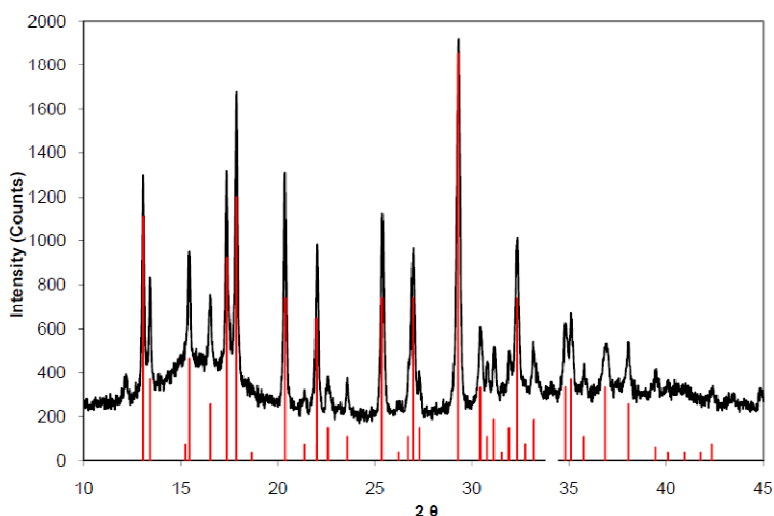


Figure 48 Median RDX particle sizes for 150- $\mu\text{m}$  nozzle a) 328 K b) 348 K.

While size analysis was highly important for the investigation, other material properties of the synthesized energetic materials can affect their sensitivity and performance. Material characterization can

yield valuable information on the structure and purity of the final product. Simply inspecting images of nano-sized particles is insufficient to properly characterize them thoroughly. Material characterization of the RESS synthesized particles was conducted as well. One concern was about the crystal quality of the final RESS synthesized powders. It was unclear whether the RESS process would synthesize crystalline materials and if they were crystalline it would be advantageous to know the crystallite size and to determine any crystal imperfections. To investigate this, powder X-ray diffraction (XRD) was performed on the synthesized samples. Along with the crystal quality, the chemical purity of the samples was also important to know. To achieve this, high performance liquid chromatography (HPLC) was used on the samples. The purpose of this technique was to investigate if the RESS process would have a purifying effect on the final powders in regards to HMX contamination.

Powder X-ray diffraction (XRD) results taken of RESS synthesized RDX can be seen in **Fig. 49**. The scanned diffraction pattern is shown in black while the location and relative intensity of spectra obtained from previous crystallography work [112] on RDX are shown as red lines. It is clearly seen that the RESS synthesized RDX has the same crystal structure as RDX from the fact that the peaks line up together. This is encouraging as it was unknown as to what type of crystalline order RDX particles would have from the rapid precipitation seen in the RESS process. Further information such as crystallite information from the Scherrer equation could not be obtained because the crystallites were so small.



**Figure 49** XRD data for RESS synthesized RDX.

Another characteristic of the RESS synthesized RDX powders that was investigated was the chemical purity. HMX impurities in RDX crystals have been shown to increase the sensitivity of RDX [113]. High performance liquid chromatography (HPLC) was used on the RDX samples to determine their purity. All samples were dissolved in a 50:50 acetone and water mixture. A gradient of methanol and water was used as the carrier fluid. A C18 silica column was used to separate the RDX from the HMX. The chromatography results from the tests can be seen in Table 3. Listed are the military grade RDX that was used in the experiments, the same RDX once it was recrystallized with acetone, and then the RESS synthesized RDX prepared from the recrystallized RDX. It can be seen that the RESS synthesized RDX is almost completely pure of HMX contamination. The reason for this is that HMX has a lower solubility in supercritical CO<sub>2</sub>. Therefore, dissolving RDX with HMX contamination dissolves proportionally more RDX than HMX, leaving some HMX in the saturation vessel. This results in RDX particles that are chemically purer. This is beneficial for synthesizing low sensitivity RDX.

**Table 3.** High performance liquid chromatography results for the chemical purity of RESS synthesized RDX

<b>RDX Sample</b>	<b>HMX mass fraction (%)</b>	<b>RDX mass fraction (%)</b>
<b>Military Grade (Class I Type II)</b>	<b>5.71</b>	<b>94.29</b>
<b>Recrystallized</b>	<b>0.86</b>	<b>99.14</b>
<b>RESS Synthesized</b>	<b>0.32</b>	<b>99.68</b>

Of greatest importance in this study is the evaluation of particle size on sensitivity. The results of the three types of sensitivities evaluated in a series of test are given in Table 4. Also, for comparison the previously determined Naval Surface Warfare Center Indian Head Division (NSWC-IHD) RDX standards are given. The main goal of synthesizing energetic materials by the RESS process is to reduce their sensitivity to accidental initiation. Therefore, confirming the sensitivity of the synthesized particles is absolutely critical. The sensitivity of the synthesized powders was investigated by introducing them to an outside stimulus from impact, friction, and electrostatic discharge (ESD). Due to the danger and equipment needed to conduct these standardized tests, testing was performed at NSWC-IHD in a collaborative work between PSU and NSWC-IHD. All sensitivity testing was conducted in accordance with the US Section of NATO Allied Ordinance Publication seven (AOP-7) [114] and included Explosives Research Lab (ERL) impact tests (Method 1012), Allegheny Ballistics Lab (ABL) friction tests (Method 1021), and Naval Surface Warfare Center (NSWC) ESD tests (Method 1031).

The ERL impact testing instrument has a maximum drop height of 3.2 m. To conduct a test, a 35±5 mg sample is loaded onto a one-inch square piece of 180 grit sand paper, which is then placed on top of a steel anvil. A steel striker is placed on top of the assembly. The striker has the geometry of a truncated cone at its top surface in order to concentrate the force in the axial direction. A magnet is employed to contact and lift the 2.5 kg weight to a desirable height. The weight is then released falling until it hits the striker which transmits the impulse to the test sample and may initiate a reaction, depending upon the level of potential energy. Ignition is mainly caused by particles shearing as a result of being forced to the outer edges of the sand paper holder. Twenty-five tests were conducted and statistical analysis was performed using the Bruceton method [115]. Ignition was determined from visual inspection of the sand paper after a test. Standard deviation of results needed to be within 0.5 to 2.0 cm of the interval size.

The ABL friction test required a test sample of 50 mg to be placed onto a steel anvil and spread to a height of 0.762 mm. To conduct the test, force is applied hydraulically through the non-rotating steel wheel to the sample which rests on an anvil. A pendulum then impacts the edge of the anvil propelling the anvil forward at a known velocity, about 2.44 m/s. Similar to the impact testing it was a go/no-go visual test, however the threshold initiation level (TIL) was found rather than a 50% value. The recorded TIL value is the hydraulic force applied to the non-rotating wheel. Twenty consecutive tests without reaction at a given force are needed to determine the material's sensitivity.

The particles showed a substantial decrease in their sensitivity to impact as expected with similar sensitivity results for friction and ESD. The testing results show the greatest decrease in the impact sensitivity. The measured H<sub>50</sub> value of synthesized nano-RDX particles is 44 cm compared to the 17 cm for the RDX standard, an increase of approximately 260 % in height. These results imply a much reduced sensitivity of nano-RDX to impact. This can be attributed to the removal of internal inclusions and surface defects, smaller size, and higher purity. However, the sensitivity to friction is slightly increased

as the threshold initiation level was slightly lower than that of the RDX standard. The sensitivity to ESD remained the same. The ESD testing result alleviated the concern that nano-RDX might have been more sensitive to electrostatic discharge. Similar to the RDX standard, the nano-RDX is designated as having medium sensitivity by the Hazard Characterization Lab at NSWC-IHD.

**Table 4.** RDX Sensitivity Testing Results Conducted Under Collaboration between PSU and NSWC-IHD

Particle Sample	ERL Impact Test 50% height [cm]	ABL Friction Test 20 TIL [psig]	ABL ESD Test 20 TIL [J]
Nano-RDX	44	100	0.165
RDX Standard	17	135	0.165

RESS results for BTAT were encouraging. Using BTAT as a solute in the RESS system produced positive results. First, it was confirmed that BTAT is soluble in supercritical CO<sub>2</sub>. Although the solubility is less than what was observed for RDX. The observed solubility was approximately 0.015 mg BTAT/g CO<sub>2</sub>. Therefore, BTAT is capable of being used in the RESS system in a similar manner to RDX. Initial experiments were run at similar conditions as previous RESS experiments for RDX. Some degree of success was observed with finely nucleated particles. FE-SEM images of these particles can be seen in **Fig. 50**. Synthesized particles were rounder and significantly smaller than the as-received particles. Many of the nucleated particles tended to be around 100 nm, however not all particles nucleated in a spherical manner. Many of the BTAT particles tended to nucleate in a more needle like manner. The needle like manner comes from the fact that crystal shape is dictated by the free energy at their growing surface. However, it is unclear as to what are the physical conditions that could be causing the inconsistency in the crystal shape of the collected particles. Also, the nucleated particles tended to bridge together which is undesirable as adequate separation of the nucleated particles could not be achieved. This suggests that during early particle nucleation and growth the precipitated particles were all individual particles and proceeded to grow as individual particles. Processes after the initial nucleation and growth such as coagulation and agglomeration probably caused particle bridging and agglomeration in the final product. The observed particle bridging is probably a result of further precipitation and coagulation after initial nucleation. This is often observed with the RESS results for RDX, but it appeared to be more severe for BTAT. Changing the expansion environment could alleviate some of these complications. To prevent bridging, newly nucleated particles should be repulsed by dispersing agents after creation. This could be achieved by expanding the supercritical solution into a water and surfactant solution as explained in the RESS-AS process. Certain surfactants would adsorb to the nucleated particles surface and repulse each other before further growth occurs.

While the RESS synthesized BTAT is not as ideal as RESS synthesized RDX, the results are encouraging. The material formed smaller nucleated particles when precipitated with the RESS process in comparison to its original form. The smaller particles are less likely to have crystalline defects and should exhibit reduced impact sensitivity in a similar manner that the RDX particles did. However, a process that would create separated particles would be ideal.

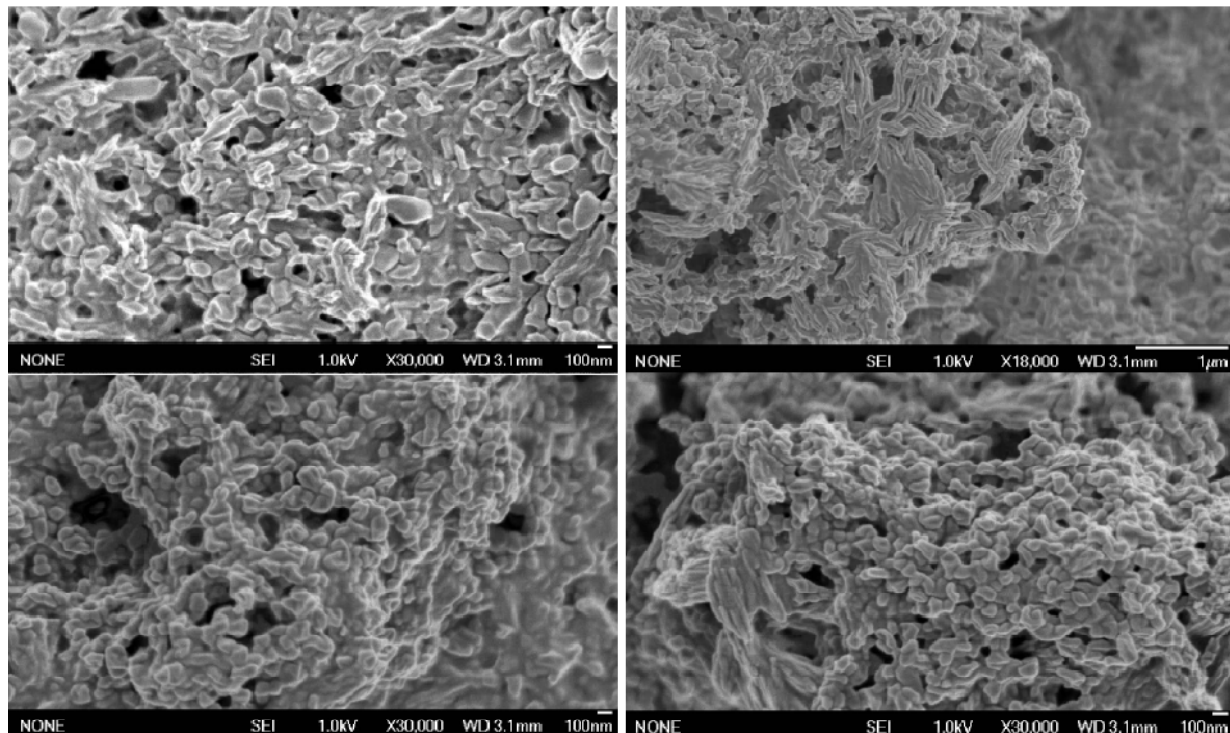


**Figure 50** FE-SEM Image of RESS Synthesized BTAT Particles ( $P_0=68.9$  MPa,  $T_0=323$  K).

#### *RESS-AS Results*

Experimental results with the RESS-AS process consist of synthesizing both RDX and BTAT in different aqueous solutions. The receiving liquids were pure water and aqueous solutions of SDS and NVP surfactants. Of the two dispersing agents used, SDS tended to foam vigorously when used. The difference between a foaming medium and a non-foaming medium can clearly be seen from **Fig. 51**. With the foaming mediums, it is necessary to have a nitrogen purge to prevent the foam from climbing the expansion vessel walls. For tests with NVP, very little foam was created. One can clearly see this in an image of the expansion jet seen in **Fig. 52**. The expansion of  $\text{CO}_2$  into water caused the receiving medium to become more acidic during a test. Most often, the pH would change from a value of 7.0 to 4.0.

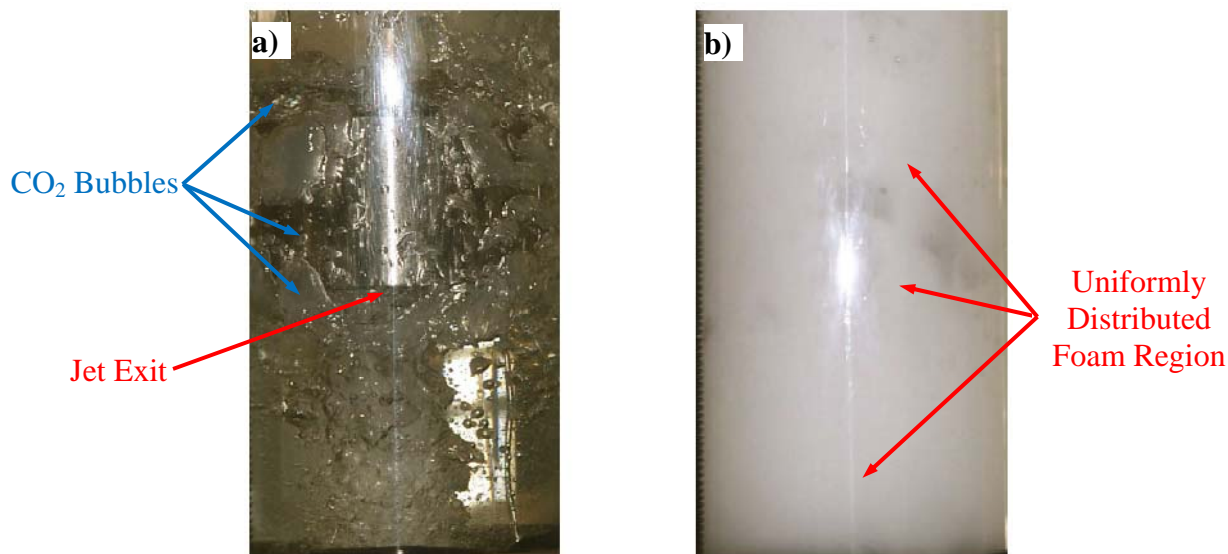


**Figure 51** Images taken during RESS-AS tests a) without a dispersing agent and b) with a dispersing agent.

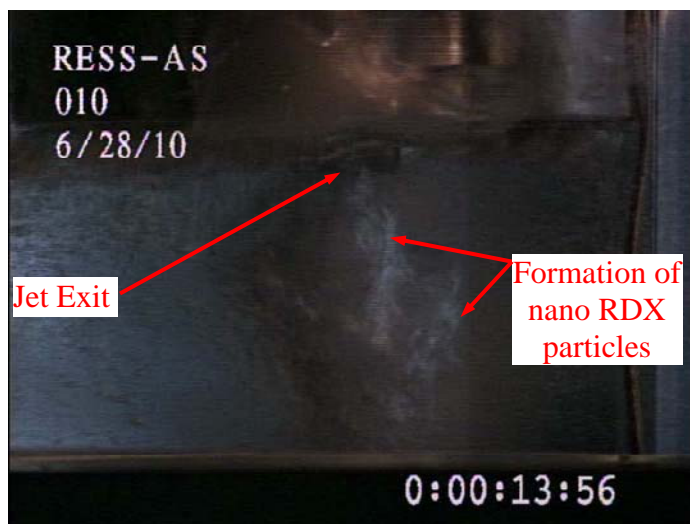


**Figure 52** Close-up view of the discharging jet during a RESS-AS test.

The results obtained with the RESS-AS process were interesting and promising. All expansion conditions were the same for all tests with a pre-expansion pressure of 34.5 MPa and a pre-expansion temperature of 85 °C. A variety of sizes and shapes were able to be synthesized. FE-SEM images of a test involving RDX expanding into neat water can be seen in **Fig. 53**. From the image one can see that the synthesized particles are very disperse and are significantly smaller than particles produced under similar conditions in the RESS process. From image analysis it was determined that the average particle size was  $44 \pm 15$  nm. These particles are quite smaller than RDX particles produced with the same expansion conditions as the RESS process which were  $95 \pm 27$  nm. The difference in size and dispersion between the RESS and RESS-AS process can be seen in **Fig. 54**. Clearly there are major advantages to using the RESS-AS process to produce nano-sized RDX particles.

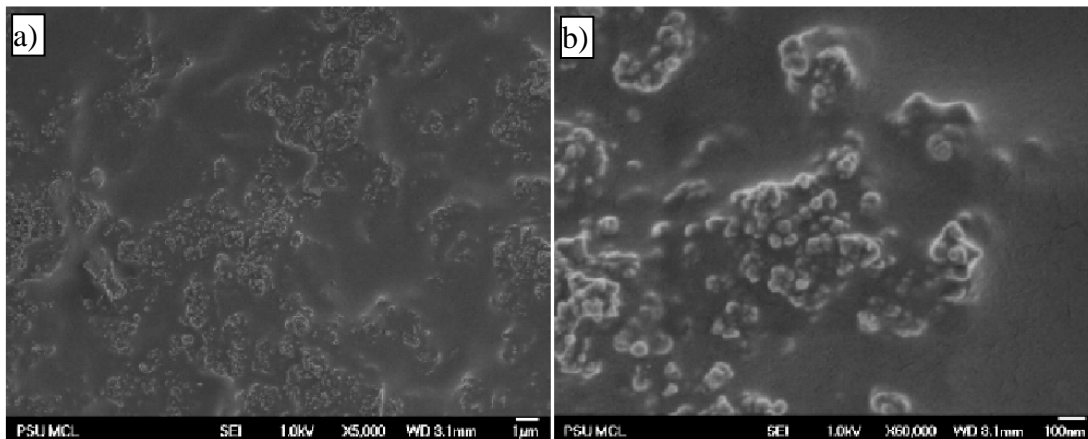


**Figure 53** RESS-AS for producing nano-sized RDX in H<sub>2</sub>O ( $T_0=353$  K,  $P_0=34.5$  MPa) at a) 5,000x magnification and b) 60,000x magnification.

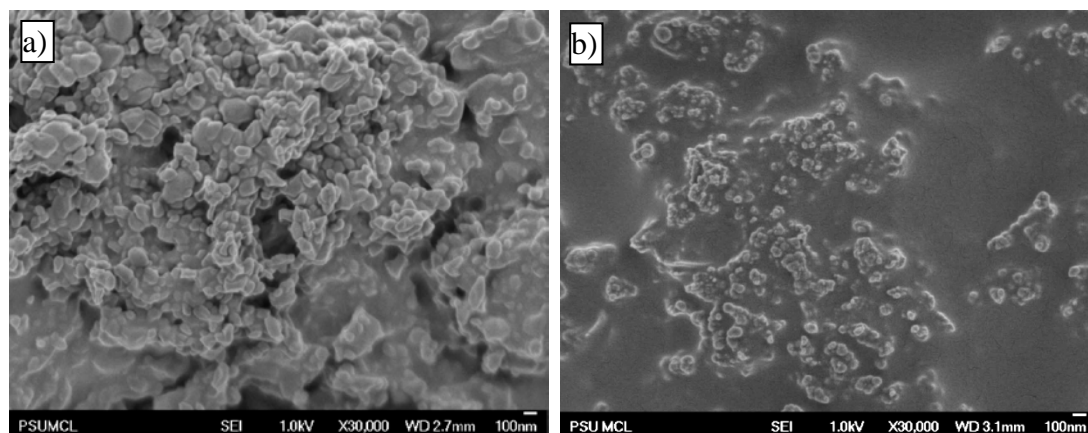


**Figure 54** Comparison of RDX particles produced at  $T_0=353$  K,  $P_0=34.5$  MPa between the a) RESS process and b) RESS-AS process in H<sub>2</sub>O under the same magnification.

RDX particles synthesized in a SDS and water solution showed very interesting results. The synthesized particles were noticeably larger than RESS particles. This implies that SDS does more than disperse the RDX particles. Rather SDS could be helping to redissolve the particles or could be introducing a phenomenon known as Ostwald ripening. This is a process in which smaller particles may be dissolved by the SDS surfactant, causing larger particles to form since less nucleation sites would be available to condense onto [116]. From this information, it can be concluded that SDS is not suitable for creating nano-sized particles but could be beneficial for creating uniform micron-sized particles.

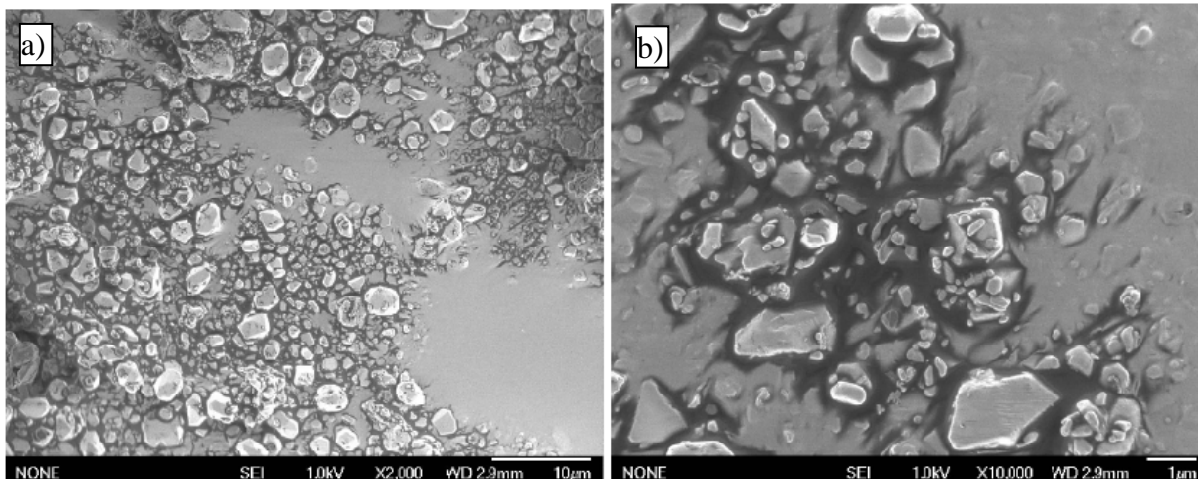


**Figure 55** RESS-AS results of produced nano-sized RDX particles using SDS surfactant at a) 2,000x magnification and b) 10,000x magnification.

Some of the most interesting results with the RESS-AS experiments deal with testing conducted with the polymer NVP as the surfactant. NVP is known to have an affinity to negatively charged surfaces. Adsorption of this polymer could potentially reduce the surface charge of the RDX particles, dispersing them more and stopping their growth. **Figure 56** displays the dynamic light scattering (DLS) results of nano-sized RDX particles synthesized by RESS-AS tests using NVP as the dispersing agent. From the size distribution results it can be seen that the average particle size is approximately 30 nm with a very narrow particle size distribution. This is a noticeable size reduction from RESS synthesized RDX particles.

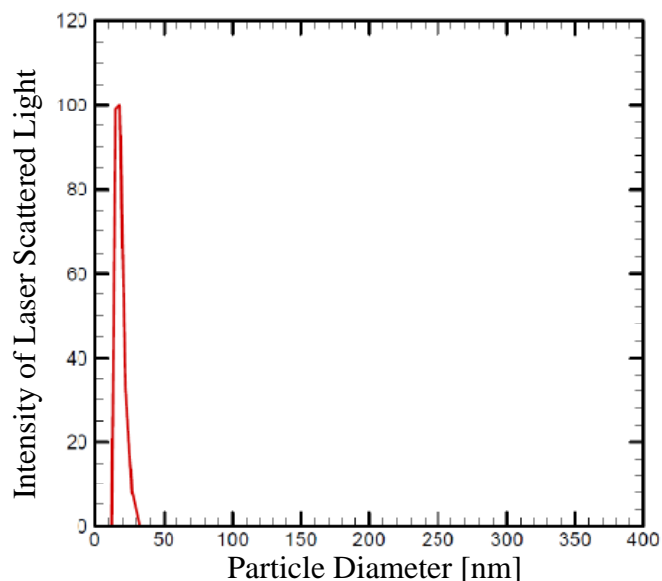


**Figure 56** Size distribution of nano-sized RDX particles synthesized by RESS-AS process, showing extremely small particle size with a narrow distribution.

BTAT testing with the RESS-AS process also had some interesting results. FE-SEM images of tests conducted with neat water as the receiving medium can be seen in **Fig. 57**. For this test, the BTAT particles tended to join together in massive agglomerates that almost have no recognizable structure. This could be caused by the fact that BTAT particles are so hydrophobic that they clump together when they are in the water receiving solution.

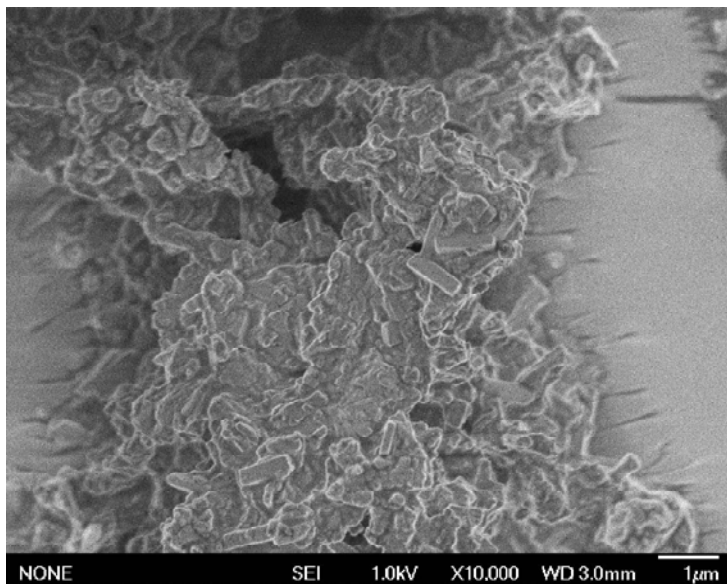


**Figure 57** FE-SEM image of RESS-AS synthesized BTAT particles with neat water, showing significant agglomeration.

In contrast, **Fig. 58** shows BTAT particles produced by expanding the supercritical solution into a SDS and water solution. BTAT particles from this test had a very unique shape. The produced particles tended to form square like rods that were about 1-2 micrometers in length with an aspect ratio of around 5. One possible explanation for the formation of rod-like material is that SDS could form micelles (aggregate of molecules with hydrophobic heads exposed to the water and their hydrophilic ends of molecules gathered inside the structure). These micelles can be adsorbed onto the newly formed BTAT particles. This process could be responsible for the formation of the crystalline rods. The shape of these synthesized BTAT particles would not be as ideal as spherical particles, but it is still an improvement over the original plate-like particles. This study shows that using different types of surfactants operating in various collecting solutions, one can change the morphology of the recovered particles.

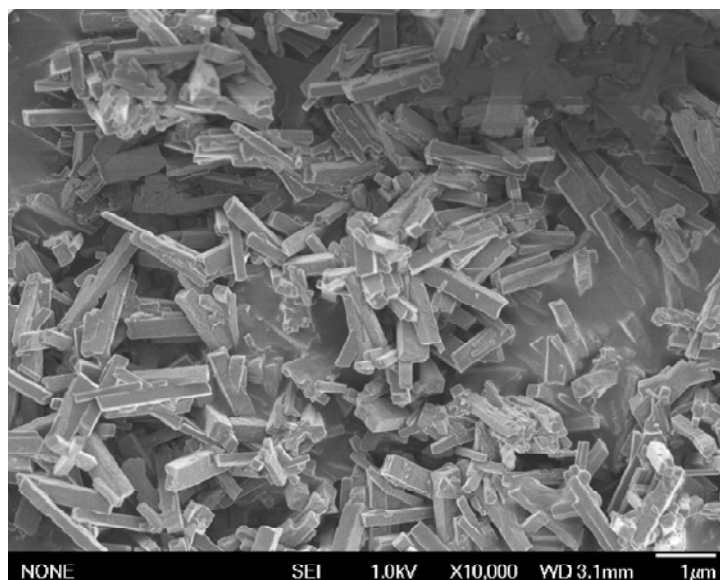


**Figure 58** RESS-AS synthesized BTAT particles in the SDS and water solution resulted in the shape of rectangular rods.

Nucleation theory and subsequent growth equations yield information on the size and number of the particles precipitated from a supersaturated solution. However, these equations assume that the precipitated material is spherical and continues to grow in this way. Generally, the size of the final precipitated particles can be related from von Weimarn's law [117] which can be expressed as:

$$\frac{1}{d} = kS \quad (1)$$

where  $d$  is the final particle diameter,  $k$  is an empirical constant, and  $S$  is the degree of supersaturation in the solution. Therefore a higher degree of supersaturation will result in smaller diameter particles.

Many solid nuclei are not perfectly spherical and their subsequent crystal growth is far from being spherical. Physical parameters that determine final crystal shape are many and their effect on the final crystal shape can be complicated. The shape of the final crystals is determined after primary nucleation has occurred during the stage of crystal growth or condensation. Ideally, crystals will form an equilibrium shape that minimizes the overall surface energy of the crystal [118]. However, during high supersaturations, such as in supercritical fluid precipitation, the crystal growth process can become diffusion limited or chemically limited.

Also of interest is that surfactants are known for changing the shape of precipitating particles. It is known that adsorbed molecules can change the surface free energy of growing crystals. Therefore, it is reasonable to believe that surfactants could change the shape of the final particles produced. From the results obtained, it is clear that different charged surfactants had an observable effect on the final particle morphology and size. Of interest is the adsorption of surfactants onto small particles as this pertains to the effectiveness of SDS and NVP surfactants in the RESS-AS process. An adsorbed polymer has loops and tails that act to repel other particles in a steric manner [119]. This prevents the particles from coming in close enough contact to agglomerate. Therefore, the molecular weight of the polymer is important as if the polymer is not large enough it may not provide enough steric hindrance to prevent agglomeration. However, if the polymer is too large it can coat the particles with too much excess material. For propellants and explosives, too much excessive polymer on energetic particles can reduce their performance. On the other hand, if one uses a suitable polymer which is equivalent to the binder in the propellant, these excess polymers can be directly used in the propellant or explosive besides being

beneficial for the mixing process and handling procedure. Ionized surfactants such as SDS are different as they can change the surface charge of particles which can drastically change the particle's final shape. This is because the free energy of the crystal surface can change from the surfactant adsorption, affecting where the solute molecules in solution can adsorb onto the growing particle.

#### RESS-N Results

Before results were obtained with the RESS-N system, the initial task was to see if ALEX<sup>®</sup> aluminum particles could flow freely through sapphire orifices with 100 to 200  $\mu\text{m}$  throat diameters. These nozzle sizes were first used with the particle entrainment vessel, but it was found that the aluminum particles clogged the nozzle throat after a short amount of time. The smallest nozzle that could be used with the entrainment vessel without any nozzle clogging was found to be a 300  $\mu\text{m}$  throat diameter. This allows for the system to have a maximum pre-expansion pressure around 34 MPa. Due to the larger throat area of the nozzle, the flow rates through the nozzle were on an order of 9 times greater than the previously conducted RESS tests at PSU with smaller sapphire orifices.

Before encapsulation of ALEX<sup>®</sup> particles can occur through the RESS-N process, the dispersion of ALEX<sup>®</sup> particles during the supercritical CO<sub>2</sub> expansion was investigated. This was to understand if large agglomerates or individual particles of ALEX<sup>®</sup> would be present during the supercritical fluid expansion process. In order to observe this, a FE-SEM stub was placed directly downstream from the discharging nozzle. ALEX<sup>®</sup> particles were then seeded into supercritical CO<sub>2</sub> and flown through the sapphire orifice while the supercritical CO<sub>2</sub> rapidly expands. It was found that the expansion of supercritical CO<sub>2</sub> was very effective at dispersing the ALEX<sup>®</sup> particles. This can clearly be seen in **Fig. 59**. Therefore, the RESS-N process is not only beneficial for promoting a high degree of supersaturation for coating by heterogeneous nucleation, it is also beneficial for dispersing nano-sized particles suspended in the flow of the CO<sub>2</sub> so that individual particles are coated during the heterogeneous nucleation process. This ensures that the process is more likely to coat individual particles and smaller agglomerates rather than larger agglomerates. These results are important as nano-sized particle dispersion is often nontrivial.

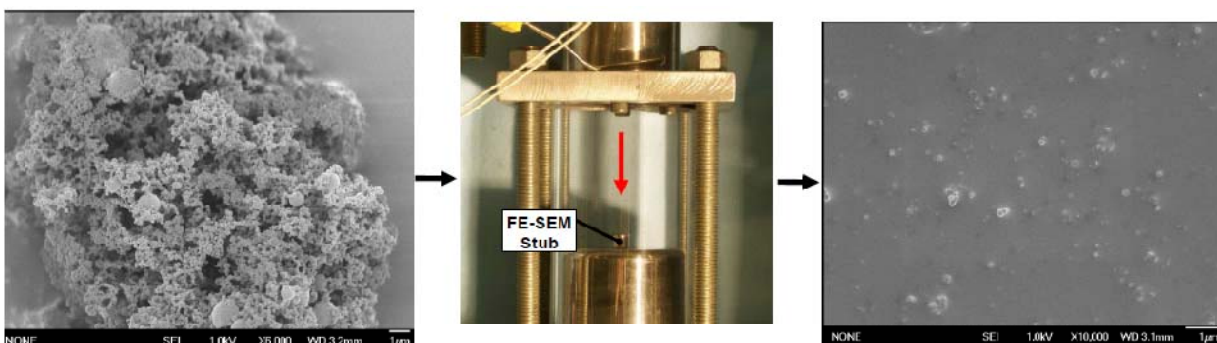


**Figure 59** Representation of supercritical fluid expansion dispersion of ALEX<sup>®</sup> particles.

After the verification of successful entrained flow of ALEX<sup>®</sup> aluminum particles through a 300  $\mu\text{m}$  sapphire nozzle, a supercritical solution containing RDX was flown through the particle entrainment vessel rather than just supercritical CO<sub>2</sub>. The goal of this was to see if any of the ALEX<sup>®</sup> particles could be coated by RDX and to understand what the quality and the size of the coating would be. A summary of tests are shown in

**Table 5.** The pre-expansion temperatures and pressures were changed to see how this would affect the coatings on the ALEX<sup>®</sup> particles.

**Table 5.** Test Conditions for the RESS-N process with the particle entrainment vessel

Test	RDX (mg)	ALEX <sup>®</sup> (mg)	P <sub>0</sub> (MPa)	T <sub>0</sub> (K)
001	210	40	22.7	313
002	240	40	32.4	333
003	200	40	20.68	328
004	200	40	34.47	318
005	150	45	34.47	353
006	200	85	34.47	353
007	150	70	34.47	333
008	200	65	34.47	333

After each test the collection container was filled with particles and dry ice. The dry ice was then placed into a clean steel collection container where the dry ice was allowed to sublimate leaving only nano-sized particles in the container. The collected samples were then placed on carbon tape mounted on an aluminum stub. The samples were then iridium coated and images were taken in a field emission scanning electron microscope (FE-SEM).

It was concluded from the collected product of tests 006 and 007 that operating at a temperature of 353 K was not beneficial for creating a large amount of dry ice. While more RDX is dissolved into a supercritical solution for these higher temperature conditions, dry ice was not created in these cases as the expansion did not make the CO<sub>2</sub> cold enough to create dry ice. Collection of the final product was difficult because of this. Lower pressure tests also did not create significant dry ice for collection purposes. Also, tests 001-005 did not use enough ALEX<sup>®</sup> powder so a large amount of the final product was pure RDX. It was discovered that the ALEX<sup>®</sup> powder tended to flow out of the system within 20 seconds of a test. Therefore, for tests that were run for extended periods of time most of the product was homogeneously nucleated RDX. From this information, optimal conditions for running the RESS-N system with the particle entrainment vessel were for short durations (< 20 sec) at the highest pressure (34.7 MPa) and for lower temperatures.

From the majority of the FE-SEM images taken of the coated ALEX<sup>®</sup> particles with RDX, it was found that most of the particles collected were pure RDX particles from homogeneous nucleation. This is caused by too much RDX in the supercritical solution in comparison to ALEX<sup>®</sup> particles. Also, with the current method of flow entrainment, aluminum particles were observed to flow through the nozzle too quickly. The aluminum particle feeder system with a controlled feeding rate did a better job of suspending ALEX<sup>®</sup> particles into the supercritical solution.

It is important to note that coated particles were observed in the particle entrainment tests. FE-SEM images of the coated particles are shown in **Fig. 60**. It is apparent from the images that ALEX<sup>®</sup> particles are coated with another substance. As spherical particles the size and shape of ALEX<sup>®</sup> particles are seen with another substance on them. Some of the coated particles also seem to be connected together in some spots while uncoated ALEX<sup>®</sup> particles do not show this behavior. While the evidence of a coating is apparent, better consistency is needed for propellant formulations in the future.

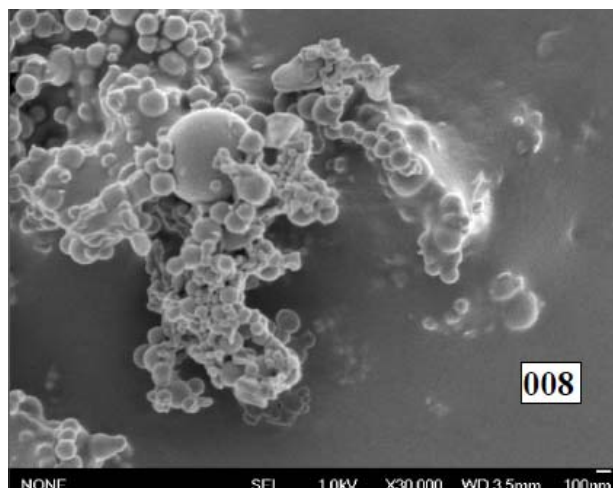


**Figure 60** FE-SEM image of RDX coated ALEX particles from the particle entrainment vessel.

In order to confirm that the material coating the ALEX<sup>®</sup> particles was indeed RDX, X-ray energy dispersive spectroscopy (EDS) was taken of the synthesized powders. An example of one of the spectrums taken can be seen in **Fig. 61**. The spectrum shows strong peaks of Al, as it was apparent from the FE-SEM images that not all of the particles were coated completely. However, the spectrum also shows peaks for carbon, oxygen, and nitrogen. This is important as these are three of the four atomic constituents in the RDX molecule (hydrogen cannot be detected by EDS). As the only other material in the RESS system with these three constituents is RDX, this confirms that the coatings on the ALEX<sup>®</sup> particles are indeed RDX. The fact that there is such a large Al peak indicates that the coatings were not perfect.

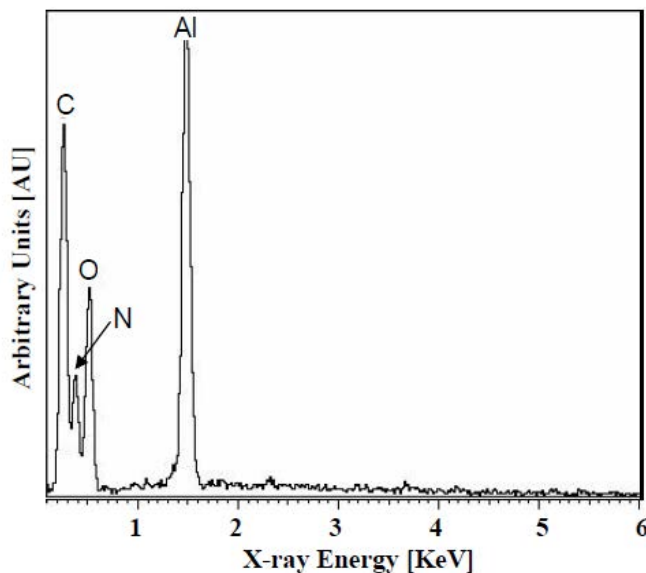


**Figure 61** EDS spectrum of a section of test sample recovered from Test 008.

While some success with coating ALEX<sup>®</sup> particles was achieved with the particle entrainment vessel, better results were achieved with the RESS-N system particle injector system. Images of the

produced particles can be seen in **Fig. 62** and **Fig. 63**. The final particles tended to range in size and were larger than what has been observed for RESS synthesized RDX. This makes sense as the particles consist of RDX deposited onto ALEX<sup>®</sup> particles that tend to be greater than 100 nm in size. Due to the better control that one has with particle introduction, the encapsulated particles are much more consistent in appearance than the ones created through with the particle entrainment vessel. The clear edges of the particles are of particular interest as this suggests that crystal faces had time to develop.

In order to investigate that the particles were RDX encapsulated ALEX<sup>®</sup>, the electron beam intensity was increased on the particles to see if their morphology would change and if the RDX material would decompose. From **Fig. 62** one can see that the particles shrink and grow rounder suggesting that the outer material can decompose, leaving ALEX<sup>®</sup> behind.

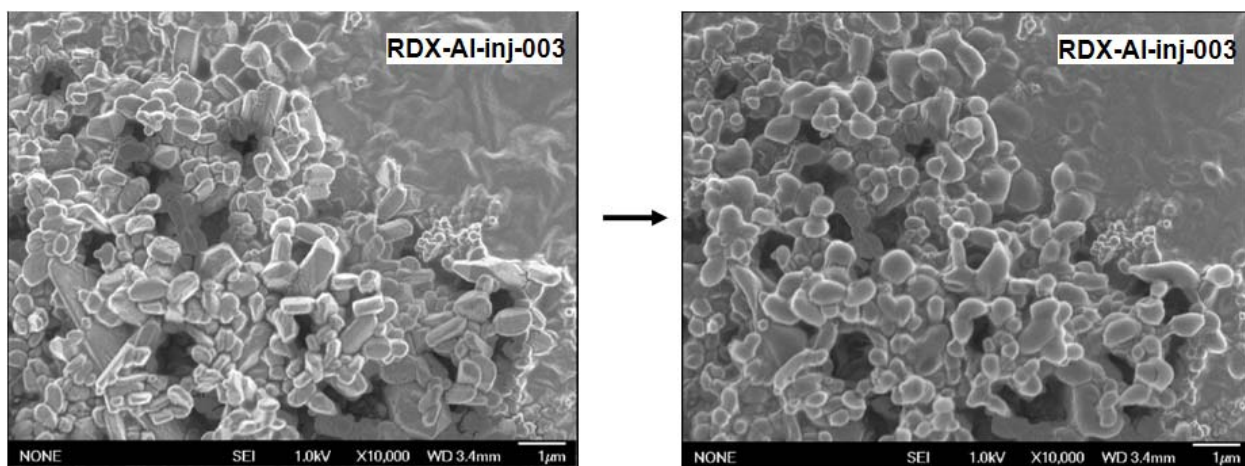


**Figure 62** Comparison of SEM images of the recovered ALEX<sup>®</sup> coated with RDX with a) before strong electron beam exposure and b) after strong electron beam exposure. These images show deformation of the particles under electron beam radiation (more round particles are seen after a portion of the RDX was decomposed).

From **Fig. 63** one can see that after prolonged electron beam exposure, ALEX<sup>®</sup> particles are clearly seen once the outer RDX material decomposes. It is important to mention that the sample in **Fig. 63** is not iridium coated, meaning that ALEX<sup>®</sup> particles will appear lighter than RDX in the image. From the results, the particle injector RESS-N system does a much better job at encapsulating ALEX<sup>®</sup> particles than the particle entrainment method. This method can be a suitable method for making propellant and explosive formulations in the future. A scale up process would be necessary to produce the material in a usable quantity in which large quantities of ALEX<sup>®</sup> powder can be injected.

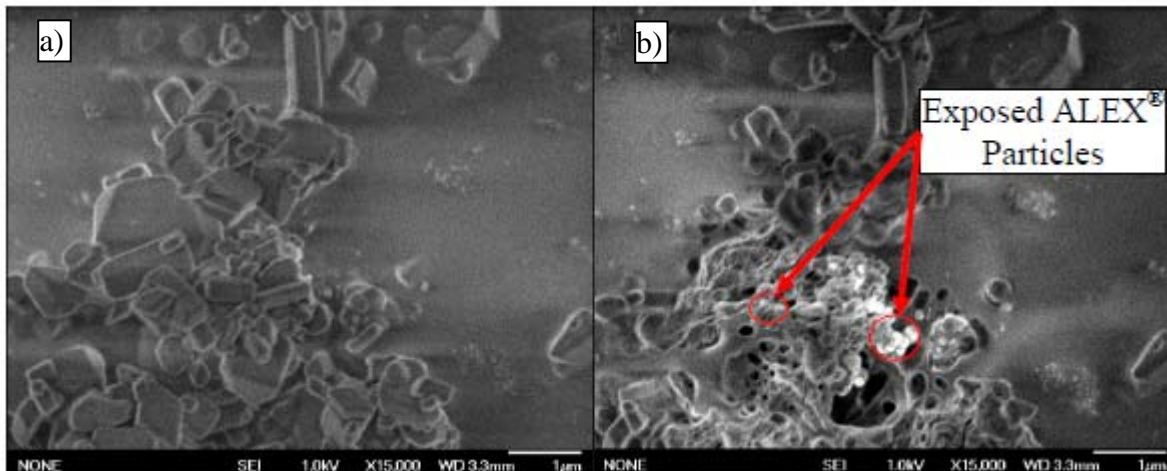


**Figure 63** Comparison of SEM images of the recovered ALEX<sup>®</sup> coated with RDX with a) before strong electron beam exposure and b) after strong electron beam exposure. These images show significant mass loss from the particles under electron beam radiation (exposed ALEX<sup>®</sup> particles are clearly seen after RDX decomposition in image b).

#### II.1.4.5 Conclusions

From the proceeding sections, it is apparent that there are many benefits to supercritical fluid precipitation of energetic materials. The RESS and RESS-AS processes have been successfully demonstrated for synthesizing nano-sized RDX and BTAT particles with sizes orders of magnitude smaller than those in conventional precipitation techniques. The morphology of these particles can also be controlled by using surfactants. The nano-sized RDX particles were shown to be significantly less sensitive to impact stimulus in comparison with the military grade RDX. Besides homogeneous nucleation of oxidizers, this work also demonstrated the feasibility for coating nano-sized aluminum particles by RDX through heterogeneous nucleation. While great control over the size and shape of the particles along with actual coating of nano-sized particles can be achieved, future research is still needed to optimize the process for synthesizing these desirable energetic materials. The performance of future propellants and explosives can be benefitted significantly by utilization of these ingredients.

Supercritical fluid precipitation is still a fairly new technology, especially in the energetic material field. Therefore, there is still significant research to be conducted. Future work could come from synthesizing other energetic materials with the RESS or RESS-AS method. Other work could come from testing the reactivity of nano-sized oxidizers, especially material synthesized with the RESS-AS process which can be 40 nm or less in size. Finally, coated material with the RESS-N process could be scaled up to see if differences in propellant performance can be achieved by placing fuel and oxidizer material in close proximity to each other.

An ultra-high pressure RESS system has been designed, tested, and fabricated at the Pennsylvania State University's High Pressure Combustion Lab. The RESS system has successfully synthesized nano-sized RDX at a variety of pre-expansion conditions. The produced particles were shown to be much less sensitive (three times) to impact than regular military grade RDX. The energetic material BTAT has also been synthesized with the RESS system with promising results. A modification of the RESS process called the RESS-AS process was then used to synthesize RDX and BTAT particles with smaller sizes and different shapes than in the RESS process. The RESS-AS process could be used to have even more control over the size and shape of the energetic oxidizers synthesized during the process.

An ultra-high pressure RESS system has been modified to coat ALEX<sup>®</sup> nano-sized aluminum particles. The RESS system has been modified to allow for ALEX<sup>®</sup> particles to be entrained in a

supercritical solution prior to rapidly expanding through a micro-orifice sapphire nozzle. It was found that a 300- $\mu\text{m}$  nozzle throat diameter is the smallest size that ALEX<sup>®</sup> particles can flow through. This allows for a maximum pre-expansion pressure of 34 MPa, which is more than adequate to promote heterogeneous nucleation. Test results have shown successful coating of RDX onto the ALEX<sup>®</sup> aluminum particles. A newly designed aluminum particle feeding system allowed for more efficient coating by controlling the aluminum particle flow rates. This new feed system together with controlling the operating conditions of the RESS system helped to optimize the coating process.

This technology can be expanded further for mass production of nano-sized RDX and BTAT as well as using other energetic materials such as HMX, CL-20, ADN, Fox-7, and Alane. The energetic material coating technology developed in this research study can also be expanded for coating other metallic energetic fuel particles by the RESS process. Both types of particles have broad applications in propellants, explosives, and solid fuels for DoD weapon systems.

## II.2 Theoretical Modeling and Simulation

The goal of this portion of the MURI project was to study nano-structured engineered energetic materials (NEEMs), using large (billion atoms) multiscale simulations that couple quantum-mechanical (QM) calculations to molecular dynamics (MD) calculations. The **USC group (Vashishta, Kalia, and Nakano)** calculates the stability, structure and energetics of metallic nanoparticles with a special focus on the relationships between particle size, shape and excess surface free energy. Multiscale modeling of the thermo-mechanical properties and microscopic mechanisms of detonation and deflagration processes of NEEMs is performed. Atomistic understanding of shear-induced initiation will lead to the prediction of material properties prior to the experimental synthesis of nano-reactive materials, so that safety and survivability will be increased with enhanced performance. These calculations couple directly to the synthesis, fabrication, and materials characterization studies of **Allara, Nuzzo, and Girolami** as well as to the dynamical characterization studies of **Dlott and Yetter**. Theoretical studies by **Yang** couple to the studies of the **USC group** at the meso/macro scale.

The **USC group** used their adaptive hierarchical quantum mechanical (QM)/molecular dynamics (MD) simulation framework, which invokes higher accuracy simulations only when and where high fidelity is required. The **USC group** has developed scalable parallel QM and MD simulation algorithms, with which we have benchmarked unprecedented scales of quantum-mechanically accurate and well validated, chemically reactive atomistic simulations—1.72 billion-atom reactive MD and 19.2 million-atom (1.68 trillion grid points) QM simulation in the framework of the density functional theory—in addition to 218 billion-atom non-reactive MD, with parallel efficiency well over 0.95 on 212,992 CPUs. The **USC group** also performed multimillion-to-multibillion atom MD simulations in house at USC on our 2,048-CPU Opteron cluster.

### *II.2.1 Scalable Parallel Algorithms for Multimillion-Atom Simulations of Chemical Reactions*

To enable large-scale atomistic simulations of material processes involving chemical reactions, the **USC group** has designed linear-scaling molecular dynamics (MD) algorithms with varying accuracy and computational complexity, based on an embedded divide-and-conquer (EDC) framework: 1) first principles-based fast reactive force-field (F-ReaxFF) MD; and 2) quantum mechanical MD in the framework of the density functional theory (DFT) on adaptive multigrids. To map these  $O(N)$  algorithms onto parallel computers with deep memory hierarchies, the group has developed a tunable hierarchical cellular decomposition (THCD) framework, which achieves performance tunability through a hierarchy of parameterized cell data/computation structures and adaptive load balancing through wavelet-based computational-space decomposition.

Scalability of the F-ReaxFF MD and EDC-DFT simulation algorithms, as well as that of our non-reactive space-time multiresolution MD (MRMD) algorithm, has been tested on a number of parallel architectures such as the IBM Blue Gene/L, IBM Power, NASA Columbia (SGI Altix-Intel Itanium), and Linux clusters consisting of AMD Opteron, Intel Xeon, and Apple G5. Benchmark tests on 212,992 BlueGene/L processors at the Lawrence Livermore National Laboratory have achieved unprecedented scales of quantum-mechanically accurate and validated, chemically reactive atomistic simulations—1.72 billion-atom F-ReaxFF MD and 19.2 million-atom (1.68 trillion grid points) EDC-DFT MD—in addition to 218 billion-atom nonreactive MRMD (**Fig. 64**). The EDC and THCD frameworks expose maximal data localities, and consequently the isogranular parallel efficiency on 212,992 processors is well over 0.95 (**Fig. 65**).

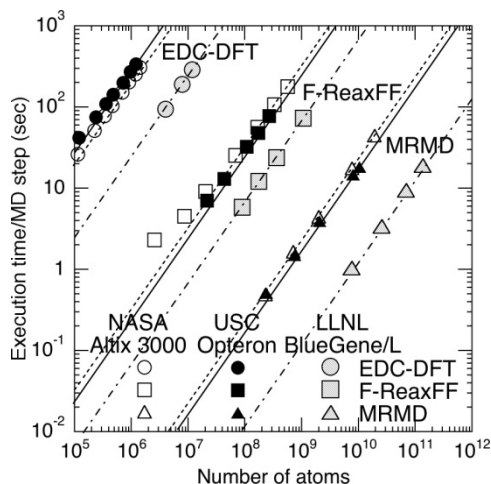


**Figure 64** Benchmark tests of reactive and nonreactive MD simulations on 1,920 Itanium2 processors of the Altix 3000 (open symbols), 2,000 Opteron processors (solid symbols), and 212,992 BlueGene/L processors. The execution time per MD step is shown as a function of the number of atoms for: EDC-DFT (circles); F-ReaxFF (squares); and MRMD (triangles). Lines show  $O(N)$  scaling.

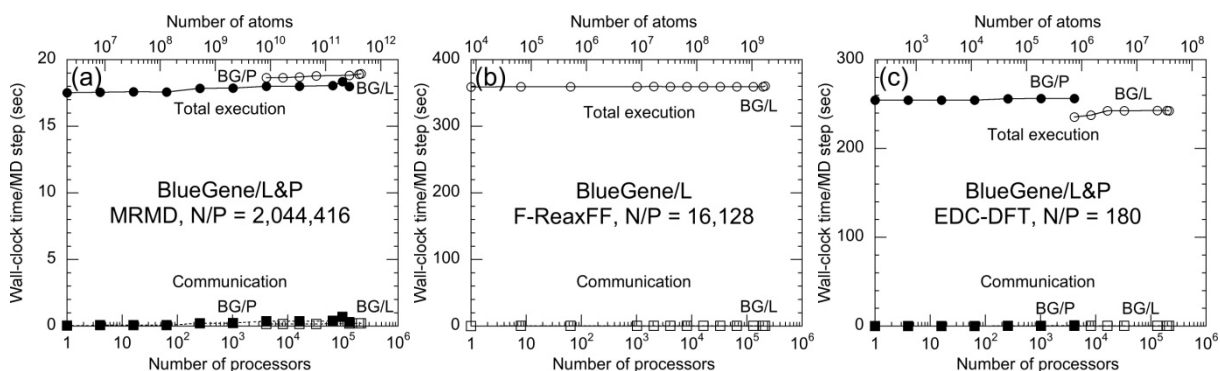


**Figure 65** Total execution (circles) and communication (squares) times per MD time step as a function of the number of processors  $P$  of BlueGene/L (open symbols) and BlueGene/P (solid symbols) for three MD simulation algorithms: (a) MRMD for 2,044,416 $P$  atom silica systems; (b) F-ReaxFF MD for 16,128 $P$  atom RDX systems; and (c) EDC-DFT MD for 180 $P$  atom alumina systems.

The USC codes have also been ported to emerging multicore platforms including Cell Broadband Engine on a cluster of Playstation3 consoles and graphics processing units (GPUs). For pLBM, the USC group has achieved speedup of: (1) 5.29 on 6 synergistic processing elements (SPEs) on each Cell; and (2) 8.76 on a GPU over a CPU.

### II.2.2 Quantum Mechanical Calculation of an RDX Molecule on Aluminum Surface

The USC group has performed an MD simulation to study the decomposition of an RDX molecule on Al (111) surface, in which interatomic forces are computed quantum-mechanically in the framework of DFT (**Fig. 66**).

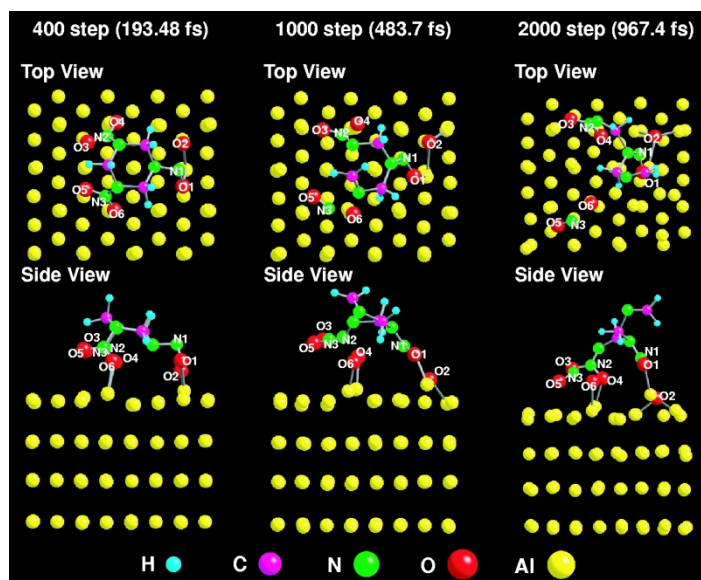


**Figure 66** Snapshots of DFT-based quantum mechanical MD simulation of an RDX molecule on Al (111) surface. At 193.48 fs, N1-O2 bond is broken and O2 starts bonding with an aluminum atom. Some other oxygen atoms are also bonding with aluminum atoms. Subsequently, more N-O bonds (N2-O4 and N3-O6) and an N-N are broken (483.7 fs), producing an NO fragment (denoted as N3-O5). Moreover, a ring of RDX, which consists of 3 carbon and 3 nitrogen atoms, is opened by a C-N bond breakage. At 967.4 fs, several oxygen atoms are completely dissociated from the RDX molecule and they oxidize the Al surface. The rest of the molecule is, however, still attached to the surface.

In **Fig. 67**, the temperatures of atomic species are compared with those of RDX and the total system. The increase in temperature of the system indicates the occurrence of exothermic chemical reactions. The temperature of oxygen atoms is especially high because of their reactions with the aluminum surface. There are large fluctuations in temperatures corresponding to carbon and nitrogen atoms. These strong thermal fluctuations cause the ring cleavage of the RDX molecule. On the other hand, the temperature of hydrogen is relatively low and fluctuates less than those of the other species. This is probably the reason why the HONO elimination from RDX is not observed, for which bond formation between a hydrogen atom and an oxygen atom is required. Since hydrogen atoms are initially bonded with carbon atoms, strong thermal fluctuations are needed to break the C-H bond and to form an O-H bond. The temperature ( $\sim 200\text{K}$ ) of aluminum atoms is relatively low compared to typical combustion conditions of Al particles. The **USC group** is currently studying the stability of RDX fragments on Al (111) surface at higher temperatures.

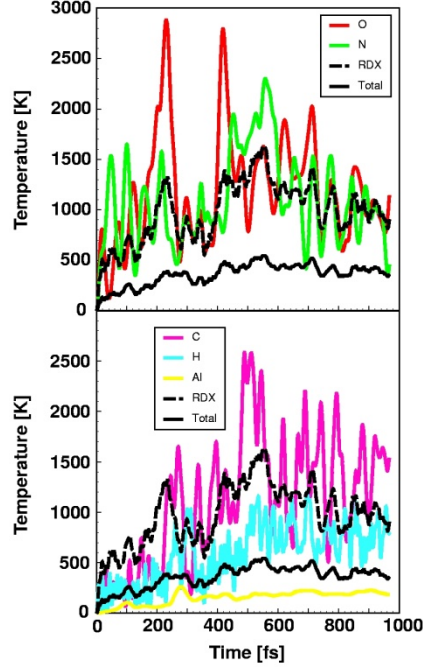


**Figure 67** Temperatures of O and N atoms (upper panel), and C, H, and Al atoms (lower panel), in comparison with that of the RDX molecule and the total system.

To quantitatively analyze bond breakage, Mulliken overlap populations are used. The projected Kohn-Sham orbital  $\phi_i(\mathbf{r})$  onto a subspace generated by the atomic pseudo wave functions  $u_{rk}(\mathbf{r})$  is expressed as

$$\phi_i(\mathbf{r}) = \sum_{rk} c_{irk} u_{rk}(\mathbf{r}), \quad (2)$$

where  $r$  and  $k$  denote atomic orbitals and atoms, respectively. The overlap population  $n(k,l)$  between the  $k^{\text{th}}$  and  $l^{\text{th}}$  atoms is calculated from the coefficients  $c_{irk}$  and the overlap integral defined as

$$S_{rksl} = \int u_{rk}(\mathbf{r}) u_{sl}(\mathbf{r}) d\mathbf{r}. \quad (3)$$

A large value of  $n(k,l)$  indicates that the bond between the  $k^{\text{th}}$  and  $l^{\text{th}}$  atoms is strong.

**Figure 68** shows the Mulliken overlap populations of N-O bonds. From **Fig. 68**, it is evident that N1-O2 bond is weakened and completely broken after 200 fs. The strengths of the other N-O bonds oscillate with time. Moreover, the overlap populations for N1-O1, N2-O4, and N3-O6 bonds are less than the initial value of 0.8. These bonds may be weakened by the presence of the aluminum surface.

The simulation shows that strong attractive forces between oxygen and aluminum atoms break N-O and N-N bonds in the RDX and, subsequently, the dissociated oxygen atoms and NO molecules oxidize the Al surface. In addition to these Al surface-assisted decompositions, ring cleavage of the RDX molecule is also observed. These reactions occur spontaneously without potential barriers, and result in the attachment of the rest of the RDX molecule to the surface. This opens up the possibility of coating Al nanoparticles with RDX molecules to avoid the detrimental effect of oxidation in high energy density material applications.

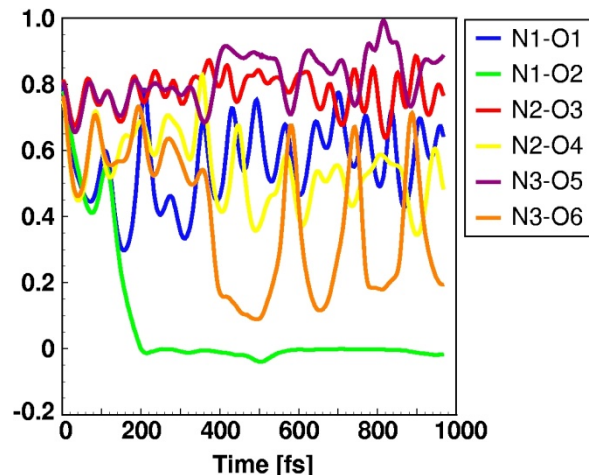


**Figure 68** Time variation of the Mulliken overlap populations of N-O bonds. N1-O2 bond is weakened and completely broken after 200 fs. The overlap populations of N1-O1, N2-O4 and N3-O6 bonds are decreased from the initial value of 0.8.

### II.2.3 Molecular Dynamics Simulation of Shock Compression of Self Assembled Monolayers

Understanding the mechanical properties of NEEMs requires the study of shock responses of various material components that constitute them. For example, recent developments in femtosecond laser-generated shock compression and vibrational sum-frequency generation (SFG) spectroscopy at **Dlott’s group** at the University of Illinois at Urbana-Champaign have enabled time-resolved spectroscopy of shock-induced ultrafast large-amplitude molecular deformation of various materials such as self-assembled monolayers (SAMs).

The **USC group** has performed MD simulations to study the shock compression of alkane-thiol SAMs,  $-S-(CH_2)_n-CH_3$  ( $n = 11-17$ ) at various temperatures (see **Fig. 69**). Shock is applied by moving the substrate upward at a constant speed (1 km/s) for 0.45 ps, while keeping a hard wall on top of the SAMs. Subsequently, the wall is lifted up at a speed of 0.25km/s for 3ps, and then we stop the wall and let the system relax for  $\sim 22$  ps. **Figure 69** shows close-up views of the system at time 3 and 30 ps for  $n = 14$  at temperature 300 K.

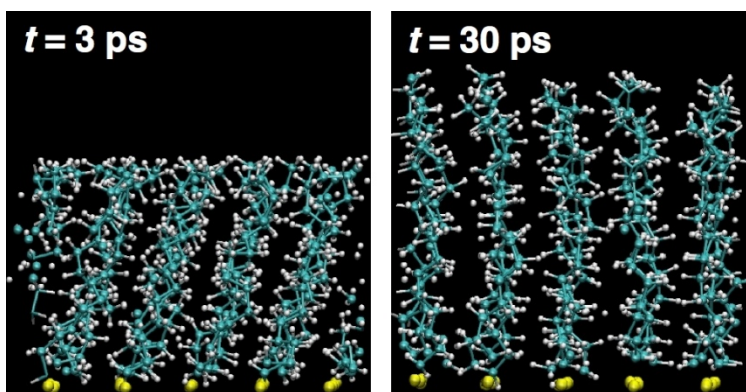


**Figure 69** Code-up views of a shock compressed alkanethiol SAM at time 3 and 30 ps for  $n = 14$  at temperature 300 K, where white, cyan and yellow spheres represent hydrogen, carbon and sulfur atoms, respectively.

SFG signal is sensitive to the instantaneous tilt angle of the SAM terminal group relative to the surface normal. **Figure 70** shows the SFG intensities as a function of the time for  $n = 14$  at 300 K, where

the SFG intensities for symmetric stretch,  $V_s$ , and asymmetric stretch,  $V_{as}$ , are calculated from the tilt angles of the terminal methyl groups.

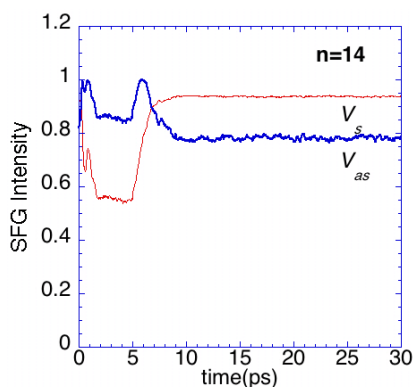


**Figure 70** SFG intensities of a shock-compressed alkanethiol SAM as a function of time for  $n = 14$  at temperature 300 K.

#### II.2.4 Fast Reaction Mechanisms of an Aluminum Nanoparticle with Crystalline and Amorphous Alumina Shells

The reactivity of NEEMs is known to differ drastically from their micron-scale counterparts. For example, experimental studies on the combustion of nanothermites, such as Al/Fe<sub>2</sub>O<sub>3</sub> and Al/MoO<sub>3</sub>, have shown that flame propagation speeds approach km/s when the size of Al nanoparticles is reduced to below 100 nm, in contrast to cm/s for traditional thermites. In laser flash-heating experiments of ALEX by **Dlott's group**, a linear relationship was found between the reaction propagation distance and laser energy, which was explained with a hydrodynamic model instead of the thermal explosion model.

Such peculiar reactive behaviors of NEEMs cannot be explained by conventional mechanisms based on mass diffusion of reactants, and thus various alternative mechanisms have been proposed. An example is a mechanochemical mechanism that explains the fast flame propagation based on dispersion of the molten metal core of each nanoparticle and spallation of the oxide shell covering the metal core. Another mechanism is accelerated mass transport of both oxygen and metal atoms due to the large pressure gradient between the metal core and the oxide shell of each metal nanoparticle. In addition, defect-mediated giant diffusivity is important for fast reactions at the nanometer scale. These mechanisms are by no means exhaustive, and some unexpected ones could operate in NEEMs. It is therefore desirable to study the reaction of nanoenergetic materials by first-principles simulations.

The USC group has investigated atomistic mechanisms of the oxidation of an aluminum nanoparticle (ANP) using multimillion-atom molecular dynamics (MD) simulations using an environment-dependent reactive interatomic potential developed by our group for this project (**Fig. 71a**). A thermal-to-mechanochemical transition of oxidation mechanism at elevated temperatures was found. The transition from thermal diffusion to mechanically enhanced diffusion to ballistic transport of atoms is accompanied by a change of intermediate reaction products from aluminum-rich to oxygen-rich clusters. Higher initial temperature of the Al core causes mechanical breakdown of the alumina shell during the expansion of the ANP. The breakage of the shell provides direct oxidation pathways for core Al atoms, resulting in faster oxidation reaction and thus faster energy release.

In laser flash-heating experiments of ALEX by **Dlott and his group**, the wavelength of laser beam is selected in the near IR regime (~1.06  $\mu\text{m}$ ), which is absorbed only by the metal core leaving the oxide shell unheated. Similarly, the Al core is heated at the start of our simulations, while the shell is maintained at room temperature. To study the effect of the initial core temperature, we heat the core of the

ANP to 3000, 6000 and 9000 K, which will be referred to as C3, C6 and C9 systems, respectively. **Figure 71b** compares the different energy release rates in the three systems, by plotting time variation of the average kinetic energy per atom. Among the three systems, higher initial core temperature releases more energy up to 200 ps. This correspondence between higher initial heat in the Al core and faster combustion of the nanoparticle is consistent with experiments by **Dlott and his group** (In their experiments, the energy release rate was inferred from the consumption rate of  $\text{ONO}_2$  by ALEX fuel.)

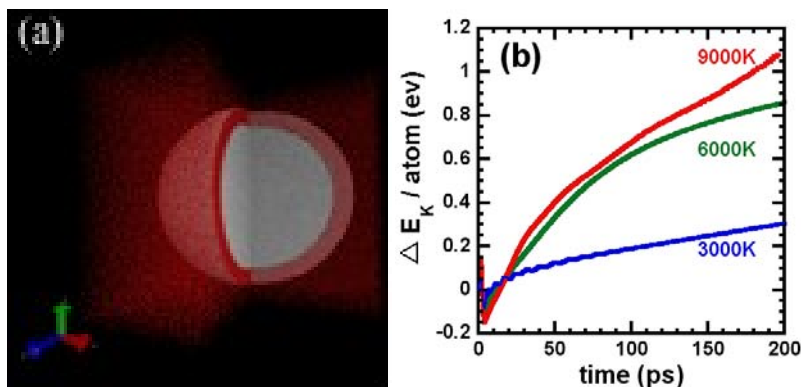


**Figure 71** (a) Initial setup of the system consisting of a single aluminum nanoparticle embedded in oxygen. Most of the oxygen atoms surrounding the nanoparticle are not shown for clarity. To show the inside of the nanoparticle, a quarter of the nanoparticle has been removed. (b) Increase of kinetic energy per aluminum atom in the process of explosion for the C3, C6 and C9 systems.

Combustion behaviors of ANP due to different initial Al core temperatures are shown in **Fig. 72**. Initially, each ANP is enclosed by an alumina shell, which protects the Al core from oxidation by environmental oxygen. When the core is heated, the shell at different temperature responds in a different manner. For the C3 system, oxidation is mainly due to thermal diffusion of shell oxygen atoms towards the core, where the inward diffusion depth at the core/shell interface is only 3.8 nm at 200 ps. Here, the shell structure is largely unchanged up to 200 ps (**Fig. 72a**).

A higher initial core temperature in C6 results in more damage to the shell. Here, the ANP first expands to form a hollow cavity inside the nanoparticle at 70 ps and then collapses to fill the cavity and form a solid body again at 200 ps, but with considerable penetration of oxygen into the core region (**Fig. 72b**). As a result of this mechanical expansion/collapse process, the original shell structure is seriously damaged and its composition becomes close to  $\text{AlO}_{1.1}$ . Consequently, delineation of the shell and the core is blurred, and some shell oxygen atoms are already seen at the center of the nanoparticle, indicating a remarkable mass transport of 20 nm within 200 ps. Oxidation mechanism of the ANP by environmental oxygen after 200 ps will still be diffusion because of the re-consolidation of the ANP, but with a much faster rate as a result of earlier mechanical mixing by expansion/collapse process—hence mechanically enhanced diffusion.

The fastest energy release is seen for C9. Here, detailed analysis of the atom migration events reveals a novel mechanism involving ballistic transport of atoms resulting from the opening of pores in the shell (**Fig. 72c**). Calculation of shell's minimum thickness shows that pores in the shell appear as early as at 22 ps. This mechanical breakdown of the shell removes the protective layer that would prevent further oxidation of the core Al atoms. The opening of pathways for oxidation ensures more complete oxidation of the nanoparticle over time, and thus much more energy is released in the C9 system than in C6.

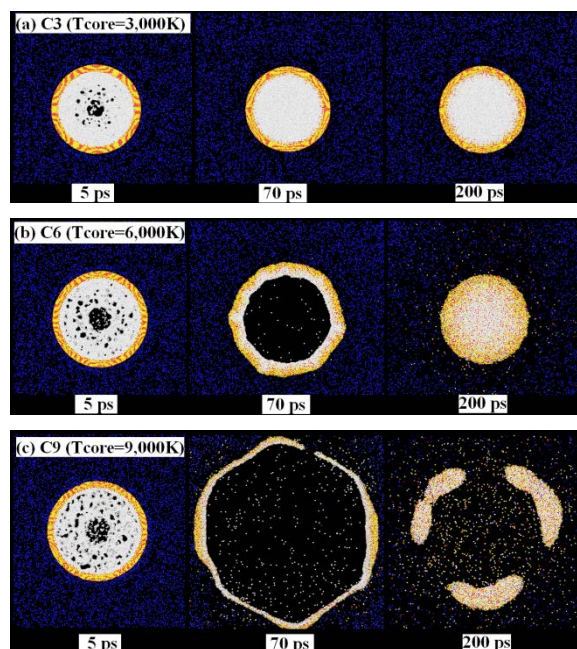


**Figure 72** Snapshots of the nanoparticle at different times with initial core temperature of (a) 3000K, (b) 6000K, and (c) 9000K. The core aluminum is shown as white; shell aluminum, yellow; shell oxygen, red; and environmental oxygen, blue.

Our multimillion-atom MD simulations also reveal significant effects of the structure of oxide shells on the burning behavior of an ANP. With a crystalline shell (CS), radial expansion of the nanoparticle followed by its contraction forms pores in the shell, resulting in enhanced oxidation reactions. With an amorphous shell (AS), formation of oxide nanoclusters by the shattering of the shell, combined with the fragmentation and dispersion of the nanoparticle, catalyzes oxidation reactions that would otherwise take much longer times. Consequently, the energy release rate of an ANP with an amorphous shell is much larger than that with a crystalline shell. Fragment analysis on the formation of oxygen-rich fragments further confirms an enhanced reaction rate with an amorphous shell.

One factor responsible for the faster energy release rate with an amorphous shell is the increased amount of core Al atoms which are dispersed into the surrounding oxygen and able to be directly oxidized by the environmental oxygen, as seen in **Fig. 73**. **Figures 73a** and **c** show the projected view of CS and AS, respectively, at 100 ps with colors indicating the local number density within the shell. **Figures 73b** and **d** show the core Al atoms (colored yellow) jetting out of CS and AS, respectively. In both systems, there are many core Al atoms jetting out, causing direct, and thus faster, oxidation reactions. But spatial symmetries of the crystalline structure result in symmetric pores in the corresponding shell (**Fig. 73a**). In contrast, the formation of pores occurs randomly in the amorphous shell (**Fig. 73c**). The opening of pores in the crystalline shell results in less overall area for the core Al atoms to move through. The amorphous shell has a much larger area corresponding to pores. As a result, far more core Al atoms jet out in the AS system, resulting in more direct oxidations in the surrounding region and a faster heat release.

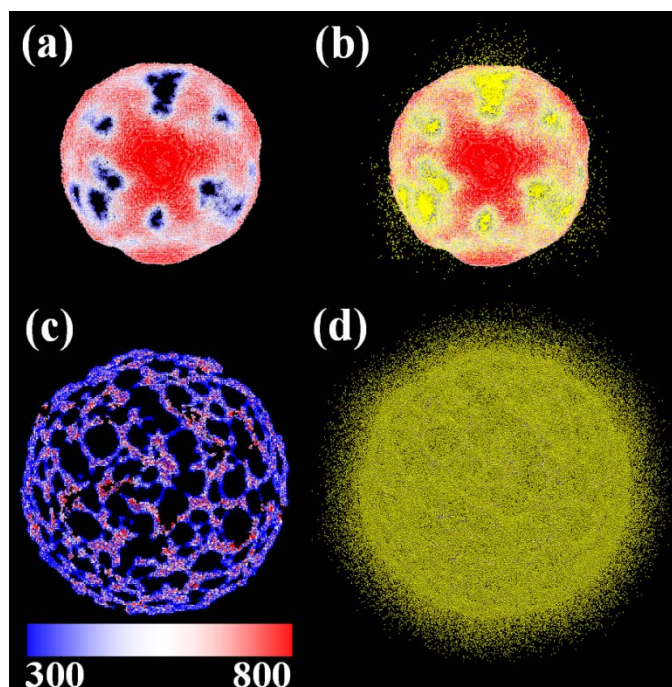


**Figure 73** (a) and (c) are snapshots of shell morphology with crystalline and amorphous shells, respectively, at 100 ps with colors representing the number density in the shell as shown by the color bar (in unit of # of atom/nm<sup>3</sup>). (b) and (d) are snapshots of the shell morphology combined with core aluminum atoms (yellow) for the two systems.

### II.2.5 Burning of Aluminum Nanoparticle by Slow Heating

The USC group has performed multimillion-atom MD simulations of slower burning ANPs in oxygen and found the onset temperature (~740 °C) at which self-heating begins. The simulation results reveal a two-stage reaction mechanism involving confined and spallation phases. Initiation is focused in hot spot areas, which develop at the inner boundary of alumina shell and aluminum core. Resulting increase in oxygen mobility provides energetically favorable migration of oxygen into aluminum core. The oxygen diffusion at the internal boundary is the primary mechanism of energy release in the first reaction phase, leading to local temperature extremes along the shell.

Simulation results show a transition to a second reaction mechanism approximately 90 ns after initial reaction. Localized heating at the shell internal boundary and development of oxygen-poor regions lead to shell weakening. Resulting shell failure leads to spallation of small aluminum clusters into surrounding oxygen, generating additional heat by direct oxidation. Mechanism of reaction in both stages and identification of transition point are confirmed via fragment analysis, radial composition/temperature analysis, and statistical particle migration calculations.

The detonation of ANPs is a complex phenomena which results from the interaction of several mechanisms taking place on scales which range from the atomic interactions of individual chemically-reacting atoms (~angstroms) to the feature size of the total particle (5-10 nanometers). In the small scale, the creation of hotspots and the oxidation of spallated fragments contribute to the initiation and detonation phases of the reaction. On the larger scales, the mechanical breaking of the shell, phase changes within the component materials, and internal pressures which develop throughout the detonation also are expected to contribute to the overall behavior. As the overall evolution of the particle itself is a combination of these mechanisms, it is impossible to gain a comprehensive view of the controlling factors of detonation without being able to look at both scales simultaneously. In the previous simulations, we examined the role of uniform flash-heating in the detonation response by looking at ANP systems, of

which the same amount of energy is homogeneously added to the cores. Although this is very useful in analyzing the effect of laser-initiation on particle detonation, it does not provide a ready comparison to experiments performed on heated systems due to the extreme energy scales at work. To this end, we performed a multi-million atom MD simulations, which studied a particle being heated to a more conventional temperature (just above the melting point of aluminum) to accomplish the following objectives:

- (1) Analyze the burning of ANPs in order to better understand the mechanisms, which control its evolution.
- (2) Identify the key components of the initiation and burning of the ANP, which must be included in any coarser simulations that seek to properly capture its behavior on a larger scale.
- (3) Provide a contrast study to the laser-initiated simulation results, allowing comparison of the two initiation methods.

Several mechanisms leading to initiation in ANP materials have been presented in the scientific literature over the last decade. One predominant mechanism proposed by Pantoya, Levitas, *et al.* for burning is that the particle remains stable until the core temperature exceeds the melting temperature of bulk aluminum ( $T_m = 933$  K). At this point, the phase change from solid to liquid in the core (with the associated 12% volume increase) results in a considerable pressure buildup on the inner boundary of the shell. This pressure is enough to mechanically fracture the shell barrier, resulting in the spallation of unoxidized aluminum clusters into the surrounding oxidizer. The direct oxidation of these clusters is said to generate a large temperature increase, resulting in the complete burning of the particle and surrounding material.

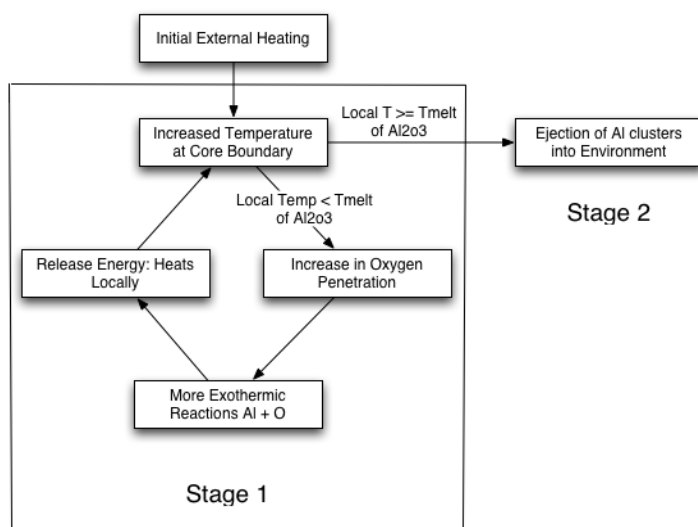


**Figure 74** Flowchart of runaway reaction leading to burning.

In contrast to these findings, the primary mechanism leading to burning in this simulation appears to rely on the chemical oxidation of the core at the core-shell boundary *prior* to shell failure. The increase in the particle's temperature creates additional mobility of oxygen atoms at the inner shell boundary, resulting in a migration of oxygen into the core. As the oxygen penetrates from the previously stable shell inward, the resulting exothermic reactions locally increase the temperature of the core-shell interface, resulting in a runaway reaction, which sustains itself until the particle reaches several thousand degrees (and total shell failure). This mechanism is summarized in **Fig. 74**.

Detailed results, analysis, and interpretation of the MD simulation are shown below in order to understand fully the above model. We first identify the stages of reaction by looking through the overall picture of the burning process. As indicated above, the complexity of the ANP burning and detonation behaviors make them difficult to analyze and describe without first breaking down the fundamental components into their respective parts. To this end, the particle evolution is divided into two stages of burn following initiation: confined burning and spallating burning. Each of these phases relies on a different set of internal mechanisms, which govern the reaction system behavior. As such, each phase can be identified by changes in the rate of heat production within the system as a whole. The temperature of the particle is presented in **Fig. 75a**, and the rate of temperature change (i.e., heat production) is presented as **Fig. 75b**. It is apparent in the above that a dramatic change in the rate of heat production occurs at 80-90 ps. This will be shown in the following to be the transition from the confined burning phase to the spallating burning phase (referred to as “Stage 1” and “Stage 2”, respectively).

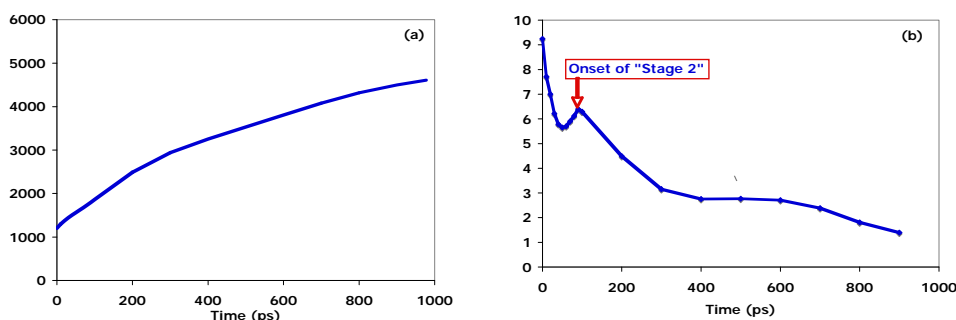


**Figure 75** (a) Temperature of particle during nanosecond simulation. (b) Rate of temperature change in system. Shift from confined burn into spallating burn (identified by red arrow).

The burning of the ANP during Stage 1 is governed by oxidation of core aluminum atoms by penetrating oxygen from the shell. In the following graph, the temperature of the particle at multiple time steps is graphed as a function of its radius (**Fig. 76**). It shows that from  $t = 0$  ps, the highest temperature region is located at the core-shell boundary. Also, by the increase in temperature over time, it is apparent that the heat generated at the core-shell boundary is building faster than the thermal transport throughout the rest of the particle, resulting in the formation of a much high interface at the internal boundary than in the rest of the particle.

Second, in the fragment analysis of the ANP for the first 130 ps (**Fig. 77**), it can be seen that the aluminum-rich fragments (left side of the graph) steadily increase (as the penetrating oxygen partially oxidizes the core atoms). The sudden boom of aluminum-poor fragments (light blue bar) occurs later, after the particle has transitioned into Stage 2. From this, it can be reasoned that the bulk of the early reactions are occurring at the inner boundary of the shell, rather than on its exterior.

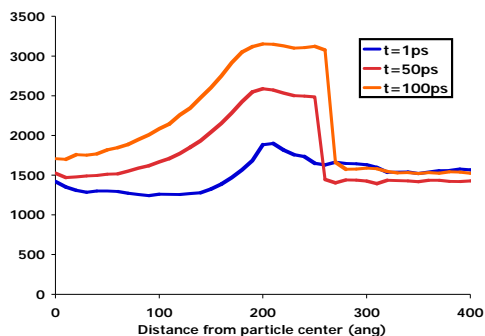


**Figure 76** Radial temperature of particle during initiation phase. Initial heating seen at core-shell (inner) boundary.

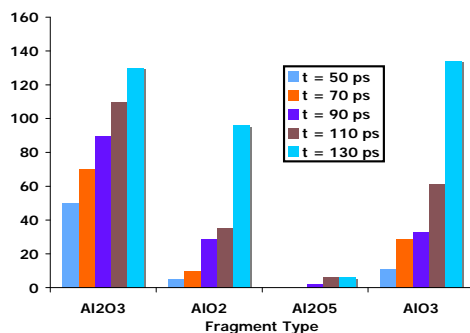


**Figure 77** Fragment analysis of ANP during initiation phase.

A third, more direct, method to detect the movement of oxygen atoms into the core can be accomplished by performing analysis on the shell as a whole. If we define the shell as all atoms that are connected (via Al-O bonds) to the largest fragment in the particle, it is possible to isolate the shell from the rest of the system. The inner radius of this entity shows the movement of oxygen into the core, expanding the shell in an inward direction. Despite the overall expansion of the particle, the area claimed by the shell is seen to deepen considerably over time (**Fig. 78**).

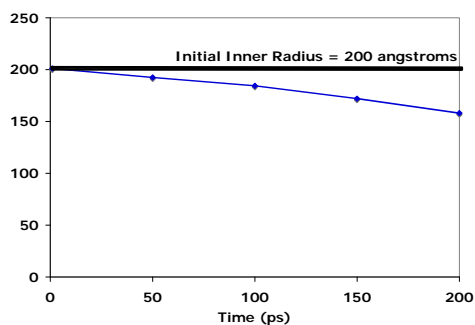


**Figure 78** Time variation of the inner radius of shell boundary, showing increasing penetration of oxygen into core area throughout phase.

Finally, the movement of atoms as a whole can be viewed by rendering a slice of the ANP at two time steps. In **Fig. 79**, the core aluminum atoms have been hidden to show the migration of the oxygen

into the core region. It can be seen that although the particle itself remains approximately the same size, a large influx of oxygen has been pulled into the inner regions.

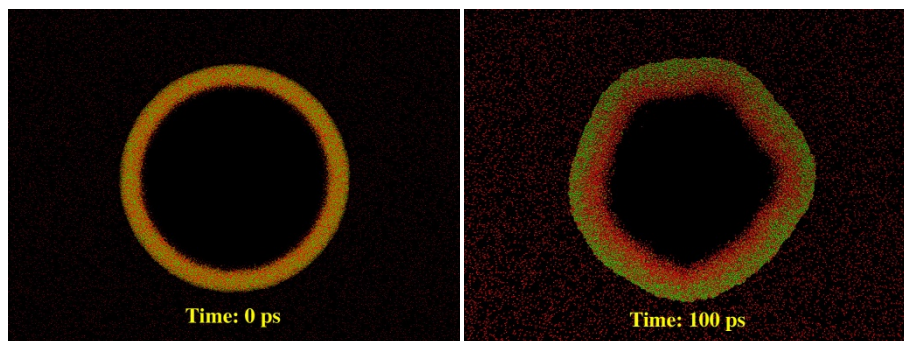


**Figure 79** Snapshots of central slice of particle during burn, hiding core Al atoms to allow viewing of oxygen penetration at 0 and 100 ps.

The reaction's stage 2, the spallating burning stage, was identified in the heat-produced graph (**Fig. 75b**) as occurring at approximately 80-90 ps. At this point, a fundamental change in the mechanism of heat production occurs within the particle, resulting in a dip in this graph (though the temperature itself continues to increase—**Fig. 75a**). The change at this point can be seen most readily in the graph of the aluminum present outside the shell boundary (as defined above). This change is highlighted by the red arrow in **Fig. 80**.

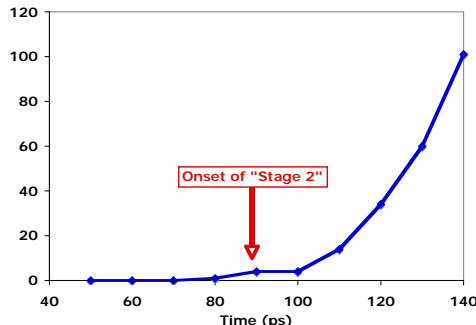


**Figure 80** Graph of aluminum atoms present outside the outer shell boundary (i.e., ejected or spalled atoms). Shows transition from confined burn to spallation burn.

From the above, it is apparent that the onset of stage 2 is connected with a sudden increase in the number of ejected aluminum atoms from the shell surface. These small clusters enter the surrounding oxygen, and are quickly oxidized. This change is accompanied by a matching change in the increase of oxygen-rich fragments in the system, seen in **Fig. 81**.

During stage 2, the particle continues to be heated by both the oxygen penetration and the aluminum ejections until the temperature plateau seen in **Fig. 75(a)** is reached. At this point, the oxygen has completely penetrated the particle core, seen in **Figs. 82a** and **82b**.

The above analysis demonstrates the importance of the inner core-shell boundary in the burning of the ANP. Unlike the laser-initiated detonation case (where the shell was fractured and ejected away from the particle upon initiation), in the heating case the shell has plenty of time to greatly contribute to the

burning process. This leads us to the conclusion that the core and the shell cannot be treated as two isolated pieces which interact only via the internal pressure. Instead, they must be considered as a chemically reacting combination.

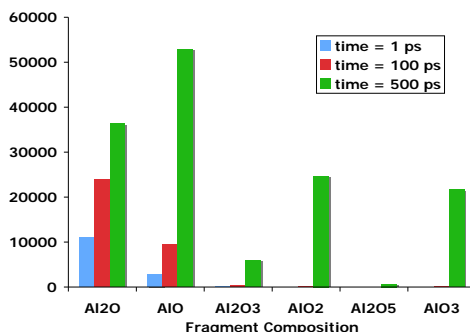


**Figure 81** Fragment analysis of ANP during spallation burn phase, showing dramatic increase in oxygen-rich fragments.

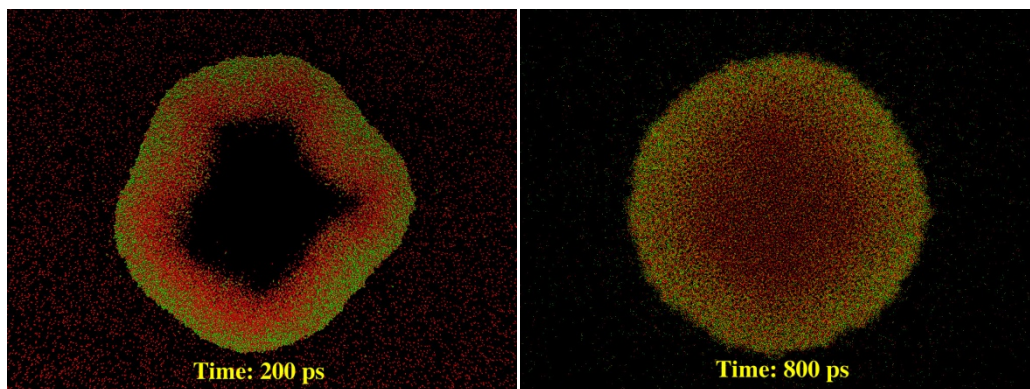


**Figure 82** Snapshots of particle at 200 and 800 ps. Core aluminum atoms have been removed to show oxidation throughout core.

### II.2.6 Enhanced Reactivity of Nanothermite

The **USC group** has also performed divide-and-conquer DFT (DC-DFT) based MD simulations to study thermite reaction at an Al/Fe<sub>2</sub>O<sub>3</sub> interface. The results reveal a concerted metal-oxygen flip mechanism that significantly enhances the rate of redox reactions. This mechanism leads to two-stage reactions—rapid initial reaction due to collective metal-oxygen flips followed by slower reaction based on uncorrelated diffusive motions, which may explain recent experimental observation in thermite nanowire arrays mentioned above. The 1152-atom DC-DFT MD simulation for 5 ps (6000 MD time steps) took 985 hours on 960 (3.2 GHz Intel Xeon) processors.

A stack of Al and Fe<sub>2</sub>O<sub>3</sub> layers was simulated involving 1152 (144 Fe<sub>2</sub>O<sub>3</sub> + 432 Al) atoms in an orthorhombic supercell with dimensions ( $L_x, L_y, L_z$ ) = (20.1 Å, 26.2 Å, 28.2 Å) with periodic boundary conditions. The hematite (Fe<sub>2</sub>O<sub>3</sub>) crystal, cut along (0001) planes to expose Fe planes, is placed in the supercell with the (0001) direction parallel to the  $z$  direction. The Fe planes of the hematite are attached to (111) planes of the face-centered cubic Al crystal at the two interfaces. Our DC-DFT method iteratively minimizes the energy functional using a preconditioned conjugate-gradient method to determine electronic wave functions. The grid spacing  $\sim 0.25$  Å (corresponding to the cutoff energy of 45 Ry in the plane wave-based method) for the real-space representation of the wave functions is sufficiently small to

obtain a good convergence of the total energy. A norm-conserving pseudopotentials and a generalized gradient approximation for the exchange-correlation energy was used. The DC-DFT method divides the system into 960 ( $= 8 \times 10 \times 12$ ) domains of dimensions  $2.51 \times 2.62 \times 2.35$  Å. Figure 10 shows the side ( $yz$ ) view of the non-overlapping cores of the domains in the supercell. Each domain is augmented with a buffer layer of depth  $\sim 2.2$  Å to avoid boundary effects. The interatomic forces thus computed quantum-mechanically are used to integrate Newton's equations of motion numerically (with a time step of 0.84 fs) in MD simulations to study atomic motions and chemical reactions. The MD simulations are carried out at temperature 2000 K in the canonical ensemble.

Snapshots of the atomic configuration are shown in **Fig. 83**, where the side ( $yz$ ) views of atomic configuration are displayed. We observe that the oxygen atoms in hematite migrate into the aluminum metal to form aluminum oxide and leaves behind liquid iron. Our DC-DFT simulation thus describes complete thermite reaction,  $2\text{Al} + \text{Fe}_2\text{O}_3 \rightarrow \text{Al}_2\text{O}_3 + 2\text{Fe}$ .

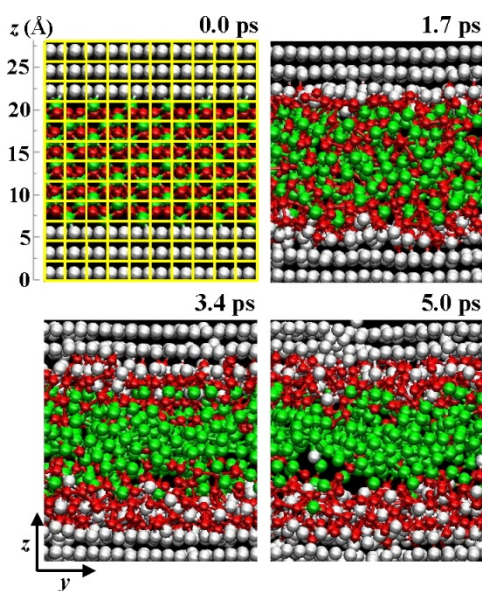


**Figure 83** Snapshots of the atomic configuration. The green, red and grey spheres show the positions of Fe, O and Al atoms, respectively. Yellow meshes at time 0 ps show the non-overlapping cores used by the DC-DFT method. Two interfacial regions are defined as slabs with a thickness of 4 Å parallel to the  $xy$  plane (length scale in angstrom is marked in the  $z$  direction). The Al- and Fe-side regions are defined between the two interfacial regions as shown in the figure.

To study mass diffusivity, **Fig. 84** shows mean square displacements of O atoms along the  $z$  direction, which are calculated using the simulation data for 0-3 ps. The solid and dashed lines are obtained from O atoms in the interfacial and Fe-side regions, respectively. Here, the boundary between iron-oxide and aluminum-oxide at each interface is located by calculating the average  $z$  coordinate of Al atoms facing Fe atoms. The interfacial regions are then defined as slabs with a thickness of 4 Å (i.e. 2 Å above and below the boundaries) parallel to the  $xy$  plane as shown in **Fig. 83**. **Figure 84** shows that O atoms in the interfacial region are much more diffusive than those on the Fe side. The four-fold accelerated diffusion constant perpendicular to the interface is  $2 \times 10^{-4}$   $\text{cm}^2/\text{s}$  in the interfacial region.

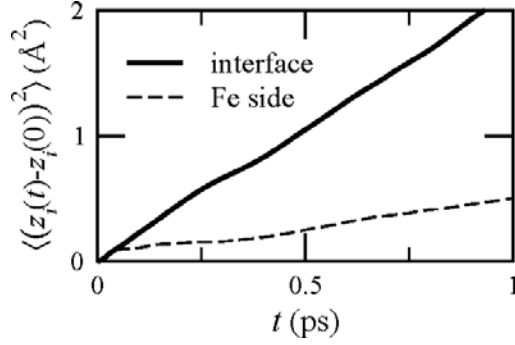


**Figure 84** Enhanced diffusion at the metal-oxide interface. Mean square displacements of O atoms along the  $z$  direction are plotted as a function of time. The solid and dashed curves are for O atoms in the interfacial and Fe-side regions, respectively.

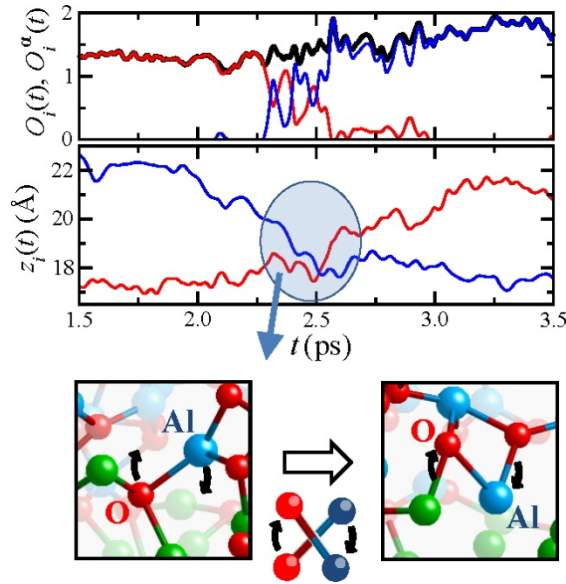


**Figure 85** Concerted metal-oxygen flip mechanism. (Top panel) Time evolution of the total and partial SBOP,  $O_i(t)$  and  $O_i^\alpha(t)$ , associated with the oxygen atom labeled as ‘O’ in the bottom panel. The black, red and blue curves show  $O_i(t)$ ,  $O_i^{\text{Fe}}(t)$  and  $O_i^{\text{Al}}(t)$ , respectively. (Middle panel) Time evolution of the  $z$  coordinates of the O and Al atoms labeled as ‘O’ and ‘Al’ in the bottom panel, respectively. (Bottom panel) Atomic configurations near the O and Al atoms of interest (labeled as ‘O’ and ‘Al’) at 2.3 and 2.8 ps. The green, red and blue spheres are Fe, O and Al atoms, respectively.

To understand the mechanism of the enhanced diffusivity at the interface, the time evolution of the atomic configuration in the interfacial region was examined and a concerted metal-oxygen flip mechanism was found. That is, O atoms switch their positions with neighboring Al atoms while diffusing in the  $z$  direction. A typical example of such events is shown in **Fig. 85**, where the middle panel shows the time evolution of the  $z$  coordinates of the O and Al atoms of interest. The O atom moves upward in concert with the Al atom moving downward. The switching motion between the O and Al atoms is shown in the bottom panel of **Fig. 85**.

To explain the quantum-mechanical origin of this mechanism, we calculate the bond-overlap population  $O_{ij}(t)$  between  $i^{\text{th}}$  and  $j^{\text{th}}$  atoms as a function of time  $t$ . We also define the sum of the bond-overlap population (SBOP) for each oxygen atom: Partial SBOP  $O_i^\alpha(t)$  for the  $i^{\text{th}}$  oxygen atom is defined as  $O_i^\alpha(t) = \sum_{j \in \alpha} O_{ij}(t)$ , where  $\alpha$  is Fe or Al; and the total SBOP is  $O_i(t) = O_i^{\text{Fe}}(t) + O_i^{\text{Al}}(t)$ . The upper panel

of **Fig. 85** shows  $O_i(t)$  and  $O_i^a(t)$  associated with the O atom. For  $t < 2.3$  ps, the oxygen atom resides in the iron-oxide region, and  $O_i^{\text{Fe}}(t)$  has finite values, while  $O_i^{\text{Al}}(t)$  is nearly zero. At  $t \sim 2.3$  ps, the oxygen atom starts to migrate into the aluminum side and  $O_i^{\text{Al}}(t)$  begins to increase. For  $2.3 \text{ ps} < t < 2.7$  ps,  $O_i^{\text{Fe}}(t)$  and  $O_i^{\text{Al}}(t)$  have comparable values while the oxygen atom is moving across the interface. For  $t > 3.0$  ps,  $O_i^{\text{Fe}}(t)$  becomes zero, while  $O_i^{\text{Al}}(t)$  converges to a finite value, indicating that the oxygen atom is chemically bonded only with Al atoms. The switching motion between O and Al atoms at the interface is thus triggered by the change of chemical bonding associated with these atoms.

To quantify the collective switching motion between O and Al atoms, the correlation function between the displacements of atoms along the  $z$  direction was calculated:

$$d_{\text{O-Al}}(t) = \langle \Delta z_i(t) \bullet \Delta z_j(t) \rangle / t^2, \quad (4)$$

where  $\Delta z_i(t) = z_i(t+t_0) - z_i(t_0)$  with  $z_i(t)$  being the  $z$  coordinate of the  $i^{\text{th}}$  ion at time  $t$ . The brackets mean the average over both the time origin  $t_0$  and atomic pairs ( $i \in \text{O}, j \in \text{Al}$ ). In the calculation, atomic pairs whose distance is less than  $2.3 \text{ \AA}$  at  $t_0$  are selected. Since we are interested in the correlation between diffusing O and Al atoms, we include atomic pairs that satisfy the conditions  $|\Delta z_i(T)| > 2 \text{ \AA}$  and  $|\Delta z_j(T)| > 2 \text{ \AA}$  at  $t = 2$  ps. The results in **Fig. 86a** (solid curve) reveal negative correlation in  $d_{\text{O-Al}}(t)$  for  $t > 0.5$  ps, which reflects the collective switching motion between O and Al atoms at the interface as shown in **Fig. 85**. Such negative correlation does not exist on the Al side (see the dashed curve in **Fig. 86a**), indicating independent diffusive motions of Al and O atoms.

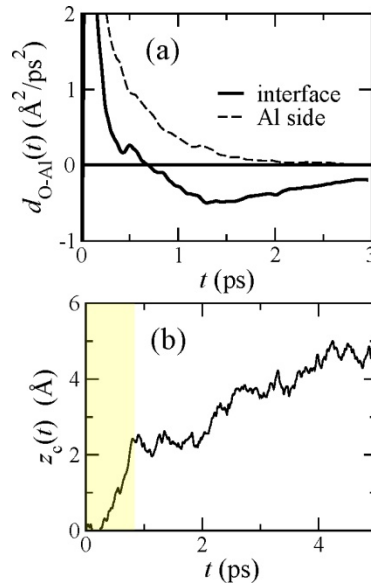


**Figure 86** (a) Negative correlation associated with concerted Al and O motions at the interface. Correlation functions between displacements of O and Al atoms along the  $z$  direction (defined in Eq. (1)) are shown as a function of time. The solid and dashed curves are obtained in the interfacial and Al-side regions. (b) Two-stage reactions of thermite. Time evolution of the positions  $z_c(t)$  of the reaction fronts. The gray shade highlights the rapid first-stage reaction due to concerted Al-O motions, which is followed by slow reaction based on uncorrelated diffusion.

The enhanced mass diffusivity at the metal-oxide interface leads to a two-stage reaction behavior. In **Fig. 86b**, the position  $z_c(t)$  of the reaction front calculated from the coordinates of oxygen atoms at the forefront of oxidation is plotted. For  $t < 1$  ps,  $z_c(t)$  increases rapidly as oxygen atoms migrate into the Al side, which is accelerated by the collective switching mechanism. This is followed by a slower reaction

due to uncorrelated diffusion of atoms. (Though slower than the concerted thermite reaction, the second-stage diffusion here could still be faster than conventional diffusion, due to defect-mediated giant diffusivity because of the depletion of O atoms in the near-interface oxides.) Such two-stage reactions may be related to the experimental observation in thermite nanowire arrays mentioned before.

### II.2.7 Multi-Scale Modeling of Nano-Aluminum Particle Ignition and Combustion

Aluminum (Al) particles have been extensively utilized and studied in the field of energetic materials since the mid-1950s because of their high energy density, high reactivity, and low cost. The ignition and combustion of micron-sized Al particles are relatively well understood [120-122]. Micron-sized Al particles have a higher ignition temperature ( $\sim 2350$  K) [120] and a tendency to agglomerate in solid rocket motor (SRM) environments [123]. In the recent past, nano-scale materials and composites, characterized by ultra fine grain sizes, have been recognized for their unusual energetic properties such as increased catalytic activity and higher reactivity [124]. In the hope of engineering a novel nano-energetic material, extensive research efforts have been made to study the burning behavior of nano-Al (nAl) particles in various oxidizer environments [125-127].

In an attempt to improve the performance of commonly used micron-sized Al particles, research efforts have been made to devise novel methods to reduce their ignition temperature and agglomeration [128]. It is found that a coating of nickel (Ni) over Al particle reduces its ignition temperature by  $\sim 800$  K [128]. However, the fundamental mechanisms behind such an observation are not well understood and theories postulated also need clarification from atomistic calculations over a broad range of particle sizes. Before moving to multi-scale modeling of the generation, transport, and combustion of nano-engineered energetic materials in flow environments, a good understanding of the ignition and combustion mechanisms of a single Al particle in a quiescent medium is required. Such a study helps in understanding the single particle behavior with high fidelity, and can also act as a sub-model in predicting the collective behavior of particles at large scales. Thus, atomistic-scale calculations in conjunction with the experimental observations are useful in establishing a unified multi-scale theory describing the ignition and combustion of Al particles. The atomistic-scale simulation framework could, in principle, be extended to study thermo-mechanical behavior of Ni-coated nAl particles, in an effort to explain their lower ignition temperature. Furthermore, on a macro-scale, in order to predict and explain the combustion characteristics of nano-engineered propellants based on Al particles (dust cloud and mixtures), development of a theoretical framework to handle Al particle combustion is very helpful.

A comprehensive review on aluminum particles at micro and nano-scales was performed by **Yang** and his group [129]. Various processes and mechanisms governing their ignition and combustion are identified. For micron-sized Al particles, a detached diffusion flame is observed and combustion is found to be similar to the hydrocarbon droplet combustion ( $d^2$ -law) with a reduced exponent [130]. The ignition of micron-sized Al particles is observed to happen close to 2350 K and is reported to be caused by the melting of the impervious oxide shell [120]. The combustion of micron-sized Al particle is well explained by Dreizin et al.'s three-stage theory [131] and is described by unique features such as brightness oscillations, disruptive burning, droplet burning speed variations, oxygen build-up within the molten particle, micro-explosions, and asymmetric burning. Research in nAl ignition and combustion is found to be in nascent stages. In general, oxidation of oxide-coated nAl particles is found to be heterogeneous and diffusion-controlled (slow diffusion of Al cations and O anions). Furthermore, nAl particles are reported to ignite at temperatures as low as 900 K [126]. No detached flame front formation is observed. The ignition of nAl particles is hypothesized to be caused by the rupture of the oxide shell due to melting of the aluminum core [132] or due to polymorphic phase transformations of the oxide layer [133]. Thus, it is clear from the literature survey that the mode of ignition and the combustion mechanism may vary depending on the particle size and no theory is available to address the relevant issues over broad range of particle sizes of interest.

In order to develop a unified theory which describes the behavior of Al particles and reconcile the diverse school of thoughts in the literature, the **Yang group** investigated the melting points of pure Al particles for a wide range of particle sizes in the nano-scale regime and also studied the thermo-mechanical behavior of oxide-coated nAl particles. This is because the ignition mechanism of Al particles is strongly linked to the melting of the Al core and the oxide shell. Hence, accurate quantitative results from the atomistic-scale calculations will help us in framing a unified theory. To this end, a molecular-dynamics (MD) simulation framework was first established to handle the thermodynamic behavior of bulk and nano aluminum. The computer program established under the MURI project can simulate micro-canonical (NVE), isobaric-isothermal (NPT) and isobaric-isenthalpic (NPH) ensembles. These algorithms are parallelized using the atomic decomposition method. A separate post-processing code is developed to superimpose the grid on the geometry under consideration, and to analyze the results using the contours of various thermodynamic properties. The code has the capability of handling multi-atom simulations and can treat liquid and solid phases. Several inter-atomic potentials (the Lennard-Jones, Glue, embedded-atom, Streitz-Mintmire, and Sutton-Chen potentials) are established to handle inter-atomic interactions prevalent in pure and oxide-coated Al particles. The MD computational framework was first used to identify suitable potential functions and was then applied to study the size-dependence of the melting points of pure Al particles in the size range of 2-9 nm [134]. The effect of pressure and influence of void size and shape on the melting points were later studied [135]. Once the melting behavior of pure nAl particles was understood, the thermo-mechanical behavior of oxide-coated Al particles was investigated [136]. The focus was primarily to quantitatively evaluate the influence of the oxide shell on the melting point of the Al core and also to evaluate the melting points of nano-scale oxide shells. Both crystalline and amorphous oxide layers were considered. The diffusion of Al cations into the oxide shell was also explored and a structural analysis was performed to ascertain the possibility of fracture of the oxide shell upon the melting of the core. Both qualitative and quantitative results of the MD simulations were then used to establish a unified multi-scale theory to describe the ignition and the combustion of Al particles [137]. Characteristic time scales of phase transformations, oxidation, heating/melting, and diffusion of ions were calculated and compared to divide the regimes of particle ignition into six modes.

The MD simulation framework developed by **Yang and his group** was extended to explore the behavior of nickel coated nAl particles in order to understand the mechanisms for their reduced ignition temperatures [138]. A suitable inter-atomic potential function was selected and MD calculations were performed over a wide range of particle sizes (4-16 nm). Results provided direct insight into the effect of nickel shell and the core size on the Al core melting point, the onset of inter-metallic alloying reactions, the adiabatic reaction temperatures, and the dependence of the relevant thermo-physical phenomena on the dimensions of the core and the shell.

On macro scales, a theoretical framework was established by the **Yang group** to predict the combustion characteristics of Al dust cloud combustion for both mono-sized and bi-modal particle size distributions [139]. The model was then extended to study the flame propagation of nAl-water mixtures [140]. The developed models give a good prediction of the burning rates and the temperature profiles in various oxidizer environments.

### II.2.7.1 Molecular Dynamics Simulations

The melting point of bulk Al is  $\sim 933$  K. However, when the particle size is reduced to the nano-scale regime, the melting point is found to decrease from its bulk value. In the present study, the melting point is determined by monitoring a combination of parameters such as the Lindemann index, translational order parameter, radial distribution function, and potential energy. The bulk Al undergoes homogenous melting at temperatures over 1000 K. The superheating is due to the absence of free surface to initiate the nucleation of the liquid phase. For nano-particles, a free surface is readily available and hence, the particle undergoes heterogeneous melting. The size dependence of the melting point is shown in **Fig. 87**. The percentage of atoms on the surface increases, as the particle size decreases. As a consequence, the surface atoms are relatively easy to displace, and a melting point depression is predicted. As can be seen in **Fig. 87**, the Glue and the Streitz-Mintmire potentials predict the size-dependence of melting points of nAl particles quite accurately. It is also found that the ultra-small nano particles (e.g., 2 nm) exhibit dynamic co-existence of solid and liquid phases in the temperature range of 400-475 K. Once the melting points of nAl particles are determined, the effect of void size on the melting

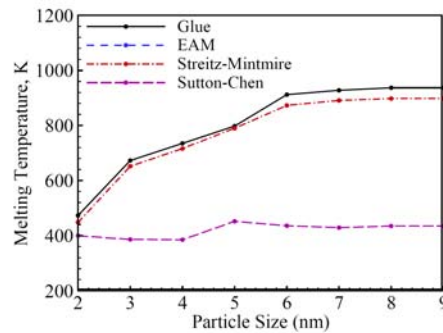


**Figure 87** Size dependence on the melting point of pure Al (in vacuum).

points of bulk and nAl is studied and the results are shown in **Fig. 88**. The melting points of bulk Al and nAl particle decrease, as the size of the void increases. The void is found to act as a nucleation site and hence, promotes the formation of the liquid phase. For bulk Al, the melting point decreases with the void size and attains a plateau near the thermodynamic melting point of Al. For very large void sizes, the crystal is found to collapse and no phase change is observed. It is also found that the melting point is independent of the shape of the void. For nAl particles, the melting point reduces only when the void size exceeds a critical void size, since the surface acts as the primary nucleation site. As before, for very large void sizes, collapse of crystal is observed. It is also observed that pressure exerts a negligible influence on the melting points of nAl particles in the range of 1-300 atm.

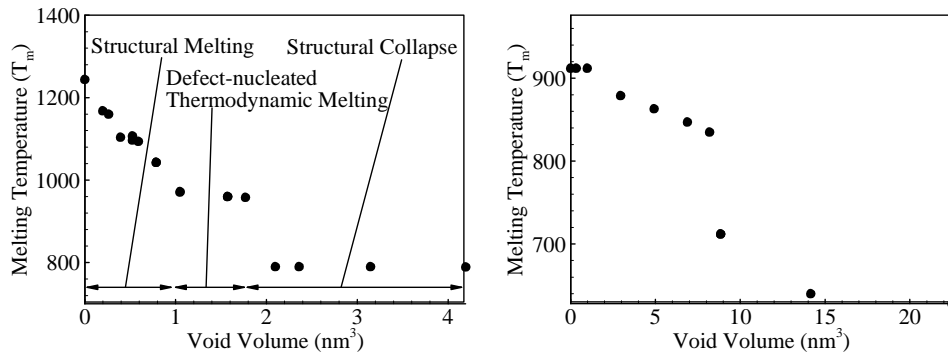


**Figure 88** Effect of void size on the melting point of (a) bulk aluminum; (b) 5.5 nm Al particle.

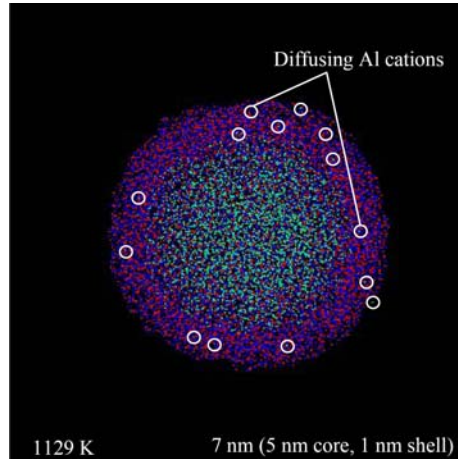


**Figure 89** Diffusion of Al cations into the oxide shell.

The MD simulation framework was then applied to investigate the thermo-mechanical behavior of oxide-coated Al particles. Diffusion of Al cations into the oxide shell is observed, as shown in **Fig. 89**. The effect of core size and shell thickness on the melting points of the core and the shell is also analyzed. The results are summarized in **Fig. 90**. As can be seen, the melting point of the core is affected by the size of the core but not by the thickness of the shell, while the melting point of the shell is affected by the thickness of the oxide shell. The melting point of the oxide particle (5 nm) is observed to be about 1284 K. This is about 1000 K lower than the bulk melting point of alumina. Interestingly, melting of the oxide shell is preceded by the solid-solid phase transformation of the oxide into a denser polymorph, as evidenced by the change in the density. Upon melting of the aluminum core, the density reduction results in a volume change of  $\sim 11\%$ . Thus, the core exerts tensile stress on the oxide shell. The tensile strength of alumina is about 0.25 GPa. The calculated stresses on the oxide shell are at least an order of magnitude higher than the tensile strength of alumina and hence, the oxide shell is likely to be ruptured. The results of the MD study, supplemented by experimental observations, are then

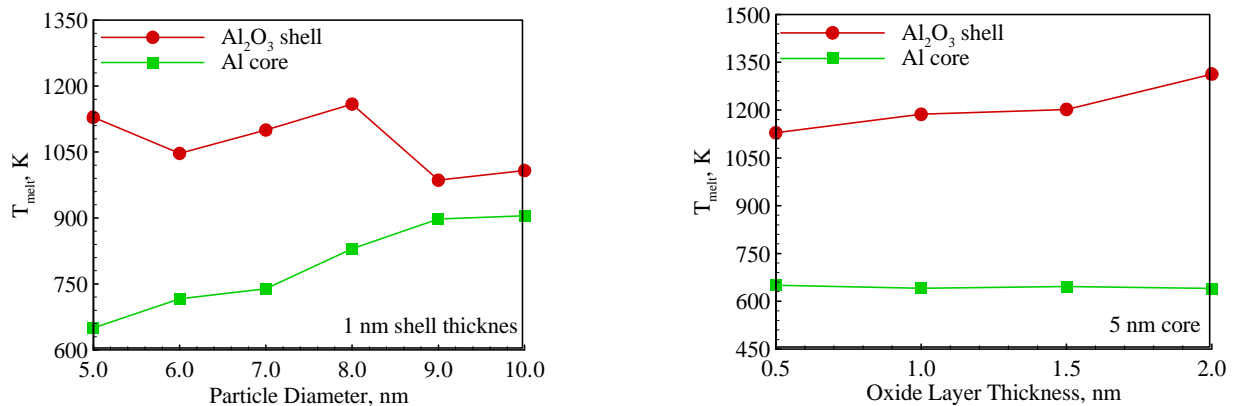


**Figure 90** Effect of core size and shell thickness on the melting points of the core and shell of nAl particles.

used to frame a unified theory for Al particle ignition and combustion for both micron-sized and nano-sized particles. The entire process involves five stages (**Fig. 91**): (1) particle heating with phase transformation; (2) melting of core and ignition due to melting/cracking; (3) heterogeneous reactions/healing of cracks; (4) melting of oxide layer to form cap; (5) vaporization of Al with detached

flame/particle burnout due to heterogeneous combustion. In addition, six different modes of ignition and oxidation are identified based on ambient conditions. As the particle is

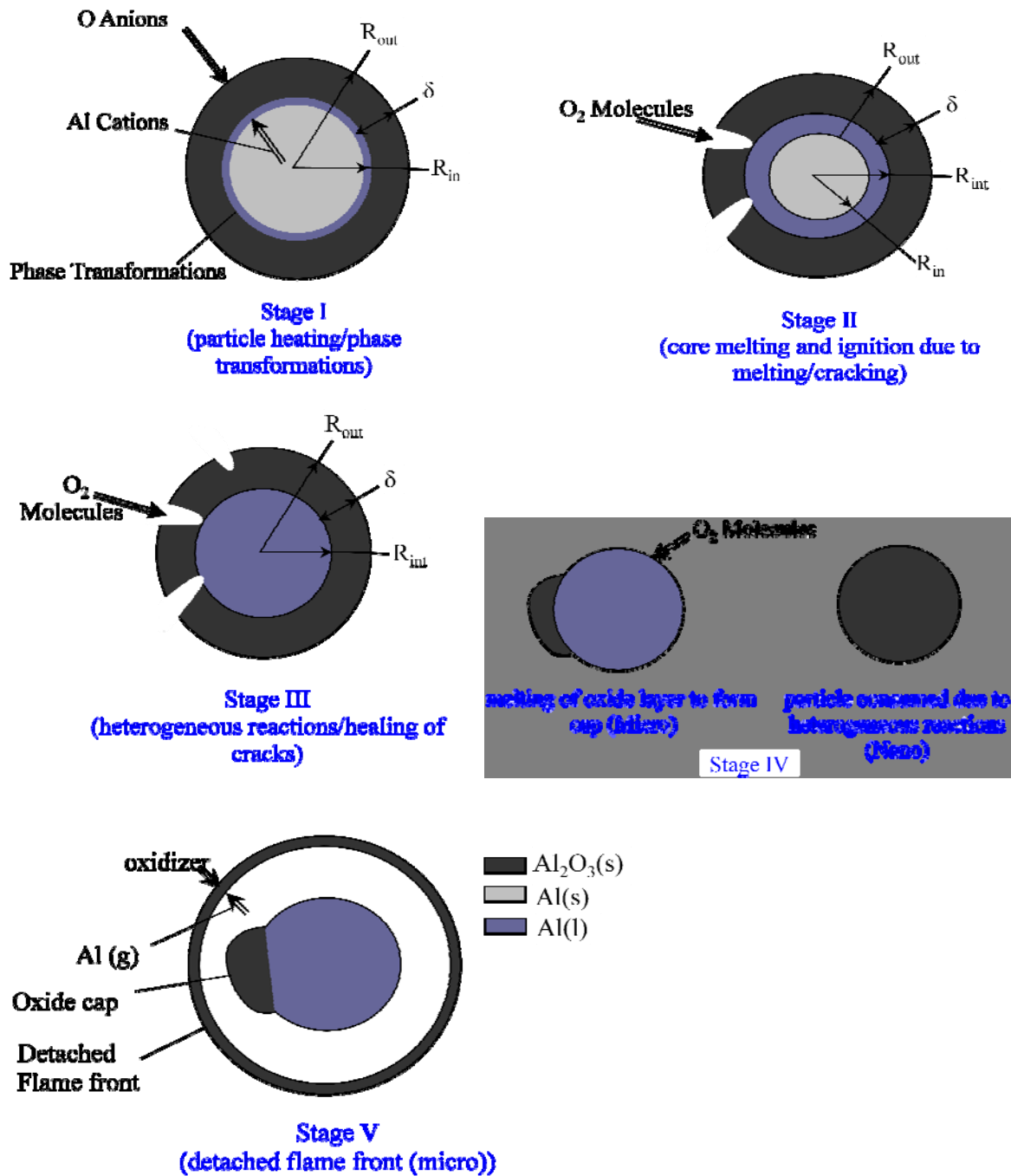
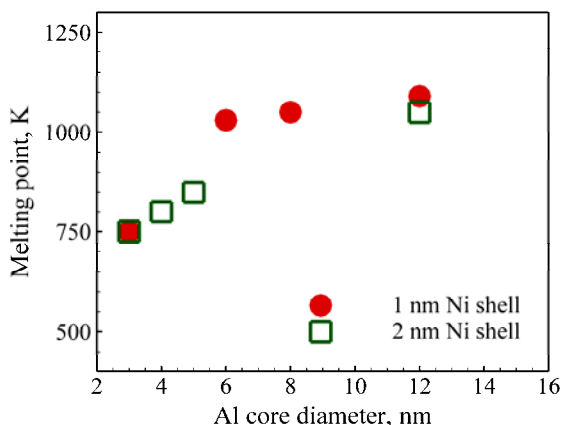


Figure 91 A unified theory on Al particle ignition and combustion.

heated, Al cations diffuse into the oxide shell and polymorphic phase transformations occur in the oxide shell. The diffusion of Al cations is also observed in MD simulations, thus substantiating this fact. The second stage begins upon the melting of the Al core. The results of the MD calculations reveal that the melting point of the Al core can be as low as  $\sim 473$  K, depending on the size of the Al core. A thermal Fourier analysis reveals that for nano-particles, energy is conducted through the shell

and thus, the melting of the core takes place at an early stage. However, for a micron-sized particle, more energy is stored in the shell due to higher thermal resistance, and consequently, the melting of the core is delayed. The onset of stage II depends on the size of the Al core. MD simulations confirm the possibility of solid-solid phase transformations in the oxide shell. Owing to the differences in densities of different polymorphs of alumina, the oxide shell could potentially be cracked. In addition, nano-scale oxide shells may melt at a lower temperature, thereby exposing the bare Al core for the attack of oxidizer molecules. These factors contribute to the reduced ignition temperature of nAl particles. Nevertheless, there is always a parallel process of healing of the oxide layer. For micron-sized Al particles, ignition cannot happen at this stage, since the stresses are not high enough to crack the oxide shell and the melting point of the oxide shell is quite high. Liquid Al is thus contained within the solid alumina shell, as the particle is heated. Stage III involves heterogeneous reactions of nano-particles and simultaneous healing of the cracks. At the end of stage III, for micron-sized particles, the oxide layer melts and forms an oxide cap exposing the bare Al. At this point, micron-sized Al particle undergoes heterogeneous reactions at the surface and nano-particles are completely consumed by heterogeneous reactions. Pressure and particle size play an important role in determining the particle behavior in stage IV (based on the Damköhler number). Micron-sized particles enter stage V and burn with a detached diffusion flame, as the vaporization temperature of Al is reached. The present theory, with the help of MD simulations and experimental observations, reconciles various hypothesis postulated to describe Al particle ignition and combustion and establishes a unified theory for a wide range of particle sizes.

The MD simulation framework was then extended to explore the thermo-mechanical behavior of Ni-coated nAl particles in order to understand the reason for the reduced ignition delay. **Figure 92** shows the melting points of the Al core as a function its size and for different shell thickness. The melting point of the core is not affected significantly by the thickness of the shell, although the presence of the shell plays an important role in dictating the core melting process. Typically, the melting point of the Al core is found to approach the homogenous melting point of Al (~1050 K), when a Ni shell covers the Al particle. This is due to the fact that the interfacial Al atoms are under the sphere of influence of the Ni atoms. Upon melting, the shell could be infiltrated by the Al atoms and inter-metallic reactions could get initiated. The temperature at which the inter-metallic reactions begin is found to be dependent on the dimensions of the core and the shell. When the core size is increased (for the same shell thickness), the Ni atoms infiltrate the shell at a lower temperature, as seen in **Fig. 93(a)**. Similarly, for the same core size, a thicker shell delays the advent of the inter-



**Figure 92** Melting points of Ni-coated Al cores.

metallic reactions. For very small core size ( $\leq 5$  nm) and very thick shells ( $\geq 2$  nm), infiltration of the shell is observed only at a higher temperature ( $\sim 1600$  K). The infiltration is accompanied with insignificant inter-metallic heat release (due to lower mass fraction of Al). In order to quantify the inter-metallic heat release in terms of the adiabatic reaction temperature, NVE simulation is performed to mimic the adiabatic condition. The adiabatic reaction temperature increases with Al mass fraction and attains a plateau close to 2300 K (the simulation starts at a temperature close to 1200 K). Upon the advent of inter-metallic reactions, self-sustaining inter-metallic reactions are

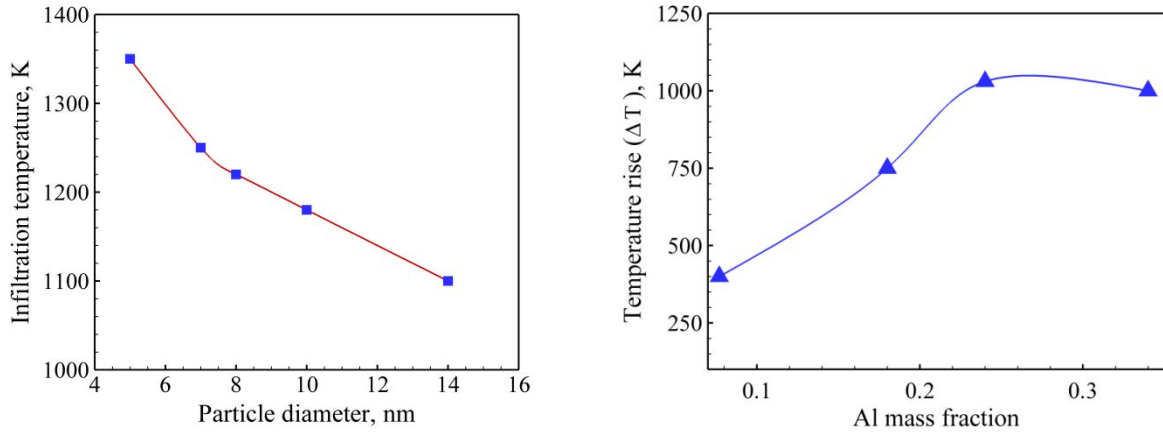


**Figure 93** (a) Infiltration temperature; (b) adiabatic reaction temperature rise.

observed which heat the particle, under adiabatic conditions, to temperatures inferred from **Fig. 93(b)**. The increase in the adiabatic reaction temperature with Al mass fraction in the particle is due to the increase in the number of Al atoms that exothermically react with the Ni atoms. However, at the limiting Al mass fraction, there are more Al atoms than Ni atoms and hence, the reaction temperature does not increase any further. The results of the MD simulations validate the claim that the Ni-coated particles undergo self-sustaining exothermic reactions even in inert environments (such as argon), provided an energy source is available to heat the particle to the temperature at which inter-metallic reactions begin. Furthermore, these inter-metallic reactions, which self-heat the particle, can also reduce the ignition delay significantly.

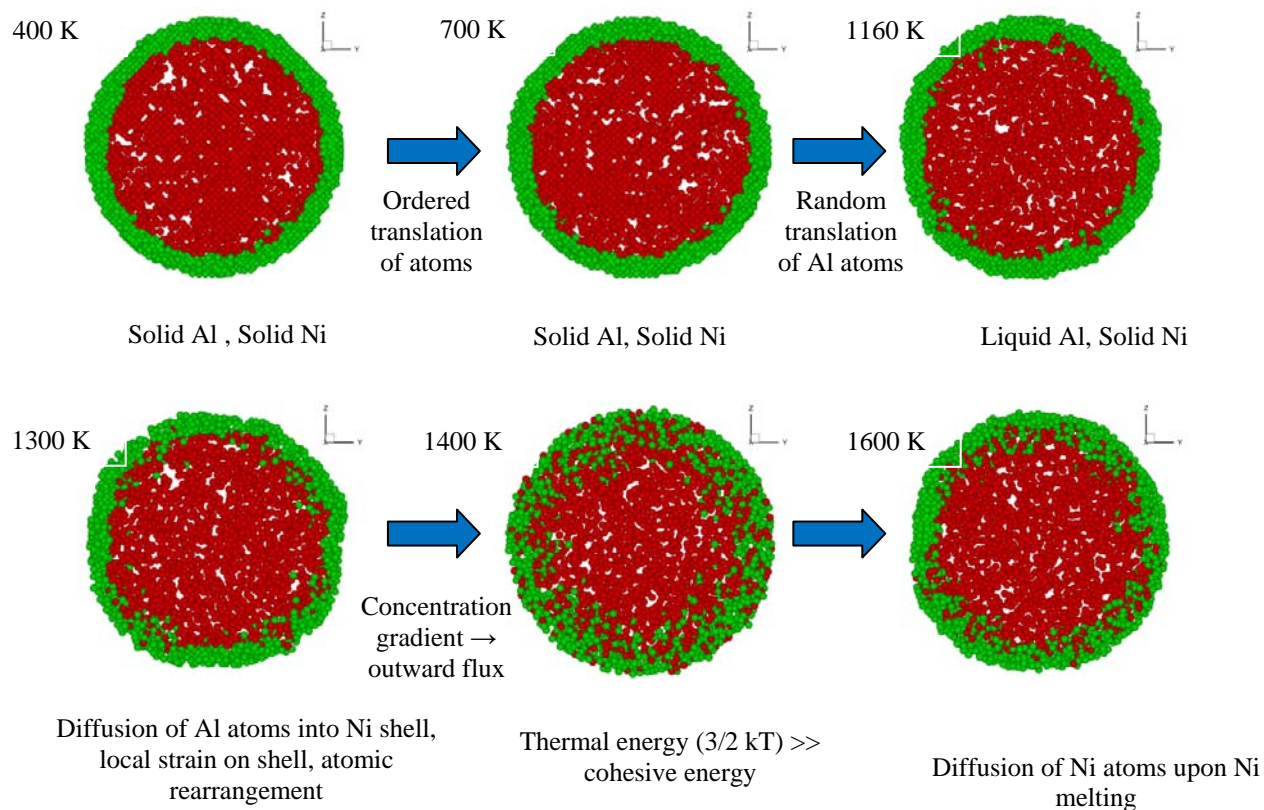


**Figure 94** Cross-sections of 14 nm particle (1 nm shell) at different temperatures (red is Al and green is Ni).

The entire time-history for a 14 nm particle is shown in **Fig. 94** to explain the key thermo-physical events. When the particle is heated to the melting point of Al core (**Fig. 92**), the order of translational motion of Al atoms is lost, and observation is made of random motion of liquid like Al atoms within the solid Ni shell. When liquid Al atoms acquire sufficient thermal energy (at the corresponding temperature), they are able to overcome the sphere of influence of neighboring atoms and hence jump into the interstitial spaces in the Ni shell. The temperature at which the infiltration takes place depends strongly on the dimensions of the core and the shell, as already shown in **Fig. 93(a)**. During this infiltration, alloying inter-metallic reactions self-heat the particle to the adiabatic reaction temperature (**Fig. 93**). Upon being heated (or self-heated) to the melting point of nickel, a gradual influx of Ni atoms extends the inter-metallic reactions until they are sufficiently alloyed. Thus, as the particles are heated in a SRM environment, these inter-metallic reactions act as an additional mode of energy release, thus, hastening the ignition of Al particles.

### II.2.7.2 Macro-scale theoretical model

A macroscopic theoretical framework was established to handle the flame propagation in aluminum dust clouds. The theoretical framework is detailed in [139]. The results are summarized in **Fig. 95**. For micron-sized and larger particles, the flame speed decreases with increasing particle size, and follows a  $d^{-0.92}$  law. When the particle size decreases to several micron-meters, transition of the burning mechanism from a diffusion to a kinetically controlled mode takes place. In the size range of 130 nm – 10  $\mu\text{m}$ , the flame speed follows a  $d^{-0.52}$  law or  $d^{-0.13}$  law, depending on the burning time correlation. When the particle size is reduced below 130 nm, continuum hypothesis becomes invalid and a more sophisticated model is necessary. Furthermore, the maximum flame speed of 5.82 m/s is expected at the molecular limit.

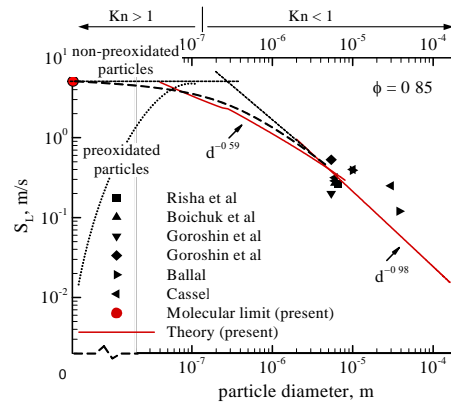


**Figure 95** Flame speed of Al-air mixture at 1 atm.

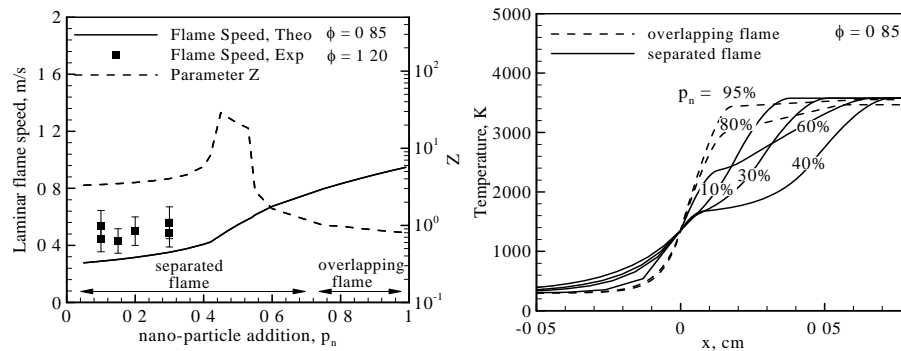


**Figure 96** Flame speed and temperature distributions of bi-modal (100 nm, 6.5  $\mu\text{m}$ ) Al-air mixtures at 1 atm.

The model has been extended to study the combustion of bi-modal dispersions of Al particles in air. The results of the analysis are shown in **Fig. 96**. The flame speed is positively affected by the addition of nano particles. Depending on the mass fraction of nAl and the equivalence ratio, either an overlapping or a flame separated flame configuration is observed. The separated flame configuration, typically observed for low mass fraction of nano-particles ( $< 0.75$ ), explains the thicker flames observed in bi-modal dust combustion experiments. This is also clearly seen in the temperature profiles in **Fig. 96**. For an over-lapping flame configuration, the heat release from the combustion of nAl particles is sufficient to heat and ignite micron-sized Al particles. However, this is not the case for a separated flame configuration. Results of the present theoretical analysis are in good agreement with experimental observations [141]. The simulation framework is also applied to study the flame propagation of nano-

aluminum and water mixtures [140]. Results of the burning rate are shown in **Fig. 97**. The pressure exponent in the linear burning rate is predicted to be about 0.6. This suggested an overall first-order chemical reaction. The combustion is controlled by collision of water molecules on the particle surface. The linear burning rate increases substantially with the equivalence ratio due to increase in the heat-release rate. Furthermore, the linear burning rate follows roughly a  $d^{-1.0}$  law. These predictions are in excellent agreement with experimental observations [125]. The model can be easily extended to handle combustion of nAl particles with mono-dispersed and bi-modal distributions in solid and liquid oxidizers.

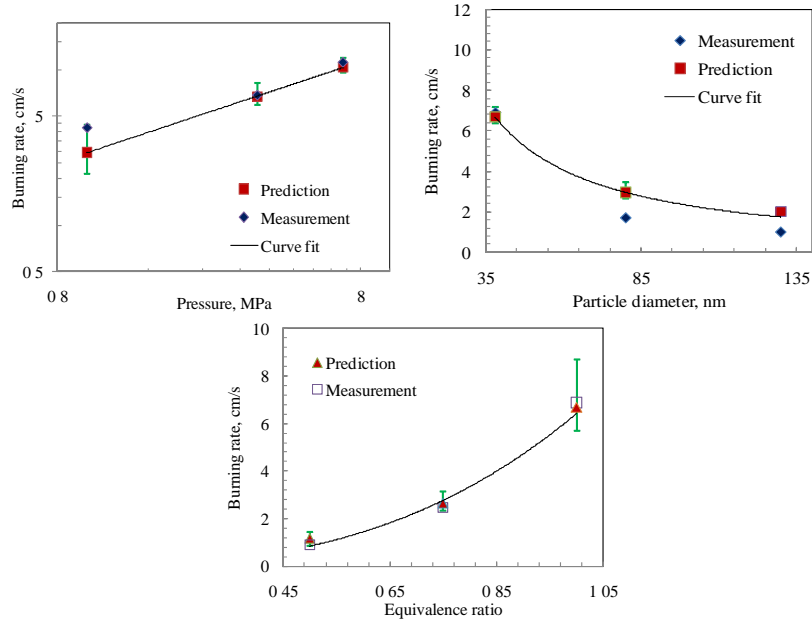


**Figure 97** Variation of linear burning rate of nAl-water mixtures with pressure (38 nm,  $\Phi=1$ ), equivalence ratio (3.65 MPa, 38 nm), and particle size (3.65 MPa,  $\Phi=1$ ).

## II.3 Experimental Characterization and Diagnostics

### II.3.1 Ultrafast Diagnostics of Nano Energetic Materials

The goal of the MURI team led by **Dlott** was to develop diagnostic techniques to probe the fundamental mechanisms of nanoenergetic materials related to performance [142]. A knowledge of these mechanisms and their dependence on structure is a route toward rational development of nanoengineered energetic materials (NEEM). Because NEEM dynamics involve high energy processes occurring at interfaces between rather complicated materials (i.e. fuel/passivation/oxidizer interface), techniques did not exist to probe NEEM dynamics at a detailed level. **Figure 98** shows the four primary techniques used by the **Dlott team**.

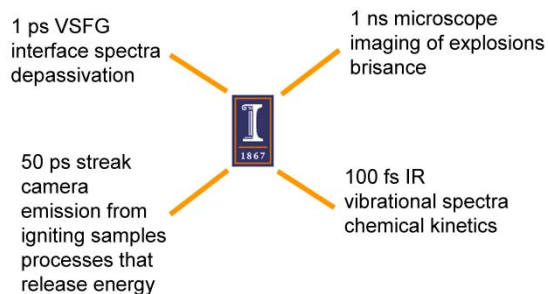


**Figure 98** Diagnostics available in the laboratories of the UIUC team.

Femtosecond broadband vibrational sum-frequency generation spectroscopy (SFG) is an interface-selective vibrational spectroscopy that is useful to understand the dynamics of passivation layers such as self-assembled monolayers (SAMs) [143]. The 1 ns ultrafast microscope allows us to image the explosion that results when a NEEM is flash-heated by a short laser pulse [142,144]. The streak camera detects emission spectra from flash-heated NEEM in order to investigate the ignition process [145,146]. The femtosecond IR system probes the vibrational transitions of the NEEM after flash heating to provide information about the initiation process [147]. Not shown in Fig. 1 is the laser-launch facility that was developed and constructed during the add-on final year of the project.

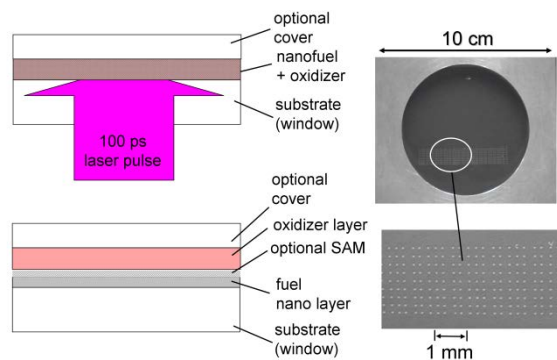


**Figure 99** Concept for flash-heating sample (left) and photos of a flash-heating array.

**Figure 99** depicts the flash-heating method [148]. A NEEM is sandwiched between confining windows and a short-duration (typically 100 ps) laser pulse suddenly heats the fuel elements [145,146]. These fuel elements then combine with oxidizers. NEEM samples are fabricated as thin films on windows having an area of 10's of  $\text{cm}^2$ . Individual explosions occur in areas of  $0.01 \text{ cm}^2$  so that thousands of experiments can be conducted on a single sample. **Figure 100** shows the explosion that results from a NEEM composed

of 30 nm Al fuel and Teflon<sup>AF</sup> oxidizer [142]. One of the confining windows was removed to show the flow of material.

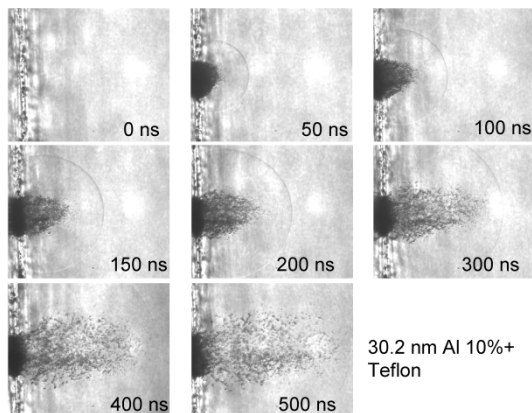


**Figure 100** Nanosecond microscopy of the laser-induced explosion of nano(Al) + Teflon. Each frame represents an area 640  $\mu\text{m}$  wide.

**Figure 101** depicts the idea of the IR measurements. So far these measurements have been conducted only on Al/Teflon<sup>AF</sup> NEEM [149]. Teflon<sup>AF</sup> is a fluoropolymer with some oxygen in its structure. The IR pulses were tuned in the region of C-F<sub>2</sub> and C-F-O stretching transitions. As the flash-heated Al began to react with Teflon<sup>AF</sup>, the C-F transitions vanished in a characteristic manner [147]. The vanishing of these transitions indicated the initiation of the NEEM.

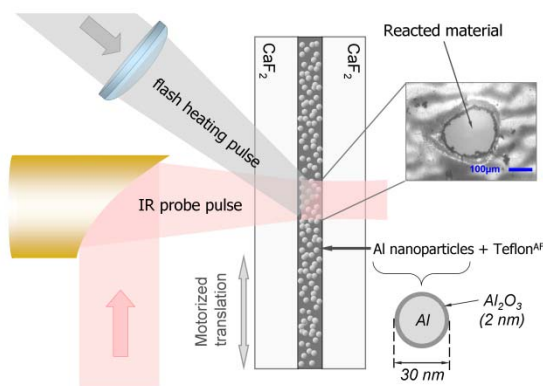


**Figure 101** Concept for ultrafast infrared probing of flash-heated nanoenergetics.

**Figure 102** depicts a block diagram of the IR laser apparatus. **Figure 103a** shows the IR spectrum of the NEEM. **Figure 103b** shows the IR spectrum of Teflon used for comparison, since Teflon has only CF<sub>2</sub> transitions. **Figure 103c** shows how the NEEM spectrum changed, i.e. the disappearance of stretching transitions, as a result of flash-heating. **Figure 104** shows how the NEEM spectrum changed as a function of time with 100 ps time resolution. From the time dependence we were able to determine the time constant for initiation and understand a great deal about the mechanism. The Al fuel reacts faster with CFO than with CF<sub>2</sub>. These were the first direct *in situ* measurements of NEEM initiation [147].

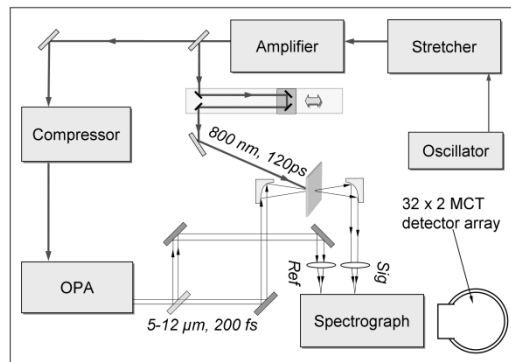


**Figure 102** Block diagram of femtosecond laser apparatus for flash-heating infrared.

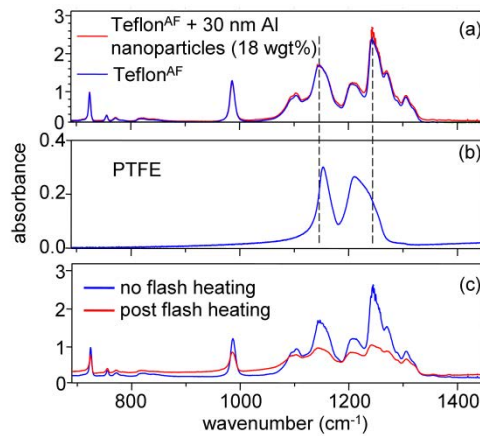


**Figure 103** (a) IR spectrum in CF stretch region of Teflon<sup>AF</sup> with and without nano(Al). (b) IR spectrum of Teflon. (c) IR spectrum of nanoenergetic before and after flash-heating.

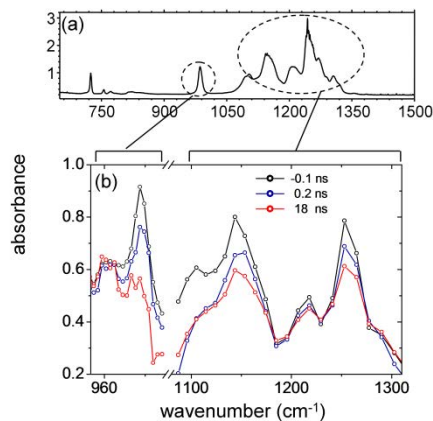


**Figure 104** Time-dependent spectra of Teflon<sup>AF</sup> + nano(Al) after flash heating.

SAMs are viewed as a possible way of advancing NEEM by providing a passivation layer with better control [150,151]. In NEEM with Al fuel, the passivation layer is usually the native oxide on Al. The passivation layer keeps the NEEM from reacting until it is initiated. But the oxide is useless

deadweight, whereas a SAM weighs much less and can contribute to chemistry. We conducted a series of flash-heating experiments with alkane SAMs on first Al and then Au. Although Au is not ordinarily used in NEEM, it was a cleaner model system. After heating the metal surface we observed the SAM using SFG spectroscopy [152]. In **Fig. 105** the spectra show that the SAM is stable until about 110°C and then it begins to decompose. Flash-heating experiments to study the time dependence used the arrangement shown in **Fig. 106a** [153,154]. Flash-heating pulses could heat the metal layer up to and beyond the melting point, which was 1064°C for Au. **Figure 106b** shows the structures of the of the SAMs we studied.

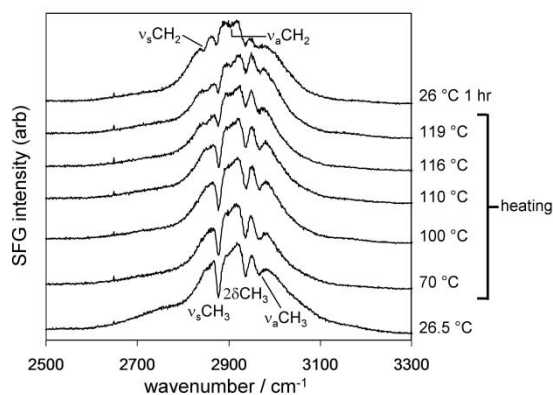


**Figure 105** Sum-frequency spectra of alkane monolayer on Au heated at indicated temperatures. The narrower dips are CH-stretch transitions. The SAM decomposes at about 120°C.

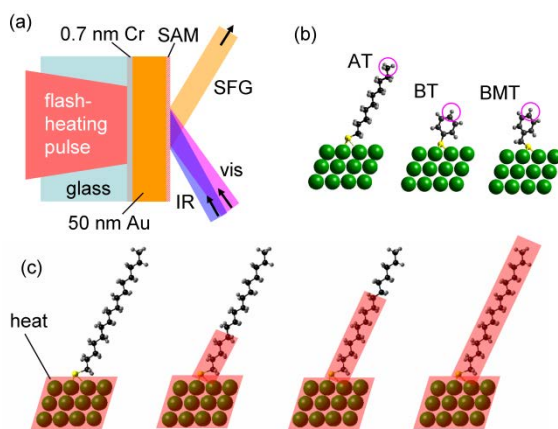


**Figure 106** (a) Schematic of ultrafast flash-heating apparatus. (b) Some self-assembled monolayers we studied. (c) Model for heat transfer from metal fuel to monolayer.

**Figure 107** is a block diagram for the time resolved SFG flash-heating measurements. **Figure 108** shows a result. There are characteristic changes in the spectrum of CH-stretch transitions of the SAM due to flash-heating to ~800°C. The temperature jump persisted for about 10  $\mu$ s and during this time, despite the very high temperatures, the SAMs remained attached to the metal surface. In other words SAMs bound to metal surfaces can survive much higher temperatures than usual if the duration of the high temperature is short. The unexpected stability of the SAM made it possible to investigate heat transfer from metal surfaces to SAMs in more detail. The idea is shown in **Fig. 106c**. The laser directly heats the metal surface but not the SAM. The SAM is heated only by heat conduction from the metal. As heat runs along the molecular chains, its effects can be seen by SFG when the heat reaches the methyl groups that terminate the SAM. In this way the first measurements of the speed of heat flow along molecular chains were made [154]. **Figure 109** shows that shorter chains with 8 carbon atoms heat up faster than longer

chains with 18 carbon atoms. Studies of the length dependence showed that heat did not diffuse along the chains, which is the usual behavior, but instead it flowed ballistically at a velocity of 1 km/s.

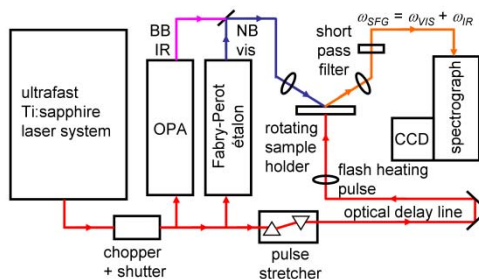


**Figure 107** Diagram of femtosecond laser apparatus used for flash-heating studies of monolayers on metal.

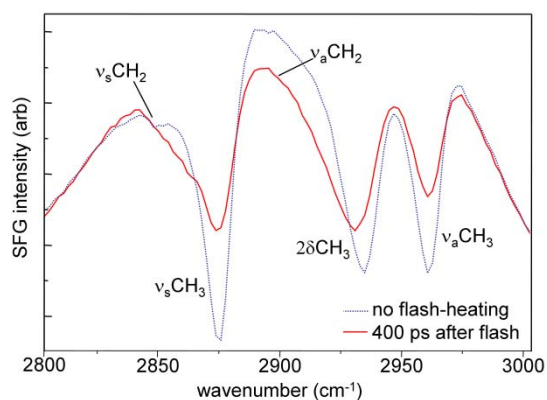


**Figure 108** Sum-frequency spectrum of alkane self-assembled monolayer after flash heating to 800°C. CH-stretch transitions are the dips with labels in the spectra.

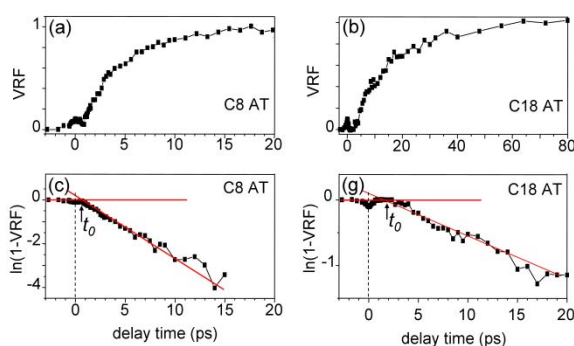


**Figure 109** Change in vibrational spectral intensity of the methyl groups at the ends of the self-assembled monolayers after flash-heating of the metal. The first real-time measurement of heat flow along a molecular chain.

SFG spectroscopy has emerged as the most powerful method to probe buried interfaces and as a consequence has soared in popularity in the last 5-10 years. One drawback of SFG that all nonlinear coherent spectroscopies have in common is the presence of a nonresonant background (NR) underneath

the vibrational transitions of interest. This NR background is particularly prominent when one surface is a metal. We have invented a method of greatly suppressing NR backgrounds based on the use of time-asymmetric time-delayed laser pulses [155]. In broadband SFG there is a fs duration IR pulse and a ps duration visible pulse. By making the visible pulse time asymmetric using an etalon, we can delay the visible pulse just beyond the IR pulse, as depicted in **Fig. 110**. Because the NR background undergoes optical dephasing much faster than resonant transitions, this method suppresses the NR background to a high degree. **Figure 111** shows some spectra obtained by this method. The superior signal to noise is evident when compared to **Fig. 108**, which are spectra of the same molecules, alkane SAMs on Au. This invention is an important advance in SFG technology. It is used routinely in our lab and has been adopted by several others, whose publications are just now appearing.

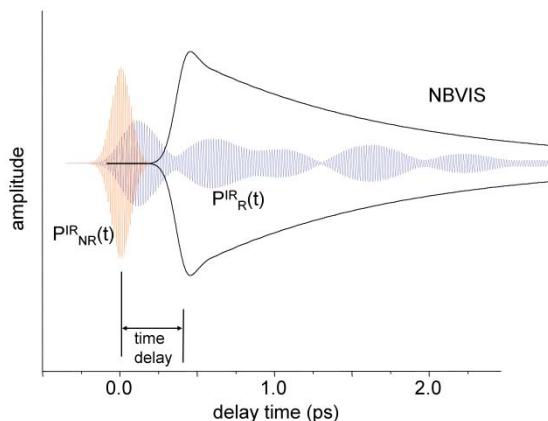


**Figure 110** Pulse sequence to suppress the nonresonant (NR) background in sum-frequency spectroscopy.

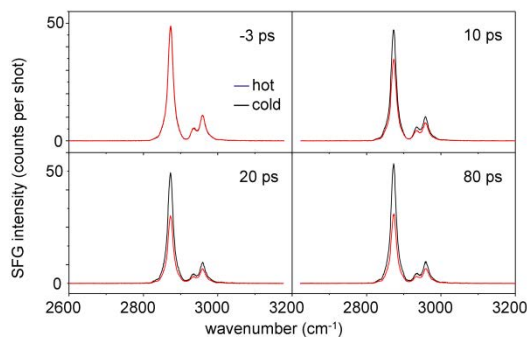


**Figure 111** Sum-frequency spectra of self-assembled monolayer with flash-heating using the non-resonant suppression method.

Our ultrafast emission apparatus uses a streak camera with <50 ps time resolution, as depicted in **Fig. 112** [145,146]. In our experiments we compared three NEEM samples, all based on 50 nm Al powder with native 2 nm oxide coating. One sample had a reactive Teflon oxidizer, one had unreactive poly(butadiene) (PB) binder and the third was Al only. The effects of flash-heating on the samples are shown in **Fig. 113**. **Figure 114** shows time-integrated emission spectra after flash-heating at fluences that increase from top to bottom and Al concentrations that increase from left to right. The Teflon samples emit considerably more light. There is no specific emission spectrum associated with the Al-Teflon reaction. In fact all samples emit the same general spectrum which shows the emitting species is Al. However the duration of emission is strongly affected by reaction. In the more reactive Al-Teflon samples, the emission burst lasts longer because heat is being created by chemistry. **Figure 115** shows the time dependence of the broad component of the emission burst. The duration of the emission burst is

clearly longer in Teflon than in PB. From these data we can estimate the time constant for ignition of flash-heated Al/Teflon as being in the 50 ps time range.

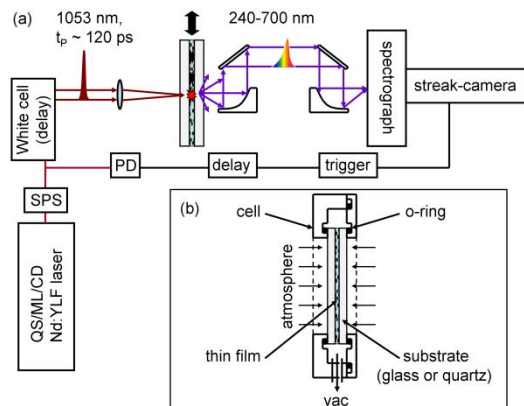


**Figure 112** Apparatus schematic for time-resolved emission measurements from flash-heated nanoenergetic materials.

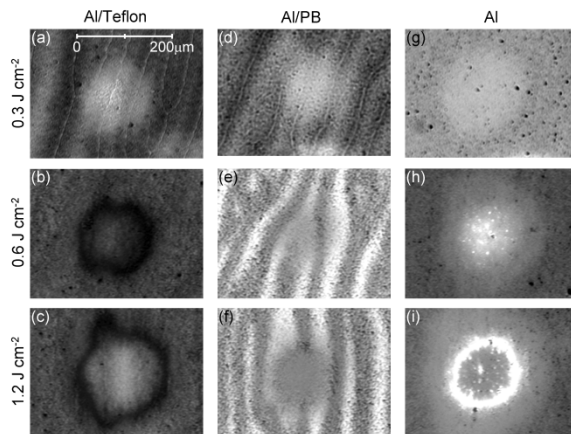


**Figure 113** Photos of nanoenergetic materials after a single flash-heating pulse at the indicated fluence. Al/PB is nano(Al) in unreactive poly-(butadiene) and Al is nano(Al) alone.

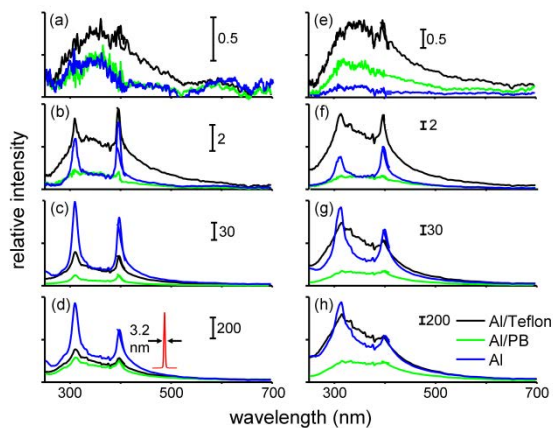


**Figure 114** Time-integrated emission after flash-heating of Al/Teflon, unreactive Al/PB and Al powder alone.

There have been a number of emission measurements from laser-heated Al and from explosions having an Al powder component [156,157]. All prior experiments have seen the gas-phase emission, which was dominated by Al and AlO. Our measurements see the condensed phase emission. The condensed phase is emphasized by confining the sample between heavy windows (**Fig. 112**) and by the short time scale of the measurement. So we have shown what the condensed phase emission looks like (**Fig. 114**), its origin (Al) and how its duration can be used to learn the time constant for energy generating reactions. We are currently finishing up closely related work using B rather than Al.

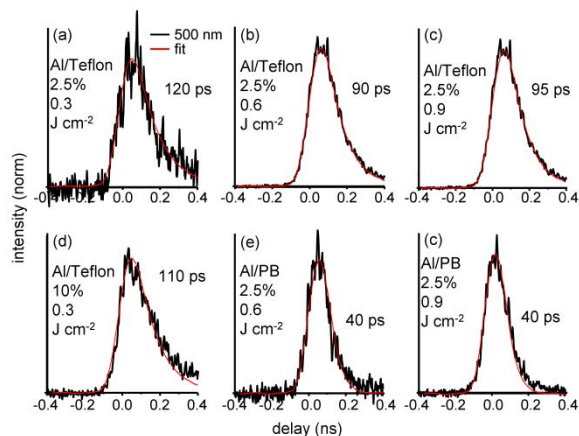


**Figure 115** Ultrafast emission of Al/Teflon after flash-heating compared to unreactive Al/PB. The longer-duration emission in Al/Teflon gives time constants for ignition.

In the fifth year of the project, we were awarded plus-up funding to develop a new capability. We decided to develop the capability of shock-initiation of NEEM based on laser-driven flyer plates. The concept is depicted in **Fig. 116**. A Nd:YAG laser passes through beam shaping optics to create a flat-top beam. It hits a target consisting of metal foil on glass [158,159]. In the present system, a 0.4 mm diameter flyer 25  $\mu\text{m}$  thick is launched by 50 mJ pulses to speeds up to 2 km/s. The flyer travels 100  $\mu\text{m}$  and impact a window that can be coated with NEEM. The impact emission can be studied with the streak camera as in **Figs. 114** and **115**. A novel fiberoptic ultrafast 8 GHz laser displacement interferometer (DISAR) was built using telecommunications components. Its arrangement is depicted in **Fig. 117**. It can closely track velocity histories for speeds up to 5 km/s. **Figure 118** shows a photo of the target, a flyer plate captured post launch, the glass witness plate impact site, an interferogram and velocity history, and the time dependence of the impact emission. The impact emission with only a glass window for target (no NEEM) originates from air shocked at the flyer plate window collision. More emission is observed from Ar, as shown in **Fig. 119**. A larger laser that will accelerate heavier plates to higher velocities has been ordered and will be delivered in Fall 2010.

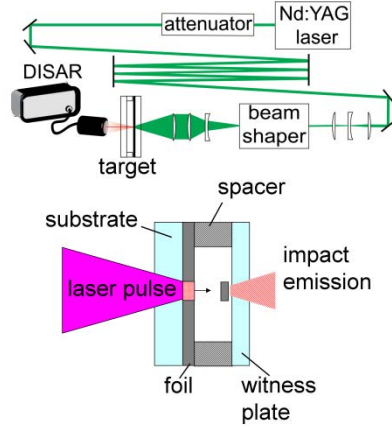


**Figure 116** Schematic diagram for laser-launched flyer plates and target array.

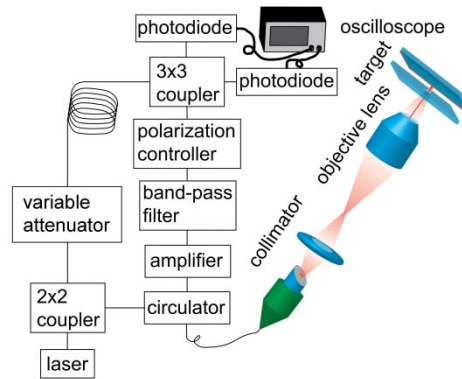


**Figure 117** Schematic of ultrafast fiber interferometer to measure the flight of laser-launched flyer plates.

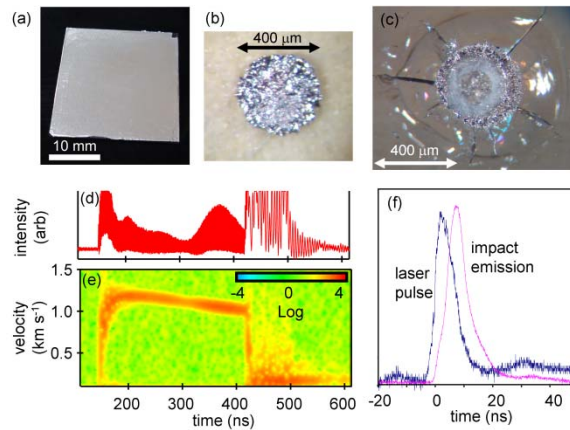


**Figure 118** (a) Target array for laser-launched flyer plates. (b) (c) recovered flyer plate and witness plate after launch. (d) Interferogram detailing launch, flight and impact at a velocity of 1.2 km/s. (f) Time dependence of emission due to impact with witness plate.

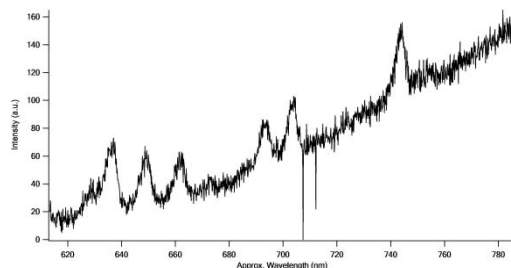


**Figure 119** Emission from Ar compressed between 1.8 km/s flyer plate and witness plate.

In summary, the **Dlott group** has developed several unique diagnostic capabilities and used them to study the fundamental mechanisms that underlie NEEM dynamic performance. The **Dlott group** obtained ultrafast images of reacting NEEM, measured initiation with ultrafast IR and ignition with ultrafast emission. The **Dlott group** studied the depassivation process using NEEM with self-assembled molecular monolayers for passivation. Finally the **Dlott group** developed a laser launch facility to detect the emission from impact-initiated NEEM.

### II.3.2 Combustion Dynamics of Nano Energetic Materials

The goal of the MURI effort led by **Yetter** and his group was to study the reactivity and combustion characteristics of nano engineered energetic materials (NEEMs). The effort was divided into examining the combustion characteristics of nanoparticulate fuels or NEEMs when reacting with different forms of oxidizers (gaseous, liquid, and solid). As part of this effort, the fabrication of nano-engineered energetic materials via self assembly of nano particulate ingredients into organized structures at the microscale was studied. As a result of plus-up funds in the final year of the effort, the combustion characteristics of cold-spray processed intermetallic materials were also studied. The research effort sought a fundamental understanding of the relationship between the structures of nano-engineered energetic materials and their reactive and mechanical behavior, particularly with regard to sensitivity, ignition, burning characteristics, and optimum loading density, thus enabling design optimization of NEEMs. During the program, close collaborations were established with Dr. Steve Son at Purdue University, and Dr. Tim Foley, Dr. Bryce Tappan, and Dr. Blaine Asay at LANL.

The approach was to use a series of combustion diagnostic techniques including: constant pressure and constant volume combustion experiments to determine reaction rates, propagation speeds, and chemical efficiency of nanoengineered energetic materials (NEEMs), high speed photography, emission and infrared spectroscopy, and gas chromatography to develop detailed understanding of the physical and chemical mechanisms of reacting NEEMs, and thermogravimetric analysis and differential scanning calorimetry to study the thermal behavior of NEEMs. A laser induced breakdown spectroscopy system (LIBS) was developed to analyze the elemental composition of reacting NEEMs. Electrostatic self-assembly was utilized to create self-assembled nanothermite microspheres (SANTMs) from a bottom-up approach.

#### II.3.2.1 Gaseous Oxidizers

Research was initiated with gaseous oxidizers in which the reaction was diffusion controlled. In addition to the important science attained on combustion mechanisms, these systems were chosen to study in order to develop the proper handling and safety protocols with nano energetic materials prior to researching premixed systems.

An understanding of the reactive and transport mechanisms in energetic systems with nano-particulate ingredients is important to deflagration and detonation phenomena of energetic materials. The

group investigated reaction front propagation during the combustion of heterogeneous condensed phase systems based on nano-aluminum in various gaseous oxidizers (Fig. 120). These experiments involved flame spread across a bed of nAl and considered the roles of diffusion, convection, and reaction chemistry on the propagation mechanism. In air, the complex burning process of nano-aluminum exhibited a rich but controllable pattern. The combustion front in a quasi-two-dimensional geometry exhibits directional fingering instability with two length scales that are determined differently – the finger width and the finger spacing. The non-dimensional control parameter is the Péclet number (Pe), which measured the relative importance of molecular advection and diffusion. Such phenomena have been observed in the flame propagation through other condensed phase media [160-162].

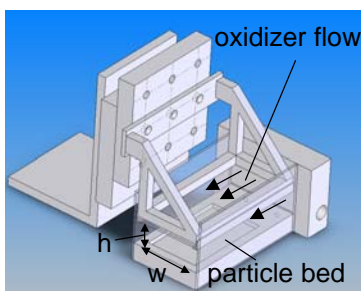


**Figure 120** Schematic representation of the experimental setup for nano aluminum propagation studies.

Three consecutive modes of flame propagation were observed over a bed of nano-aluminum burning with a counter-flowing oxidizer of 20% oxygen and 80% argon by volume, each displaying significantly different characteristics (Fig. 121). The first mode consisted of a rapid front propagating down the length of the bed over the surface. The second mode was a slower front propagating in the opposite direction as the first, with reaction into the bed. The third mode consisted of a cellular flame structure with propagation throughout the bed.

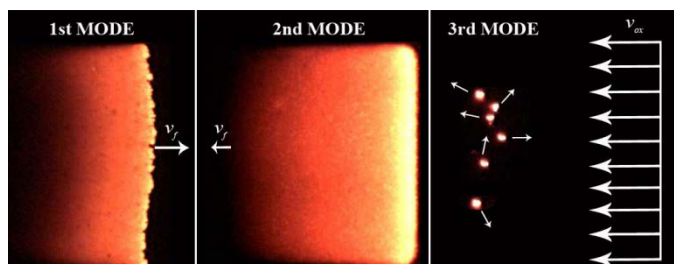


**Figure 121** Three consecutive waves in baseline run with velocity ( $v_{ox}$ ) of 20 cm/s and oxygen concentration (% $O_2$ ) of 20%.

The first mode of propagation was examined within the critical Rayleigh and Peclet number regime where three-dimensional buoyancy effects were hindered and the fingering thermal-diffusive instability occurred. Fingering flame spread was observed and characterized for various Peclet numbers, top plate heights and particle sizes to gain a better understanding of the reaction mechanism associated with the combustion of nano-particles in close contact (Fig. 122). Results indicate that the first mode of flame propagation over a bed of nano-aluminum has spread rates an order of magnitude greater than that of cellulose fuels. This mode of propagation appears to be associated with the low temperature ignition of nAl particles, and the structural change of the nearly uniform amorphous oxide layer to a new alumina polymorph with a non-uniform oxide layer. Furthermore, faster propagation speeds occur with smaller particles because of their increased specific surface area. The widths of the fingers grow and more of the surface is burned with increasing particle size due to the longer time scale available for lateral growth.

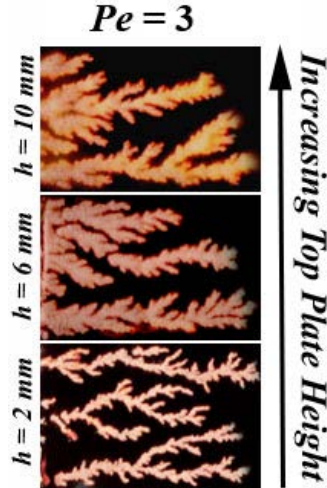


**Figure 122** Photographs of fingering instability for nAl combustion reacting in air that show the integrated flame histories of beds of 38 nm nAl and a Peclet number ( $Pe$ ) of 3.

For conditions where the critical Peclet number was exceeded, a flat flame front was present with no fingering instabilities. Under these conditions, the velocity of the oxidizer, thickness of the aluminum bed, diameter of the nano-particles, and oxygen content in the oxidizer were varied to give insight into the mechanisms associated with nano-aluminum combustion. Results indicated that the velocity of the oxidizer increased the flame length and light intensity, but had no effect on the spread rate of the flame for the first wave. The thickness of the bed had no effect on any property of the first wave, but with the thinnest bed, no flame front for the second mode was present underneath. The spread rate of the first wave varied inversely squared with the diameter of the particles (**Fig. 123**). The oxygen content in the oxidizer obeyed a power law dependence for both the spread rate of the first wave and the downward velocity of the second wave (**Fig. 123**). The third wave occurred for most conditions and consisted of cellular flames traveling in all three dimensions through the bed.

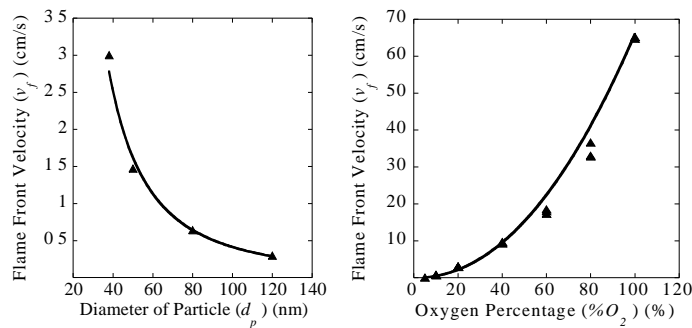


**Figure 123** Flame front velocity ( $v_f$ ) vs. diameter of particle ( $d_p$ ). Flame front velocity ( $v_f$ ) vs. oxygen percentage ( $\%O_2$ ) in oxidizer

In summary, the flame spread experiments have demonstrated similar yet new characteristics about the combustion of nano particles in relation to other fuels, e.g., polymers (binders). It is also important to realize that these propagating reaction fronts do not occur with micron particles. The nanoscale aluminum (nAl) powders achieved relatively fast counter-flow flame spread rates compared to typical fuels such as Poly(methyl methacrylate) or cellulose at similar conditions. Their fast speed allowed for the dominant forward heat transfer mechanism to be through the solid fuel at higher applied oxidizer velocities. Because of the porosity of the nAl powder, the gaseous oxidizer diffuses into the bed and reactions within the solid phase become important. Using an energy balance applied to only the solid

phase, an analytical model was also developed which predicts the experiments for flame spread over a nAl bed. Moreover, an explanation for fingering phenomenon was established based on the effective Lewis and Damko" hler numbers. This allowed for an explanation of why flame spread over a bed of nAl will demonstrate fingering instability in a quiescent, 1 g environment without a top plate to hinder buoyant flows. Further details can be found in Refs. [163,164].

### II.3.2.2 Liquid Oxidizers

As an initial examination of nano particulate fuels in quasi-premixed systems, liquid oxidizers premixed with the fuels were studied. Combustion experiments on mixtures of nano-aluminum (nAl) and liquid water were conducted to investigate the effects of pressure, mixture ratio, particle size, and oxide layer thickness on the burning characteristics. The results have practical importance to underwater propulsion, underwater explosives, and solid hydrogen storage for hypersonic air-breathing propulsion and rocket propulsion. The results were also important towards obtaining fundamental understanding of the combustion processes of nAl particles and the resulting flame structure of a simple two-component heterogeneous system. The fundamentals learned from this system were applied to other more complex nanoenergetic systems such as metastable intermolecular composite systems (MICs), where the oxidizer is a solid metal oxide, generally in a particulate form just as the metal (e.g., nAl and  $\text{MoO}_3$ ).

The linear burning rates for a stoichiometric mixture of nAl and liquid water as a function of pressure are shown in **Fig. 124**. For pressures below 3MPa, a pressure exponent of 0.47 in the burning rate formula was attained, suggesting an overall-first order chemical process. The burning rates of the nAl-liquid water system are also observed to be considerably faster than other energetic oxidizers. Above 3 MPa, the burning rate was observed to be independent of pressure. The mass-burning rate per unit area was found to increase from  $\sim 1.0$  to  $5.8 \text{ g/cm}^2\text{-s}$  for a variation in equivalence ratio from 0.5 to 1.25. The burning rate was also found to vary inversely to particle diameter, increasing by 157% when the particle diameter was decreased from 130 to 50 nm at  $\phi=1.0$ . The efficiency of the reaction as a function of pressure for a stoichiometric mixture is shown in **Fig. 125** and ranged from approximately 90-95%. The high rates of this reaction are extremely surprising, particularly since the initial step is expected to be a heterogeneous reaction between water vapor and the aluminum surface (or interface between the aluminum and the oxide shell).

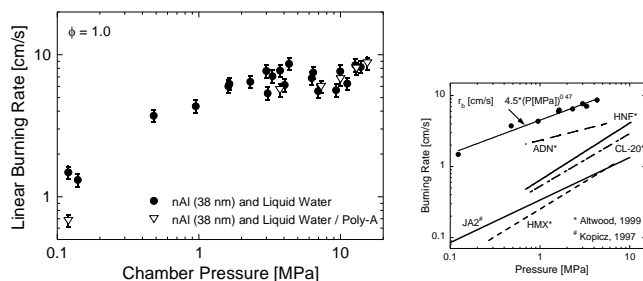


**Figure 124** Burning rates of the Al- liquid water system as a function of pressure.

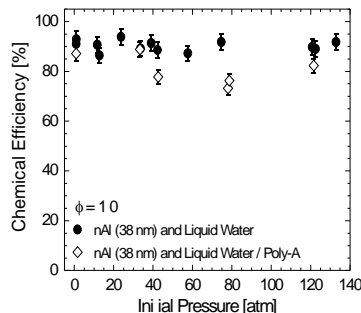


**Figure 125** Chemical efficiency of the Al-liquid water reaction.

In addition to pure water, mixtures of nAl with water and hydrogen peroxide and with nitromethane were also studied. Steady-state burning rates were obtained at room temperature using a windowed pressure vessel over an initial pressure range of 0.24 to 12.4 MPa in an argon atmosphere, using average nAl particle diameters of 38 nm,  $\phi$  from 0.5 to 1.3, and  $\text{H}_2\text{O}_2$  concentrations between 0 and 32% by mass. At a nominal pressure of 3.65 MPa, under stoichiometric conditions, mass-burning rates per unit area ranged between  $6.93 \text{ g/cm}^2\text{-s}$  (0%  $\text{H}_2\text{O}_2$ ) and  $37.04 \text{ g/cm}^2\text{-s}$  (32%  $\text{H}_2\text{O}_2$ ), which corresponded to linear burning rates of 9.58 and 58.2 cm/s, respectively. An example of the deflagration process is illustrated in Fig. 126. The effect of  $\text{H}_2\text{O}_2$  on the burning rates is shown in Fig. 127. Burning rate pressure exponents at room temperature of 0.44 and 0.38 were found for stoichiometric mixtures containing 10% and 25%  $\text{H}_2\text{O}_2$ , respectively, up to 5 MPa. Burning rates are reduced above  $\sim 5$  MPa due to voids in the reactant mixture filled with argon gas. Mass burning rates were not measured above  $\sim 32\%$   $\text{H}_2\text{O}_2$  due to an anomalous burning phenomena, which caused an over-pressurization within the quartz sample holder leading to tube rupture. High-speed videography displayed fingering or jetting ahead of the normal flame front. Localized pressure measurements were taken along the sample length, determining that the combustion process proceeded as a normal deflagration prior to tube rupture, without significant pressure buildup within the tube. In addition to burning rates, chemical efficiencies of the combustion reaction were determined to be within approximately 10% of theoretical maximum at all conditions studied.

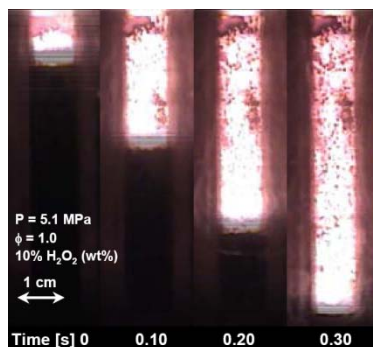


**Figure 126** Captured images of the normal deflagration process of a nAl- $\text{H}_2\text{O}$ - $\text{H}_2\text{O}_2$  mixture.

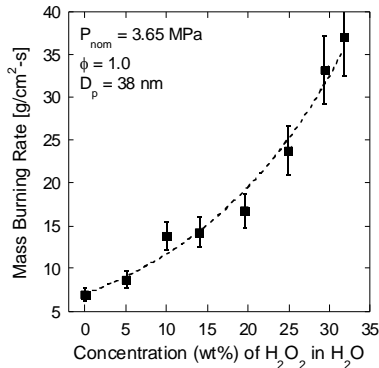


**Figure 127** Effect of H<sub>2</sub>O<sub>2</sub> concentration on the mass burning rate per unit area of nAl/H<sub>2</sub>O mixtures.

Similar to the studies in which nAl was mixed with H<sub>2</sub>O and H<sub>2</sub>O<sub>2</sub>, the effects of aluminum nanoparticle addition to nitromethane (NM) were also studied in terms of overall mixture burning rate using an optical pressure vessel up to 14.2 MPa. Nitromethane was gelled using fumed silica (Cab-O-Sil), as well as by the nanoaluminum (nAl) particles themselves. Use of the nanoscale metallic particles slightly increased burning rates compared to larger diameter particles, however distinct increases in burning rates were found when Cab-O-Sil was removed and replaced with more energetic aluminum nanoparticles, whose high surface area allowed them to act as the gallant (**Fig. 128**). Burning rates of 2.34 cm/s were seen at 14.1 MPa and 12.5% aluminum loading using 38-nm particles. Using the same nAl particles, 4% aluminum and 3% Cab-O-Sil loading, burning rates of 0.88 cm/s were obtained at approximately the same pressure. In both cases, mixture consistencies were roughly the same. Larger, 80-nm aluminum particles were also used in conjunction with Cab-O-Sil gellant, yielding a linear burning rate of 0.65 cm/s at 14.2 MPa (4% Al-3% Cab-O-Sil). In all mixtures, burning rate pressure exponents less than the pure nitromethane case were observed with fumed silica addition, while the exponents were increased when using nAl as the gellant.

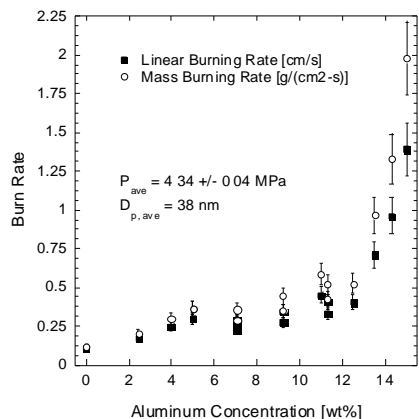


**Figure 128** Linear and mass burning rates of mixtures of 38-nm aluminum particles and nitromethane as a function of aluminum loading.

The heterogeneous interaction between nitromethane (NM) and particles of nanoscale aluminum (38 and 80 nm diameter) and fumed silica were also examined in terms of detonation characteristics. Failure diameters of mixture detonations were found to vary significantly as a function of 38 nm aluminum particle loading, reducing more than 50% from that of neat nitromethane with 12.5 % aluminum loading. Failure diameter results indicated a relative minimum with respect to particle

separation (% loading) which was not observed in other heterogeneous mixtures. Additional details on nano fuels (including graphene) with liquid oxidizers can be found in Refs. [165-171].

### II.3.2.3 Solid Oxidizers

In the present research, a series of experimental configurations were produced to study the combustion dynamics of nanothermites including a high pressure optical closed combustion chamber, an open-ended acrylic tube experiment (ID = 3.175 mm), and micron-sized (submillimeter) channels to measure propagation speeds and transient pressures and temperatures. The initial design of the first two of these systems was similar to those of **Son** (now at Purdue) and his former colleagues at LANL.

Microscale combustion is of interest in small volume energy demanding systems, such as power supplies, actuation, ignition, and propulsion. Energetic materials can have high burning rates that make them advantageous, especially for microscale applications where the rate of energy release is important or where air is not available as an oxidizer. In this study we examine the combustion of mixtures of nanoscale aluminum with molybdenum trioxide in microscale channels. Nanoscale composites can have very high burning rates that are much higher than typical materials. Quartz and acrylic tubes are used, as well as steel channels (**Fig. 129**). The optimum mixture ratio for propagation rate is found to be aluminum-rich (**Fig. 130**). The results from equilibrium calculations suggest that the propagation is dominated by a convective process where hot liquid molybdenum and product gases are propelled forward heating. Furthermore, this is the first time the dependence of propagation rate on tube diameter has been measured for this class of materials. The propagation rate was found to vary inversely with  $1/d$  (**Fig. 131**). The propagation remains high in tubes or channels with dimensions down to the scale of 100  $\mu\text{m}$ , which makes these materials applicable to micro combustion applications. Classical energetic material would have difficulty igniting and propagating in these small tubes and slots. These results show the nanoscale thermites can ignite and propagate well in microchannels. Consequently, these materials may have applications in various microenergetic (or micropropyrotecnic) applications.

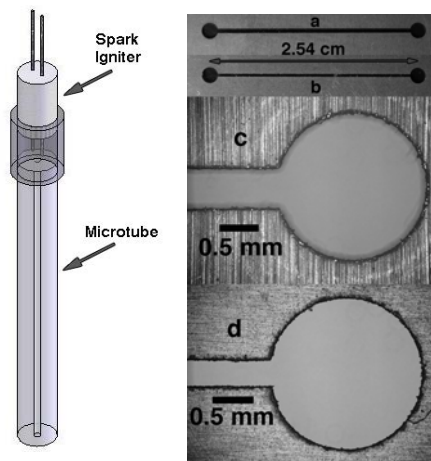


**Figure 129** Schematic of tube (left) and slot (right) experiments. The largest tube used was acrylic. The smaller tubes are borosilicate glass thick walled capillary tubes. On the right are examples of two metal slot sizes showing the entire channel and the reservoir at the ends of the channels.

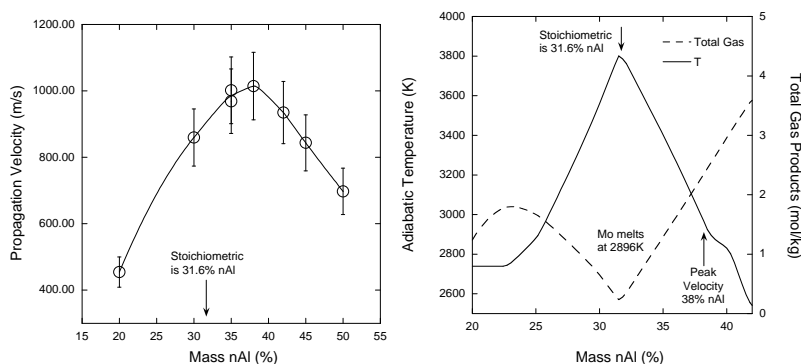


**Figure 130** Part a) is the measured propagation rate as a function of mass fraction of nAl (%). In part b), calculated adiabatic temperature and total gas products are shown.

The effect of stoichiometry on the combustion behavior of the nanoscale aluminum molybdenum trioxide (nAl/MoO<sub>3</sub>) thermite was studied in collaboration with Steve Son in a burn tube experiment by characterizing the propagation velocity and pressure output of the reaction. Changing the stoichiometry affects the combustion through changes in the product temperature, phase, and composition. The mixture ratios of the composites were varied over an extremely wide range (5% nAl (95% MoO<sub>3</sub>)–90% nAl (10% MoO<sub>3</sub>)). Results revealed three separate combustion regimes: a steady high speed propagation (~100–1000 m/s) from approximately 10% to 65% nAl, an oscillating and accelerating wave near 70% nAl, and a steady-slow speed propagation (~0.1–1 m/s) from approximately 75% to 85% nAl. Propagation was observed to fail both <10% nAl and >85% nAl. The instrumented tube tests revealed peak pressures over 8 MPa near stoichiometric conditions in the steady high speed propagation region, no measurable pressure rise at low speed propagation, and building pressures for accelerating waves. The results suggest the propagation mode to be a supersonic convective wave for near stoichiometric mixtures and a conductive deflagration for extremely fuel-rich mixtures.

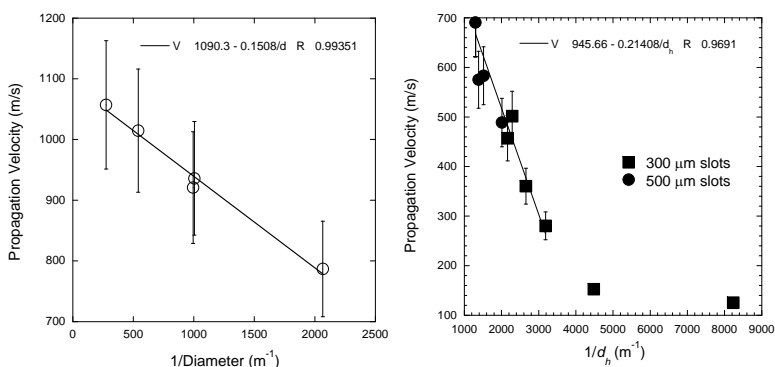


**Figure 131** Propagation velocity as a function of inverse diameter. Propagation velocity as a function of the inverse of hydraulic diameter.

One aspect of nano thermite materials that is not well understood is the mode by which energy is transferred ahead of the reaction front to sustain the propagation, or the propagation mechanism. Several propagation mechanisms may be considered when examining the reaction propagation: radiation, conduction, acoustics, compaction, and convection [172]. Solid energetic materials are controlled by conduction, when deflagrating, which can be enhanced by radiation [173,174]. Acoustics (shock

processes) and compaction become important when a reaction produces pressures sufficient to induce volume changes in the material. This occurs during detonation or the transition to detonation. Convection is possible if the material is porous and hot interstitial gas, reactants, or products can be propelled forward through the material by high reaction zone pressures [175,176]. Nano-scale thermites exhibit combustion velocities ( $\sim 1000$  m/s) approximately four orders of magnitude greater than that of the micron-scale thermites ( $\sim 0.1$  m/s) [177,178]. The drastic increase in velocity is due to the extremely small time scales associated with mass diffusion and reaction rates brought about by the small particle sizes. This does not allow time for any heat loss or depressurization within the reaction zone leading to high pressure, hot gases that can be propelled ahead of the front. Therefore, these systems are thought to be controlled by a convective propagation mechanism [172].

Because the controlling propagation mechanism is convection, both gas production and temperature, should be important factors when optimizing for the fastest burning rate. Sanders *et al.* [179] observed that for four different metal oxides ( $\text{Bi}_2\text{O}_3$ ,  $\text{MoO}_3$ ,  $\text{CuO}$ , and  $\text{WO}_3$ ), the burning rate on a burn tray was maximized for the mixture ratio that also produced the highest peak pressure in the pressure cell. Moreover, equilibrium calculations showed that all of the optimum stoichiometric ratios were related to the gas production and phase of the products. This optimum stoichiometry was found to be fuel-rich ( $\sim 1.4$ ) for all of the metal oxides except copper oxide, which optimized at an equivalence ratio close to 1. This difference was attributed to the fact that one of the main products, copper, has a relatively high boiling point of 2835 K and needed the high temperature of a stoichiometric reaction to keep it in the gas phase. Similar to varying the stoichiometry, adding a diluent into the system will decrease the overall temperature of the reaction. Adding the end product as a diluent, particularly  $\text{Al}_2\text{O}_3$ , was a common practice in micron-scale thermite SHS in order to reduce combustion temperatures and change the mechanical properties of the products [180,181]. Moreover, the decrease in combustion temperature gave way to slower reaction velocities and decreasing amounts of gaseous species [178].

In the present work, the effects of dilution by alumina nano-particles on the combustion properties of the Al/CuO nano-scale thermite were investigated. Three types of experiments were performed: the constant volume pressure cell, the unconfined burn tray, and the instrumented burn tube. The nAl had a nominal particle size of 80 nm with 88% active aluminum and the copper oxide particles were assumed to have cylindrical geometry with dimensions of 21 nm  $\times$  100 nm. Mixing of reactants was achieved by sonication of the reactants in hexane. Examination of the dried mixture with SEM and TEM indicated that inhomogeneities remained in the mixedness of the reactants, emphasizing the importance of the self-assembly techniques described above. The results showed that the addition of  $\text{Al}_2\text{O}_3$  decreased the pressure output and reaction velocity in all three experiments. Burn tube measurements showed three reaction velocity regimes (**Fig. 132**): constant velocity observed when 0% (633 m/s) and 5% (570 m/s) of the total weight is  $\text{Al}_2\text{O}_3$ , constant acceleration observed at 10% (146 m/s to 544 m/s over a distance of 6 cm) and 15% (69 m/s to 112 m/s over a distance of 6 cm)  $\text{Al}_2\text{O}_3$ , and an unstable, spinning spiraling combustion wave at 20%  $\text{Al}_2\text{O}_3$ . The pressure measurements correlated to these three regimes showing a drop-off in peak pressure as  $\text{Al}_2\text{O}_3$  was added to the system, with relatively no pressure increase observed when 20% of the total weight was  $\text{Al}_2\text{O}_3$ . Equilibrium calculations showed that the addition of  $\text{Al}_2\text{O}_3$  to an Al/CuO mixture lowered the flame temperature, reducing the amount of combustion products in the gas phase, thus, hindering the presumed primary mechanism mode of forward heat transfer, convection. The measured pressure at the flame front was in agreement with equilibrium calculations when a constant volume reaction was assumed (**Fig. 133**).

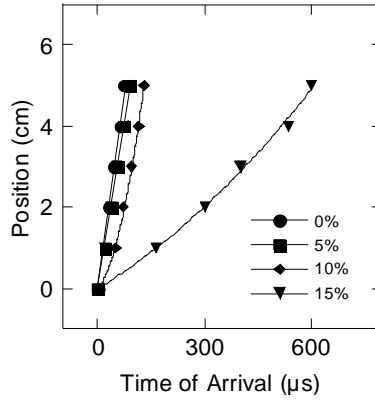


**Figure 132** Typical position versus time graphs for reaction waves in the burn tube with various weight percentages of Al<sub>2</sub>O<sub>3</sub>.

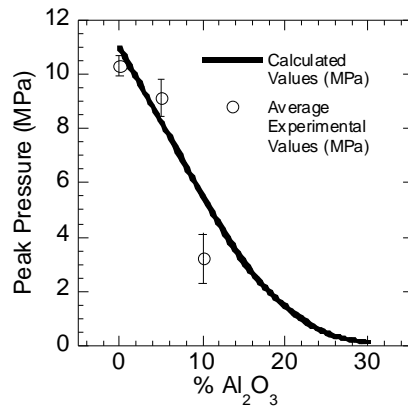


**Figure 133** Comparison of average experimental peak pressure values in the burn tube to the calculations for the peak pressure with added Al<sub>2</sub>O<sub>3</sub> percentage for constant volume explosion.

In order to further understand the propagation mechanism for the Al/CuO nanoscale system, experiments were conducted as a function of initial pressure. The combustion of the nanothermite was examined at various pressures in an argon atmosphere. The results of these experiments revealed an increase in propagation speed when increasing the ambient pressure from 100 to 180 psig, followed by a significant drop-off in propagation speed at higher pressures (Fig. 134). At atmospheric pressure in air, the propagation speed was approximately 900 m/s. The trends appear to result from a trade-off between increasing temperature and decreasing gas-pressure at the reaction front with the increase in system pressure. These results are generally consistent with the behavior of micron-sized thermites [178], although the propagation speeds are considerably higher.

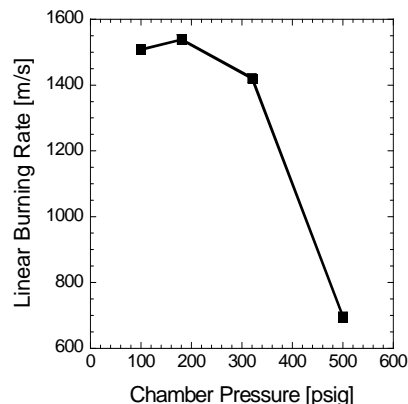


**Figure 134** Linear burning rate versus chamber pressure for nanoscale Al/CuO.

As discussed earlier in this report, thermite reactions with nanoscale particles have attracted much study due to their high flame temperatures and combustion velocities. The mechanism by which the reaction propagates is not well understood. The reaction temperature, the heating rate, and the reaction zone thickness are critical parameters to understanding the mechanism. In the present effort, measurements of the reaction temperature for the Al/CuO, Al/MoO<sub>3</sub>, and Al/Fe<sub>2</sub>O<sub>3</sub> nano-thermite systems were made using multi-wavelength pyrometry for two experimental configurations. In one experiment, the radiative emission from the reaction of a small, unconfined pile (~10 mg) of reacting nano-thermite was collected over a 50 ms integration time and the temperature is measured. In a second experiment, the radiative emission was collected from a single spot, with a diameter of 1.5 mm, on a transparent tube filled with the nano-thermite as the combustion wave passed and the spectrum was temporally resolved using a streak tube and detected using an intensified CCD camera. Temperature traces from these experiments showed a temperature ramping period followed by a plateau in temperature. For Al/CuO, the average temperature from the unconfined pile experiment was 2390±150 K, and the average plateau temperature for the temporally resolved measurements was approximately 2250±100 K. For Al/MoO<sub>3</sub>, the unconfined pile experiment yielded an average temperature of 2150±100 K, and the average plateau temperature was the same. The temperature measured from the Al/Fe<sub>2</sub>O<sub>3</sub> unconfined pile experiment was 1735±50 K. The measured temperatures suggest that the gases generated during the reactions are primarily from the decomposition or vaporization of the various metal oxides. Furthermore, for Al/CuO and Al/MoO<sub>3</sub>, which can be classified as ‘fast’ nano-thermites, it was shown that the length scale associated with the temperature rise is much longer than classical conduction driven reactions.

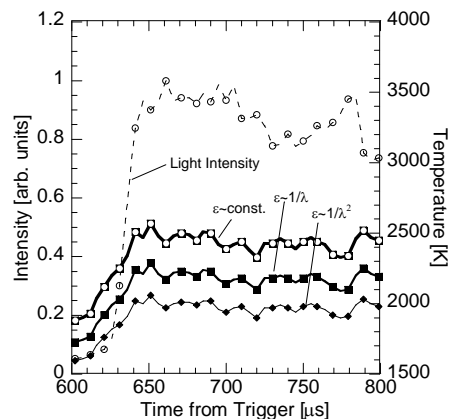


**Figure 135** Intensity and temperature versus time results for Al/CuO ( $\Phi=1.1$ ) nano-thermite burn tube experiment.

**Figure 135** shows the normalized intensity and temperature versus time for the data taken from a sample spot of an Al/CuO experiment. For these experiments, the spectrometer was set so that light at a wavelength of 700 nm impinged on the center of the intensified CCD detector, giving a spectral range of 590-810 nm. The temperature curves on this plot represent the temperature calculated by three different methods: gray body assumption (constant  $\epsilon$ ), assuming  $\epsilon \sim \lambda^{-1}$ , and assuming  $\epsilon \sim \lambda^{-2}$ . The first method is the simplest and most often used, while the second method is more appropriate for measurements on the products expected in these reactions, and the third method corresponds to that used by Goroshin *et al.* in [182] for emission from nano-particles. The temperature curves show the temperature ramping up to a level at which it plateaus. For the  $\epsilon \sim 1/\lambda$  temperature curve, the average plateau temperature was approximately  $2250 \pm 100$  K for Al/CuO, and  $2150 \pm 100$  K for Al/MoO<sub>3</sub>. Assuming a kinetically controlled reaction with Arrhenius kinetics, the highest rate of chemical energy release from the reaction is at the high temperatures. Therefore, the bulk of reactions can be assumed to take place over the measurable temperature range, approximately 1700-2250 K. The time scale for this temperature rise is approximately 50  $\mu$ s and the thickness of this zone is 40 mm (using a reaction front speed of 800 m/s). This suggests that, unlike a gas-phase hydrocarbon flame where the reaction zone thickness is typically less than a millimeter, the apparent reaction zone thickness for thermite reactions can be quite large. **Figure 136** is a sequence of images from an Al/CuO experiment, further illustrating this point. The dotted line represents the radiative emission sampling spot. Although in the final frame, the reaction has propagated all the way to the bottom of the tube, the temperature is still rising at the sampling point, suggesting that reactions are still taking place and are still releasing energy. This result suggests that the rate of propagation is not necessarily tied to the time scale for the reaction to attain its highest temperature or completion. For Al/CuO, the measured reaction temperatures appear to be very close to the melting temperature of bulk Al<sub>2</sub>O<sub>3</sub> (2345 K), but lower than the boiling point of Al (2792 K) and Cu (2835 K). This, along with the absence of AlO vibrational emission in the spectra, suggests that reactions take place in the condensed phase. However, the experimental measurements of dynamic pressure found in the literature show pressure overshoots on the order of 100 atm, suggesting that gaseous species are formed as the reaction evolves which contribute to the rise in pressure. In the case of Al/CuO, the gaseous species produced are most likely resulting from the decomposition of CuO. TGA/DSC results by Dean *et al.* [183] show that CuO undergoes a mass loss of 9.3% at approximately 1290 K. This corresponds to the conversion to copper (II) oxide (Cu<sub>2</sub>O) and the release of gaseous oxygen as in Eq. 5.

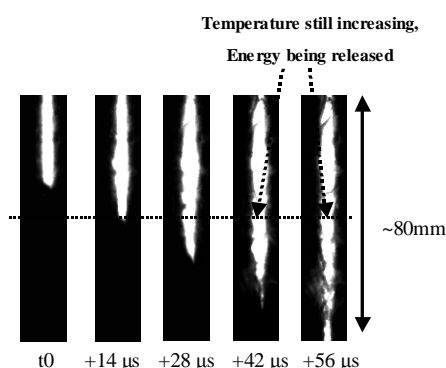
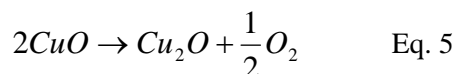


**Figure 136** High speed camera images for Al/CuO ( $\Phi=1.1$ ) nano-thermite burn tube experiment, illustrating the thickness of the temperature rise.

This decomposition was investigated using the CHEETAH 4.0 [184] equilibrium code with the JCZS product library developed by Hobbs and Baer [185]. **Figure 137** shows the equilibrium composition at a pressure of 1 atm for a range of temperatures, and again illustrates the release of O<sub>2</sub> gas from the decomposition.

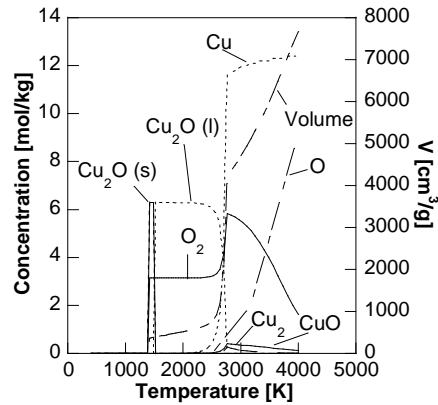


**Figure 137** Equilibrium species concentration and gas generation for CuO decomposition assuming constant pressure (1 atm) and temperature conditions.

Results from combustion experiments, in which the fuel and oxidizer particle sizes of Al/CuO and Al/MoO<sub>3</sub> thermites were varied between the nanometer and micrometer scale, are presented to gain further insight into the factors governing their rate of propagation. The experiments were performed with thermite mixtures loosely packed in an instrumented burn tube. Critical properties, including linear propagation rates, dynamic pressure, and spectral emission, were measured and compared to determine if the scale of one constituent had more influence over the rate of propagation than the other. It was found that, although nano-fuel/nano-oxidizer composites propagated the fastest for both the Al/CuO and Al/MoO<sub>3</sub> thermites, composites containing micron-aluminum and a nano-scale oxidizer propagated significantly faster than a composite of nano-aluminum and a micron-scale oxidizer (**Fig. 138**). The impact of nano-scale oxidizer versus nano-scale Al is twofold. Firstly, mixtures containing nano-aluminum have a greater mass percentage of Al<sub>2</sub>O<sub>3</sub>, which reduces reaction temperatures and propagation rates. Secondly, reactions in porous nano-thermites propagate through a convective mechanism; with heat transfer being driven by flow induced by large pressure gradients. Mixtures containing nano-scale oxidizer particles show faster pressurization rates. Because the majority of gas generation is due to the decomposition or vaporization of the oxide in these reactions, and oxide particles on the nano-scale have shorter heat up times and smaller length scales for gas diffusion than micron particles, convective burning is greatly enhanced with the nano-scale oxidizer.

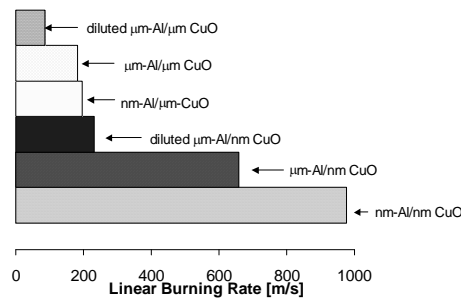


**Figure 138** Linear burning rates of Al/CuO thermites ( $\phi=1.1$ ).

Representative pressure traces taken from the Al/CuO experiments are given in **Figs. 139a–139d**. Each line on the graph represents the response of one pressure transducer located at a different side-wall position down the length of the tube. The pressure overshoot measured as the combustion wave passes depends on several factors. If the reaction front is slowly deflagrating through the mixture, the gas generated by the reaction will have sufficient time to diffuse into the ambient environment, resulting in little or no increase in pressure as the combustion wave passes. However, a transient pressure increase is always observed, indicating that this process lies somewhere between a constant volume and constant pressure process, generally favoring the former. In other words, the peak pressure observed depends on both the reactive mixtures potential for generating gaseous species, and the rate at which those species are produced. Take for example **Figs. 141a** and **141b**, which present the measured pressure traces of the nm-Al/nm-CuO and  $\mu\text{m}$ -Al/ $\mu\text{m}$ -CuO thermites, respectively. At thermodynamic equilibrium, the total gas produced by the latter would be greater, since this corresponds to a lower percentage of  $\text{Al}_2\text{O}_3$  and higher temperatures. However, since the reaction propagation rate of the  $\mu\text{m}$ -Al/ $\mu\text{m}$ -CuO mixture is nearly an order of magnitude less than that of the nm-Al/nm-CuO mixture, the time scale for gas generation will be much less. Therefore, the  $\mu\text{m}$ -Al/ $\mu\text{m}$ -CuO case exhibits a lower peak pressure. The packing density of the thermite in the burn tube also affects the pressure overshoot. The more gas-generating material that is packed into a given volume, the greater the pressure overshoot will be. However, the higher densities also decrease the permeability of the thermite, hindering convective burning. Also, note that in addition to having a greater peak pressure, the pressurization and depressurization rates are much faster for the nm-Al/nm-CuO than the  $\mu\text{m}$ -Al/ $\mu\text{m}$ -CuO. Additional information on the research conducted on nanothermites can be found in Refs. [186-193].

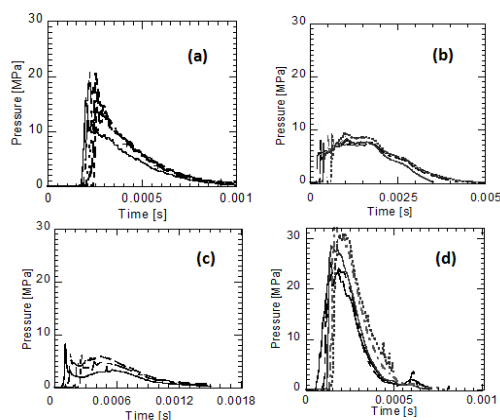


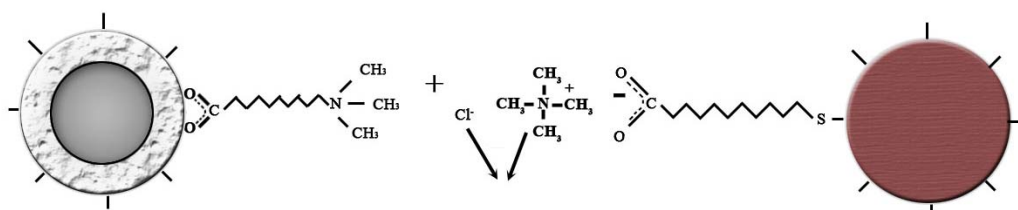
**Figure 139** Pressure traces from dynamic pressure transducers positioned along the length of the burn tube during combustion of (a) nm-Al/nm-CuO, (b)  $\mu\text{m}$ -Al/ $\mu\text{m}$ -CuO, (c) nm-Al/ $\mu\text{m}$ -CuO, and (d)  $\mu\text{m}$ -Al/nm-CuO.

#### II.3.2.4 Electrostatic Self-Assembly of a Nanoscale Thermite System into ordered Microspheres

The **Yetter group** in collaboration with **Dr. Tim Foley** of Los Alamos National Laboratory has used electrostatic self-assembly to create a nanoscale thermite system from nAl and nCuO particles [194]. The nAl had a spherical shape with a nominal particle diameter of 38 nm and an active aluminum content of 49%. The nCuO particles were spherical with a nominal particle size of 33 nm. Ligands with a positive or negative  $\omega$ -functionalization were attached to the surface of each nanoparticle to create a charged self-assembled monolayer (SAM). The ligand used to functionalize the surfaces of the aluminum particles was an  $\omega$ -trimethylammonium (TMA) functionalized carboxylic acid,  $\text{HOOC}(\text{CH}_2)_{10}\text{NMe}_3^+\text{Cl}^-$ . The nCuO surfaces were treated with the  $\omega$ -carboxylic acid functionalized thiol, or mercaptoundecanoic

acid (MUA),  $\text{HS}(\text{CH}_2)_{10}\text{COOH}$ . The positively charged nanoaluminum and negatively charged nanocupric-oxide were each suspended in a separate solution and upon mixing the two constituents, they self-assembled into microspheres with diameters on the order of  $1\ \mu\text{m}$  (**Fig. 140**). Examples of the micron-sized composite particles formed are shown in **Fig. 141**. These self-assembled nanothermite microspheres (SANTMs) are the first known energetic thermite systems created from the bottom-up. This method allows for the mixing of the two constituents to be performed without sonication, and could potentially create a highly ordered system with minimal diffusion distances between the two constituents. These self-assembled nano thermite micro spheres (SANTMs) are essentially an ordered matrix of nAl and nCuO particles held together by an infrastructure of long carbon chains. This is ideally how a heterogeneous energetic material with a carbonaceous binder should be created to ensure maximum performance. Gaining a better understanding of this type of nanoscale manipulation and construction will allow for specific tailoring of the burning characteristics by varying the most fundamental of building blocks.

### STEP 1: SALT FORMATION



### STEP 2: PARTICLE SELF-ASSEMBLY

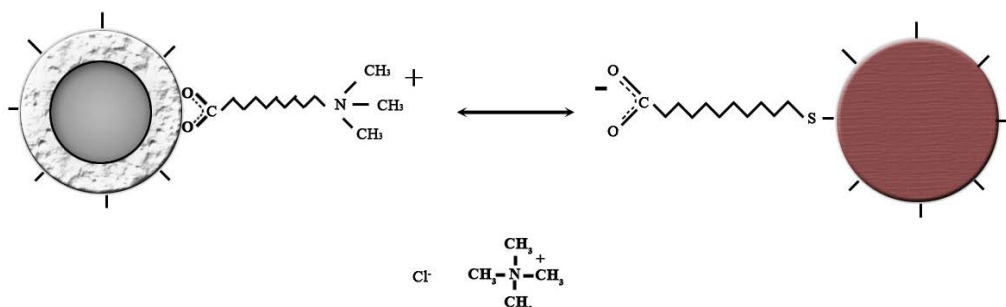


**Figure 140** Schematic of salt formation and electrostatic self-assembly of particles.

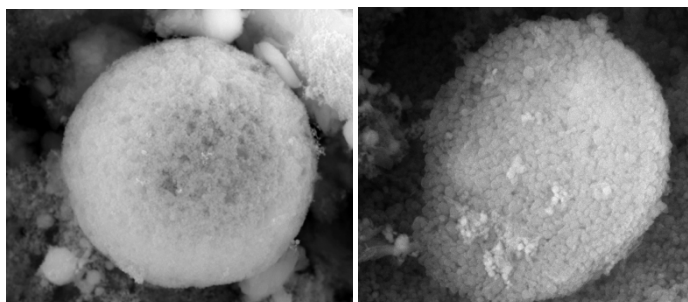


**Figure 141** SEMs of nAl and nCuO self-assembled nanothermite microspheres (SANTMs). The particles shown are a few micron in diameter.

This work was the first to implement self-assembly to create nanocomposite reactive microspheres, and experiments were applied to analyze their reactive properties. The microspheres had diameters approximately 2 orders of magnitude greater than those of the constituent nanoparticles, demonstrating a bottom-up assembly process. Unlike sonicated material with similar amounts of hydrocarbon ligands, these materials show the ability to ignite and self-sustain a reaction in channels with dimensions on the microscale. This empirically suggests that a more ordered structure favorable for reaction is created by the self-assembly process.

### II.3.2.5 Energetic Properties of Ni/Al Composites Formed Through HVPC

With **Eden** at the Applied Research Laboratory at Penn State, efforts were started during the last year of the program in collaboration with **Matthew Trexler** at the Army Research Laboratory to produce highly dense bulk reactive materials consisting of Al and other metals such as Ni and Ti using the cold spray process. This process involves injecting micron scale powders into a high speed gas jet. The powder-seeded gas flows through a nozzle that greatly increases its speed. When the jet impacts a substrate the entrapped powder deforms and a material layer is built up with a density that approaches that of the bulk powder constituents. The thermodynamics of several reactive mixtures have been studied and the cold spray process has already been used to generate various bulk materials, some of them reactive. These studies complement the foil studies where the effect of varying the surface chemistry of the initial powders by adding SAMs and other materials to the mixture to modify its mechanical and chemical properties is being investigated.

High Velocity Particle Consolidation (HVPC), commonly referred to as “Cold Spray,” is a particle deposition method in which small (generally  $<50\ \mu\text{m}$ ) particles are entrained in a carrier gas, usually  $\text{N}_2$  or He, heated to temperatures below their melting points and sprayed through a converging-diverging nozzle at supersonic velocities onto a substrate (**Fig. 142**). The impinging particles mechanically interact with the substrate and form a bond with it. Multiple passes can be made over already deposited material to rapidly build up coatings of significant thickness. A schematic of the HVPC apparatus is shown in the figure below.

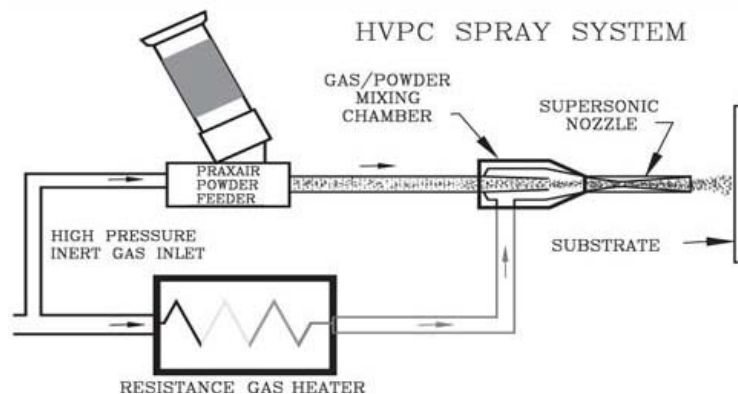


**Figure 142** Schematic of the HVPC system [195].

The HVPC process heretofore has been mainly used to create various coatings to enhance surface properties such as wear resistance [195]. In this study HVPC is used to make a high dense energetic material by depositing a premixed powder consisting of Al and Ni. The powder mixture was deposited onto an aluminum substrate to a thickness of approximately 2.5 mm. The HVPC material was then cut from the substrate for compositional and energetic analysis. Due to the complex interactions involved in particle entrainment and impingement during the HVPC process the prediction of deposition efficiency is challenging [196], so that the pre-mixed powder composition rarely matches the composition of the deposited material. In order to determine the composition of the consolidated sample optical micrographs

were taken and analyzed based on contrast to determine area percentages of Al, Ni and voids. All sprayed samples had porosities of less than 1%.

In order to determine the effects of the consolidated material's high density on reaction properties axially-pressed pellets were produced with compositions identical to the cold sprayed samples with densities varying from 70% to 80% of the composition's theoretical maximum density (TMD). A density of 100% TMD is defined as the mass weighted average of the densities of the components in the composite. The composition of the HVPC material was 38.1% Al / 61.9% Ni.

To determine the energetic properties of the Cold Sprayed and axially-pressed pellet samples, both were ignited using a 100 W CO<sub>2</sub> laser. After ignition the propagation rate of the reaction front was recorded using a Phantom v7.3 (Vision Research) high speed digital video camera set to record at 1000 frames per second. Due to the high reflectance of some samples black high temperature spray paint was used on ends of the samples to decrease ignition delay times and reduce the risk to the operator caused by reflected laser light. The relative energy output of the various compositions tested was determined by the use of differential scanning calorimetry (DSC). The samples were heated at 20 °C/min to a temperature of 1400 °C.

Propagation rates of the axially pressed pellets and as deposited HVPC material are shown in **Fig. 143**. Pellets were also made at a stoichiometric equivalence ratio of 31.5% / 68.5% Ni for comparative purposes. The Al and Ni powder used to make the stoichiometric pellets was identical to that used to make the HVPC material and pellets.

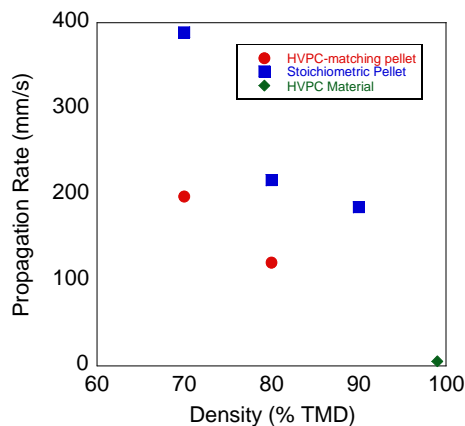


**Figure 143** Al/Ni propagation rates versus density.

The propagation rates of the samples are observed to decrease with increasing density, which is an unexpected result. The stoichiometric Al/Ni pellets also propagated significantly faster than those made to match the HVPC material, indicating a strong dependence of propagation rate on composition.

**Figure 144** shows a series of single frame images taken from the high speed video for ignition of an HVPC-matching 70% TMD pellet. The pellet is positioned horizontally. The ignition begins on the lower edge of the pellet and propagates both vertically and axially through the pellet. The “slumped” shape of the pellet shown in the 22.8 ms picture is caused by the pellet melting during combustion.

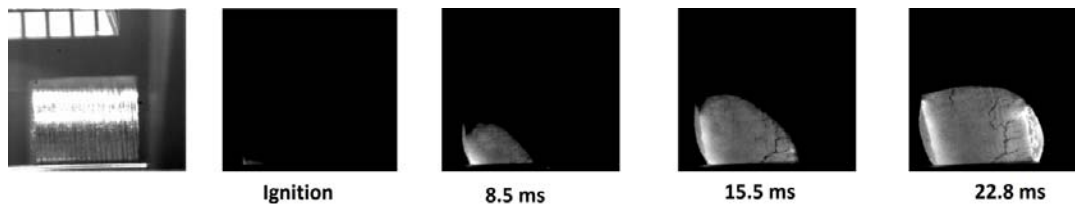


**Figure 144** Images of an Al/Ni HVPC-matching pellet ignition and combustion (70% TMD).

In **Fig. 145**, the propagation of a reaction front through one of the HVPC samples is shown. The sample deforms into a “C” shape during the reaction due to growth/expansion of the sample during combustion. Due to the added complexity of calculating speed based on a moving reference frame, changes in shape of the sample were not taken into consideration when calculating the speed of the reaction, so the actual propagation rate will be somewhat higher than that shown.

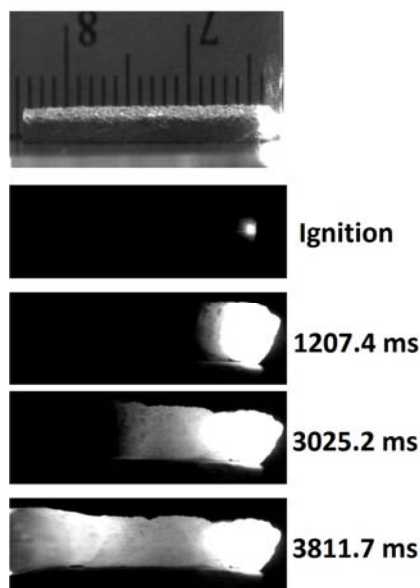


**Figure 145** Images of a HVPC material ignition and propagation.

**Figure 146** shows DSC traces for the stoichiometric powder and the powder matching the HVPC material. The same powder mass was placed into the DSC for both tests, so the vertical axis gives a qualitative comparison between the energy output of the two samples. The stoichiometric powder mixture produces a much higher spike of energy output, while the HVPC-matching powder produces much less energy. The endotherms visible at higher temperatures in the HVPC-matching curve correspond with known phase changes in Ni-Al alloys. These endotherms are present in the stoichiometric graph, though not visible due to the scaling needed to capture the exotherm spike.

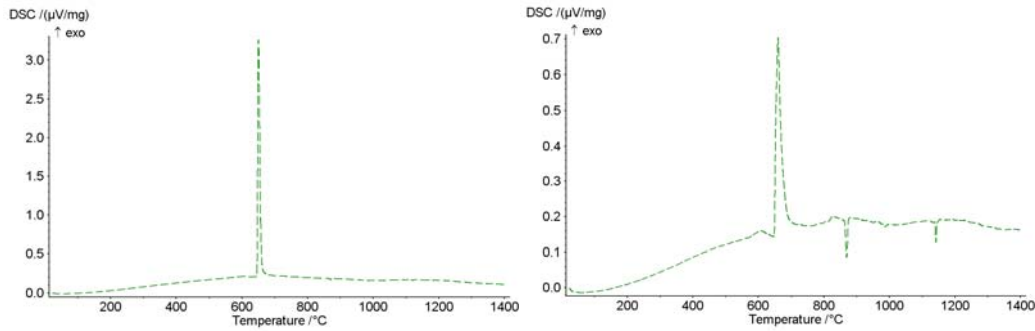


**Figure 146** (left) DSC analysis of stoichiometric Ni/Al powder and (right) DSC analysis of HVPC-matching powder.

A DSC analysis was also performed on a small sample of the as-deposited HVPC material. **Figure 147** shows a comparison of the HVPC deposited material and the HVPC-matching powder.

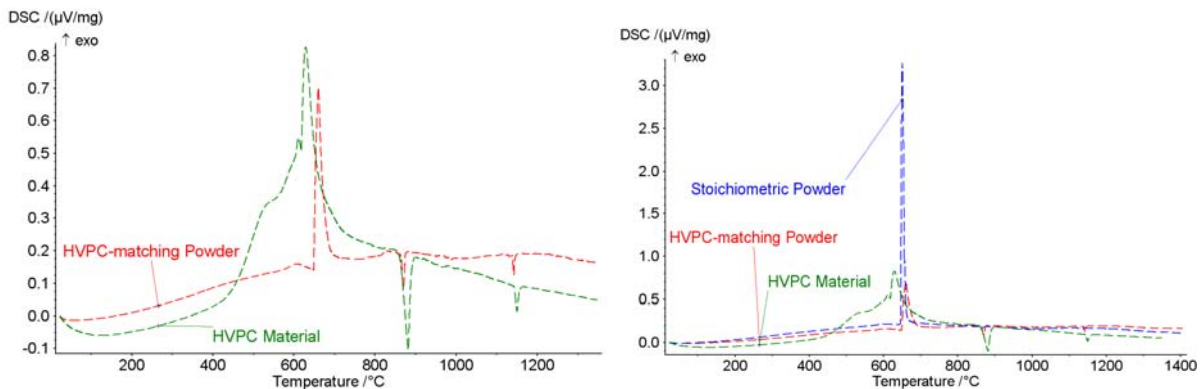


**Figure 147** (left) DSC of HVPC-matching powder and HVPC material and (right) DSC data from all tested materials.

The effect of the HVPC process on onset temperature is clearly seen in **Fig. 147**. The exothermic reaction in the loose powder samples both initiate with Al melting (660 °C), while the HVPC material initiates at approximately 450 °C. This is most likely due to the intimate mixing of the Ni/Al powder that happens as a result of the Cold Spray process.

Laser induced breakdown spectroscopy (LIBS), an emerging method of elemental analysis, uses the spectroscopic signature of atomic emission to determine elemental composition of a sample. With LIBS, a high-energy laser pulse is focused on the matter of interest, creating a ‘plasma spark’ and heating the material to extremely high temperatures (10,000-20,000 K). This matter can be in any state (solid, liquid, or gas). At these high temperatures, the matter is broken-down into excited atoms and ions. After a very short time, the atoms and ions decay from their excited states, releasing radiation at distinct frequencies (corresponding to distinct wavelengths). Since each atomic element has different spacing between its energy levels, the frequency of the emitted radiation is different depending on what atoms or ions are present. Therefore, it is possible, when the emitted light has been separated by wavelength, to identify which atoms are present within the plasma spark.

LIBS is applicable to very small samples with little or no preparation. Additionally, measurement time is very short and the experimental set-up is relatively simple. Since the plasma spark emission is intense and typically in the visible regime, the optical components and detectors for an LIBS system are

comparatively inexpensive and widely available. These advantages have created interest in LIBS as a method for detecting hazardous materials and explosives in the field [197]. Among the disadvantages of LIBS is the fact that quantitative analysis is very difficult and requires the use of some extremely pure calibration material. Additionally, the spectroscopic signal may be subject to interference from the breakdown of air surrounding the sample or the substrate the sample is placed on.

**Figure 148** shows a schematic of the LIBS experiment. A Q-switched ND:YAG laser ( $\lambda=1064$  nm), is used to ablate and breakdown/ionize the sample. The model of laser used (Litron Lasers Nano-L) has a specified max power of 300 mJ per 4 ns pulse. The laser light is turned using a  $45^\circ$  mirror and focused on the sample using a 25 mm focal length lens, creating a plasma spark, as shown in **Fig. 149**. The sample is placed inside a vacuum chamber to reduce the signal from the breakdown of ambient air or impurities. Collection optics and a 400  $\mu\text{m}$  core optical fiber are used to collect the emission from the plasma spark and transport it to the spectrometer. The UV/VIS/NIR spectrometer was purchased from Catalina Scientific (EMU-65 HTU1), and is configured for high throughput, with the grating blazed at 475 nm. After the light is dispersed by the spectrometer, an image is taken with an intensified CCD camera (Andor iXon+).

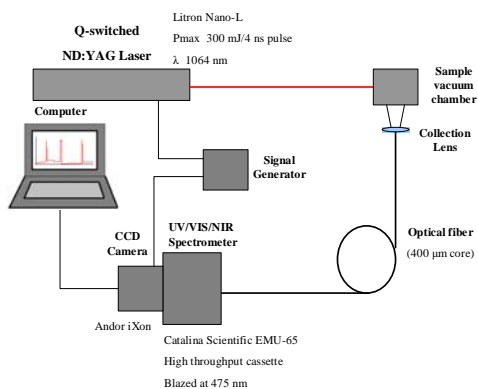


**Figure 148** Schematic of LIBS experiment.

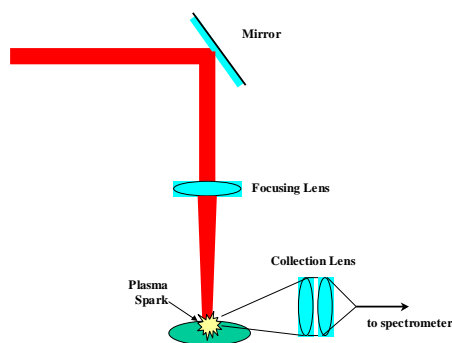


**Figure 149** Illustration of laser induced plasma generation.

**Figure 150** shows spectra from an LIBS experiment performed on a sample of cold-sprayed Al-Ni post reaction. At 1064 nm, a signal is seen from the reflected ND:YAG laser light. The strongest peaks in the spectra, 394 and 396 nm, are attributed to the presence of atomic aluminum in the plasma spark. A series of peaks corresponding to nickel were observed at 242 nm and 509 nm. Some unexpected peaks occurred around 309 nm and 352 nm, which were attributed to tungsten and molybdenum, respectively. Additionally, several peaks, such as the ones at 776 nm and 966 nm, could not be accounted for.

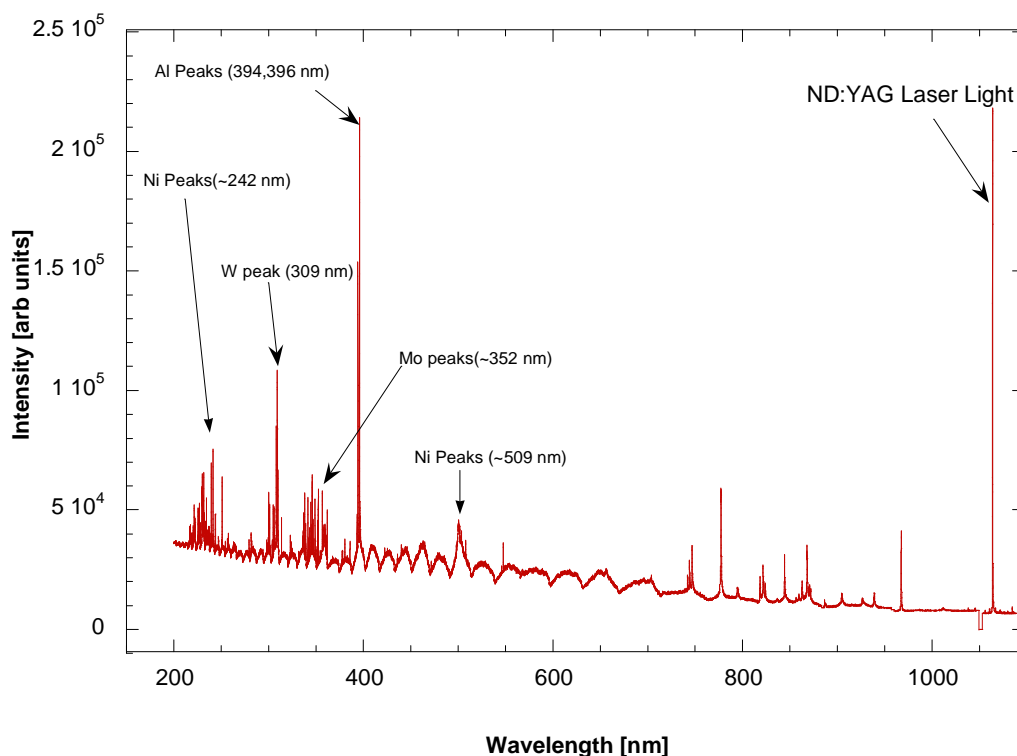


**Figure 150** LIBS spectra taken from cold-sprayed Al-Ni post reaction.

### III. Summary of Research

As discussed throughout this report and in the publications produced from the research, there are many accomplishments from this MURI effort. While significant progress has been made towards the original objectives of the program and towards the critical observations noted of the energetic materials field in general, there is still much research to be done. The outcomes of the present research have indicated directions for future research efforts in the field of nanoenergetics. A brief summary of the program's accomplishments are listed below.

- New methodologies for synthesis and assembly of nano-structured energetic materials were developed. New methods to generate metal nanoclusters that are stabilized against environmental degradation while preserving their high energy content were investigated. New strategies for manipulating the larger mesoscopic organization of high-energy nanoscale materials were developed
  - In particular, highly pure boron nanoparticles were synthesized by the gas phase pyrolysis of decaborane. The surface of the particles was further functionalized by halogenation. Thermal analysis studies of the particles showed that an exothermic combustion reaction takes place at temperatures above 500 °C, and that surface halogenation somewhat passivates the particles against further oxidation. Studies were performed to further exploit this new ability to prepare surface-functionalized boron nanoparticles.
  - From the synthesis and functionalization of aluminum nanoparticles, the formation of decorated particles rather than core-shell structures resulted, i.e., treating the Al particles with a solution of a transition metal salt does not result in the formation of a uniform coat, but instead generates nanocrystals of the zerovalent transition metal randomly distributed over the surface of the existing aluminum particles.

- Various rapid expansion supercritical solution processes (RESS, RESS-AS, RESS-N) were developed and applied to synthesize nanosized particulate oxidizers and organic oxidizer shell/fuel particle core composites
  - Nano-sized RDX and BTAT particles were synthesized with sizes orders of magnitude smaller than those in conventional precipitation techniques.
  - Particle morphology was controlled by use of surfactants.
  - Nano-sized RDX particles were shown to be significantly less sensitive to impact stimulus in comparison with the military grade RDX.
  - The feasibility for coating nano-sized aluminum particles by RDX through heterogeneous nucleation was demonstrated.
- Surface science and experimental chemistry methods were applied to study the structures and energy releasing reaction pathways of nano-structured energetic materials (NEEMs).
  - New types of self-assembled monolayers (SAMs) containing NO<sub>2</sub> groups were prepared that served as models for the surfaces of explosive material particles.
  - The SAMs were exposed to precise doses of reactive metal vapor to model the metal nanoparticle and oxidizer particle reaction interface inherent in any energetic system.
  - Extensive research was performed to develop instruments for in-situ tracking of the metal/SAM reactions.
  - Density functional theory (DFT) calculations were designed and performed to gain insight into the behavior of the metal/SAM systems.
  - The results conclusively showed that an exposed NO<sub>2</sub> group at a surface when exposed to nascent Al atoms from a vapor source only reacts partially to form Al-O-N types of metallo-organic complexes, as opposed to the expected highly exothermic reaction to form Al nitrides, oxides and carbides. Thus, when an Al atom impinges on a NO<sub>2</sub> oxidizer molecule at ambient temperatures only a small fraction of the potential energy is released. Clearly there is a large energy barrier to be overcome before the thermochemical maximum exotherm can be realized. The data suggests that this barrier may require in excess of ~400 K or so at the sample before energetic reaction.
- Unique diagnostic capabilities were developed and applied to study the fundamental mechanisms that underlie nanoengineered energetic materials (NEEM) dynamic performance.
  - Ultrafast images of reacting NEEMs were obtained.
  - NEEM initiation with ultrafast IR and ignition with ultrafast emission was measured.
  - The depassivation process using NEEMs with self-assembled molecular monolayers for passivation was studied.
  - A laser launch facility to detect the emission from impact-initiated NEEM was developed.
- Combustion mechanisms of various NEEMs, including nanothermites and nanoparticulate fuel/liquid oxidizer systems, were analyzed.
  - Measurements of propagation rates were obtained and underlying mechanisms were proposed for nanothermites as a function of stoichiometry, particle size, system pressure, dilution, density and overall system size. New results indicated increasing system pressure slows propagation rates of low density systems while decreasing oxidizer particle size is as important or more important than decreasing fuel particle size on increasing propagation rates
  - Reaction temperatures were measured of propagating nanothermites, which indicated the importance of oxidizer decomposition on the propagation rates.
  - A self-assembly process to create nanocomposite reactive microspheres from nAl and nCuO particles was developed and experimentally tested for reactivity. The results showed that the organization through self assembly led to an enhanced reaction.
  - Reactive materials were fabricated using high velocity particle consolidation (cold spray process) and their thermal ignition and propagation characteristics were experimentally analyzed.

- The reactive and thermal characteristics of nano-structured engineered energetic materials (NEEMs) were studied using large (billion atoms) multiscale simulations that couple quantum-mechanical (QM) calculations to molecular dynamics (MD) calculations. In particular, the stability, structure and energetics of metallic nanoparticles with a special focus on the relationships between particle size, shape and excess surface free energy was studied. Multiscale modeling of the thermo-mechanical properties and microscopic mechanisms of detonation and deflagration processes of NEEMs was performed.
  - Scalable parallel algorithms for multimillion-atom simulations of chemical reactions were developed.
  - Quantum mechanical calculations were performed of an RDX molecule on an aluminum surface.
  - Molecular dynamics simulation of shock compression of self-assembled monolayers was performed.
  - The fast reaction mechanisms of an aluminum nanoparticle with crystalline and amorphous alumina shells were analyzed.
  - Burning of aluminum nanoparticles by slow heating was studied.
  - The reactivity of nanothermites was studied.
- A unified theory of ignition and combustion of aluminum particles for a wide range of sizes, from nano to meso scales was established.
  - A comprehensive review on ignition and combustion of aluminum particles at micron and nano scales was conducted.
  - Molecular dynamics studies were performed to examine the thermodynamic behavior of aluminum particles at nano scales.

Details of the results and specific outcomes of these accomplishments may be found in the 70+ publications that resulted from the program.

#### IV. Technology Transfer and Interactions

As discussed throughout the report, the team developed strong interactions among themselves. In addition, all team members have had close working relationships with various DoD and DoE laboratories. Several collaborative programs with scientists and engineers at **ARL**, **ARDEC**, **NAVSEA-IH**, and **LANL** were established during the program. The MURI team visited many DoD and DoE laboratories to discuss their research and many scientists from the DoD laboratories visited the university laboratories. In addition, several of the graduate students spent extended periods of time at the DoD and DoE laboratories.

At Penn State, **Dr. Steven F. Son** took a year sabbatical from Los Alamos National Laboratory (LANL) to conduct collaborative research with **Yetter**, **Kuo**, **Yang**, and **Allara** on the MURI program. After accepting a position at Purdue, the MURI team continued to collaborate with **Dr. Son**. This collaboration resulted in the publication of a special section in the *Journal of Propulsion and Power* on Nano Composite Energetic Materials, with **Son**, **Yetter** and **Yang** as co-editors. Also contributing to this issue was **Vashishta**, **Kalia**, and **Nakano** at **USC** in collaboration with **Dr. Barrie Homan** and **Dr. Kevin McNesby** of the **Army Research Laboratory**. The collaboration with **LANL** continued throughout the duration of the program with collaborations with **Drs. Tim Foley**, **Bryce Tappan**, and **Blaine Asay**. **Eden** and **Yetter** at **PSU** have also been collaborating with **Matthew Trexler** at the **Army Research Laboratory** on cold spray of reactive materials and combustion analysis. **Allara** and **Yetter** collaborated on depositing layer by layer intermetallic structures and measuring the heat release as a function of the multifilm structure. **Allara** and **Diott** have collaborated on ultra fast thermal propagation in SAMs. **Allara** and the **USC group** have collaborated on DFT/MD calculations.

Before the RESS system design was fully developed the **Penn State MURI** team visited the Picatinny Arsenal to confer about the RESS process with **Dr. Victor Stepanov** of New Jersey Institute of Technology. His system from Thar Technologies was discussed and he showed the team the different components and explained their functions. Nozzle design and future flow visualization studies were also discussed. While **Dr. Stepanov's** system was rated to 10,000 psi, the concept for nano-particle design is similar and his advice and input was very helpful in directing the Penn State design process. He also recommended collecting the synthesized particles in a dry ice environment.

Another civilian Army personnel member that the **Penn State MURI** team talked to was **Dr. Jeff Morris**. He was very helpful in explaining how his solubility tests were set up and executed. His familiarity with the carbon dioxide and RDX reactions at elevated pressures was helpful in determining the pressure and temperature limits which were placed on the Penn State RESS system. **Jeff Morris** also directed the team to other research activities associated with RESS systems and the most recent progress on the theoretical modeling of RDX solubility.

From industry, **Val Krukonis** of **Phasex Corporation** was contacted. His book is cited in this paper. He was contacted in the search of more information in reference to naphthalene's solubility in supercritical carbon dioxide. A chart of naphthalene's solubility in supercritical carbon dioxide was found in his book, but for more information of the topic he referred us to a paper by McHugh and Paulitis. This interaction was most useful due to **Val Krukonis's** background with RESS and his knowledge of naphthalene solubility in supercritical carbon dioxide.

Sensitivity testing was performed on the synthesized particles by **Timothy Wawiernia** and **Kuo** at Penn State and **Dan Remmer** and **Ruth Doherty** at the **Naval Surface Warfare Center Indian Head Division** (NSWC-IHD) in Indian Head, Maryland. The NSWC portion of the collaborative work was supported by **Dr. Cliff Bedford** of **ONR**.

Particle zeta potential measurements and dynamic light scattering of particles was performed in collaboration with Professor **James Adair** at the particulate characterization laboratory at **Penn State**. **Dr. Adair** was helpful in suggesting dispersing agents to this team.

The atomistic understanding gained in this project will lead to the development of new and improved materials and structures with enhanced energy density and reduced sensitivity for a wide range of DoD applications, by significantly accelerating the pace of experimental research and through the **USC group's** extensive collaborations with DoD scientists (**Dr. William Wilson** at **DTRA**; joint paper “multimillion atom reactive simulations of nanostructured energetic materials” in *Journal of Propulsion and Power* with **Dr. Barrie Homan** and **Dr. Kevin McNesby** at **ARL**; our students' internships with **Dr. Betsy Rice** and **Dr. Margaret Hurley** at **ARL**; and mutual visits by **Dr. Brad Forch** and **Dr. Shashi Karna** at **ARL**). Our dual-degree students (Ph.D. in the physical sciences or engineering with MS in Computer Science specialized in High Performance Computing and Simulations) continue to do internships with our DoD collaborators.

At **UIUC**, **Dlott**, **Nuzzo**, and **Girolami** have discussed their research extensively with collaborators at the DOE labs LAN, LLNL, and Argonne. **Dlott** has also discussed simulations of self-assembled monolayers with **Vashishta** at **USC**, and spectroscopy of fluorocarbon-coated nanoparticles with **Dr. Jason Jouet** of **NSWC**. **Yetter** collaborated with **Nuzzo** and **Girolami** conducting combustion studies on the boron nano particles produced at UIUC. In an extension of the aluminum nanoparticle work, **Girolami** has collaborated with **UES, Inc.**, to develop new methods to coat steel parts with aluminum to improve their corrosion resistance.

## V. References

1. Politzer, P.; Lane, P.; Concha, M. C. In *Chemistry at Extreme Conditions*; Manaa, M. R., Ed.; Elsevier, 2005.
2. Yeh, C. L.; Kuo, K. K. *Prog. Energy Combust. Sci.* **1997**, *22*, 511-541.
3. Natan, B.; Gany, A. *J. Propul. Power* **1991**, *7*, 37-43.
4. Gany, A.; Netzer, D. W. *J. Propul. Power* **1986**, *2*, 423-427.
5. Casey, J. D.; Haggerty, J. S. *J. Mater. Sci.* **1987**, *22*, 737-744.
6. Johnston, H. L.; Hersh, H. N.; Kerr, E. C. *J. Am. Chem. Soc.* **1951**, *73*, 1112-1117.
7. Si, P. Z.; Zhang, M.; You, C. Y.; Geng, D. Y.; Du, J. H.; Zhao, X. G.; Ma, X. L.; Zhang, Z. D. *J. Mater. Sci.* **2003**, *38*, 689-692.
8. Pickering, A. L.; Mitterbauer, C.; Browning, N. D.; Kauzlarich, S. M.; Power, P. P. *Chem. Commun.* **2007**, 580-582.
9. Quandt, A.; Boustani, I. *ChemPhysChem* **2005**, *6*, 2001-2008.
10. Xu, T. T.; Nicholls, A. W.; Ruoff, R. S. *NANO* **2006**, *1*, 55-63.
11. Siegel, B.; Mack, J. L. *J. Phys. Chem.* **1958**, *62*, 373-374.
12. Cirri, G. F.; Fidanzati, G.; Forlani, F. *Thin Solid Films* **1976**, *36*, 487-491.
13. Croft, W. J.; Tombs, N. C.; Fitzgerald, J. F. *Mater. Res. Bull.* **1970**, *5*, 489-494.
14. Pierson, H. O.; Mullendore, A. W. *Thin Solid Films* **1981**, *83*, 87-91.
15. Nakamura, K. *J. Electrochem. Soc.* **1984**, *131*, 2691-2697.
16. Shirai, K.; Gonda, S. *J. Appl. Phys.* **1990**, *67*, 6286-6291.
17. Kamimura, K.; Ohkubo, M.; Shinomiya, T.; Nakao, M.; Onuma, Y. *J. Solid State Chem.* **1997**, *133*, 100-103.
18. Kamimura, K.; Nagaoka, T.; Shinomiya, T.; Nakao, M.; Onuma, Y.; Makimura, M. *Thin Solid Films* **1999**, *343-344*, 342-344.
19. Kamimura, K.; Yoshimura, T.; Nagaoka, T.; Nakao, M.; Onuma, Y.; Makimura, M. *J. Solid State Chem.* **2000**, *154*, 153-156.
20. Naslain, R. *Prep. Methods Solid State Chem.* **1972**, 439-485.
21. Talley, C. P. *J. Appl. Phys.* **1959**, *30*, 1114-1115.
22. Jiang, J.; Senkowitz, B. J.; Larbalestier, D. C.; Hellstrom, E. E. *Supercond. Sci. Technol.* **2006**, *19*, L33-L36.
23. Decker, B. F.; Kasper, J. S. *Acta Cryst.* **1959**, *12*, 503-506.
24. Hoard, J. L.; Newkirk, A. E. *J. Am. Chem. Soc.* **1960**, *82*, 70-76.
25. Ronning, C.; Schwen, D.; Eyhusen, S.; Vetter, U.; Hofsass, H. *Surf. Coat. Technol.* **2002**, *158-159*, 382-387.
26. Moulder, J.; Stickle, W.; Sobel, P.; Bomben, E. *Handbook of X-Ray Photoelectron Spectroscopy*; Physical Electronics Division, Perkin-Elmer Corp.: Eden Prairie, 1995.
27. Ennaceur, M. M.; Terreault, B. *J. Nucl. Mater.* **2000**, *280*, 33-38.
28. Ito, Y.; Arakawa, T.; Nishikawa, M. *Plasma Sources Sci. Technol.* **1996**, *5*, 305-310.
29. Wilson, D. E.; Schroder, K. A.; Willauer, D. L.; Bless, S.; Russell, R. T. Patent Application: US 2009301337.
30. Apperson, S. J.; Bezmelnitsyn, A. V.; Thiruvengadathan, R.; Gangopadhyay, K.; Gangopadhyay, S.; Balas, W. A.; Anderson, P. E.; Nicolich, S. M. *J. Propul. Power* **2009**, *25*, 1086-1091.
31. Puszynski, J. A. *J. Therm. Anal. Calorim.* **2009**, *96*, 677-685.
32. Johnson, C. E.; Higa, K. T.; Albro, W. R. *Proc. Int. Pyrotech. Semin.* **2008**, *35th*, 159-168.
33. Muravyev, N.; Frolov, Y.; Pivkina, A.; Monogarov, K.; Ivanov, D.; Meerov, D.; Fomenkov, I. *Cent. Eur. J. Energ. Mater.* **2009**, *6*, 195-210.
34. Hahma, A. Patent Application: WO 2009127784.
35. Jayaraman, K.; Anand, K. V.; Bhatt, D. S.; Chakravarthy, S. R.; Sarathi, R. *J. Propul. Power* **2009**, *25*, 471-481.

36. Umbrajkar, S. M.; Seshadri, S.; Schoenitz, M.; Hoffmann, V. K.; Dreizin, E. L. *J. Propul. Power* **2008**, *24*, 192-198.
37. Pantoya, M. L.; Hunt, E. M. *Appl. Phys. Lett.* **2009**, *95*, 253101/253101-253101/253103.
38. Gromov, A.; Strokova, Y.; Kabardin, A.; Vorozhtsov, A.; Teipel, U. *Propellants, Explos., Pyrotech.* **2009**, *34*, 506-512.
39. Sinditskii, V. P.; Egorshchev, V. Y.; Serushkin, V. V.; Levshenkov, A. I.; Berezin, M. V.; Filatov, S. A.; Smirnov, S. P. *Thermochim. Acta* **2009**, *496*, 1-12.
40. Bhattacharya, A.; Guo, Y. Q.; Bernstein, E. R. *J. Chem. Phys.* **2009**, *131*, 194304/194301-194304/194308.
41. Li, H.; Meziani, M. J.; Lu, F.; Bunker, C. E.; Gulians, E. A.; Sun, Y.-P. *J. Phys. Chem. C* **2009**, *113*, 20539-20542.
42. Cheng, J.; Hng, H. H.; Ng, H. Y.; Soon, P. C.; Lee, Y. W. *J. Mater. Res.* **2009**, *24*, 3220-3225.
43. Fenski, D.; Longoni, G.; Schmid, G. *Clusters and Colloids: From Theory to Applications*; VCH: New York, 1994.
44. Parker, A. J.; Childs, P. A.; Palmer, R. E.; Brust, M. *Appl. Phys. Lett.* **1999**, *74*, 2833-2835.
45. Brust, M.; Fink, J.; Bethell, D.; Schiffrin, D. J.; Kiely, C. *Chem. Commun.* **1995**, 1655-1656.
46. Sanchez-Lopez, J. C.; Gonzalez-Elipse, A. R.; Fernandez, A. *J. Mater. Res.* **1998**, *13*, 703-710.
47. Lyashko, A. P.; Il'in, A. P.; Savel'ev, G. G. *Zh. Prikl. Khim.* **1993**, *66*, 1230-1233.
48. Kwon, Y.-S.; Gromov, A. A.; Ilyin, A. P.; Rim, G.-H. *Appl. Surf. Sci.* **2003**, *211*, 57-67.
49. Jouet, R. J.; Warren, A. D.; Rosenberg, D. M.; Bellitto, V. J.; Park, K.; Zachariah, M. R. *Chem. Mater.* **2005**, *17*, 2987-2996.
50. Foley, T. J.; Johnson, C. E.; Higa, K. T. *Chem. Mater.* **2005**, *17*, 4086-4091.
51. Pasricha, R.; Bala, T.; Biradar, A. V.; Umbarkar, S.; Sastry, M. *Small* **2009**, *5*, 1467-1473.
52. Bala, T.; Enoki, T.; Prasad, B. L. V. *J. Nanosci. Nanotechnol.* **2007**, *7*, 3134-3139.
53. Ankamwar, B.; Damle, C.; Ahmad, A.; Sastry, M. *J. Nanosci. Nanotechnol.* **2005**, *5*, 1665-1671.
54. Selvakannan, P. R.; Sastry, M. *Chem. Commun.* **2005**, 1684-1686.
55. Bala, T.; Arumugam, S. K.; Pasricha, R.; Prasad, B. L. V.; Sastry, M. *J. Mater. Chem.* **2004**, *14*, 1057-1061.
56. Sanchez, S. I.; Small, M. W.; Sivaramkrishnan, S.; Wen, J.-g.; Zuo, J.-M.; Nuzzo, R. G. *Anal. Chem.* **2010**, *82*, 2599-2607.
57. Cooper, A. S. *Acta. Crystallogr.* **1962**, *15*, 578-583.
58. Chen, S. W.; Chuang, Y. Y.; Chang, Y. A.; Chu, M. G. *Metall. Trans. A* **1991**, *22A*, 2837-2848.
59. Arkharov, V. I.; Magat, L. M. *Fiz. Met. Metalloved.* **1958**, *6*, 809-811.
60. Ageev, N. V.; Shoyket, D. *J. Inst. Met.* **1933**, *52*, 119-129.
61. Ning, Y.; Zhou, X. *J. Alloys Compd.* **1992**, *182*, 131-144.
62. Elliott, R. P.; Shunk, R. A. *Bull. Alloy Phase Diagrams* **1981**, *2*, 70-75.
63. Ozolins, V.; Majzoub, E. H.; Udovic, T. J. *J. Alloys Compd.* **2004**, *375*, 1-10.
64. Du, Y.; Clavaguera, N. *J. Alloys Compd.* **1996**, *237*, 20-32.
65. Tonejc, A.; Rocak, D.; Bonefacic, A. *Acta Met.* **1971**, *19*, 311-316.
66. Ellner, M.; Kattner, U.; Predel, B. *J. Less-Common Met.* **1982**, *87*, 117-133.
67. Huch, R.; Klemm, W. *Z. Anorg. Allg. Chem.* **1964**, *329*, 123-135.
68. Guex, P.; Feschotte, P. *J. Less-Common Met.* **1976**, *46*, 101-116.
69. Lin, W.; Nuzzo, R. G.; Girolami, G. S. *J. Am. Chem. Soc.* **1996**, *118*, 5988-5996.
70. Lin, W.; Wiegand, B. C.; Nuzzo, R. G.; Girolami, G. S. *J. Am. Chem. Soc.* **1996**, *118*, 5977-5987.
71. Crane, E. L.; You, Y.; Nuzzo, R. G.; Girolami, G. S. *J. Am. Chem. Soc.* **2000**, *122*, 3422-3435.
72. Armstrong, R.W., Coffey, C.S., DeVost, V.F., and Elban W.L. (1990) "Crystal Size Dependence for Impact Initiation of Cyclotrimethylenetrinitramine Explosive," *J. Appl. Phys.*, **68**, 1990, 979-984
73. Armstrong, R.W., "Dislocation-Assisted Initiation of Energetic Materials," *Proceedings of 8<sup>th</sup> International Seminar: New Trends in Research of Energetic Materials*, Pardubice, Czech Republic, 2005, 28-43.

74. Van der Heidjen, A. E. D. M., Bouma, R. H. B., and Van der Steen, A. C., "Physiochemical Parameters of Nitramines Influencing Shock Sensitivity," *Prop. Exp. Pyr.*, **29**, 2004, 304-313
75. Czerski, H. and Proud, W. G., "Relationship Between the Morphology of Granular Cyclotrimethylenetrinitramine and its Shock Sensitivity," *J. App. Phys.*, **102**, 2007, 113515-1-113515-8
76. Doherty, R. "Wrestling with New Energetic Ingredients," *J. Energ. Mat. Chem. Prop.*, **7**, 2008, 1-16
77. Pivkina, A., Ulyanova, P., Frolov, Y., Zavyalov, S., and Schoonman, J., "Nanomaterials for Heterogeneous Combustion," *Prop. Exp. Pyr.*, **29**, 2004, 39-48
78. Gash, A. E., Simpson, R. L., Babushkin, Y., Lyamkin, A. I. Tepper, F., Biryukov, Y., Vorozhtsov, A., and Zarko, V., "Nanoparticles," in *Energetic Materials: Particle Processing and Characterization* ed. by Teipel, U., 2005. Wiley-VCH, Weinheim, Germany., 267-289
79. Kubota, N., *Propellants and Explosives: Thermochemical Aspects of Combustion*, 2nd edition, Wiley & Co., 2007
80. Bucher, P., Yetter, R. A., Dryer, F. L., Vicenzi, E. P., Parr, T. P., and Hanson-Parr, D. M., "Condensed-Phase Species Distributions about Al Particles Reacting in Various Oxidizers," *Combustion and Flame*, **117**, 1999, 351-361
81. Simonenko, V. N. and Zarko, V. E., "Comparative Study of the Combustion Behavior of Composite Propellants Containing Ultra Fine Aluminum," in *Proceedings of the 30th International Annual Conference of ICT, Karlsruhe, Germany, 1999*, 21
82. Meda, L., Marra, G., Galfetti, L., Severini, F., and De Luca, L., "Nano-Aluminum as Energetic Material for Rocket Propellants," *Mats. Sci. Eng. C*, **27**, 2007, 1393-1396
83. Mikhaylo, A., Schoenitz, M., Dreizin, E. L., "Ignition of Aluminum Powders Under Different Experimental Conditions," *Prop. Exp. Pyr.* **30**, 2005, 36-43
84. Yetter, R. A., Risha, G. A., and Son, S. F., "Metal Particle Combustion and Nanotechnology," *Proc. Of Comb. Inst.*, **32**, 2009, 1819-1838
85. Brousseau, P., Dubois, C., "Polymer-Coated Ultra-Fine Particles," *Mater. Res. Soc. Symp. Proc.* **896**, 2006, 2.1-2.11
86. Brousseau, P. and Dubois, C., "Polymer-Coated Ultra-Fine Particles", *Material Research Society Symposium Proceedings*, **896**, 2006, 1-11
87. Dubois, C., Lafleur, P. G., Roy, C., Brousseau, P., and Stowe, R. A., "Polymer-Grafted Nanoparticles for Fuel Applications," *Journal of Propulsion and Power*, **23**, 2007, 651-658
88. Glebov, E. M., Yuan, L., Krishtopa, L., G., Usov, O. M., and Krasnoperov, L., N., "Coating of Metal Powders with Polymers in Supercritical Carbon Dioxide," *Ind. Eng. Chem. Res.*, **40**, 2001, 4058-4068
89. van der Heijden, A. E. D. M., Bouma, R. H. B., Van der Steen, A. C., and Fischer, H. R., "Application and Characterization of Nanomaterials in Energetic Compositions," *Materials Research Society Symposium Proceedings*, **800**, 2004, 1-18
90. Kavetsky, R., Anand, D. K., Goldwasser, J., Bruck, H., Doherty, R., and Armstrong, R., "Energetic Systems and Nanotechnology-a Look Ahead," *International Journal of Energetic Materials and Chemical Propulsion*, **6**, 2007, 39-48
91. Teipel, U. and Mikonsaari, I., "Size Reduction," in *Energetic Materials: Particle Processing and Characterization* ed by Teipel, U., Wiley-VCH Verlag GmbH & Co. KGaA, Weinheim, 2005, 27-52.
92. Adair, J. H., "Colloidal Lessons Learned for Dispersion on Nanosize Particulate Suspensions," in *Lessons in Nanotechnology from Traditional and Advanced Ceramics* edited by Baumard, J. F., Techna Group, 2005, 93-146
93. Redner, P., Kapoor, D., Patel, R., Chung, M., and Martin, D., "Production and Characterization of Nano-RDX," *Army Science Conference*, 2006, 1-6
94. Tom, J. W., Debenedetti, P. G., "Particle Formation with Supercritical Fluids-A Review," *J. Aerosol. Sci.*, **22**, 1991, 555-584

95. Morris, J.B. "Solubility of RDX in Dense Carbon Dioxide at Temperatures between 303K and 353K," *J. Chem. Eng. Data*, **43**, 1998, 269-273
96. McHugh, M. A. and Krukonis, V. J., *Supercritical Fluid Extraction, Principle and Practice*, 2<sup>nd</sup> Edition, Butterworth-Heinemann, 1994
97. Tom, J.W. and Debenedetti P.G. "Particle Formation with Supercritical Fluids- A Review," *J. Aerosol Sci.*, **22**, 1991, 555-584.
98. Jung, J. and Perrut, M. (2001) Particle Design Using Supercritical Fluids: Literature and Patent Survey, *J. Supercritical Fluids*, Vol. 20, pp. 179-219.
99. Debenedetti, P.G., "Homogeneous Nucleation in Supercritical Fluids," *AIChE Journal*, **36**, 1990, 1289-1298
100. Teipel, U., Krober, H., and Krause, H. H., "Formation of Energetic Materials Using Supercritical Fluids," *Prop. Exp. Pyr.*, **22**, 2001, 168-173
101. Stepanov, V., "Production of Nanocrystalline Nitramine Energetic Materials by Rapid Expansion of Supercritical Solutions", Masters Thesis, New Jersey Institute of Technology, NJ, August 2003.
102. Weber, M. and Thies, M. C., "A Simplified and Generalized Model for the Rapid Expansion of Supercritical Solutions," *J. Sup. Fl.*, **40**, 2007, 40, 402-419
103. Sun, Y., Meziani, M. J., Pathak, P., and Qu, L., "Polymeric Nanoparticles from Rapid Expansion of Supercritical Fluid Solution," *Chem. Eur. J.*, **11**, 2005, pp. 1366-1373
104. Young, T. J., Mawson, S., and Johnston, K. P., Henriksen, I. B., Pace, G. W., Mishra, A. K., "Rapid Expansion from Supercritical to Aqueous Solution to Produce Submicron Suspensions of Water-Insoluble Drugs," *Biotechnol. Prog.*, **16**, 2000, 402-407
105. Türk, M. and Lietzow, R., "Stabilized Nanoparticles of Phytosterol by Rapid Expansion from Supercritical Solution into Aqueous Solution," *AAPS PharmSciTech*, **5**, 2004, 1-10
106. Sane, A. and Thies, M. C., "The Formation of Fluorinated Tetraphenylporphyrin Nanoparticles via Rapid Expansion Processes: RESS vs RESOLV," *J. Phys. Chem. B*, **109**, 2005, 19688-19695
107. Todorova, S., Schmelzer, J. W. P., and Gutzow, I., "Nucleation Catalysis in Metastable Liquids: Inborn Active Sites," *Cryst. Res. Tech.*, **35**, 2000, 515-527
108. Mishima, K., Matsuyama, K., Tanabe, D., Yamauchi, S., Young, T. J., and Johnston, K. P., "Microencapsulation of Proteins by Rapid Expansion of Supercritical Solution with a Nonsolvent," *American Institute Chemical Engineers Journal*, **46**, 2000, 857-865
109. Göbel, M. and Klapötke, T. M., "Development and Testing of Energetic Materials: The Concept of High Densities Based on the Trinitroethyl Functionality," *Advanced Functional Materials*, **19**, 2009, 347-365.
110. Adair, J. H., Krarup, H. G., "The Role of Solution Chemistry in Understanding Colloidal Stability of Ceramic Suspensions," *Advances in Process Measurements for the Ceramic Industry*, Edited. By Jillavenkatesa, A., Onoda, G. Y., 1999, American Ceramic Society, 205-221
111. Pathak, P. Meziani, M. J., Desai, T., and Sun Y., "Nanosizing Drug Particles in Supercritical Fluid Processing," *J. Am. Chem. Soc. Comm.*, **126**, 2004, 10842-10843
112. Choi C. S. and Prince E. "The crystal structure of cyclotrimethylene-trinitramine ," *Acta Cryst.*, **B28.**, 1972, 2857-2862
113. Doherty, R. M. and Watt, D. S., "Relationship Between RDX Properties and Sensitivity," *Prop. Exp. Pyr.*, **33**, 4-13
114. Dept. of Defense, "Safety and Performance Tests for the Qualification of Explosives (High Explosives, Propellants, and Pyrotechnics)," MIL-STD-1751A, 2001.
115. Dixon, W. J., Massey, F. M., *Introduction to Statistical Analysis* 4th ed., 1983, McGraw-Hill, New York.
116. Tadros, T. F., "Assessment of the Properties of Suspensions," In *Solid-Liquid Dispersions*, Tadros, T. F., Academic Press: Orlando, FL, 1987, 293-326
117. Von Weimarn, P. P., "The Precipitation Laws," *Chem. Rev.*, **2**, 1925, 217-242
118. Söhnel, O. and Garside, J., *Precipitation: Basic Principles and Industrial Applications*, Butterworth-Heinemann, Oxford, 1992, 112-193

119. Adamson, A. W. and Gast, A. P., *Physical Chemistry of Surfaces* 6<sup>th</sup> ed., John Wiley & Sons, New York, 1997, 398-404
120. A.G. Merzhanov, Yu. M. Grigorjev, Yu. A. Gal'chenko, *Combustion and Flame*, Vol. 29, 1977, pp.1-14.
121. M.A. Gurevich, K.I. Lapkina, E.S. Ozerov, *Fizika Goreniya i Vzryva*, Vol. 6 (2), 1970, pp. 172-175.
122. M.A. Trunov, M. Schoenitz, E.L. Dreizin, *Propellants, Explosives, Pyrotechnics*, Vol.30, 2005, pp. 36-43.
123. E.W. Price, R.K. Sigman, in: V.Yang, T.B. Brill, W.Z. Ren (Eds.), *Solid Propellant Chemistry, Combustion and Motor Ballistics*, in: *Progress in Astronautics and Aeronautics*, vol. 185, AIAA, Reston, VA, 2000, p.663.
124. A. Pivkina, P. Ulyonova, Y. Frolov, S. Zavyalov, J. Schoonman, *Propellants, Explosives, Pyrotechnics*, Vol. 29, 2004, pp. 39-48.
125. G.A. Risha, S.F. Son, R.A. Yetter, V. Yang, B.C. Tappan, *Proceedings of the Combustion Institute*, Vol. 31(2), 2007, pp.2029-2036 .
126. T. Parr, C. Johnson D. Hanson-Parr K. Higa, K. Wilson, *JANNAF Combustion Subcommittee*, 2003.
127. V.G. Ivanov et al., *Combustion, Explosion, and Shock Waves*, Vol. 30(4), 1994, pp. 569-570.
128. T.A. Andrzejak, E. Shafirovich, A. Varma, *Combustion and Flame*, Vol. 150, 2007, pp. 60-70.
129. P. Puri, D.S. Sundaram, V. Yang, *Progress in Energy and Combustion Science*, In Preparation
130. M.W. Beckstead, von Karman Institute for Fluid Dynamics, *Lecture Series*, Belgium, May 2002.
131. E.L. Dreizin, *Combustion and Flame*, Vol. 105, 1996, pp. 541-556.
132. A. Rai, D. Lee, K. Park, M.R. Zachariah, *Journal of Physical Chemistry*, Vol. 108 (9), 2001, pp. 14793-14795.
133. E.L. Dreizin, *Combustion, Explosion, and Shock Waves*, Vol. 39 (6), 2003, pp.681-693.
134. P. Puri, V. Yang, *Journal of Physical Chemistry C*, Vol.111, 2007, pp.11776-11783.
135. P. Puri, V. Yang, *Journal of Nanoparticle Research*, Vol. 11 (5), 2009, pp.1117-1127.
136. P. Puri, V. Yang, *Journal of Nanoparticle Research*, 2010, Available Online (DOI: 10.1007/s11051-010-9889-2).
137. P. Puri, D.S. Sundaram, V. Yang, *Combustion and Flame*, In Preparation.
138. D.S.Sundaram, P.Puri, V.Yang, 49<sup>th</sup> AIAA Aerospace Sciences Meeting, Orlando, Florida, Submitted.
139. Y. Huang, G.A. Risha, V. Yang, R.A. Yetter, *Combustion and Flame*, Vol.156, 2009, pp.5-13.
140. D.S. Sundaram, Y. Huang, P. Puri, G.A. Risha, R.A. Yetter, V. Yang, *Combustion and Flame*, In Preparation.
141. Y. Huang, G.A. Risha, V. Yang, R.A. Yetter, *Proceedings of the Combustion Institute*, Vol. 31, 2007, pp. 2001-2009.
142. Yu, H., Hambir, S. A., and Dlott, D. D., "Ultrafast dynamics of nanotechnology energetic materials," in *Multifunctional Energetic Materials*, edited by R. W. Armstrong, N. N. Thadhani, W. H. Wilson *et al.* (MRS Symp. Proc., 2006), Vol. 896, pp. 0896-H0803-0801
143. Richter, L. J., Petralli-Mallow, T. P., and Stephenson, J. C., *Vibrationally resolved sum-frequency generation with broad-bandwidth infrared pulses*, *Opt. Lett.* **23**, 1594-1596 (1998).
144. Yu, H., Dlott, D. D., and Kearney, F. R., *Time-resolved microscopy analysis of laser photothermal imaging media*, *J. Imag. Sci. Tech.* **50**, 401-410 (2006).
145. Conner, R. W. and Dlott, D. D., *Ultrafast condensed-phase emission from aluminized explosives: Nano-aluminum in Teflon*, *J. Phys. Chem.* **114**, 6731-6741 (2010).
146. Conner, R. W. and Dlott, D. D., *Ultrafast emission spectroscopy measurements of ignition of nano-aluminum in Teflon*, *Proceedings of the 2010 Technical Meeting of the Central States Section of The Combustion Institute submitted Feb 2010*, 2010).

147. Zamkov, M. A., Conner, R. W., and Dlott, D. D., Ultrafast chemistry of nanoenergetic materials studied by time-resolved IR spectroscopy: Aluminum nanoparticles in Teflon, *J. Phys. Chem. C* **111**, 10278-10284 (2007).
148. Wang, S., Yang, Y., Sun, Z., and Dlott, D. D., Fast spectroscopy of energy release in nanometric explosives, *Chem. Phys. Lett.* **368**, 189-194 (2002).
149. Parker, L. J., Ladouceur, H. D., and Russell, T. P., Teflon and Teflon/Al (nanocrystalline) decomposition chemistry at high pressures, *AIP Conf. Proc.* **505**, 941-944 (2000).
150. Jouet, R. J., Warren, A. D., Rosenberg, D. M., and Bellitto, V. J., "Surface passivation of bare Aluminum nanoparticles using perfluoroalkyl carboxylic acids," in *Synthesis, Characterization and Properties of Energetic/Reactive Nanomaterials, MRS Symp. Proc.*, edited by R. W. Armstrong, N. N. Thadhani, W. H. Wilson *et al.* (2004), Vol. 800, pp. in press.
151. Jouet, R. J., Carney, J. R., Granholm, R. H., Sandusky, H. W., and Warren, A. D., Preparation and reactivity analysis of novel perfluoroalkyl coated aluminum nanocomposites *Mat. Sci. Tech.* **22**, 422-429 (2006).
152. Lagutchev, A. S., Patterson, J. E., Huang, W., and Dlott, D. D., Ultrafast dynamics of self-assembled monolayers under shock compression: Effects of molecular and substrate structure, *J. Phys. Chem. B* **109**, 5033-5044 (2005).
153. Wang, Z., Cahill, D. G., Carter, J. A., Koh, Y. K., Lagutchev, A., Seong, N.-H., and Dlott, D. D., Ultrafast dynamics of heat flow across molecules, *Chem. Phys.* **350**, 31-44 (2008).
154. Wang, Z., Carter, J. A., Lagutchev, A., Koh, Y. K., Seong, N.-H., Cahill, D. G., and Dlott, D. D., Ultrafast flash thermal conductance of molecular chains, *Science* **317**, 787-790 (2007).
155. Lagutchev, A., Hambir, S. A., and Dlott, D. D., Nonresonant background suppression in broadband vibrational sum-frequency generation spectroscopy, *J. Phys. Chem. C* **111**, 13645-13647 (2007).
156. Pangilinan, G. I. and Russell, T. P., Role of Al-O<sub>2</sub> chemistry in the laser-induced vaporization of Al films in air, *J. Chem. Phys.* **111**, 445-448 (1999).
157. Carney, J. R., Miller, J. S., Gump, J. C., and Pangilinan, G. I., Time-resolved optical measurements of the post-detonation combustion of aluminized explosives, *Rev. Sci. Instrum.* **77**, 063103 (2006).
158. Fujiwara, H., Brown, K. E., and Dlott, D., Laser-driven flyer plates for reactive materials research, *AIP Conf. Proc.* **1195**, 1317-1320 (2010).
159. Fujiwara, H., Brown, K. E., and Dlott, D. D., High-energy flat-top beams for laser launching using a Gaussian mirror, *Appl. Opt.* **49**, 3723-3731 (2010).
160. Zik, O., Olami, Z., and Moses, E., "Fingering Instability in Combustion," *Physical Review Letters*, **81**, 18, 3868-3871, 2 November 1998.
161. Hwang, S., Mukasyan, A.S., and Varma, A., "Mechanisms of Combustion Wave Propagation in Heterogeneous Reaction Systems, *Combust. Flame*, **115**, 354-363, 1998.
162. Pojman, J.A., Craven, R., Khan, A., and West, W., "Convective Instabilities in Traveling Fronts of Addition Polymerization," *J. Phys. Chem.*, **96**, 7466-7472, 1992.
163. J.Y. Malchi, R.A. Yetter, S.F. Son, and G.A. Risha, Nano-Aluminum Flame Spread with Fingering Combustion Instabilities, *Proceedings of the Combustion Institute*, **31**, 2617-2624, 2007.
164. J.Y. Malchi, J.Y. Prosser, R.A. Yetter, and S.F. Son, Realizing the microgravity flame spread at 1g over a bed of nano-aluminum powder, *Proceedings of the Combustion Institute*, **32**, 2437, 2009.
165. G.A. Risha, S.F. Son, R.A. Yetter, V. Yang, and B.C. Tappan, Combustion of Nano-Aluminum and Liquid Water, *Proceedings of the Combustion Institute*, **31**, 2029-2036, 2007.
166. Risha, G. A., Sabourin, J.L., Yang, V., Yetter, R.A., Son, S. F., and Tappan, B. C., Combustion and conversion efficiency of nanoaluminum-water mixtures, *Combustion Science and Technology*, **180**,12, 2127, 2008.
167. J.L. Sabourin, G.A. Risha, R.A. Yetter, S.F. Son, and B.C. Tappan, Combustion Characteristics of Nanoaluminum, Liquid Water, and Hydrogen Peroxide Mixtures *Combustion and Flame*, **154**, 3, 587, 2008.

168. Sabourin, JL; Yetter, RA; Asay, BW, et al., Effect of Nano-Aluminum and Fumed Silica Particles on Deflagration and Detonation of Nitromethane, PROPELLANTS EXPLOSIVES PYROTECHNICS 34, 5, 385-393, 2009.
169. Sabourin, JL; Yetter, RA; Parimi, S, Exploring the Effects of High Surface Area Metal Oxide Particles on Liquid Nitromethane Combustion, JOURNAL OF PROPULSION AND POWER 26, 5, 1006-1015, 2010.
170. Sabourin, JL; Dabbs, DM; Yetter, RA; Dryer, FL; Aksay, IA, Functionalized Graphene Sheet Colloids for Enhanced Fuel/Propellant Combustion, ACS NANO 3, 13, 3945-3954, 2009.
171. Yetter, RA; Risha, GA; Son, SF Metal particle combustion and nanotechnology PROCEEDINGS OF THE COMBUSTION INSTITUTE Volume: 32 Pages: 1819-1838 Published: 2009
172. Asay, B. W., Son, S. F., Busse, J. R., and Oschwald, D. M. (2004) Ignition characteristics of metastable intermolecular composites. Prop., Exp., Pyro., 29, 4, pp. 216-219.
173. Son, S. F. and Brewster, M. Q. (1995) Radiation augmented combustion of homogeneous solids. Combust. Sci. Technol., 107, 127.
174. Begley, S. M. and Brewster, M. Q. (2007) Radiative properties of MoO<sub>3</sub> and Al nanopowders from light-scattering measurements. J. Heat Trans., 05-1167 (in publication)
175. Kuo, K.K., Chen, A. T., Davis, T. R., Convective burning in solid propellant cracks. AIAA Journal, 16, 6, pp. 600-607, 1978.
176. Ershov, A. P., Kupershtokh, A. L., Medvedev, D. A. (2001) Simulation of convective detonation waves in a porous medium by the lattice gas method. Comb., Exp., and Shock Waves, 37, 2, pp. 206-213.
177. Bockmon, B. S., Pantoya, M. L., Son, S. F., Asay, B. W. and Mang, J. T. (2005) Combustion velocities and propagation mechanisms of metastable interstitial composites. J. App. Phy., 98, 064903.
178. Wang, L. L., Munir, Z. A., and Maximov, Y. M. (1993) Thermite reactions: their utilization in the synthesis and processing of materials. J. Mat. Sci., 28, 3693.
179. Sanders, V. E., Asay, B. W., Foley, T. J., Tappan, B. C., Pacheco, A. N., and Son, S. F. (2006) Combustion and reaction propagation of four nanoscale energetic composites. 33rd Int. Pyro. Sem., pp. 113-121.
180. Varma, A., Lerat, J. P. (1992) Combustion synthesis of advanced materials. Chemical Engineering Science, 17, 9-11, pp. 2179-2194.
181. Munir, Z. A., and Anselmi-Tamburini, U. (1989) Self-propagating exothermic reactions: the synthesis of high-temperature materials by combustion. Mat. Sci. Reports, Vol. 3, 7-8, pp. 277-365.
182. S. Goroshin; J. Mamen; A. Higgins; T. Bazyn; N. Glumac; H. Krier, Proceedings of the Combustion Institute 31 (2007) 2011-2019.
183. S. W. Dean. The Influence of Gas Generation on Flame Propagation for Nano-Al Based Energetic Materials. Texas Tech University, Lubbock, TX, 2008.
184. L. E. Fried; K. R. Glaesemann; W. M. Howard; P. C. Souers; P. A. Vitello, in: 4.0 ed.; Lawrence Livermore National Laboratory: Livermore, C.A., 2004.
185. M. L. Hobbs; M. R. Baer; B. C. McGee, Propellants, Explosives, and Pyrotechnics 25 (5) (1999) 269-279.
186. Son, SF; Yetter, RA; Yang, V Introduction: Nanoscale composite energetic materials JOURNAL OF PROPULSION AND POWER Volume: 23 Issue: 4 Pages: 643-644 JUL-AUG 2007.
187. Son, SF; Asay, BW; Foley, TJ, et al., Combustion of nanoscale Al/MoO<sub>3</sub> thermite in microchannels JOURNAL OF PROPULSION AND POWER Volume: 23 Issue: 4 Pages: 715-721 JUL-AUG 2007.
188. Foley, T; Pacheco, A; Malchi, J, et al., Development of nanothermite composites with variable electrostatic discharge ignition thresholds, PROPELLANTS EXPLOSIVES PYROTECHNICS Volume: 32 Issue: 6 Pages: 431-434 2007.

189. Malchi, JY; Yetter, RA; Foley, TJ, et al. The effect of added Al<sub>2</sub>O<sub>3</sub> on the propagation behavior of an Al/CuO nanoscale thermite COMBUSTION SCIENCE AND TECHNOLOGY Volume: 180 Issue: 7 Pages: 1278-1294 2008.
190. Weismiller, MR; Malchi, JY; Yetter, RA, et al. Dependence of flame propagation on pressure and pressurizing gas for an Al/CuO nanoscale thermite PROCEEDINGS OF THE COMBUSTION INSTITUTE Volume: 32 Pages: 1895-1903 2009.
191. Dutro, GM; Yetter, RA; Risha, GA, et al. The effect of stoichiometry on the combustion behavior of a nanoscale Al/MoO<sub>3</sub> thermite PROCEEDINGS OF THE COMBUSTION INSTITUTE Volume: 32 Pages: 1921-1928 2009.
192. Weismiller, MR; Lee, JG; Yetter, RA Effects of Fuel and Oxidizer Particle Dimensions on the Propagation of Aluminum Containing Thermites, PROCEEDINGS OF THE COMBUSTION INSTITUTE Volume: 33, DECEMBER 2009.
193. Weismiller, MR; Lee, JG; Yetter, RA, Multiwavelength Pyrometry of Aluminum Containing Nano-Thermite Reactions PROCEEDINGS OF THE COMBUSTION INSTITUTE Volume: 33, DECEMBER 2009.
194. Malchi, JY; Foley, TJ; Yetter, RA, Electrostatically Self-Assembled Nanocomposite Reactive Microspheres ACS APPLIED MATERIALS & INTERFACES Volume: 1 Issue: 11 Pages: 2420-2423, 2009.
195. Wolfe, D. E., Eden, J. T., Potter, J. K., & Jaroh, A. P. (2006). Investigation and characterization of Cr<sub>3</sub>C<sub>2</sub>-based wear-resistant coatings applied by the cold spray process. *Journal of Thermal Spray Technology*, 400-412.
196. Stoltenhoff, T., Kreye, H., & Richter, H. J. (2001). An analysis of the cold spray process and its coatings. *Journal of Thermal Spray Technology*, 542-550.
197. DeLucia, F.C., Samuels, A.C., Harmon, R.S., Walters, R.A., McNesby, K.L., LaPointe, A., Winkel, R.J., Miziolek, A.W., *IEEE Sensors Journal*, Vol. 5 (4), 2005.

